Universidad de Valladolid

Escuela de Doctorado Universidad de Valladolid

PhD PROGRAMME IN INDUSTRIAL ENGINEERING

DOCTORAL THESIS:

ADVANCED MODELING AND OPTIMIZATION OF THE OXY-COMBUSTION NET POWER CYCLE AND HEAT TRANSFER IN SUPERCRITICAL CO_2 MICROFLOWS FOR HIGH-PERFORMANCE COMPACT HEAT EXCHANGERS

Submitted by:

D. Iván Velázquez Palencia

In fulfillment of the requirements for the:

PhD Degree by the University of Valladolid (Spain)

Supervised by:

Miriam Reyes Serrano, PhD

Universidad de Valladolid

Escuela de Doctorado Universidad de Valladolid

PROGRAMA DE DOCTORADO EN INGENIERÍA INDUSTRIAL

TESIS DOCTORAL:

MODELADO Y OPTIMIZACIÓN AVANZADOS DEL CICLO DE OXÍ-COMBUSTIÓN NET POWER Y DE LA TRANSFERENCIA DE CALOR EN MICROFLUJOS DE CO_2 SUPERCRÍTICO PARA INTERCAMBIADORES DE CALOR COMPACTOS DE ALTO DESEMPEÑO

Presentada por:

D. Iván Velázquez Palencia

Para optar al grado de:

Doctor por la Universidad de Valladolid (España)

Dirigida por:

Dra. Miriam Reyes Serrano

Thesis summary

This PhD thesis contributes to the technological advancement and performance improvement of the NET Power thermodynamic cycle, an innovative oxy-combustion-based energy production technology that employs supercritical CO_2 ($scCO_2$) as a working fluid. A major objective is to conduct a comprehensive experimental and computational investigation on heat transfer in horizontal $scCO_2$ microflows within the operating conditions of the NET Power cycle, reaching up to 30 MPa. This study aims to constitute a first research step towards the replacement of the currently established printed circuit heat exchanger units by novel, high-performance, and compact micro shell-and-tube heat exchanger (MSTHE) units for the low-temperature section of the NET Power cycle recuperator, the key component of the cycle for achieving high thermal efficiencies.

The study begins by performing a complete detailed thermodynamic model of the most advanced NET Power cycle embodiment. The binary interaction parameters of several equations of state are optimized to characterize the working fluid properties, under the specific pressure, temperature, and composition ranges of the cycle. A novel hybrid optimization algorithm is developed to propose the optimal set of operating parameters for maximum cycle efficiency. Moreover, the part-load performance of the cycle is analyzed, offering new valuable insights into its operational flexibility, and defining the operating boundaries of the recuperator for conducting the subsequent heat transfer investigation.

An experimental system is built to conduct pioneer heat transfer experiments, up to 30 MPa, in $scCO_2$ flows through a uniformly heated, horizontal microtube. The effect of key parameters such as the pressure, mass flux, heat flux, inlet fluid temperature, buoyancy and thermal acceleration, on the heat transfer performance are investigated through sensitivity studies. To predict the heat transfer coefficients, empirical models, including an artificial deep neural network, are developed. These models provide a foundation for the thermal design of MSTHE units for the low-temperature section of the recuperator. Then, the empirical heat transfer model is integrated into a one-dimensional thermal-hydraulic model to assess the MSTHE performance. The results demonstrate high operational effectiveness and structural advantages of MSTHE over conventional heat exchange architectures, positioning MSTHEs as a promising high-performance, and cost-effective alternative for future deployment.

Resumen de la tesis

Esta tesis doctoral contribuye al avance tecnológico y a la mejora del desempeño del ciclo termodinámico NET Power, una innovadora tecnología de producción energética basada en la oxí-combustión, que utiliza CO_2 supercrítico ($scCO_2$) como fluido de trabajo. Uno de los objetivos principales es realizar una investigación experimental y computacional sobre la transferencia de calor en microflujos horizontales de $scCO_2$, bajo las condiciones operativas del ciclo NET Power, alcanzando presiones de hasta 30 MPa. Este estudio representa un primer avance en la investigación orientada a reemplazar las unidades de intercambio de calor de circuito impreso, actualmente establecidas, por novedosas unidades compactas y de alto rendimiento, basadas en intercambiadores de carcasa y microtubos, para el recuperador del ciclo NET Power, componente clave para alcanzar elevadas eficiencias térmicas.

El estudio comienza con el desarrollo de un modelo termodinámico completo de la configuración más avanzada de ciclo NET Power. Los parámetros de interacción binaria de varias ecuaciones de estado (EoS) son optimizados para caracterizar las propiedades del fluido, bajo los rangos específicos de presión, temperatura y composición del ciclo. Un algoritmo híbrido de optimización eficiente es desarrollado para proponer el conjunto óptimo de parámetros operativos que maximicen la eficiencia térmica del ciclo. A partir de la configuración óptima propuesta, el comportamiento del ciclo en cargas parciales es analizado, proporcionando nuevas y provechosas proyecciones sobre su flexibilidad operativa, y definiendo los límites de operación del recuperador que permiten la realización del estudio posterior de transferencia de calor.

Un sistema experimental fue construido para realizar experimentos pioneros de transferencia de calor, hasta 30 MPa, en flujos de $scCO_2$ por un microtubo horizontal uniformemente calentado. Se investiga el efecto de variables clave como la presión, flujo másico, flujo de calor, temperatura de entrada del fluido, flotabilidad y aceleración del flujo sobre el desempeño de la transferencia de calor a partir de estudios de sensibilidad. Para predecir los coeficientes de transferencia de calor convectivos, se desarrollan modelos empíricos, incluyendo una red neuronal artificial profunda. Estos modelos constituyen una base sólida para el diseño termo-hidráulico de las unidades MSTHE. Posteriormente, el modelo empírico de transferencia de calor se integra en un modelo termo-hidráulico unidimensional para evaluar el desempeño del MSTHE.

La combinación de las EoSs GERG-2008 y LKP demostró la mayor precisión, optimizando parámetros operativos que elevaron la eficiencia neta del ciclo de 54.41% a 55.94%. Bajo condiciones de carga parcial, el ciclo mantiene buena eficiencia hasta 50% de carga, destacando su versatilidad operativa. En paralelo, se investigó la transferencia de calor en microtubos con $scCO_2$ hasta 30 MPa. Se identificaron efectos de flotabilidad que generan perfiles térmicos asimétricos y estructuras de convección natural, afectando la eficiencia del intercambiador. El modelo de transferencia de calor basado en una red

neuronal logró predecir los coeficientes de transferencia de calor con una desviación de 6.74%. Finalmente, se determinó que los intercambiadores de microtubos presentan mejor tolerancia estructural que los de circuito impreso bajo cargas variables, constituyendo una alternativa robusta y eficiente para el ciclo NET Power.

El estudio demuestra que un modelado termodinámico preciso y una optimización de parámetros operativos permiten mejorar significativamente la eficiencia del ciclo NET Power. Los intercambiadores de microtubos, por su capacidad de adaptación térmica y resistencia a gradientes de temperatura axiales, pueden ser propuestos como alternativas de alto desempeño frente a los intercambiadores de circuito impreso. Además, el uso de $scCO_2$ en microtubos reveló fenómenos térmicos complejos, como convección mixta y microvórtices inducidos por flotabilidad, que deben considerarse en el diseño. En conjunto, estos hallazgos contribuyen de forma sustancial al desarrollo de tecnologías más eficientes y confiables para ciclos de energía con captura de carbono.

General index

Figure Index

Table index

Nomenclature

A	heat exchange area, m^2
$\hat{a}$	molar Helmholtz free energy, $J \cdot mol^{-1}$
a, b, c, d, C, m	fitting coefficients (when accompanied by subindices)
b	bias
C_f	skin friction coefficient
c_p	specific heat at constant pressure, $J \cdot kg^{-1} \cdot K^{-1}$
$\hat{c}_p$	molar specific heat at constant pressure, $J \cdot mol^{-1} \cdot K^{-1}$
c_v	specific heat at constant volume, $J \cdot kg^{-1} \cdot K^{-1}$
D	characteristic length (i.e., diameter for tubes), m
D_h	hydraulic diameter, m
d_s	specific diameter
E_T	Ackermann correction factor
F	flow parameter
f	friction factor
G	mass flux, $kg \cdot m^{-2} \cdot s^{-1}$
g	gravitational acceleration, $m \cdot s^{-2}$
Gr	Grashof number
H	stagnation enthalpy, $J \cdot kg^{-1}$
h	specific mass enthalpy, $J \cdot kg^{-1}$
$\hat{h}$	specific mole enthalpy, $J \cdot mol^{-1}$
$\Delta\hat{h}_v$	molar evaporation enthalpy, $J \cdot mol^{-1}$
I	current intensity, A
Ja	Jackson parameter for buoyancy
k	turbulent kinetic energy, $m^2 \cdot s^{-2}$
K_1, K_2, K_3	calibration parameters of the turbine model
k_{ij}	binary interaction parameters
K_v	McEligot parameter for flow acceleration
K_τ, K_f	film drag coefficients
L	length, m
$\mathcal{L}$	characteristic length of the film flow, m
Le	Lewis number
M	molar mass, $g \cdot mol^{-1}$
$\dot{m}$	mass flow rate, $kg \cdot s^{-1}$
N	number of points
$\dot{N}$	molar flow rate, $mol \cdot s^{-1}$
$\dot{n}$	locally condensing molar flux, $mol \cdot m^{-2} \cdot s^{-1}$
N_s	number of sections
n_s	specific velocity
N_t	number of tubes

Nu	Nusselt number
p	pressure, MPa/bar
P_k	turbulent kinetic energy production, $kg \cdot m^{-1} \cdot s^{-3}$
Pr	Prandtl number
P_t	pitch (separation between tubes), m
$\dot{Q}$	heat flow, MW
$\dot{q}$	volumetric heat generation rate, $W \cdot m^{-3}$
$\dot{q}_w$	heat flux, $W \cdot m^{-2}$
R	universal constant of gases, $J \cdot mol^{-1} \cdot K^{-1}$
r	radial distance, m
Re	Reynolds number
Ri	Richardson number
s	specific entropy, $J \cdot kg^{-1} \cdot K^{-1}$
T	temperature, ºC/K
T_c	critical temperature, K
T_r	reduced temperature; (T/T_c)
ΔT_c	cold-side temperature difference, ºC
ΔT_h	hot-side temperature difference, ºC
TI	turbulence intensity, %
ΔT_{lm}	log-mean temperature difference, ºC
U	overall heat transfer coefficient, $W \cdot m^{-2} \cdot K^{-1}$
$\mathcal{U}$	voltage, V,
u	flow velocity, $m \cdot s^{-1}$
u_τ	friction velocity, $m \cdot s^{-1}$
$\dot{V}$	volumetric flow rate, $m^3 \cdot s^{-1}$
v	kinematic viscosity, $m^2 \cdot s^{-1}$
$\dot{W}$	work flow, MW
w	specific work, $J \cdot kg^{-1}$, or synaptic weight of the neural network
$\mathcal{X}$	binary diffusion coefficient, $m^2 \cdot s^{-1}$
x	axial distance, m
$\bar{x}$	molar composition of the mixture
$\hat{x}$	molar fraction in the liquid phase
y	distance from the tube wall, m
$\hat{y}$	molar fraction in the gas phase
z	compressibility factor

Greek symbols

α	convective heat transfer coefficient, $W \cdot m^{-2} \cdot K^{-1}$, or alpha function
β	volumetric expansivity, K^{-1}
γ	polytropic coefficient
δ	film thickness, μm

ε	effectiveness, %, or turbulent dissipation rate, $W \cdot kg^{-1}$, or absolute roughness, mm
ϵ	intermittency factor
ζ	surface area density, $m^2 \cdot m^{-3}$
η	efficiency parameter, %
Θ	flow coefficient
θ	mass transfer coefficient, $m \cdot s^{-1}$
ϑ	volumetric vapor content
λ	thermal conductivity, $W \cdot m^{-1} \cdot K^{-1}$
μ	dynamic viscosity, Pa·s
ξ_{ac}	coefficient of acceleration resistance
ξ_{Pe}	coefficient of friction resistance
ρ	mass density, $kg \cdot m^{-3}$
$\hat{\rho}$	molar density, $mol \cdot m^{-3}$
σ	experimental uncertainty
ς	isothermal compressibility, Pa^{-1}
τ	shear stress, MPa
υ	specific volume, $m^3 \cdot kg^{-1}$
$\hat{\upsilon}$	molar volume, $m^3 \cdot mol^{-1}$
υ_r	reduced volume; $(\frac{p_r}{RT_r\rho})$
φ	work coefficient
ψ	Jackson parameter for flow acceleration
ω	angular velocity, $rad \cdot s^{-1}$, or specific turbulent dissipation rate, s^{-1}, or acentric factor
Ω	distillation column diameter, m

Subscripts

1	H_2O
2	CO_2
b	bulk
c	cold
cr	critical
e	equivalent
f	film
g	gas
h	hot/heated
i	index/inner
in	inlet
j	index
k	heat exchange section
lam	laminar flow regime

min	minimum
o	outer
off	off-design
on	on-design
out	outlet
pc	pseudo-critical
r	relative
s	shell
sat	saturation
sq	square tube configuration
t	tube
th	threshold
tra	transitional flow regime
tri	triangular tube configuration
tur	turbulent flow regime
w	wall

Superscripts

0	simple fluid
assoc	association term of the PC-SAFT EoS
disp	dispersion term of the PC-SAFT EoS
hc	hard-chain term of the PC-SAFT EoS
hs	hard-sphere term of the PC-SAFT EoS
in	inlet
R	reference fluid
res	residual
out	outlet
+	dimensionless
−	mean term (Reynolds-averaged)
~	mean term (Favre-averaged)
′′	fluctuating term
∗	guessed variable
°	drag
^	molar quantity

Acronyms

AARD	average of absolute relative deviation (%)
AGM	algebraic multigrid method
AKN	Abe-Kondoh-Nagano k-ε turbulence model
ASU	air separation unit
BWRS	Benedict-Webb-Rubin-Starling
CCC	cold composite curve

CCUS	carbon capture usage and storage
CFD	computational fluid dynamics
CHE	compact heat exchanger
CMF	corrected mass flow
COT	combustor outlet temperature
CPA	cubic-plus-association
CSTE	conventional shell-and-tube exchanger
DC	direct current
DNN	deep neural network
DNS	direct numerical simulation
EoS	equation of state
EOS-CG	equation of state of combustion gases
HCC	hot composite curve
HPC	high-pressure column
HTS	hot-temperature section
HU	hidden unit
LHV	low heating value
LKP	Lee-Kesler-Plöcker
LPC	low-pressure column
LS	Launder-Sharma k-ε turbulence model
LTS	low-temperature section
MSTHE	micro shell-and-tube heat exchanger
MTS	medium-temperature section
NG	natural gas
NTU	number of transfer units
PCHE	printed circuit heat exchanger
PC-SAFT	perturbed chain – statistical associating fluid theory
PR	Peng-Robinson
PSO	particle swarm optimization
$pVT\bar{x}$	pressure-volume-temperature-composition
PWM	pulse width modulation
RANS	Reynolds averaged Navier Stokes equations
RD	relative deviation
RHE	recuperative heat exchanger
RNG	RNG k-ε turbulence model
SAFT	statistical associating fluid theory
$scCO_2$	supercritical carbon dioxide
scH_2O	supercritical water
SRK	Soave-Redlich-Kwong
SST	SST k-ω turbulence model
TIP	turbine inlet pressure
TOP	turbine outlet pressure

TOT	turbine outlet temperature
VLE	vapor-liquid equilibrium
YS	Yang-Shih k-ε turbulence model

Chapter 1
Introduction

1 Introduction

Anthropogenic greenhouse gas emissions, primarily from fossil fuel combustion in the energy sector, which accounted for about 87% of global emissions in 2023, have led to unprecedented atmospheric concentrations of CO_2, CH_4, and NO_x [1]. These emissions are the primary cause of the increment in the Earth's surface temperature since the mid-20th century. To limit this temperature rise to 1.5 ºC, and to meet the net-zero emissions target by 2050, global emissions must be reduced by 5 to 10 gigatons per year [2]. However, the use of fossil fuels is expected to continue in the medium term due to their economic relevance and widespread availability. In this context, carbon capture usage and storage (CCUS) systems, among which oxy-combustion is particularly promising due to the high concentration of CO_2 in the flue gases [3,4], are emerging as key technologies to mitigate the environmental impact.

Oxy-combustion consists of burning fuel with pure O_2 at near stoichiometric conditions, and recirculate the flue gases (mainly CO_2 and water vapor) to moderate the combustion temperature [5]. Since atmospheric N_2 is not used as a diluent in the combustion process, NO_x formation is nearly eliminated, and the high CO_2 concentration in the flue gases reduce the energy demand of the subsequent purification stages. Among the different oxy-combustion-based power cycle embodiments, the innovative NET Power cycle, patented in 2011, has demonstrated the highest overall cycle performance [6].

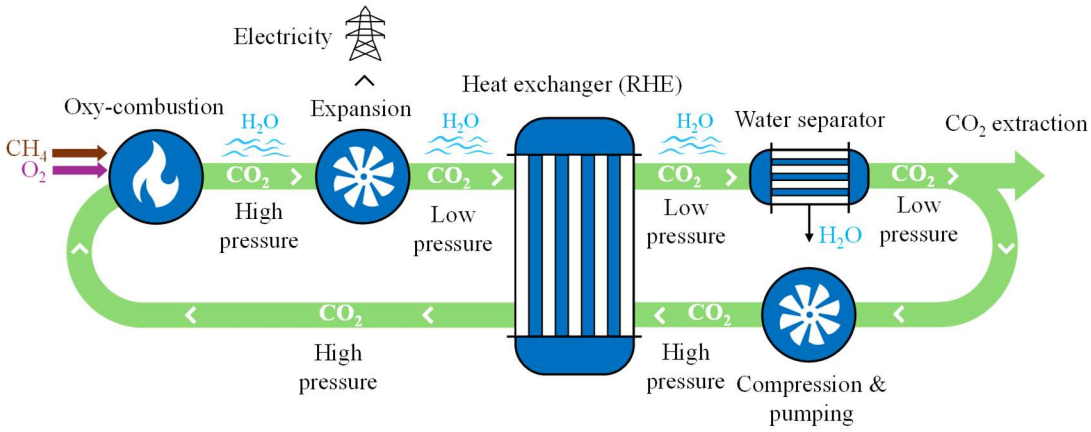

Fig. 1.1. Schematic representation of a $scCO_2$-based oxy-combustion turbine power plant.

Fig. 1.1 presents a schematic representation of the NET Power cycle. The oxy-combustion of natural gas with oxygen occurs in a supercritical CO_2 ($scCO_2$)-rich environment that acts as a temperature moderator. The flue gases at high pressure (~ 30 MPa) and temperature (~ 1150 ºC), are expanded through a turbine until a pressure of ~ 3 – 4 MPa and a temperature of ~ 750 ºC, while producing energy. Part of the residual heat is transferred to the recirculating working fluid via a recuperative heat exchanger

(RHE). After water condensation and removal, the CO_2-enriched stream is compressed in the supercritical phase, preheated in the RHE, and recirculated to the oxy-combustor [7].

The high density ($\rho \sim 10^3$ kg·m^{-3}) and low viscosity ($\mu \sim 10^{-5}$ Pa·s) characterizing the recirculating scCO_2 fluid provide two key advantages: (i) low volumetric flow rate, enabling the use of compact turbomachinery; and (ii) low specific compression work, allowing thermal efficiencies of up to 55. 1%. Nevertheless, a major challenge arises from the need to cool the turbine exhaust gases to the near critical temperature of CO_2 (~ 31 ºC) in order to optimize the compression stage. This process involves an exceptionally high enthalpy change within the RHE, making the use of conventional heat exchanges unfeasible due to the impractically large exchange area required. As a result, printed circuit heat exchangers (PCHEs) have been adopted as the standard compact heat exchanger architecture for the RHE [8].

Recent advances in compact heat exchange technologies have shown that micro shell-and-tube heat exchangers (MSTHE) offer superior performance compared to PCHEs, as being more compact, easier to maintain and cost-effective [9]. In this context, replacing PCHE units with MSTHEs in the RHE could turn the oxy-combustion-based CO_2 capture NET Power cycle into a more efficient, cost-effective, flexible, and ultimately competitive zero-emissions energy technology, in line with the climate goals set for 2050.

Before addressing the technical challenges associated with the heat exchanger design, it is important to highlight that the NET Power cycle configuration has further evolved since its original patent in 2011 [10]. This means that the optimal set of cycle parameters that maximizes the efficiency of the most updated cycle embodiment has not yet been determined and reported in the literature. Identifying this optimal configuration, and analyzing off-design cycle behavior, is essential to, among other technical purposes, guide subsequent research on heat transfer in scCO_2 microflows applicable to MSTHEs. In addition to the research gap in the thermodynamic modeling of the NET Power cycle, a significant limitation has been identified in the widespread use of the uncalibrated Peng-Robinson (PR) equation of state (EoS) for cycle modeling purposes. The PR EoS has shown notable deficiencies in predicting the volumetric properties of scCO_2-rich mixtures, and particularly estimating the compositions of the phases in equilibrium of CO_2 – H_2O mixtures. This undermines the reliability of the outcomes derived from the NET Power cycle thermodynamic models reported in literature, considering the strong real gas effects experienced by the working fluid. Regarding heat transfer, the heat transfer process in scCO_2 through microtubes, under the operating pressure range of the NET Power cycle (10 – 30 MPa), has not been previously investigated in literature.

This PhD Thesis addresses these key research challenges related to the NET Power cycle: (i) thermodynamic modeling of the advanced NET Power cycle embodiment, including calibration and assessment of EoSs for reliably predicting the volumetric and phase behavior of the supercritical working fluid; and (ii) investigation and modeling of

the heat transfer process in $scCO_2$ flows through microtubes at pressures up to 30 MPa, for application in high-performance MSTHEs within the NET Power cycle RHE.

1.1 Antecedents

The motivation for this PhD thesis arose from a stay at Engie Laborelec (Belgium), between February and June 2022, in the framework of the Master's Thesis for obtaining the master's degree in Industrial Engineering, carried out by the author of this thesis work. The main purpose of the Master's Thesis was to conduct a first theoretical study and modeling of the advanced NET Power cycle, using a process flow diagram provided directly by NET Power Inc. The purpose was to understand the thermodynamic processes of the cycle, evaluate its performance and capabilities, as well as to explore the main technological challenges for its successful implementation, with a special focus on its applicability to the European energy market.

As a result of the Master's Thesis work, the high potential of the NET Power cycle as an efficient zero greenhouse gas emission power generation technology was identified, aligned with the European climate targets for 2050. Furthermore, three key challenges were outlined that require a specific research effort to encourage its development:

i. Development of the turbine, specifically to operate with $scCO_2$-rich mixtures under supercritical conditions.
ii. Improvement of the thermodynamic models of the NET Power cycle, with particular attention to the reliability in the prediction of the thermodynamic properties of the supercritical working fluid by an EoS.
iii. Understanding the impact of a potential migration from PCHEs towards MSTHEs for the main cycle recuperator, to improve maintenance and operational flexibility, increase compactness, reduce mass and, thus, thermal inertia. This last feature is particularly relevant to accelerate the dynamic response of the cycle to load variations, which is critical in the context of the European electricity market, characterized by its high variability degree due to the availability of renewable assets.

Currently, the development of challenge (i) is being addressed by an external entity. However, challenges (ii) and (iii) are not receiving sufficient attention in scientific literature or in current technological initiatives. NET Power Inc. itself considers these aspects as critical and essential to increase the efficiency and competitiveness of their technology. Consequently, NET Power Inc., Engie and TES-H2 agreed to support a PhD thesis that deals with challenges (ii) and (iii), with the objective of filling the existing knowledge gaps through a research work whose specific objectives are detailed in the following section.

1.2 Objectives

The initial objectives of this PhD thesis are defined with the intention of contributing to the technological development and future commercialization of the NET Power cycle, by addressing the knowledge gaps related to challenges (ii) and (iii) previously outlined in Section 1.1.

These objectives are structured into two main thematic areas: on the one hand, the thermodynamic modeling of the advanced NET Power cycle, and volumetric and phase properties of the working fluid; and on the other hand, the investigation of the heat transfer process in $scCO_2$ flows through microtubes, under the operating conditions representative for the NET Power cycle, as a first step towards the implementation of MSTHEs in the thermal recuperator of the cycle. More specific, the proposed objectives are as follows:

1. Thermodynamic modeling of the advanced NET Power cycle and working fluid.
    1. Evaluate and improve the reliability of the EoSs, commonly used in literature to model $scCO_2$-rich mixtures, through the calibration of binary interaction parameters from experimental density and vapor-liquid equilibrium data collected from the literature within the specific pressure, temperature and composition ranges of the working fluid of the NET Power cycle.
    2. Develop a reliable thermodynamic model of the most up-to-date NET Power cycle embodiment, capable of accurately projecting the cycle's behavior under both nominal and off-design conditions.
    3. Determine the optimal parametric configuration set that maximizes the thermal efficiency of the advanced NET Power cycle, by applying the developed thermodynamic model in combination with a suitable optimization algorithm.
    4. Analyze the thermodynamic performance of the cycle under part-load conditions, identifying the complete ranges of pressure, temperature, and mass flow rates of the fluid flows within the recuperator of the cycle, in order to provide a solid basis for the subsequent heat transfer research.
2. Investigation of the heat transfer in $scCO_2$ flows through a microtube up to 30 MPa for application in MSTHEs.
    1. Experimentally investigate the heat transfer process in $scCO_2$ flowing through a microtube (with hydraulic diameters lower than 1 mm) and at pressures up to 30 MPa, representative within the low-temperature section of the NET Power cycle recuperator, where real gas effects become significant and influence heat transfer mechanisms. The study includes an assessment of the influence of key variables such as mass flux, heat flux, inlet fluid temperature, buoyancy, and thermal flow acceleration on local convective heat transfer coefficients.

2. Design and build a dedicated experimental test rig to conduct the investigation described above. This task constitutes an intrinsic objective of the Thesis work.
3. Develop an empirical heat transfer model for $scCO_2$, based on a correlation and, if necessary to improve the model accuracy, on artificial intelligence techniques. The objective is to provide predictive tools for heat transfer coefficients that are directly applicable in the design of high-performance MSTHEs for the NET Power cycle recuperator.
4. Establish the theoretical basis for heat transfer mechanisms in $scCO_2$, based on fluid dynamics analysis, to explain the experimental results. This includes the development of CFD models, and the validation of first-order RANS turbulent models against the acquired experimental data points.
5. Model a MSTHE for integration into the low-temperature section of the NET Power cycle recuperator and assess its thermal-hydraulic performance as a function of: (i) the main geometric design parameters and (ii) the cycle load degree.

1.3 Structure

In order to attain the objectives established in Section 1.2, the Thesis has been organized into three major thematic parts:

Part 1: State of the art (Chapter 2)

Chapter 2 provides a thorough literature survey on the state of art on the NET Power cycle, outlining its relevance within the current climate context and its role as an oxy-combustion CO_2 capture technology in the framework of CCUS systems. The cycle is described in detail, as well as the major advances and scientific contributions that have driven its technological development since its original patent. Particular attention is devoted to the progress in the thermodynamic modeling of the working fluid, and the thermal recuperator. Finally, the most relevant compact heat exchange technologies are reviewed in detail, comparing PCHEs and MSTHEs, and exposing the advantages of the former to justify the motivation for this Thesis work.

Part 2: Thermodynamic modeling of the NET Power cycle (Chapters 3 & 4)

This Part addresses the general objective 1 stated in Section 1.2: *Thermodynamic modeling of the advanced NET Power cycle and working fluid*.

Chapter 3 details the methodology followed for the calibration of the binary interaction parameters of the EoSs, and their validation against experimental data available in literature. In addition, the thermodynamic model of the NET Power cycle under off-design conditions is presented, together with the optimization algorithm developed to find the operating configuration that maximizes the cycle efficiency.

Chapter 4 presents the results obtained from the EoSs assessment and the NET Power cycle modeling. The optimal operating point is given, the impact of the EoS choice is analyzed, and the operating ranges of the fluid flows within the recuperator are determined as a function of the cycle load, which serves as the basis for the third Part.

Part 3: Heat transfer investigation in $scCO_2$ and MSTHE assessment (Chapters 5 & 6)

This Part addresses the general objective 2 stated in Section 1.2: *Investigation on heat transfer in $scCO_2$ flows through microtubes up to 30 MPa for application in MSTHEs*.

Chapter 5 describes the experimental system built to measure the heat transfer coefficients of $scCO_2$ flows through a microtube, for pressures up to 30 MPa. The CFD numerical models are also presented, and the turbulence models are validated against the experimental data. Finally, the MSTHE thermal-hydraulic modeling approach is exposed.

Chapter 6 discusses the experimental results obtained through a sensitivity study of the main experimental variables such as pressure, mass flux, heat flux and inlet temperature on heat transfer in $scCO_2$. The predictive heat transfer models, fitted from the acquired experimental heat transfer coefficients, are developed. In addition, heat transfer mechanisms associated with buoyancy and flow acceleration are investigated using CFD models to explain the experimental observations. Finally, the evaluation of the thermal-hydraulic performance of the MSTHE is presented.

1.4 Publications and contributions

The journal publications and conference contributions that support the results of this work are detailed in Appendix D of this document.

Chapter 2
State of the art

2 State of the art

The NET Power cycle is an innovative, efficient, and potential cost-effective technology, derived from the original Allam-Fetvedt thermodynamic cycle patented in 2011, for zero-emission energy production through an oxy-combustion process of natural gas and pure oxygen in a supercritical CO_2 ($scCO_2$) atmosphere. This system captures essentially 100% of its CO_2 emissions without additional capture systems [7].

This chapter describes the NET Power cycle and reviews the advancements attained to date since it was originally designed. As a CO_2 capture method for clean energy production, the chapter begins by situating the NET Power cycle within the current environmental climate change context and the existing carbon capture, usage and storage (CCUS) systems. Then, the most up-to-date cycle embodiment is described in detail, reviewing the adaptations that have been suggested by researchers to improve its performance. The NET Power cycle adopts circulating $scCO_2$ as a working fluid, whose behavior, characterized by strong real gas effects, especially near the critical conditions, differs significantly from constant property fluids of traditional gas turbine power cycles. Hence, a thermodynamic mapping of the cycle is presented to demonstrate the capabilities, advantages and challenges derived by applying a supercritical fluid as the working fluid. The main progress and findings achieved in the development and understanding of the cycle, and in the modeling of the supercritical working fluid, are then reviewed.

2.1 CCUS systems

Climate change, mainly caused by rising CO_2 levels in the atmosphere, affects all natural life as a result of the increase in temperature of the earth's atmosphere [11]. Global primary energy consumption was 619.63 Exajoules in 2023, rising 1.4% since 2013. However, the total CO_2 emissions from energy augmented 0.7% in the same period [1]. According to the Intergovernmental Panel on Climate Change, the global rate of anthropogenic gas emissions should be annually reduced between 5 – 10 Gigatons to achieve the net zero emissions targets by 2050, and limit the earth's surface temperature rise by 1.5 ºC [2,12]. Numerous proposals for the decarbonization of the industrial sector have been put forward, including CCUS systems, which will play a key role in the decarbonization of the industrial cement, glass, metals, petrochemicals and power generation sectors. CCUS systems consist of the following stages: CO_2 capture, purification and compression, transport, and use or storage [13].

There are essentially three types of CO_2 capture systems associated with the combustion process: post-combustion, pre-combustion and oxy-fuel combustion [3], the latter being the most promising technology for zero-emission energy production. A

general outline of the thermochemical processes that take place in the CO_2 capture technologies are shown in Fig. 2.1. Post-combustion systems capture CO_2 by chemical absorption/desorption processes with amines, once the combustion process has taken place in a conventional combined cycle gas turbine. Air is used as an oxidant in the combustion process, which means that the CO_2 concentration in the flue gas is low, and the post-combustion CO_2 capture unit processes a high volumetric flow. Thus, large equipment is required for the CO_2 capture, which leads to expensive technology [14]. In pre-combustion systems [15], the fuel is treated prior to the combustion process by removing carbon from fuel by steam reforming, partial oxidation or autothermal reforming, demanding a considerable energy input [4]. Oxy-combustion consists of burning fuel with high-purity O_2, instead of air, at near stoichiometric conditions. Therefore, the resulting combustion gases are mainly composed of CO_2, vapor steam, and a reduced impurity content (CO, N_2, O_2, Ar, H_2, CH_4). Steam is condensed and separated from the mainstream, and the impurities are removed in a purification unit [16], resulting in a high-purity sequestered CO_2 stream. High-purity O_2 is obtained from distillation-based cryogenic air separation units, which are energy intensive [17,18]. The CO_2-rich flue gases are expanded prior to being captured while producing energy, and the CO_2 that is not captured is recompressed and recirculated back to the combustor, forming a semi-closed cycle which results in the oxy-combustion turbine power plants that will be introduced in Section 2.2.

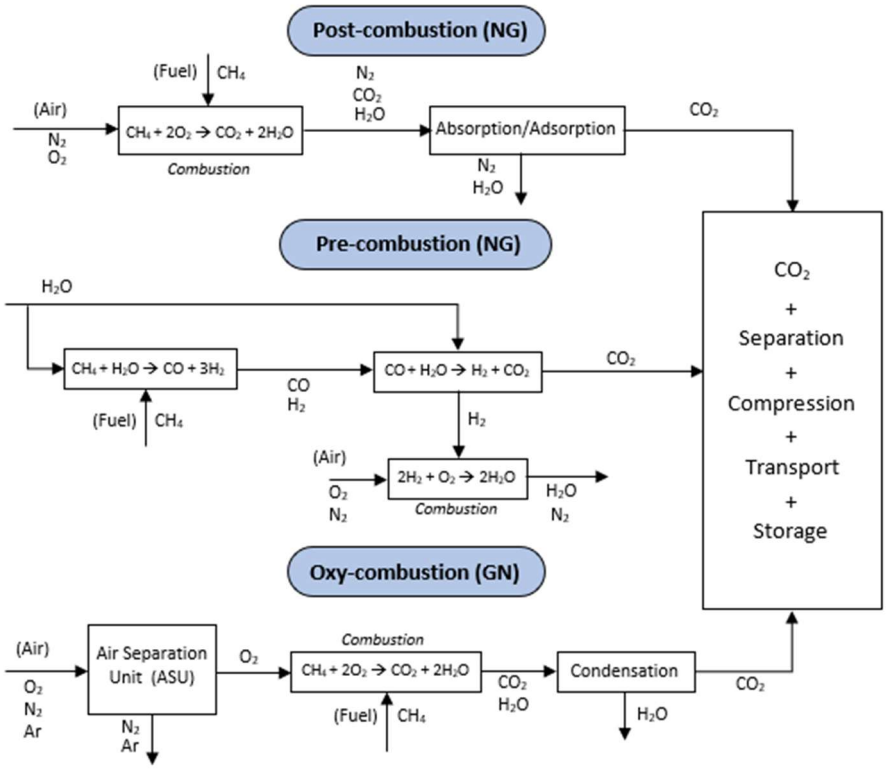

Fig. 2.1. Post-combustion, pre-combustion and oxy-fuel combustion CO_2 capture technologies for natural gas (NG).

Once the CO_2 is captured, it is purified and compressed in a carbon purification unit for transport either by pipeline, ship or truck. These transport systems require CO_2 purities above 95% [19], with a reduced content of impurities such as H_2O, O_2 and CO to avoid corrosion phenomena [20]. This demand for high quality CO_2 influences both the selection of the capture technology and the carbon purification unit. It is generally preferable to transport the CO_2 in the supercritical dense-phase (at pressures of 9 – 12 MPa and ambient temperature) due to its gas-like viscosity and liquid-like density [21,22].

Then, purified CO_2 can be stored or used directly after capture and transport. CO_2 can be stored in algae, underground geological formations, and minerals being the most common storage option due to the experience already developed on gas reservoirs and injection techniques. In terms of use, CO_2 can be used in the food and pharmaceutical industry [23], or for enhanced oil recovery [24]. In addition, CO_2 may be used indirectly in the production of synthetic fuels such as e-methane or methanol by hydrogenation of CO_2 [25], as well as in high value-added chemicals such as olefins or aromatics.

2.2 Oxy-combustion turbine power cycles

Oxy-combustion systems are the most promising CO_2 capture technology for emission-free energy production [26]. Based on oxy-combustion technology, several power cycle embodiments have been proposed, including the Semi-Closed Oxy-Combustion Combined Cycle [27], the MATIANT cycles [28], the NET Power cycle [29], the Graz cycle [30], the CES cycle [31] and the AZEP cycle [32]. A complete revision of these cycles can be found in Mancuso et al. [33]. The Semi-Closed Oxy-combustion Combined Cycle, MATIANT, and NET Power cycle use recirculating $scCO_2$ as a combustion temperature moderator. Hence, the working fluid in these cycles is a mixture composed mainly of $scCO_2$. These cycles are called CO_2-based oxy-combustion turbine power cycles. The GRAZ and CES cycles use supercritical H_2O (scH_2O) as combustion temperature moderator instead of CO_2. In these cycles, the working fluid consists mainly of H_2O. These cycles are called H_2O-based oxy-combustion turbine power cycles. In the Semi-Closed Oxy-combustion Combined Cycle, MATIANT, NET Power, GRAZ and CES cycles, high-purity O_2 is obtained by distillation-based cryogenic air separation units. AZEP and ZEITMOP cycles use a high temperature membrane to separate the O_2 from the air stream.

A generic schematic diagram of a CO_2-based oxy-combustion turbine power plant was presented in Fig. 1.1. The fuel, usually natural gas, is burned together with high-purity O_2 at near stoichiometric conditions in the oxy-combustion chamber. The resulting high-pressure, high-temperature gases, consisting of CO_2 (95% mol) and H_2O, are expanded over a turbine, generating electrical energy. The remaining thermal energy of the low-

pressure gases is delivered to the high-pressure recirculation stream using a recuperative heat exchanger (RHE). The condensed H_2O is removed from the cycle, and the remaining CO_2 is compressed in supercritical dense phase at high pressure to be recirculated back to the combustor.

The net efficiency of oxy-combustion cycles is significantly high, ranging between 43.6 – 65%, as a result of the highly recuperative set-up and low specific volume of the supercritical fluid during compression. Only the AZEP, CES and NET Power cycles can currently be considered in an advanced stage of development [6]. In fact, the CES and NET Power cycles have been built at pilot scale to demonstrate their feasibility [7,34]; while components of the AZEP cycle have been tested at laboratory scale [32]. Mancuso et al. [33] concluded that the NET Power cycle is the most promising oxy-combustion power cycle, presenting the lowest estimated total plant specific cost of 1560 €·kW^{-1}; and a net electrical efficiency of 55.1%. A description of the NET Power cycle is provided in Section 2.3. Climent Barba et al. [6] extended the comparison performed by Mancuso et al., conducting a risk analysis considering political, environmental, social, technological, legislative and economic factors. When all of these factors have the same weight, the NET Power cycle has the best average performance. Considering exclusively the cycles using a CO_2-rich mixture in the recirculation (NET Power, SCOC-CC and MATIANT), Rogalev et al. [35] pointed out that the NET Power cycle presents 5.6% and 11.5% higher efficiency than SCOC-CC and MATIANT, respectively. In addition, CO_2 emissions are 11 – 12 times lower, with an estimated 46% lower installed power cost. According to the current state-of-art, the NET Power cycle is the most promising oxy-combustion power cycle architecture for CO_2 capture in CCUS systems.

2.3 The oxy-combustion NET Power cycle

The NET Power cycle is a highly recuperative, high compression ratio, semi-closed oxy-combustion power cycle that recirculates a dense-supercritical CO_2-rich mixture as a combustion temperature moderator. The cycle was originally developed and patented by Rodney John Allam and Jeremy Eron Fetvedt in 2011 [36], to whom it owes its original name (Allam-Fetvedt cycle).

2.3.1 Description of the oxy-combustion NET Power cycle

Fig. 2.2 shows the most up-to-date process flow diagram of the NET Power cycle, and the distillation-based cryogenic air separation unit for high-purity O_2 production. In addition, Fig. 2.3 depicts the evolution of the working fluid in a pressure (p) – specific enthalpy (h) thermodynamic diagram. In the supercritical region, shaded in grey and orange, the fluid presents liquid-like and gas-like properties, respectively. Details about

the behavior of supercritical fluids will be provided in Section 2.4.1. Table 2.1 shows the base nominal operating conditions of the power cycle, provided by NET Power, Inc.

Natural gas enters the pressurized oxy-combustor together with an oxidizing stream (OX-3), which contains the necessary oxygen (diluted in CO_2 for safety reasons [37]) to carry out the oxy-combustion process with a percentage of oxygen excess of 3%. The high-pressure recirculation stream (RE-7), composed mainly of CO_2, acts as a combustion temperature moderator. The resulting flue gas (FG-1) is at 300 bar and 1150 ºC (Table 2.1), and consists of approximately 93% mol CO_2, 6% mol H_2O and 1% mol impurities from the combustion and air separation processes. FG-1, together with a fraction of the pressurized recirculated CO_2 stream, TC-2, which serves as a turbine coolant, are expanded up to 34 bar while producing mechanical work on the turbine shaft.

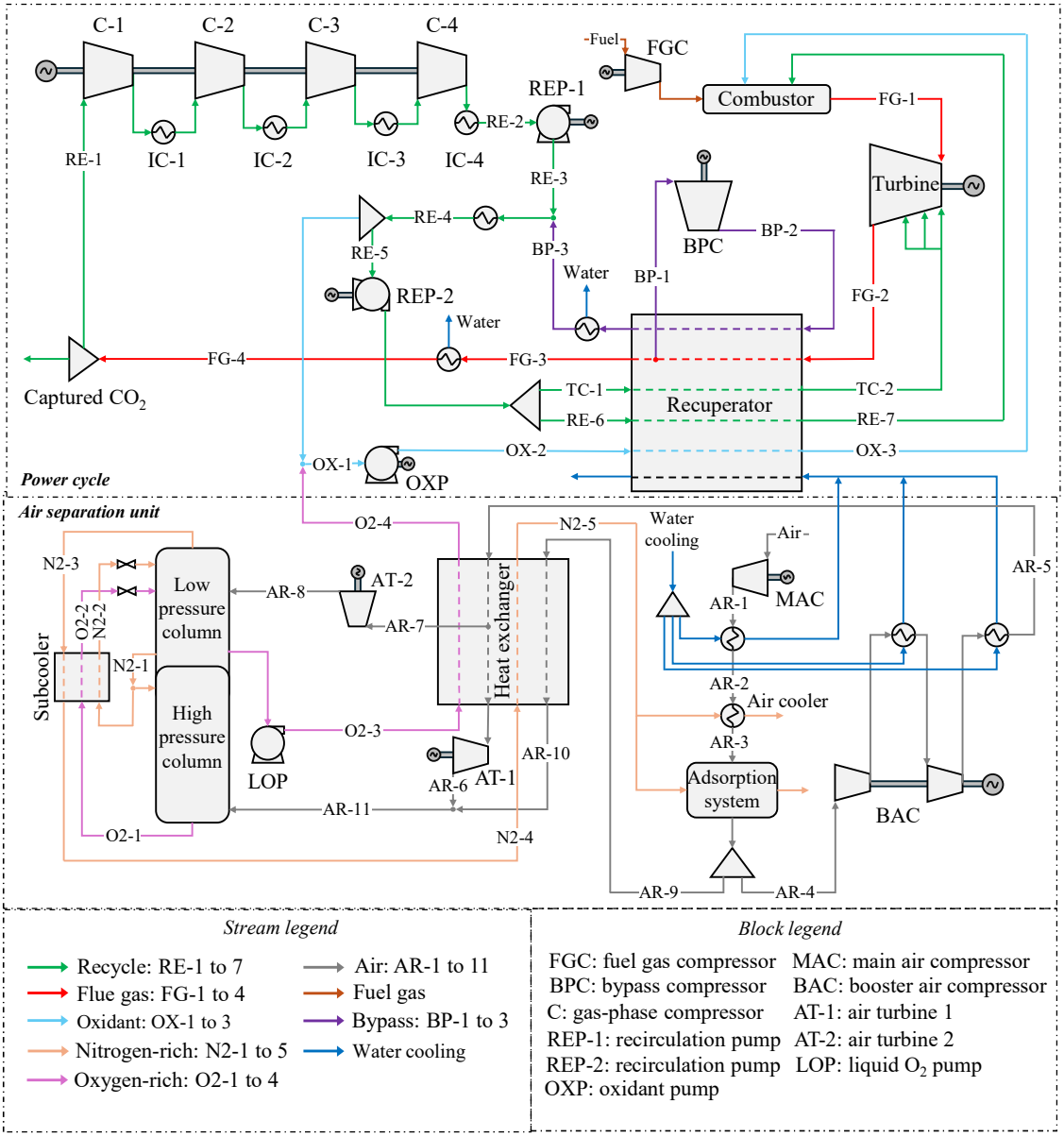

Fig. 2.2. Process flow diagram of the most up-to-date oxy-combustion NET Power cycle embodiment.

The hot turbine exhaust gas (FG-2) is passed through the RHE to partially preheat the recirculating streams TC-1, RE-6 and OX-2, preferably cooling the exhaust gases to a temperature below the dew point of the mixture after leaving the recuperator. Adiabatic heat of compression from: (i) a minor bypassed fraction of FG-2 (BP-1 and BP-2) and (ii) the process air of the ASU, are also used in the RHE as hot streams. At the cold-side of the recuperator (FG-3), a cooling step condenses and removes water derived from combustion. A fraction equivalent to the CO_2 generated in the combustion minus the system losses, is then extracted from the cycle and conducted to a carbon purification unit.

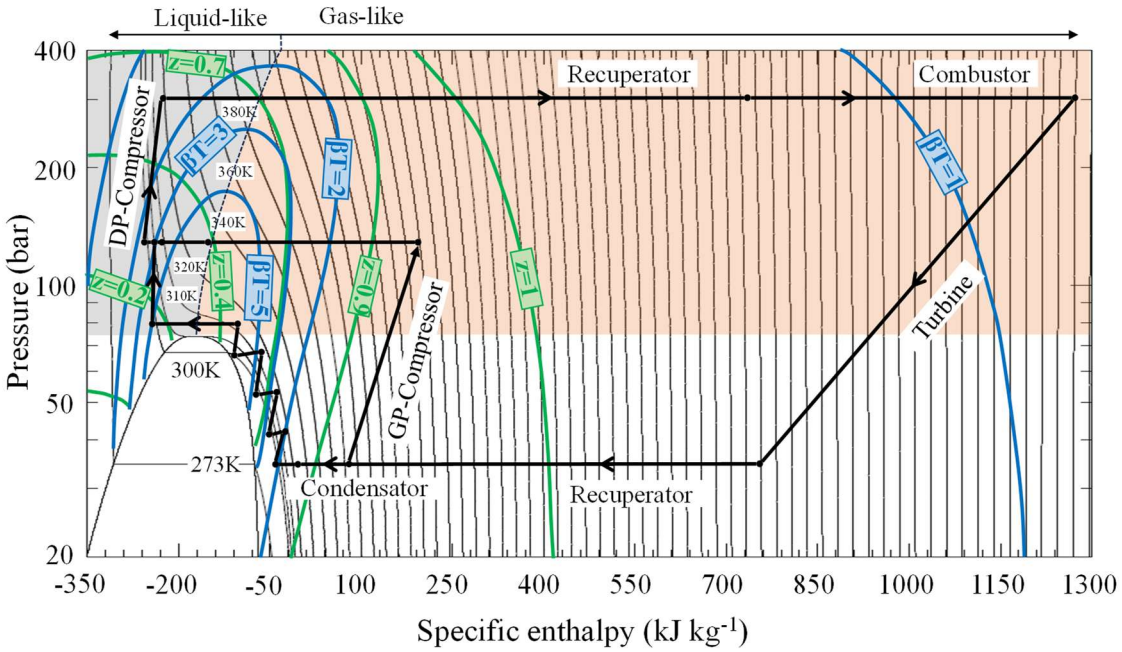

Fig. 2.3. Representation of the thermodynamic NET Power cycle in a pressure – specific enthalpy diagram for pure CO_2. Isocontours of z and βT were included. DP denotes Dense-Phase and GP Gas-Phase.

The recirculation gas (RE-1) is compressed in an intermediate cooling multistage gas-phase compressor. The compressor outlet pressure is set as a function of the ambient air and cooling tower conditions. This pressure is approximately 80 bar for a minimum cycle temperature of 26 °C [38,39]. After the gas-phase compressor discharge (orange domain in Fig. 2.3), the fluid is cooled until it reaches a liquid-like supercritical state (grey domain in Fig. 2.3), which presents high density ($\rho \sim 1000$ kg·m^{-3}) and low viscosity ($\mu \sim 10^{-5}$ Pa·s). RE-2 is compressed to 120 bar, which is the pressure of the high-purity (99.5% mol O_2) ASU-derived O_2 stream. The RE-4 stream is then split into two streams: (i) RE-5, which is composed of the combustion temperature moderating and turbine coolant stream; (ii) the remainder, which is used as an O_2 diluent to form the oxidizing stream (OX-1). The CO_2 mass flow used as a O_2 diluent is set such that the resulting oxidizing

stream has an O_2 mole fraction between 13 – 25% mol [29]. Both streams are compressed in dense-phase to the upper cycle pressure of 300 bar and sent to the thermal recuperator to complete the cycle. By compressing RE-2, RE-5 and OX-1 in liquid-like conditions, compression work is significantly minimized, allowing for high cycle efficiencies. Section 2.4.2 shows, on the basis of a thermodynamic analysis of the cycle, that by placing the dense-phase compression in the liquid-like domain, the specific work of compression is significantly lower than the specific expansion work.

Table 2.1. Nominal base load cycle conditions of the NET Power cycle.

Parameter	Unit	Value
Thermal energy of feedstock (LHV)	MW_{th}	768.19
Combustor outlet temperature (COT)	°C	1150
Turbine inlet pressure (TIP)	bar	300
Turbine outlet pressure (TOP)	bar	34
Bypass stream split fraction	%	6
Recuperator hot-side temperature difference	°C	10
Recuperator pinch-point	°C	5
Minimum cycle temperature	°C	26
Multi-stage intercooled compressor outlet pressure	bar	80
Intermediate $scCO_2$ pump outlet pressure	bar	120

The ASU, depicted in the lower part of Fig. 2.2, is based on a cryogenic air distillation system for high-pressure O_2 production proposed by Allam et al. [40]. The air separation method consists of a double distillation column system, with a lower part operating at a pressure of 5.4 bar, the high pressure column (HPC), and an upper part operating at a pressure of 1.25 bar, the low pressure column (LPC).

The inlet ambient air stream is compressed in the adiabatic main air compressor to 5.6 bar. The thermal energy of the pressurized air (AR-1) is then utilized in the main recuperator of the power cycle, leaving the heat exchanger at a temperature of 54 °C (AR-2) [41]. The air is cooled again in the air cooler to 15 °C [41] from a chilled water stream (not shown) obtained by direct contact of an inlet cooling water stream with a portion of residual N_2. The pressurized cooled air (AR-3) enters the purification system where CO_2, H_2O, and hydrocarbon traces are removed [42]. The purification system is composed of adsorption beds regenerated with residual nitrogen.

A portion of the purified air (30% vol.) enters a booster air compressor (BAC) to be compressed to 90 bar. The resulting high-pressure air stream (AR-5) is partially cooled in the main recuperative heat exchanger. A portion, corresponding to 20% vol. (AR-7), is expanded in a turbine to a pressure of 1.25 bar and a temperature of approximately -189 °C [40], and then introduced into the middle section of the LPC. The remaining air is further cooled in the heat exchanger to -101 °C [40] and expanded in the turbine AR_TUBR-1 to a pressure of 5.4 bar (AR-6).

Table 2.2. Summary and description of the main streams of the NET Power cycle and ASU at nominal conditions.

Stream	Description	From	To	Pressure (bar)	Temperature (ºC)
		Power cycle			
Fuel	Natural gas	-	FG-C	70	15
FG-1	Flue gases	Combustor	Turbine	300	1150
FG-2	Flue gases	Turbine	RHE	34	73433
FG-3	Flue gases	RHE	Condenser	33	57
FG-4	Flue gases	Condenser	CO_2 capture	33	26
RE-1	Recirculating CO_2	CO_2 capture	C1	33	26
RE-2	Recirculating CO_2	C4	REP-1	80	43
RE-3	Recirculating CO_2	REP-1	Mixer	120	34
RE-4	Recirculating CO_2	Mixer	Splitter	119	26
RE-5	Recirculating CO_2	Splitter	REP-2	119	26
RE-6	Recirculating CO_2	REP-2	RHE	305	47
RE-7	Recirculating CO_2	RHE	Combustor	303	724
BP-1	Bypass flow	RHE	BPC	34	138
BP-2	Bypass flow	BPC	RHE	125	283
BP-3	Bypass flow	RHE	Mixer	124	57
OX-1	Oxidant (CO_2/O_2)	Splitter	OXP	119	15
OX-2	Oxidant (CO_2/O_2)	OXP	RHE	305	42
OX-3	Oxidant (CO_2/O_2)	RHE	Combustor	303	724
TC-1	Turbine coolant	REP-2	RHE	305	47
TC-2	Turbine coolant	RHE	Turbine	303	315
		Air separation unit			
Air	Supply air	-	MAC	1	15
AR-1	Air	MAC	RHE cooler	6	226
AR-2	Air	RHE cooler	Air cooler	6	57
AR-3	Air	Air cooler	Adsorption	6	15
AR-4	Air	Adsorption	BAC	6	15
AR-5	Air	BAC	HX	90	21
AR-6	Air	AT-1	Air mixer	5	-174
AR-7	Air	HX	AT-2	90	-35
AR-8	Air	AT-2	LPC	1	-189
AR-9	Air	Adsorption	HX	6	15
AR-10	Air	HX	Air mixer	6	-166
AR-11	Air	Air mixer	HPC	5	-174
O2-1	O_2	HPC	Subcooler	5	-174
O2-2	O_2	Subcooler	LPC	5	-184
O2-3	O_2	LOP	HX	120	-177
O2-4	O_2	HX	Power cycle	120	18
N2-1	N_2	LPC	Subcooler	5	-178
N2-2	N_2	Subcooler	LPC	5	-184
N2-3	N_2	LPC	Subcooler	1	-194
N2-4	N_2	Subcooler	HX	1	-174
N2-5	N_2	HX	Adsorption	1	-54

As for the main air stream AR-9, it is cooled in the heat exchanger and joined with AR-6, so that the resulting stream feeds the lower part of the HPC (AR-11) at its saturation temperature (-174 °C) with a vapor fraction of 77% [40]. The liquid N_2 stream (N2-1), formed in the boiler/condenser, is used as reflux for the HPC and LPC. Both the former and the O_2-enriched liquid stream, obtained from the bottom of the HPC, are subcooled

below their respective saturation temperatures against the residual N_2 leaving the top of the LPC. The resulting streams, prior to feeding the LPC, are expanded at constant enthalpy in valves up to the LPC operating pressure. N2-2 is introduced at the top, and O2-2 is introduced in the same section as AR-8. The high-purity liquid O_2 stream leaving the LPC as a product at the bottom, is pumped up to 120 bar and used as a cold stream, along with the residual N_2, in the heat exchanger.

Table 2.2 and Table 2.3 comprise the main streams and blocks of the NET Power cycle and the ASU, to provide a summary reference to support the entire document.

Table 2.3. Summary and description of the main blocks of the NET Power cycle and ASU.

Block	Description
	Power cycle
FG-C	Fuel gas compressor
Combustor	Oxy-combustion chamber
Turbine	High pressure ratio expander
RHE	Recuperative heat exchanger
Condenser	Water condenser
C-1	1st gas-phase compressor stage
C-2	2nd gas-phase compressor stage
C-3	3rd gas-phase compressor stage
C-4	4th gas-phase compressor stage
REP-1	1st recirculating pump
REP-2	2nd recirculating pump
OXP	Oxidant pump
BPC	Bypass compressor
	Air separation unit
MAC	Main air compressor
Air Cooler	Process air cooler
Adsorption	Adsorption unit
BAC	Booster air compressor
HX	Heat exchanger
AT-1	High-pressure air turbine
AT-2	Low-pressure air turbine
LPC	Low-pressure distillation column
HPC	High-pressure distillation column
Subcooler	Subcooler of the intermediate distillation products
LOP	Liquid O_2 pump
O_2 tank	Liquid O_2 storage tank

2.3.2 State of the art in the development of the oxy-combustion NET Power technology

Since Allam and Fetvedt patented the first NET Power cycle embodiment in 2011, the promising potential of this cycle has attracted the attention of numerous academics and companies that have made important contributions to develop the technology. The company that is currently leading the development of the technology is NET Power Inc, from which the cycle receives its current name. NET Power Inc, founded in January 2010, has made significant progress towards the commercial development of the technology. The major milestone was the construction of a 50 MW_{th} demonstration test facility built

in LaPorte, Texas, which was successfully synchronized to the grid in 2021, validating the core of the NET Power cycle technology [7]. In the pilot plant, the original combustor-turbine group was designed and built by Toshiba, and the heat exchangers of the RHE by Heatric. Fig. 2.4 shows pictures of the primary components of the NET Power demonstration plant, taken in February 2024. Fig. 2.4(a) shows the oxidant pump (OXP) on the left and the recirculation pump (REP-2) on the right. Fig. 2.4(b) shows the hot gas compressor, which is referred to as bypass compressor (BPC) in Fig. 2.2. Fig. 2.4(c) shows the compressor of the gaseous fuel of the pilot plant, which is natural gas. Fig. 2.4(d) shows two heat exchangers, without thermal insultation, out of a total of three that make up the RHE unit (recuperator in Fig. 2.2) of the pilot plant. Finally, Fig. 2.4(e) shows the direct contact cooling tower, which cools the turbine exhaust gases at the outlet of the RHE to condense and to remove the water. NET Power expects the first utility-scale plant to be operational in 2028.

(a)

(b)

Fig. 2.4. (a) Oxidant pump (left) and recirculation pump (right), (b) hot gas compressor of the 50 MW_{th} demonstration pilot plant in LaPorte, Texas.

(c)

(d)

(e)

Fig. 2.4 (continued). (c) fuel-gas compressor, (d) printed circuit heat exchangers of the RHE, and (e) contact-direct cooling tower with the CO_2 stack in the back, of the 50 MW_{th} demonstration pilot plant in LaPorte, Texas.

Besides NET Power Inc, numerous researchers have conducted parametric analysis and optimization processes on the NET Power cycle. However, most of the studies available in literature only focus on an outdated power cycle embodiment (without considering the ASU integration and the bypass recompression system), using models valid exclusively for on-design conditions. In contrast, within this work, the most up-to-date NET Power cycle embodiment, including the ASU, was modeled at off-design conditions. This has allowed, as a novelty, to conduct parametric studies of the technological performance at partial loads, to find the operative configuration that maximizes the efficiency as a function of the load degree and to predict the flow, temperature and pressure ranges in which all the system components operate, with a special focus on the RHE. The modeling and numerical optimization methodology of the cycle are described in Section 3.

Mancuso et al. [33] carried out a complete technical and economic modeling of the SCOC-CC, MATIANT, NET Power, GRAZ, CES, AZEP and ZEITMOP oxy-combustion turbine power plants. The authors found that the predicted thermal efficiencies of the cycles ranged from 55% for the NET Power cycle to about 49% for other cycles. The NET Power cycle reported the lowest installation cost. However, the authors stated that the development of the turbine, the oxy-combustion chamber and the RHE represent a significant technological challenge.

The NET Power cycle analysis carried out by Mancuso et al. [33] was extended by Scaccabarozzi et al. [38] and Colleoni et al. [43]. The authors performed parametric studies by varying the combustor outlet temperature, the turbine inlet and outlet pressures, the minimum cycle temperature, the isentropic efficiency of the turbomachines and the specific consumption of the ASU. These parametric analyses were conducted from a thermodynamic model at on-design conditions. In addition, the configuration of the main operating parameters that maximize the efficiency was found, resulting in a maximum cycle efficiency of 54.8%. Zaryab et al. [44] incorporated off-design performance maps for the compressors, pumps and the turbine, to study different control strategies at partial loads. The results pointed out that the net cycle efficiency could be increased with 4.71% points, by acting on the turbine partial admission and minimum cycle pressure, in addition to the traditional variable inlet guide vanes regulation on the compressor. Rogalev et al. [39] developed the construction of a high-power supercritical CO_2 gas turbine with optimal thermodynamic parameters and carried out a technical, economic and environmental evaluation on the NET Power cycle. The results reported that, for a turbine inlet temperature and pressure of 1083 ºC and 30 MPa, a turbine outlet pressure of 3 MPa, and a turbine coolant temperature of 200 ºC, the efficiency reaches a maximum value of 56.6%. In addition, the specific emissions to the atmosphere were found to be 3.8 $gCO_2 \cdot kWh_{el}^{-1}$, and the total cost the NET Power cycle per kW of installed power was found to be 1307.5 $. On the other hand, Haseli et al. [45] found that the maximum

efficiency could reach 58.2% based on a thermodynamic model with respect to the turbine inlet and exhaust pressures.

In the previously presented studies on the NET Power cycle, the authors focused exclusively on the power cycle. Therefore, the specific work consumed by the ASU was estimated, without integrating it within the power cycle. Haseli et al. [42] integrated an ASU model to the power cycle and numerically analyzed the thermodynamic performance of the assembly. The authors demonstrate that the power cycle exhibited maximum efficiency when the MAC discharge pressure was 4.2 bar. In addition, they carried out an optimization process, using a genetic algorithm, to find the maximum efficiency point of the assembly. The authors reported that, for a turbine inlet temperature of 1500 K, and a turbine inlet and outlet pressure of 305.5 bar and 28.1 bar, the maximum efficiency of the cycle was 59.7%. From the ASU embodiment of [40] and the NET Power cycle layout of [29], Mitchell et al. [41] incorporated a cryogenic liquid O_2 storage to displace the energy penalty of the ASU and improve the operational flexibility of the plant. When the O_2 demanded by the NET Power cycle is provided by a storage tank, peak efficiencies of 66.1% were reported. The O_2 storage incorporated into the NET Power cycle promises to be an opportunity in energy systems where a substantial part of the electricity production comes from renewable sources [46]. In order to use the NET Power cycle as a flexible asset, a reduction of the mass inertia, by piping and the main process cycle heat recuperator will be major challenges.

Other authors have proposed novel layouts of the NET Power cycle. Chan et al. [47] introduced an expansion with intermediate reheating into the original NET Power cycle arrangement. Sensitivity studies were carried out for the new configuration, finding that the minimum cycle temperature, and the exhaust temperature of the second oxy-combustor, have a significant impact on the cycle performance. In addition, the authors conducted a cycle optimization process, reporting a maximum net efficiency of 49.32%. Despite the cycle configuration with reheating, the maximum cycle efficiency found in this study was lower than that obtained by [38,39,42,43,45] with the original cycle layout. Xie et al. [48] proposed an integrated cogeneration system consisting of a NET Power cycle and a heat pump that recovers CO_2 heat from the gas compression train. The original cycle efficiency was improved by up to 1.56% with the integrated cogeneration arrangement. The original NET Power cycle layout works by using conventional natural gas as a fuel. Instead, Yu et al. [49] suggested the use of liquified natural gas as a fuel, proposing strategies to use its cold energy to cool the CO_2 in the gas compression train. Wang et al. [50] proposed a novel system to simultaneously generate power, methane and freshwater, with a NET Power cycle efficiently governing the assembly. An artificial neural network was trained to emulate the energy behavior of the system. A multi-objective optimization was conducted to maximize the freshwater mass flow, exergy efficiency and cost rate, resulting in 378.5 $kg \cdot s^{-1}$, 39%, and 11 $\$ \cdot h^{-1}$, respectively. Xie et

al. [51] proposed a modification in the compression train of the cycle to produce freshwater and clean energy. Heat from compression is employed in an evaporative desalination system to produce freshwater. The efficiency of the system resulted in 49.1%, with a capacity to generate 292.6 kg·s^{-1} of freshwater. In addition, authors revealed that a 1 ºC rise in ambient temperature augments water production by 0.6%, while efficiency decreases by 0.06%. On the other hand, Luo et al. [37] performed an exergy analysis of a coal-fired NET Power cycle, reporting an overall exergy efficiency of 40.6%. Combining a coal-fired NET Power cycle with a coal gasification process, Zhao et al. [52] conducted a parametric study on the main process variables, resulting in a net efficiency of 38.9%.

2.4 General thermodynamic mapping of the NET Power cycle

The NET Power cycle exploits the liquid-like properties of CO_2 at supercritical pressures to achieve reduced compression works and high thermal efficiencies. The behavior of the supercritical fluids, characterized by experiencing strong real gas effects caused by intermolecular interactions, is significantly different from the behavior of constant property fluids, used on traditional gas turbine power cycles. Thus, a brief analysis of the real gas effects appearing in the supercritical working fluid, and their influence on the thermodynamic process taking place in the power cycle, is presented in this section on the basis of general thermodynamic relations.

2.4.1 CO_2-rich mixture at supercritical pressure as a working fluid

In the representation of the NET Power cycle in a p-h diagram in Fig. 2.3, isocontours of the compressibility factor (z), and of the product of the volumetric expansivity (β) and temperature, βT, were included. z denotes the deviation of a real gas from the ideal gas behavior, and is defined in Eq. (2.1).

$$z = \frac{pv}{RT} \tag{2.1}$$

Thus, for a gas exhibiting ideal gas behavior, z = 1. The volumetric expansivity represents the change in the specific volume of a fluid with temperature at constant pressure, and is defined as:

$$\beta = \frac{1}{v}\left(\frac{\partial v}{\partial T}\right)_p, \tag{2.2}$$

where the subscript in the derivative denotes the property that remains constant in the differentiation. For ideal gases, βT = 1. This result can be justified from the general relation of the total change in specific enthalpy for real gases [53],

$$dh = c_p dT + v(1 - \beta T)dp. \tag{2.3}$$

In an ideal gas, the enthalpy is an exclusive function of the temperature. Thus, according to Eq. (2.3), necessarily $\beta T = 1$. When the enthalpy is an exclusive function of temperature, the isotherm lines are vertical lines in a p - h diagram, since

$$\left(\frac{\partial h}{\partial p}\right)_T = v(1 - \beta T) = 0. \tag{2.4}$$

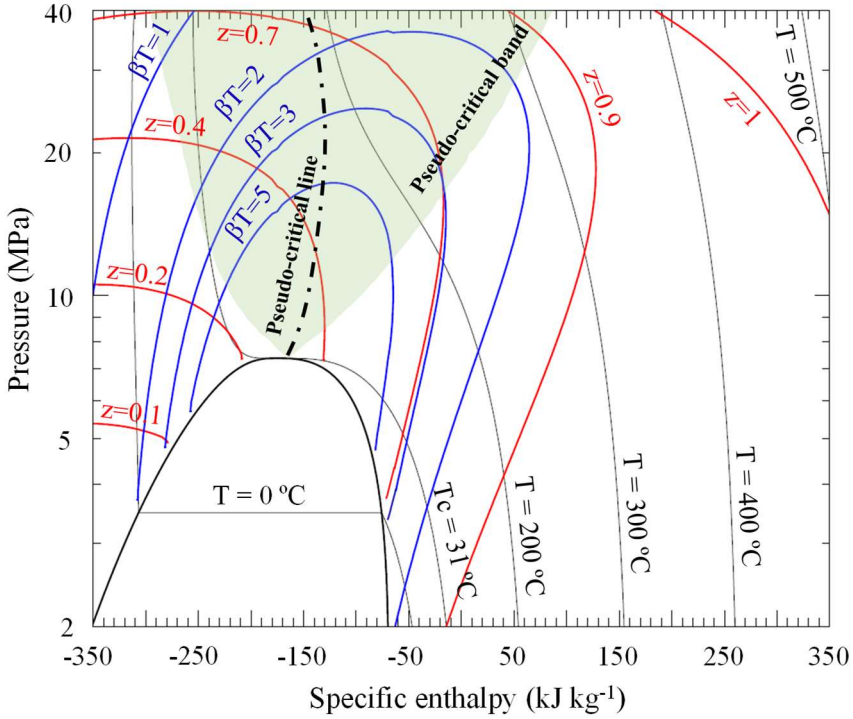

Fig. 2.5. Pressure – specific enthalpy diagram for pure CO_2 in the region close to the critical point, including isothermal lines, and isocontours of z and βT.

Vertical isotherms and values of z and βT equal to one are found in Fig. 2.3 in the expansion region of the NET Power cycle, where the turbine is located, due to the high temperature of the gas in this region. In the cycle domains close to the critical temperature of CO_2 (~ 31 ºC), i.e., in the compression and low-temperature heat transfer stages, the fluid departs from the ideal gas behavior, which implies that intermolecular forces can no longer be neglected. This is deduced by the abrupt decrease of z in Fig. 2.3. Fig. 2.5 shows an extension of the region near the critical point (also known as the pericritical region [54]), where it is noticed that βT increases near the critical point. According to Eq. (2.4), an increase in βT drives a deflection of the isotherm lines toward lower enthalpy values

as the pressure increases. The slope of the isotherm lines becomes steeper as the fluids approach the critical point, since βT becomes infinite. This strong deflection of the isothermal lines would cause that a small temperature change at constant pressure leads to a large enthalpy change, as if it was a phase change (at subcritical pressure). In fact, the fluid undergoes a phase change, with the difference that liquid and vapor phases do not coexist during such a process. However, the thermodynamic and transport properties of the fluid undergo strong variations, as shown in Fig. 2.6. The slope of the properties variation and their peak value decreases as the pressure increases, since βT decreases and, hence, the slope of the isotherm lines.

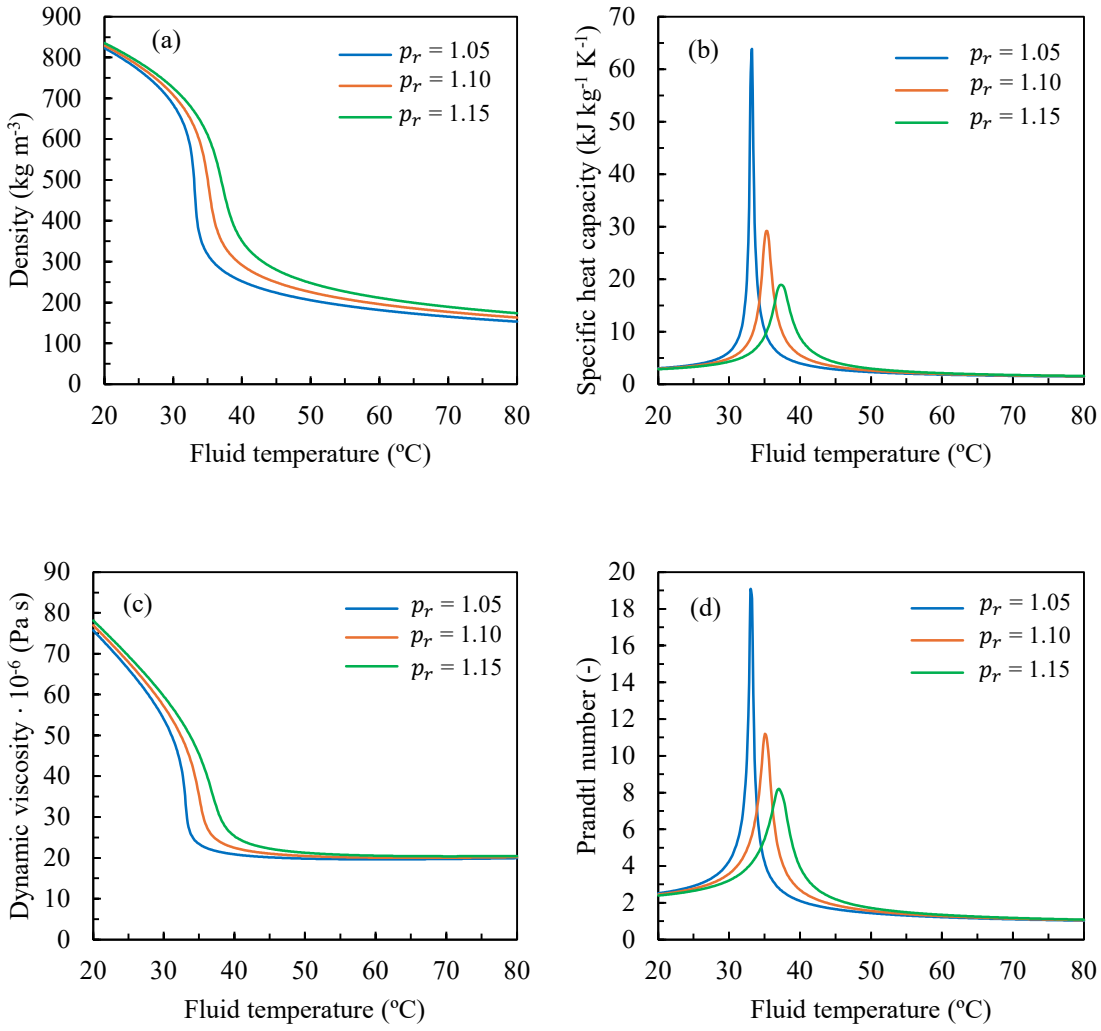

Fig. 2.6. Variation of the (a) density, (b) specific heat capacity, (c) dynamic viscosity, and (d) Prandtl number, as a function of the fluid temperature and reduced pressure (p_r) for pure CO_2. The thermodynamic and transport properties were obtained using the Span & Wagner equation of state [55].

The specific heat at constant pressure, c_p, increases sharply until reaching a maximum value and then decreases, similar to what occurs in a subcritical phase change. The

temperature at which c_p reaches the maximum value for a given pressure, is referred to as the pseudo-critical temperature (T_{pc}). Fig. 2.5 shows the pseudo-critical line, which is formed by connecting the pseudo-critical temperatures at different pressures. T_{pc} increases with increasing pressure. The density varies significantly near the pseudo-critical point. At temperatures below T_{pc} (i.e., to the left of the pseudo-critical line in Fig. 2.5), the fluid presents a liquid-like behavior, and above T_{pc} a gas-like behavior. The liquid-like phase is characterized by high densities and viscosities, while the gas-like phase by low densities and viscosities. The phase change that takes place between the liquid-like and gas-like phases occurs within a certain temperature range, which widens with increasing pressure, since the variation of properties occurs in a continuous fashion. The temperature range in which the supercritical phase change takes place is represented by the pseudo-critical band in Fig. 2.5.

The compression and heat transfer processes of the cycle that occur within the pseudo-critical region will be influenced by the rapid variation of the physical properties of CO_2. Therefore, reliable computational models of thermodynamic and transport properties suitable for real gases are required in order to properly model and design each stage of the NET Power cycle. In addition to the strong real gas effects experienced by the CO_2, it is important to note that the CO_2 working fluid is mixed with traces of other components. The presence of impurities in the pseudo-critical domain can significantly vary the properties of CO_2 in a highly non-ideal manner [56], [57], tending in general to decrease the density of the mixture. The main diluted impurities in the circulating CO_2 are H_2O, CO, H_2, O_2, N_2, Ar and CH_4. H_2O is a combustion product, and experimental evidence reveals that its presence in the CO_2 stream, even in trace amounts, significantly impacts the thermo-physical behavior of the mixture, which becomes crucial in the modeling of the condensing turbine exhaust gas stream [57], [58]. CO, H_2 and CH_4 are intermediate products of combustion or unburned gases. O_2, which is produced by the ASU, is present in important quantities in the oxidizing stream, while in nearly negligible quantities in the other streams, since the combustion process is performed at near stoichiometric conditions. Although the purity of the ASU-derived O_2 obtained by the distillation process is high, ~ 99.5% , a certain degree of contamination with N_2 and Ar is unavoidable.

The strong real gas effect experienced by the working fluid in the pseudo-critical region, and the strong molecular interactions between the mixture components, lead to the necessity of establishing complex mathematical formulations for the mixing rules of the equations of state (EoS) in the supercritical region. While the real gas effects for pure CO_2 can be accurately predicted using the Span & Wagner EoS [55], uncertainties still exist when dealing with CO_2 mixtures present in the NET Power cycle. Consequently, the NET Power technology demands EoSs capable of accurately describing the pressure, volume, temperature, composition ($pVT\bar{x}$) behavior of such mixtures [59]. Experimental

data for multi-component CO_2 mixtures over a wide $pVT\bar{x}$ range are scarce, which is the main limiting factor for the calibration of the EoSs [60].

To characterize scCO_2-rich mixtures, several approaches have been applied. Cubic EoSs, which use Van der Waals one fluid as a mixing rule [57], have proven to give satisfactory results in volumetric calculations. Theoretical models based on statistical mechanics theories, such as Statistical Associating Fluid Theory (SAFT) and Cubic-Plus-Association (CPA) [61] have been used to describe the volumetric properties of CO_2-rich mixtures, demonstrating more accurate results for highly asymmetric mixtures [60], [57]. Multiparametric EoS, formulated in terms of the Helmholtz free energy, such as GERG-2008 EoS [62] and the Equation of State of Combustion Gases (EOS-CG) [63] have demonstrated to be the most accurate in predicting the density of CO_2-rich mixtures. These models include an EoS for pure fluids and sophisticated departure functions.

Li et al. [64] studied the reliability of seven cubic EoSs, including Peng-Robinson (PR), Patel-Teja, Redlich-Kwong, Soave-Redlich-Kwong (SRK), modified SRK, modified PR, and improved SRK, in predicting the gas and liquid volumes of supercritical binary mixtures of CO_2 containing CH_4, H_2S, SO_2, Ar and N_2, based on a comparison with experimental data collected from literature. The temperature and pressure ranges of the collected experimental data were between 89 – 511 K and 0.1 – 69 MPa, respectively. The authors concluded that the PR and Patel-Teja EoSs are generally superior to the rest for all mixtures analyzed. In addition, they pointed out that the binary interaction parameters have a huge effect on the accuracy of the volumetric calculations of the EoSs, especially in the liquid phase.

For bubble point predictions of CO_2-rich systems ($CO_2 – CH_4$, $CO_2 – O_2$, $CO_2 – Ar$, and $CO_2 – N_2$), Okoro et al. [65] compared the performance of the PR EoS with multi-fluid Helmholtz energy-based models. Within a temperature range of 228.15 – 273.15 K, PR EoS registered deviations of less than 5% for all data points. Furthermore, authors observed that the calibration of the binary interaction coefficients significantly affects the performance of the PR EoS. Xiong et al. [66] presented a novel general cross-association explicit formulation for different bonding types with the aim of increasing the computational efficiency of the CPA EoS. Accurately modeling the phase behavior of CO_2-rich systems, the new formulation resulted in a CPU time decrease of 70%.

Mazzoccoli et al. [67] selected for comparison the Advanced PR, CPA and GERG-2008 EoSs. Density data for 27 CO_2 mixtures, and vapor-liquid equilibrium (VLE) data for 20 different CO_2 mixtures, in a pressure - temperature range of 0 – 20 MPa and 253.15 – 313.15 K were collected. GERG-2008 EoS reported more accurate results for density and bubble point. However, the GERG-2008 EoS, which was developed for natural gas mixtures, presents shortcomings concerning the modeling of the phase behavior of CO_2 mixtures, underestimating the solubility of gases in the aqueous phase [63].

The equation of state of combustion gases (EOS-CG), developed by Gernert et al. [63], addresses the deficiencies of the GERG-2008 EoS, proposing new adapted departure functions for the mixtures $CO_2 – H_2O$, $CO_2 – N_2$, $CO_2 – O_2$, $CO_2 – Ar$ and $CO_2 – CO$, while maintaining the mathematical formulation of the GERG-2008 EoS. The authors compared the performance of the EOS-CG with the GERG-2008, predictive SRK and Lee-Kesler-Plöcker (LKP) EoSs based on experimental data of binary and multicomponent mixtures with high CO_2 content, including H_2O, N_2, O_2, Ar, and CO. The results indicated a clear superiority of the EOS-CG over all other EoSs, including water-containing blends. The EOS-CG model was recently updated and extended into a new model EOS-CG-2021 [68]. 72 binary mixture models were added, five departure functions and 14 binary mixture models with fitted reduced parameters were elaborated.

Rivas et al. [69] measured the density of $CO_2 – CH_4$ and $CO_2 – CO$ mixtures, for CO_2 mole fractions higher than 0.97, in a pressure and temperature range of 0.1 – 20 MPa and 304.21 – 308.14 K. From the measured experimental data, the performance of the PR, Perturbed Chain-SAFT (PC-SAFT) and GERG-2008 EoSs in volumetric predictions was compared. Deviations of less than 3.5% for PR, 2.8% for PC-SAFT and 1.0% for GERG-2008 were reported, with the GERG-2008 EoS demonstrating the highest reliability.

Perez et al. [70] compared the capability of the PR, SRK, PC-SAFT EoSs in modeling the VLE and density of 108 binary CO_2 mixtures typical for CCUS systems, including gaseous components such as CH_4, C_2H_6, N_2 and H_2S. The VLE and density experimental data were collected from literature. The results pointed out that, in general, the VLE and densities of the investigated mixtures were most accurately captured using the PC-SAFT EoS. Yang et al. [71] measured the density of the $CO_2 – N_2$ and $CO_2 – Ar$ binary mixtures. The mole fraction of CO_2 in the $CO_2 – N_2$ mixture was 0.05, and 0.01 in the $CO_2 – Ar$ mixture. Density measurements were carried out in a pressure and temperature range of 11 – 31 MPa and 298.15 – 423.15 K. The volumetric prediction of the GERG-2008 and EOS-CG EoSs were compared with the experimental density data obtained. The relative deviations were within 0.1% for the $CO_2 – N_2$ mixture and within 0.5% for the $CO_2 – Ar$ mixture.

Ke et al. [72] experimentally obtained new pressure – temperature phase equilibrium diagrams for two ternary mixtures $CO_2 – Ar – N_2$ and $CO_2 – Ar – H_2$ in a temperature range of 268 – 303 K. CO_2 was the major component in both mixtures, with a mole fraction ranging between 0.90 and 0.98. In addition, they measured the density of the $CO_2 – Ar – N_2$ ternary mixture (with a mole fraction of Ar and N_2 of 0.05) in a temperature range between 293.15 – 333.15 K up to a pressure of 23 MPa. Then, the authors used the obtained experimental phase equilibrium and density data to carry out a comparative reliability study of the GERG-2008, EOS-CG and PR EoSs. The EOS-CG gave the lowest relative deviation for both phase equilibrium and density.

McKay et al. [73] analyzed the capability of the PR, SRK, PC-SAFT, GERG-2008 and EOS-CG models to characterize CO_2-rich mixtures. Results revealed relative errors of the PR and SRK EoSs predicting the CO_2 solubility in H_2O of 88.6% and 89.9%, respectively. The PR EoS performs significantly better with the Huron-Vidal mixing rules, reporting an error of 3.5%. GERG-2008 and EOS-CG reported an error of less than 1% computing the density of multicomponent CO_2-rich systems over a temperature and pressure range of 273.15 – 423.15 K and 11 – 1260 bar. PR and SRK EoSs, with the Peneloux volume shift, reported deviations of 2.8% and 4.8% within the supercritical phase. SAFT models demonstrated similar performance to the cubic EoSs.

2.4.2 Thermodynamic analysis of the NET Power cycle

In the following, some expressions revealing the influence of the real gas effects on the thermodynamic behavior of the cycle are derived. Particularly, it is demonstrated that placing the compression stage in the liquid-like domain (i.e., where the compressibility factor is low) reduces the specific work of compression with respect to expansion, resulting in high cycle efficiencies. For this purpose, a single compression and expansion processes will be assumed, both taking place at constant entropy. To maintain the analysis at a manageable level, pure CO_2 as a working fluid is considered. To calculate the specific work of compression and expansion, it is necessary to obtain a relation for the temperature and specific volume change as a function of the pressure at constant entropy, appropriate for real gases [74]. For this purpose, from the following Maxwell's equation

$$\left(\frac{\partial T}{\partial p}\right)_s = \left(\frac{\partial v}{\partial s}\right)_p, \tag{2.5}$$

and the following relation:

$$\left(\frac{\partial v}{\partial s}\right)_p \left(\frac{\partial s}{\partial T}\right)_p \left(\frac{\partial T}{\partial v}\right)_p = 1, \tag{2.6}$$

The following expression can be obtained:

$$\left(\frac{\partial T}{\partial p}\right)_s = \left(\frac{\partial v}{\partial T}\right)_p \Big/ \left(\frac{\partial s}{\partial T}\right)_p. \tag{2.7}$$

The derivative in the numerator of the right-hand side of Eq. (2.7) can be expressed as a function of β using Eq. (2.2) as βv. The derivative in the denominator is equal to c_p/T [53]. Therefore, Eq. (2.7) results in:

$$\left(\frac{\partial T}{\partial p}\right)_s = \frac{zRT(\beta T)}{pc_p}. \tag{2.8}$$

Where a generic EoS relation for real gases, $pv = zRT$, was substituted. Eq. (2.8) represents the isentropic evolution of temperature with pressure for a real gas. To obtain a relation for the change of the specific volume with pressure at constant entropy, the triple product rule is used for the following differential relations:

$$\left(\frac{\partial p}{\partial T}\right)_v = -\frac{\left(\frac{\partial v}{\partial T}\right)_p}{\left(\frac{\partial v}{\partial p}\right)_T} = \frac{\beta}{\varsigma}, \tag{2.9}$$

where the derivative in the numerator was expressed as a function of β and that in the denominator as a function of the isothermal compressibility ς [75]. Substituting this result into the expression for the total change in specific entropy,

$$ds = \frac{c_v}{T}dT + \left(\frac{\partial p}{\partial T}\right)_v dv, \tag{2.10}$$

and considering a reversible process ($ds = 0$), the following expression is obtained:

$$\frac{c_v}{T}dT + \frac{\beta}{\varsigma}dv = 0. \tag{2.11}$$

Replacing in Eq. (2.11) the result found in Eq. (2.8), the isentropic change of the specific volume as a function of pressure can be written as:

$$\left(\frac{\partial v}{\partial p}\right)_s = -\frac{zc_v Rv(\beta T)^2}{pc_p(c_p - c_v)}, \tag{2.12}$$

where the Mayer's relation, $c_p - c_v = vT\beta^2/\varsigma$, was employed. Therefore, the specific work of expansion between the pressure at the turbine inlet p_1, and the pressure at the compressor suction, p_0, turns to be:

$$w_t = \int_p^{p_1} vdp = \int_p^{p_1} \frac{v_1 p^{-c_v/c_p}}{{p_1}^{-c_v/c_p}} dp = \frac{RT_1}{k}(1 - r^{-k}), \tag{2.13}$$

where the relation between the specific volume and pressure was obtained by integrating Eq. (2.12), assuming that the gas behaves as an ideal gas during expansion (i.e., $z = 1$, $\beta T = 1$ and $R = c_p - c_v$). In Eq. (2.13), r is the compression ratio and $k = (\gamma - 1)/\gamma$. The specific work of compression is obtained similarly to that of expansion,

with the difference that the ideal gas simplifications are not applicable. Thus, the relation between the specific volume and pressure would result:

$$\frac{v}{v_0} = \left(\frac{p}{p_0}\right)^{-\frac{zc_v R(\beta T)^2}{c_p(c_p - c_v)}} = \left(\frac{p}{p_0}\right)^{-m}, \tag{2.14}$$

where the exponent in Eq. (2.14) was renamed as m. Thus, the specific compression work results:

$$w_c = \int_{p_0}^{p} v dp = \int_{p_0}^{p} \frac{v_0 p^{-m}}{{p_0}^{-m}} dp = \frac{z_0 R T_0}{1-m}(r^{1-m} - 1) \tag{2.15}$$

At the pressure and temperature conditions at which the compressor admission point is located in the NET Power cycle, it can be assumed that $m \approx 0$. Therefore, the specific work of compression can be simplified, resulting in:

$$w_c = z_0 R T_0 (r - 1). \tag{2.16}$$

The ratio between the specific compression and expansion work, w_c/w_t, is obtained by dividing Eqs. (2.16) and (2.13), resulting:

$$\frac{w_c}{w_t} = \frac{z_0 R T_0 (r-1)}{T_1(1 - r^{-k})}. \tag{2.17}$$

The ratio w_c/w_t is a useful indicator of the cycle performance. The lower the ratio, the lower is the compression work with respect to the expansion work, which implies a higher internal cycle efficiency. According to Eq. (2.17), the fact of locating the admission of the compression process in the liquid-like state domain, and the expansion process in the ideal gas region (gas-like phase), implies that both T_0 and z_0 are low, and T_1 is high. This tends to decrease the w_c/w_t ratio significantly, allowing the NET Power cycle to reach high efficiencies.

In order to take advantage of the favorable CO_2 properties in liquid-like state to achieve high cycle efficiencies, as explained, the circulating CO_2 needs to be cooled in the RHE below T_{pc}, which implies that the heat flux exchanged in the RHE is extremely high; being about 1 GW at nominal base cycle conditions. This can also be deduced from Fig. 2.3 by the substantial enthalpy change experienced by the working fluids within the RHE. This implies that the RHE becomes a key element to achieve high cycle efficiencies. Therefore, attaining an effective, high-performance RHE design becomes a critical milestone in the successful development of the NET Power technology.

2.5 The recuperative heat exchanger of the NET Power cycle

This section reviews the main heat transfer characteristics and state of the art of the NET Power cycle RHE. The RHE exchanges an extremely high heat flux, between multiple hot and cold streams, in a complex and non-linear manner due to the rapid variation of the physical properties of the supercritical fluid. Conventional heat exchangers would require heat exchange areas not achievable in practice to comply with the unique heat transfer requirements of the RHE. Thus, a novel generation of compact heat exchangers (CHE) have emerged as a potential solution. The most promising CHE technologies, and their state of development, are reviewed. Special attention is given to the micro shell-and-tube heat exchanger (MSTHE) architecture, which according to literature promises to be the best performer under the exceptional operating conditions of the NET Power cycle, and which is subject of study of this PhD thesis work.

2.5.1 Heat transfer characteristics of the recuperative heat exchanger of the NET Power cycle

Fig. 2.7 shows a detailed flow diagram of the NET Power cycle RHE, previously introduced in Fig. 2.2, and Fig. 2.8 a diagram of composite curves. The RHE is divided into three heat exchange sections: a high-temperature section (HTS), a medium-temperature section (MTS), and a low-temperature section (LTS). The hot streams are: the expanded hot gases (FG-2), the adiabatically heated bypass flow (BP-2) and the hot air from the ASU (AR-1). The cold streams are: the combustion moderating CO_2 recirculation (RE-6), the turbine coolant CO_2 recirculation (TC-1) and the oxidizer recirculation (OX-2). FG-2 is cooled to a temperature slightly above the dew point, 138 ºC, at the outlet of the MTS. Then, about 6% (BP-1) is adiabatically recompressed in the BPC up to ~ 300 ºC (BP-2) to be reinjected into the hot-section of the MTS [29] together with adiabatically heated air (AR-1) at 275 ºC from the MAC and BAC [7]. The remaining part of FG-2 is cooled and condensed in the LTS, with all hot streams leaving the RHE through the cold-section of LTS. RE-6 and OX-2 are passed through LTS, MTS and HTS, while TC-1 leaves the hot-side of MST at ~ 310 ºC.

The injection of additional heat into the RHE (i.e., BP-2 and AR-1) is necessary because the heat transfer process within the RHE is deeply conditioned by the variations of the thermo-physical properties of the fluid near T_{pc} [43]. Close to T_{pc}, the heat capacity of CO_2 on the high-pressure side of the RHE is higher than that on the low-pressure side [76], as shown in Fig. 2.9. This would limit the maximum temperature that the pressurized recirculation streams can reach within the RHE. To attenuate this undesired effect, the application of additive heating into the RHE, from additional thermal energy sources, is used. The addition of additive heating at different temperatures, water condensation of flue gases, and real gas effects near T_{pc} cause changes in the heat capacity fluxes ($\dot{m}c_p$)

of the cold composite curve (CCC) and hot composite curve (HCC) through the RHE, as presented in Fig. 2.10.

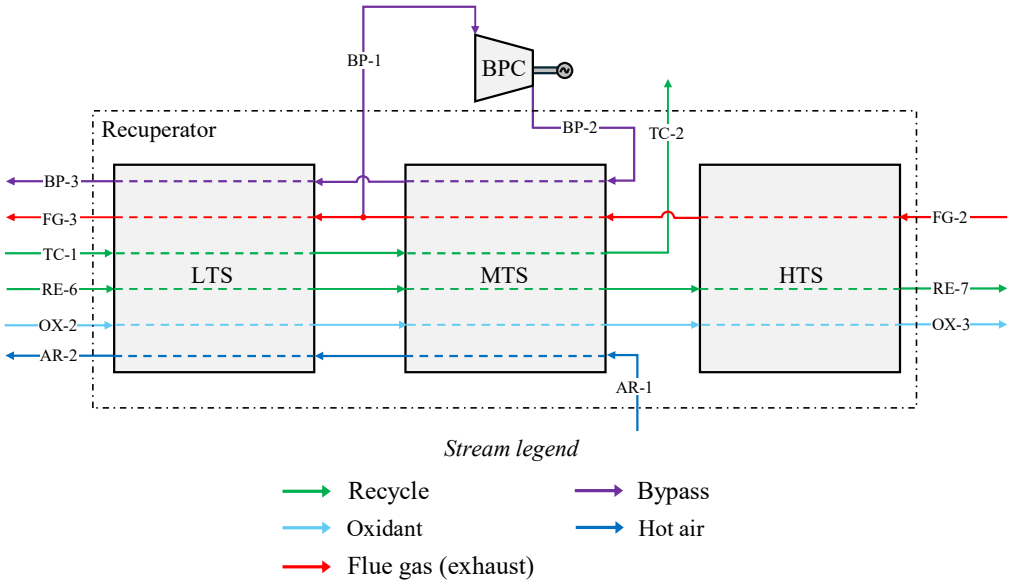

Fig. 2.7. Detailed view of the RHE of the NET Power cycle divided into three heat exchange sections: high-temperature section (HTS), medium-temperature section (MTS), and low-temperature section (LTS).

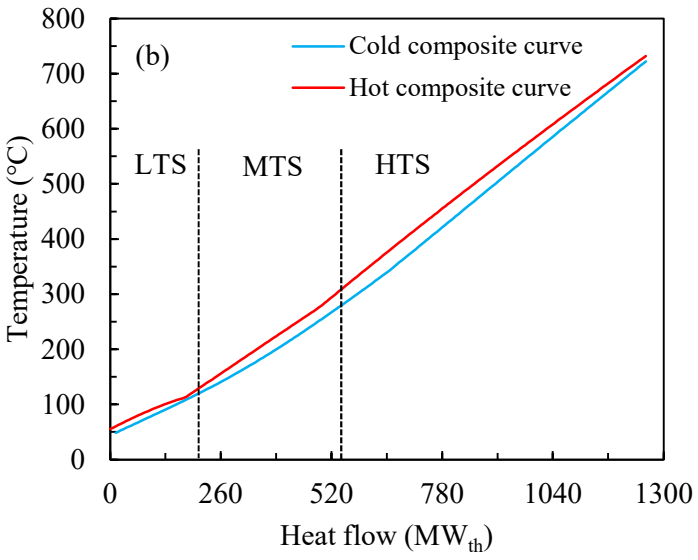

Fig. 2.8. Heat exchange section of the RHE in a composite curve diagram.

For the CCC, $\dot{m}c_p$ decreases as the fluid heats up above T_{pc}, presenting a step reduction when the turbine coolant is removed. Regarding HCC, three abrupt changes of $\dot{m}c_p$ appear due to: (i) the injection of the hot air from the MAC, (ii) the exit of the bypass stream and (iii) condensation. The pinch-point coincides with the dew point at nominal

conditions and may eventually be shifted to the cold-side of the RHE at off-design conditions [38]. The non-linear variations of $\dot{m}c_p$ make the complexity of the thermal analysis of the RHE high.

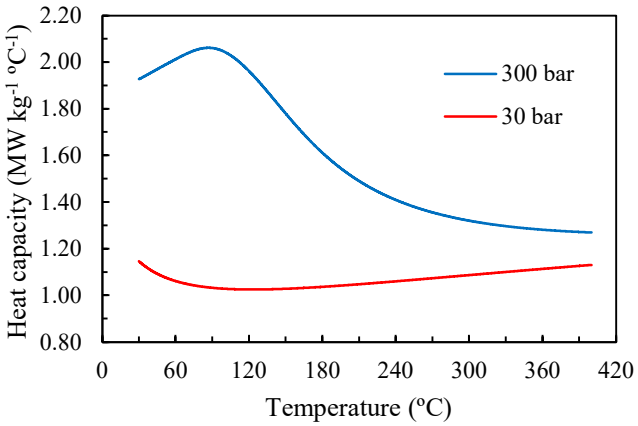

Fig. 2.9. Heat capacity of CO_2 as a function of temperature at pressures of 30 bar and 300 bar.

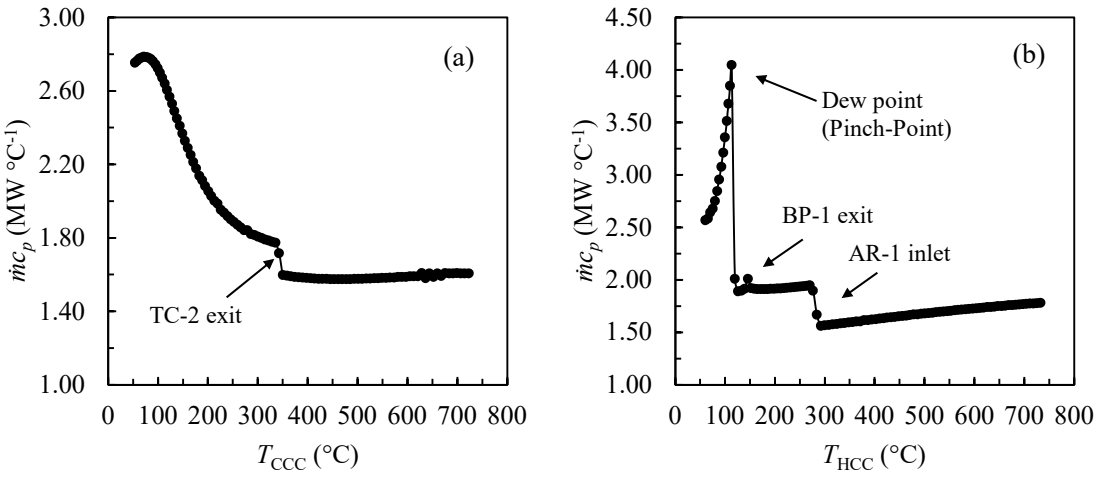

Fig. 2.10. Specific heat fluxes ($\dot{m}c_p$) as a function of temperature for the (a) cold composite curve and (b) hot composite curve.

2.5.2 Compact heat exchangers

As discussed, the NET Power cycle exploits the liquid-like properties of CO_2 at supercritical pressures to achieve a reduced compression work and, thus, a high thermal efficiency. For this purpose, the recycling CO_2 needs to be cooled in the RHE below T_{pc}, which implies that the heat flux exchanged in the RHE is extremely high. Moreover, the pinch-point is normally set at 5 ºC [7] to promote maximum heat transfer effectiveness.

As a consequence of this, traditional heat exchangers would require intolerable heat exchange areas to attain such unique exchange requirements. As a result, a new generation of compact heat exchangers (CHE) emerged as a potential solution. CHEs are based on reducing the hydraulic diameter of the flow channels to the microscale (D_h ~ 1 – 1000 μm), taking advantage of the high heat exchange area of a bundle of small diameter flow channels [76]. Hence, by significantly increasing the number of flow microchannels in the bundle, CHEs achieve higher heat exchange areas per unit of volume compared to conventional heat exchangers. The surface area density, ζ ($m^2 \cdot m^{-3}$), is the parameter that characterizes the compactness capability of the heat exchanger. In addition, CHEs are particularly advantageous for the NET Power cycle by exploiting the liquid-like properties of CO_2 at supercritical pressures to achieve microconfined turbulence, overcoming the traditional limitation of CHEs to operate within the laminar flow regime [77].

Currently, the five candidate CHE architectures, for application in oxy-combustion power cycles, are: (i) printed circuit heat exchanger (PCHE), (ii) micro shell-and-tube heat exchanger (MSTHE), (iii) plate fin heat exchanger, (iv) additive manufacturing heat exchanger, and (v) polymer derived ceramic composite heat exchanger. A review of the state of the art of current CHEs technologies under development (i)-(v) [8] reveals that the PCHE and MSTHE promise to be the most appropriate architectures in the medium-term to comply with the NET Power cycle specific operating conditions.

2.5.2.1 Printed circuit heat exchangers

PCHE is an established technology, originally developed after research efforts conducted at the University of Sydney in the 1980s, mainly manufactured by the company Heatric [78]. PCHEs consist of flat metal plates on which flow channels, usually in a zig-zag arrangement, are chemically etched; using methods similar to those used in the construction of printed circuit boards in the electronics industry [79]. The etched plates are stacked alternatively between hot and cold stream plates, and are diffusion bonded, forming a compact heat transfer block. Diffusion bonding is a high-temperature solid-state joining process that promotes grain growth through the metal [80]. Fig. 2.11 shows (a) an etched plate with zig-zag configuration, and (b) a heat exchange block pressed by diffusion bonding.

Meshram et al. [81] studied the thermohydraulic performance of a PCHE with straight and zig-zag channels in fully turbulent flow regime for scCO_2 power cycle applications. The pressure of CO_2, on the high-pressure side, was set at 225 bar, and on the low-pressure side at 90 bar. The boundary condition of fluid inlet temperatures was set at 400 ºC and 600 ºC, and 500 ºC and 730 ºC. Findings reveal that decreasing the diameter of the flow

channels increases the heat transfer coefficient, but the pressure drop also increases significantly.

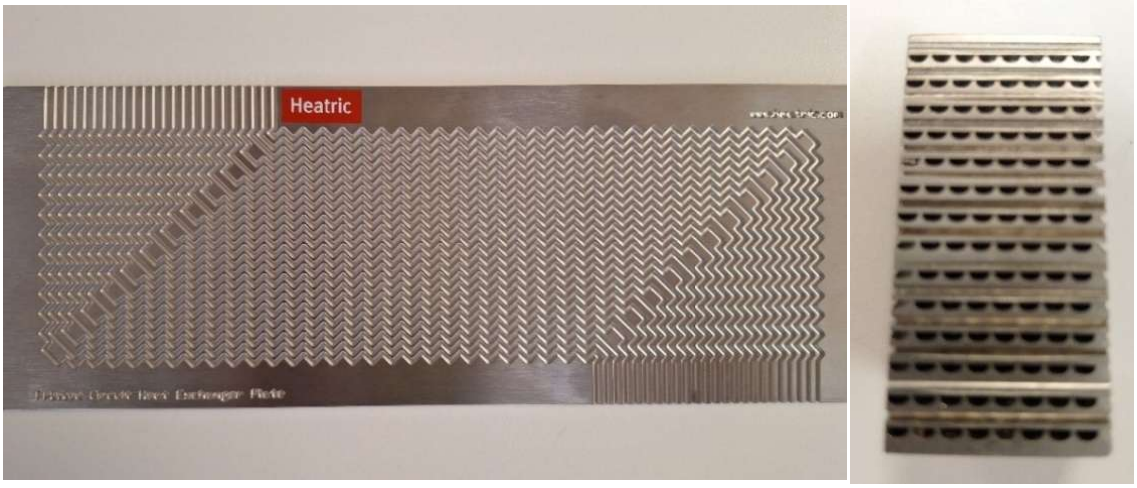

(a) (b)

Fig. 2.11. (a) Etched stainless steel plate with zig-zag configuration, (b) compact heat exchanger joined by diffusion bonding.

For the zig-zag channel arrangement, higher heat transfer rates were reported for higher bend angles and lower linear pitch, with the zig-zag configuration presenting in all cases better heat transfer performance than the straight flow channel arrangement. Marchionni et al. [82] studied the PCHE transients, of a $scCO_2$ power cycle, during start-up, shutdown and operation point changes using a one-dimensional numerical model, validated from a three-dimensional computational fluid dynamics (CFD) model. The authors concluded that thermal fluid expansion caused by axial reduction in density and an increase in system pressure, can induce sudden temperature changes and thermal stresses, affecting equipment integrity, mainly at start-up conditions.

2.5.2.2 Micro shell-and-tube heat exchangers

MSTHEs can be conceived as miniaturized conventional shell-and-tube heat exchangers (CSTE), featuring an elevated number of tubes (~ 80,000 as maximum) of diameters within the order of 1 mm to increase the surface area density ζ. The high-pressure cold fluid is located in the microtube-side, and the low-pressure hot fluid flows through the remaining space between the shell and the microtubes. In contrast to CSTEs, MSTHEs typically do not feature baffles, since sufficiently high heat transfer rates are achieved with a counter-flow arrangement. Thus, the large pressure drop in the shell-side caused by the cross-flow pattern is prevented. However, the baffleless configuration may induce tube buckling issues and high amplitude vibrations induced by turbulent flow.

Therefore, the long term mechanical performance, and optimal design are crucial for the large-scale MSTHE.

The MSTHE architecture is relatively novel in the field of CHEs, which means that a reduced number of researches, mainly academic studies, have been performed. The main experimental and computational studies of heat transfer on $scCO_2$ have been conducted for large-diameter single straight tubes in either vertical or horizontal orientation, under heating or cooling conditions. By using a single testing tube instead of a tube bundle, the complexity of the experimental setup is reduced, allowing to obtain local heat transfer coefficients, which are used to adjust useful correlations for the design of heat exchangers.

A supercritical turbulent flow in a heated straight tube experiences an enhancement of heat transfer in the vicinity of the pseudo-critical point by virtue of the steep increase in the Prandtl number (Fig. 2.6) [83]. The exact magnitude of this enhancement is influenced by the changes in the flow structure and turbulence levels caused by axial and radial density gradients [84]. Axial density gradients cause a flow acceleration effect to satisfy the continuity of mass. To produce such flow acceleration, a favorable axial pressure gradient is imposed on the turbulent boundary layer, which potentially can produce a reduction of the shear stress gradient in the near-wall fluid region. This results in a *re-laminarization* of the flow, increasing the thickness of the viscous sublayer and reducing the production of turbulent quantities, impairing turbulent heat diffusion. Radial density gradients cause buoyancy forces which modify the velocity profile shape and transverse shear stress distribution. Buoyancy effects act to either enhance or deteriorate heat transfer depending on the orientation of the heated tube.

For upward flows, previous research reported the appearance of a wall temperature peak due to a heat transfer impairment caused by buoyancy [85,86]. This is because buoyancy forces, acting in the flow direction, increase the velocity gradient in the near-wall region and flatten it in the flow core [87]. This causes the reduction of the shear stress and turbulent kinetic energy production (P_k), deteriorating turbulent heat transport. Eventually, the fluid velocity in the near-wall region increases until it becomes higher than in the flow core, forming an M-shaped velocity profile, which enhances turbulence production, entering in a heat transfer recovery regime [88]. Some studies found a second wall temperature peak due to the increase of the velocity in the flow core region due to the thermal flow acceleration [89–91]. For downward flow cases, an enhancement of heat transfer occurs with increasing buoyancy influence [92,93]. This is because the buoyancy forces experienced by the low-density fluid within the near-wall region occur in the opposite direction of core flow. Hence, free convection leads to a sharper velocity profile, turbulence production is improved, and heat diffusion by turbulent action becomes more effective [94].

In a horizontal turbulent flow in a heated tube, as the fluid in the near-wall region reaches T_{pc}, buoyancy forces are induced in the cross-flow direction. These buoyancy

forces transport low-density heated fluid from the bottom to the top region along the wall, while high-density fluid flows downward through the core of the tube, transferring momentum to the lower half. Hence, a secondary flow circulation in the radial direction of the tube, that enhances turbulent mixing is gradually formed [95,96].

Table 2.4 shows the experimental studies on heat transfer of $scCO_2$ in horizontal tubes that have been conducted. Adebiyi et al. [97] used in their experimental study a large horizontal tube with an inner diameter of 22.14 mm, and an inlet Reynolds number range of about $2{\cdot}10^4$ to $2{\cdot}10^5$. The results revealed that the wall temperature at the top surface of the tube is higher than at the bottom surface because of the buoyancy-induced secondary cross flow. This demonstrates an enhancement of heat transfer at the bottom of the tube, and a deterioration at the top. Experimental studies conducted by Kim et al. [98] confirmed the results obtained by Adebiyi et al. [97] by obtaining higher heat transfer coefficients at the bottom wall than at the top wall. To explain the experimental results, Chu et al. [99] conducted a computational study of heat transfer to $scCO_2$ in 1 mm and 2 mm heated horizontal tubes for an inlet Reynolds number of 5400 using direct numerical simulation (DNS). The results showed that, as a consequence of the induced secondary flow, low-density flow accumulates in the top region of the tube and high-density flow concentrates at the bottom, resulting in a stratified flow. Hence, the thickness of the boundary layer on the top wall increases and turbulent production is suppressed, impairing heat transfer. At the bottom wall, the radial velocity gradient increases progressively as the peak velocity is pushed downward, P_k increases and turbulent heat transport improves.

Table 2.4. Experimental studies on heat transfer of $scCO_2$ in horizontal tubes.

Authors	Diameter *ID* (mm)	Testing pressure p (bar)	Inlet temperature T_i (ºC)	Mass flux G (kg m^{-2} s^{-1})	Heat flux $\dot{q}_w$ (kW m^{-2})	Method
Adebiyi et al. [97]	22.14	76	10.0-30.1	103.9-392.2	5.1-26.9	heating
Liao et al. [100]	0.7, 1.4, 2.16	74-120	20	90.97-909.7	10-200	heating
Yoon et al. [101]	7.73	75-88	50-80	225-450	-	cooling
Dang et al. [102]	1-6	80, 90, 100	30-70	200-1200	6-33	cooling
Huai et al. [103]	1.31	74-85	22-53	113.7-418.6	0.8-9	cooling
Son et al. [104]	7.75	75-100	90-100	200-400	-	cooling
Oh et al. [105]	4.55, 7.75	75-100	90-100	200-600	-	cooling
Pita et al. [106]	4.72	77.9-134.2	91-126	1120.2-2211.8	40-70	cooling
Liu et al. [107]	4, 6, 10.7	75-85	25-67	74.1-795.8	-	cooling
Jajja et al. [108]	0.75	76-81.2	16-50	500-1000	200-400	heating
Kim et al. [98]	7.75	73.8-77.4	24.5-30.1	52.1-250.5	1.2-25.9	heating
Wang et al. [109]	0.5, 0.75, 1	76.6-90.0	31	848.8-3395.3	124.8-281.8	heating
Theologou et al. [110]	4, 8	77.5	5-25	400, 800	30-130	heating
Öztabak et al. [111]	0.509	80	27	79-141	6.4-9.3	heating

Theologou et al. [110] experimentally examined the influence of Reynolds number and heat to mass flux ratio on thermal stratification in heated horizontal tubes of 4 mm and 8 mm. The heat to mass ratios were set between 38 – 225 J·kg^{-1}. Increasing Reynolds numbers for a given heat flux, and tube diameter, reduces the temperature difference

between the top and bottom of the tube. Increasing the tube diameter and the heat to mass flux ratio produces a more pronounced thermal stratification [112]. Indeed, a marked heat transfer deterioration under high heat flux conditions was found in the numerical studies conducted by Zhang et al. [113] and Wang et al. [114].

In recent years, research on $scCO_2$ heat transfer in horizontal tubes was focused on microchannels found in the new generation of CHEs. Jajja et al. [108] determined whether heat transfer mechanisms in large horizontal tubes can be extrapolated to the microscale. Experiments with flow channels with a hydraulic diameter of 0.75 mm, under non-uniform heat flow conditions, were conducted. The authors concluded that buoyancy forces and flow acceleration are significant enough to influence the heat transfer process at the microscale.

Wang et al. [109] experimentally investigated the heat transfer characteristics in horizontal tubes of diameters of 1.0 mm, 0.75 mm and 0.5 mm. The heat transfer coefficients improved near the pseudo-critical point, finding that the configuration with higher mass flux, lower inlet temperature and smaller diameter exhibited the best heat transfer performance. In addition, authors concluded that the buoyancy effect may be insignificant for hydraulic diameters equal or smaller than 0.75 mm, although it was substantial for the 1 mm flow channel.

Öztabak et al. [111] experimentally investigated the heat transfer characteristics of $scCO_2$ flowing through a horizontal 0.509 mm inner diameter microtube, and compared the heat transfer performance with vertical flow configurations. Tests were conducted at a pressure of 8 MPa and low Reynolds numbers at the tube inlet, ranging from 400 to 1000. An evaluation of the Richardson number, which denotes the relative importance of natural convection in relation to forced convection, showed that buoyancy forces near the wall, not in the core, significantly influence the heat transfer process. An increase in wall heat flux results in a reduction of the Nusselt number in the region near the pseudo-critical point. However, away from the pseudo-critical region, the Nusselt number trends were independent of the wall heat flux and mass flux.

As far as MSTHEs are concerned, Jiang et al. [9] optimized the number of tubes, tube diameter and tube distance in the bundle of a MSTHE, without baffles, for application in the recuperator of a closed $scCO_2$ Brayton cycle using the Aspen Plus HX model library. Moreover, they compared the thermal-hydraulic performance of the MSTHE and a PCHE under steady and dynamic conditions. At nominal conditions, the heat transfer coefficients of the MSTHE were higher than those of the PCHE, implying that the MSTHE requires less heat transfer area and metal mass. As a result, MSTHE achieved higher values of ζ and dynamic response velocities than PCHE. These results were confirmed in the review report performed by Kwon et al. [8], who reported that PCHEs reach ζ values of up to 2500 $m^2 \cdot m^{-3}$, while MSTHEs reach up to 4500 $m^2 \cdot m^{-3}$ for tube diameters of 1 mm.

Cai et al. [115] numerically investigated the heat transfer characteristics between $scCO_2$ and water in a MSTHE with tubes of inner diameter of 1.6 mm and $scCO_2$ flowing through the microtubes at low Reynolds numbers, being cooled by water on the shell-side. The parametric studies conducted indicated that the heat transfer coefficient of CO_2 increases with increasing CO_2 mass flow, while it is not influenced with increasing water mass flow. Buoyancy effects were significant at low Reynolds conditions, inducing a secondary flow pattern that impairs the heat transfer coefficient in the lower region of the tube, and improves it in the upper region. In addition, authors analyzed the effect on heat transfer of the shell-side water flow pattern. The counter-flow configuration resulted in higher heat transfer coefficients than cross-flow. Nevertheless, the experimental study of heat transfer between $scCO_2$ and water in a 37 tube MSTHE of 1.6 mm diameter and 500 mm length conducted by Cai et al. [116] revealed that baffles on the shell lead to a significant heat transfer enhancement effect, with the heat transfer coefficient increasing as baffle spacing decreases, while pressure drop also augments [117]. This apparent discordance may be due to the fact that, as buoyancy forces gain greater influence on heat transfer for low Reynolds numbers, the cross-flow pattern results in thermal stratified $scCO_2$ flow and deteriorated heat transfer.

Jin et al. [118] conducted over forty experimental series to investigate the thermal-hydraulic performance in a fabricated five-cell MSTHE using $scCO_2$ and air as working fluids, with the Reynolds numbers ranges between 9000 to 17000 and 2000 to 18000, respectively. The experimental outcomes were used to validate the thermal-hydraulic models and correlations employed by [119,120]. The results showed a good agreement with model predictions, reporting deviations within 10% for all key performance metrics, including thermal conductance and pressure drop.

The largest experimental advancement on MSTHEs to date was conducted by Thar Energy, LLC. They designed and manufactured a prototype MSTHE featuring approximately 20,000 microtubes in a single shell for application on the recuperator of a $scCO_2$ Brayton power cycle to withstand high differential pressures and elevated temperatures [121]. The hot-side of the shell was constructed from Inconel 625, while the cold-side used stainless steel 316L. Moreover, a single-flange asymmetric pressure vessel was developed to enhance structural performance and reduce manufacturing costs.

2.5.2.3 Comparison between printed circuit heat exchangers and micro shell-and-tube heat exchangers

The NET Power cycle demonstration plant owned by NET Power Inc, in LaPorte, Texas, uses PCHEs consisting of 1.6 mm zig-zag etched plates, manufactured by Heatric, for the RHE equipment [7]. As the RHE is divided into three heat exchange sections: LTS,

MTS and HTS, the RHE is constituted by three PCHEs. Fig. 2.12 shows the low-temperature PCHE of the NET Power cycle demonstration plant.

Fig. 2.12. PCHE for the low-temperature section of the RHE of the NET Power cycle demonstration pilot plant.

Since the construction of the NET Power's demonstration pilot plant, in 2016, to date, advances in CHE research have revealed considerable advantages of novel MSTHEs over established PCHEs. Especially for the specific operating conditions of the NET Power cycle.

The surface area density of a MSTHEs can reach 4500 $m^2 \cdot m^{-3}$, while PCHEs reach 2500 $m^2 \cdot m^{-3}$ [8]. This implies that MSTHEs require much less mass to comply with the heat exchange requirements, so the transient response to operating point changes, start-ups and shutdowns is much faster. This feature is critical in order to export the NET Power technology from the United States (base load operation stand point) to Europe, where rapid load changes will be expected due to the high percentage of power generation from fluctuating renewable sources, characteristic for Europe [122–125]. Reducing the amount of RHE material also reduces manufacturing costs. This is especially important for the high-temperature heat exchanger section, built from costly exotic Nickel (Ni)–based superalloys (Inconel-625, -282, -740H, -617), since mechanical stresses caused by the large differential pressure exceeds the allowable creep and deformation resistance of SS316L. In addition, each PCHE unit must be made of the same material, which implies that the PCHE of the high-temperature section is constructed entirely of Ni-based alloy. In contrast, MSTHEs may be built with different materials, limiting the use of Ni-based alloys to the high-temperature head and using cost-effective SS316L for the rest of components, further reducing the amount of Ni-based alloys requirements.

Another important phenomenon to consider is the corrosion of the heat exchanger materials, and thus their cleanability and maintainability. It has been demonstrated by numerous experimental studies [20,126–132] that steels, either Ni- or Fe-based, exposed

to CO_2 environments experience high levels of oxidation, which affect structural integrity and heat exchange capacity. The corrosion degree can be significantly reduced by using alloys with high chromium content (> 20% wt.), as the dissociated O_2 from CO_2 reacts with the Cr contained in the outer layer of the material, to form an outer chromium oxide (Cr_2O_3) layer that protects the material from corrosion. Although materials commonly used in the RHE, SS316L and Inconel 625, have high Cr content, it is to be expected that frequent maintenance operations will have to be planned to prevent clogging of the flow microchannels and heat transfer impairment. Due to the nature of the manufacturing method, the PCHE cannot be dissembled without destroying the core to reveal the interior once it has been fully manufactured. This will significantly complicate maintenance labors and limits the cleaning process of channels to high-pressure chemical injection. In contrast, MSTHEs allow access to the interior by simply removing the outer flange, facilitating mechanical cleaning, inspection and tube replacement.

Another important advantage of MSTHEs over PCHEs is related to the manufacturing process technology. The complex diffusion bonding and chemical etching techniques of PCHEs are limited to a reduced number of companies, which implies higher manufacturing costs. However, the manufacturing technology of MSTHEs is inherited from CSTEs, for which there is a widespread supply chain, and the manufacturing processes have been optimized.

In the state of the art of the NET Power cycle, PCHEs were established as the prevailing technology for application in the RHE. In fact, PCHEs are applied within the RHE of the demonstration pilot plant of the cycle, as previously discussed in the first paragraph of the section. However, a thorough literature survey reveals numerous techno-economic advantages of MSTHEs over PCHEs. This finding has motivated the principal objective of this Thesis work, which is to initiate an investigation to carry out a migration from the PCHE architecture to the MSTHE; evaluating the potential of MSTHEs to work under the challenging operating conditions of the NET Power cycle. In particular, the present research focuses on the heat transfer process between the $scCO_2$-rich recirculating stream RE-6 (see Fig. 2.7) and the humid exhaust gases FG-2 in the low-temperature section of the RHE. This approach is justified by two main reasons:

- RE-6 is essentially composed of $scCO_2$, operating within the pseudo-critical region (see Fig. 2.5) in the low-temperature section pressure and temperature ranges, where the rapid variation of the fluid properties influence the heat transfer process.
- FG-2 reaches saturation conditions in the low-temperature section, forming a H_2O-rich condensing film around the tube surfaces, whose dynamics influence the effectiveness of the heat transfer process.

The remaining streams (OX, PB, AR), as well as the medium- and high-temperature exchange sections, operate beyond the pseudo-critical region, where the sensible heat

exchange between the ideal-like gases can be tackled on the basis of conventional constant-property flows.

To address this study, a working methodology was defined after identifying in this chapter the following knowledge gaps related to the NET Power cycle:

i. The open literature does not collect studies that evaluate the predictive capability of thermodynamic property methods applied to scCO$_2$-rich mixtures, under the specific conditions of pressure, temperature and composition of the cycle. Also, the most advanced cycle embodiment, proposed by NET Power, has not been modeled, so its detailed thermodynamic performance, and the maximum efficiency operating conditions remain unknown. Similarly, a detailed analysis of the cycle's performance under partial load conditions is not available.
ii. There are few studies, either experimental or numerical, that address heat transfer in scCO$_2$ microflows. In particular, no investigations have been reported under the specific operating conditions of the NET Power cycle heat recovery unit. Consequently, the detailed behavior of the heat transfer process as a function of operating variables is unknown, and no specific predictive models applicable to this context are available.

Based on these research gaps, the methodology depicted in Fig. 2.13 was adopted. The document is divided into two thematic parts, each including a methodology and results sections. The first part, formed by steps 1, 2, 3 and 4, aims to model in off-design conditions the NET Power cycle to derive the MSTHE operating ranges within the RHE. These operating ranges are required for the second part, formed by steps 5, 6 and 7, to investigate heat transfer in scCO$_2$ microflows, and to study the thermal-hydraulic performance of a MSTHE working in the low-temperature section of the RHE. The methodology and results of the first part are presented in Sections 3 and 4. Then, the methodology and results concerning the second part are discussed in Sections 5 and 6. Based on the adopted methodology and in light of the previously identified research gaps, the present study aims to address the following scientific questions:

i. Which EoSs most accurately describe the volumetric and phase equilibrium properties of CO$_2$-rich mixtures under the specific conditions of the NET Power cycle?.
ii. How does the choice of EoS influence the prediction of thermodynamic performance and the design of critical components (such as pumps or heat exchangers) of the NET Power cycle.
iii. What is the optimal parametric configuration that maximizes the thermal efficiency of the advanced NET Power cycle, and how can it be found in a computationally efficient way?.

iv. How does the thermodynamic performance of the NET Power cycle vary under part-load conditions, and what implications does this have on the operating ranges of pressure, temperature and mass flow rate in its thermal recuperator?.

v. How does the heat transfer process perform in $scCO_2$ flows in microtubes, characteristics of MSTHEs, at pressures up to 30 MPa, especially at conditions representative of the low-temperature section of the NET Power cycle recuperator?.

vi. What effects do buoyancy, flow acceleration, and other key variables (such as mass flux, heat flux, and inlet temperature) have on local heat transfer coefficients in $scCO_2$ microflows?.

vii. How can $scCO_2$ heat transfer be modeled empirically and computationally, using correlations and/or machine learning techniques, for application in the design of high-performance MSTHEs?.

viii. What thermal and mechanical limitations are present in MSTHEs operating under actual NET Power cycle conditions, and how do they affect the design of these devices versus other technologies such as PCHEs?.

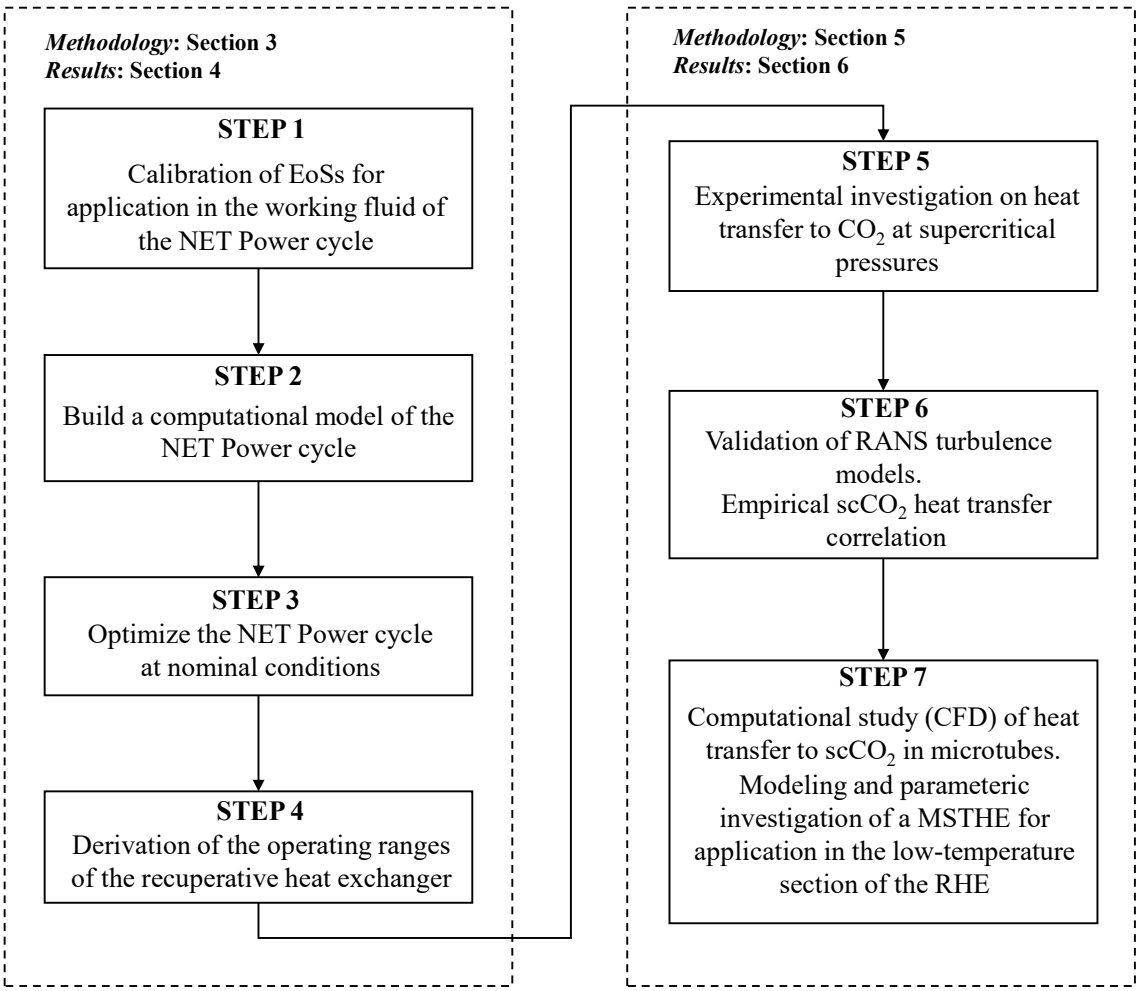

Fig. 2.13. Scheme of the methodology.

Chapter 3
Thermodynamic modeling approach of the NET Power cycle

3 Thermodynamic modeling approach of the NET Power cycle

This chapter presents the methodology applied to model the most up-to-date NET Power cycle embodiment at off-design conditions in Aspen Plus. Section 3.1 describes the procedure for the numerical calibration of the EoSs. This step is necessary to ensure reliability of the EoSs in predicting the volumetric and phase behavior of the supercritical working fluid of the NET Power cycle. In Section 3.2, the modeling approach of the NET Power cycle, including the control strategy of the cycle at partial loads, are detailed. In addition, the hybrid numerical optimization algorithm, developed as a novelty in this work, is also described. This algorithm allows finding the operative configuration for maximum cycle efficiency.

3.1 Calibration of the EoSs for application in the working fluid of the NET Power cycle

In the MSTHE, a turbulent flow of $scCO_2$ flows through the microtubes on the high-pressure side, where it is heated within the pseudo-critical region by a hot, condensative CO_2 – H_2O stream. This CO_2 – H_2O stream flows in counterflow through the annular space between the shell and the microtubes (low-pressure side). The heat transfer mechanisms on the high-pressure side are expected to be significantly affected by the pronounced variations in the thermophysical properties of the fluid near the pseudo-critical point. Therefore, it is crucial to ensure that the thermodynamic model used provides reliable property predictions of the NET Power working fluid in the supercritical regime.

Furthermore, since the MSTHE operates in the low-temperature section of the RHE, the low-pressure hot gases are cooled below the saturation point. As a result, part of the transferred heat flux corresponds to latent heat of condensation. The condensate, which is formed by H_2O and small traces of dissolved CO_2, likely forms a circumferential thin film around the outer surface of the microtubes. At the interface between the condensate film and the surrounding hot gas mixture, thermodynamic equilibrium between CO_2 and H_2O takes place. Therefore, to calculate the vapor transport from the gas phase to the condensate, where the vapor condenses, it is essential to reliably predict the composition of CO_2 and H_2O in equilibrium at the interface.

The aforementioned factors can be synthesized in the need to establish reliable and accurate prediction models of the volumetric behavior of the supercritical working fluid of the NET Power cycle, and of the phase behavior of the CO_2 – H_2O mixture. However, the literature survey on EoSs, conducted in Section 2.4.1, indicated that the performance of the existing EoSs for CCUS systems has not been evaluated within the p, T, $\bar{x}$ ranges relevant to the NET Power cycle supercritical fluid mixture [133]. Consequently, this

research work is initiated with the calibration of the mixing rules of several EoSs, commonly employed in CCUS systems. This numerical calibration is based on experimental density and VLE data of $scCO_2$-rich binary mixtures, under the p, T, $\bar{x}$ conditions analogous to those of the NET Power cycle. The methodology for conducting the numerical calibration of EoSs is detailed in this section.

3.1.1 Selected equations of state: mathematical formulation and mixing rules

Six EoSs were selected as candidates to accurately predict the volumetric and phase behavior of $scCO_2$ mixtures within the NET Power cycle:

- Peng-Robinson (PR) and Soave-Redlich-Kwong (SRK) cubic-type EoSs.
- Lee-Kesler-Plöcker (LKP) and Benedict-Webb-Rubin-Starling (BWRS) virial-type EoSs.
- Perturbed Chain – Statistical Associating Fluid Theory (PC-SAFT) and Cubic-Plus-Association (CPA) SAFT-type EoSs.

The mathematical formulation, parameters and mixing rules of these EoSs are presented in Table 3.1. The binary interaction parameters that are calibrated were highlighted in bold in Table 3.1. These EoSs were chosen because: (i) they are the most widely used EoSs for modeling purposes of CCUS [134], and (ii) they are integrated in the Aspen Plus software. The former is fundamental since Aspen Plus is the process simulation software used in this work to develop the thermodynamic model of the NET Power cycle. Therefore, the calibrated EoSs derived from this study can be easily applied in the NET Power cycle modeling. It is worth noting that Aspen Plus contains the formulation of the EoSs given in Table 3.1, which ensures that the results presented in this work can be reproduced without the need to use Aspen Plus as a computational package. In Table 3.1, x_i represents the mole fraction of component i in the mixture, with the summations running over all components. Pure component parameters, required for the computation of the EoSs, such as critical parameters ($p_{c,i}$, $T_{c,i}$, $\rho_{c,i}$), acentric factors (ω_i), number of spherical segments in a chain (m_i), segment diameters (σ_i), dispersion energies (ε_i/k), number of sites (N_i), and association volume parameters (β_i), for the components CO_2, H_2O, CO, H_2, O_2, N_2, Ar and CH_4, are provided in the Appendix A of this document. In addition, specific expressions and constants required by the LKP, BWRS and PC-SAFT EoSs are also given in Appendix A. The PC-SAFT EoS is expressed in terms of the molar residual Helmholtz free energy, $\hat{a}^{\mathrm{res}}$. $\hat{a}$ is one of the fundamental state functions in thermodynamics. Therefore, all thermodynamic properties can be calculated easily from derivatives of a with respect to the density and temperature. For more details on the derivation of the properties from a see [62]. The performance of these EoSs was compared with the multiparametric GERG-2008 EoS. The detailed mathematical formulation of the GERG-2008 EoS can be found in [62].

Table 3.1. Mathematical formulation, parameters, and mixing rules of the selected EoSs. The adjustable binary interaction parameters are highlighted in bold.

EoS	Functional form	Parameters and mixing rules of the EoSs
PR [135]	$p = \frac{RT}{\hat{v}-b} - \frac{a}{\hat{v}(\hat{v}+b)+b(\hat{v}-b)}$	$a = \sum_i \sum_j x_i x_j (1-\boldsymbol{k}_{ij})\sqrt{a_i a_j}$; $b = \sum_i x_i b_i$; $k_{ij} = \boldsymbol{k}_{ij}^{(1)} + \boldsymbol{k}_{ij}^{(2)} T + \frac{\boldsymbol{k}_{ij}^{(3)}}{T}$, $(k_{ij} = k_{ji})$; where a_i and b_i are calculated based on $p_{c,i}$, $T_{c,i}$, ω_i, and the alpha function α_i: $a_i = \alpha_i 0.45724 \frac{R^2 T_{c,i}^2}{p_{c,i}}$; $b_i = 0.07780 \frac{RT_{c,i}}{p_{c,i}}$; $\alpha_i = \left[1 + (0.37464 + 1.54226\omega_i - 0.26992\omega_i^2)(1 - T_r^{0.5})\right]^2$.
SRK [136]	$p = \frac{RT}{\hat{v}-b} - \frac{a}{\hat{v}(\hat{v}+b)}$	$a = \sum_i \sum_j x_i x_j (1-\boldsymbol{k}_{ij})\sqrt{a_i a_j}$; $b = \sum_i x_i b_i$; $k_{ij} = \boldsymbol{k}_{ij}^{(1)} + \boldsymbol{k}_{ij}^{(2)} T + \frac{\boldsymbol{k}_{ij}^{(3)}}{T}$, $(k_{ij} = k_{ji})$; Where a_i and b_i are calculated based on $p_{c,i}$, $T_{c,i}$, ω_i, and the alpha function α_i: $a_i = \alpha_i 0.42747 \frac{R^2 T_{c,i}^2}{p_{c,i}}$; $b_i = 0.08664 \frac{RT_{c,i}}{p_{c,i}}$; $\alpha_i = \left[1 + (0.48508 + 1.55171\omega_i - 0.15613\omega_i^2)(1 - T_r^{0.5})\right]^2$.
LKP [137]	$z = z^0 + \frac{\omega}{\omega^{\mathrm{R}}}(z^{\mathrm{R}} - z^0)$ z^0 and z^{R} rely on the functional form of the BWR EoS. z^0 is an EoS for simple fluids and z^{R} is an EoS for a reference fluid (*n*-octane): $z^{(0 \text{ or } \mathrm{R})} = 1 + \frac{B}{v_r} + \frac{C}{v_r^2} + \frac{D}{v_r^5} + \frac{c_4\tau^3}{v_r^2} + \left(\beta + \frac{\gamma}{v_r^2}\right)\exp\left(-\frac{\gamma}{v_r^2}\right)$	$B = b_1 - b_2\tau - b_3\tau^2 - b_4\tau^4$; $C = c_1 - c_2\tau + c_3\tau^3$; $D = d_1 + d_2\tau$; where: $v_r = \frac{p_r}{RT_r\rho}$; $\tau = T_r/T$; $\delta = \rho/\rho_r$. The mixing rules are the following: $T_r = \rho_r^{0.25} \sum_i \sum_j x_i x_j v_{c,ij}^{0.25} T_{c,ij}$; $\frac{1}{\rho_r} = \sum_i \sum_j x_i x_j v_{c,ij}$; $p_r = (0.2905 - 0.085\omega)RT_r\rho_r$; with: $T_{c,ij} = (1+\boldsymbol{k}_{ij})(T_{c,i} \cdot T_{c,j})^{0.5}$, $(k_{ij} = k_{ji})$; $v_{c,ij} = \left(v_{c,i}^{1/3} + v_{c,j}^{1/3}\right)^{3/8}$; $v_{c,i} = (0.2905 - 0.085\omega_i)\frac{RT_{c,i}}{p_{c,i}}$; $\omega = \sum_i x_i \omega_i$; Constants b_1, b_2, b_3, b_4, c_1, c_2, c_3, c_4, d_1, d_2, β and γ are given in Table A.2 [138].
BWRS [139]	$p = \hat{\rho}RT + \left(B_0RT - A_0 - \frac{C_0}{T^2} + \frac{D_0}{T^3} - \frac{E_0}{T^4}\right)\hat{\rho}^2 + \left(bRT - a - \frac{d}{T}\right)\hat{\rho}^3 + \alpha\left(a + \frac{d}{T}\right)\hat{\rho}^6 + \frac{c\hat{\rho}^3}{T^2}(1+\gamma\hat{\rho}^2)\exp(-\gamma\hat{\rho}^2)$	$B_0 = \sum_i x_i B_{0,i}$; $A_0 = \sum_i \sum_j x_i x_j A_{0,i}^{\frac{1}{2}} A_{0,j}^{\frac{1}{2}} (1-\boldsymbol{k}_{ij})$; $C_0 = \sum_i \sum_j x_i x_j C_{0,i}^{\frac{1}{2}} C_{0,j}^{\frac{1}{2}} (1-\boldsymbol{k}_{ij})^3$; $D_0 = \sum_i \sum_j x_i x_j D_{0,i}^{\frac{1}{2}} D_{0,j}^{\frac{1}{2}} (1-\boldsymbol{k}_{ij})^4$; $E_0 = \sum_i \sum_j x_i x_j E_{0,i}^{\frac{1}{2}} E_{0,j}^{\frac{1}{2}} (1-\boldsymbol{k}_{ij})^5$, $(k_{ij} = k_{ji})$; where: $a = \left[\sum_i x_i a_i^{\frac{1}{3}}\right]^3$; $b = \left[\sum_i x_i b_i^{\frac{1}{3}}\right]^3$; $c = \left[\sum_i x_i c_i^{\frac{1}{3}}\right]^3$; $d = \left[\sum_i x_i d_i^{\frac{1}{3}}\right]^3$; $\alpha = \left[\sum_i x_i \alpha_i^{\frac{1}{3}}\right]^3$; $\gamma = \left[\sum_i x_i \gamma_i^{\frac{1}{2}}\right]^2$; Parameters $A_{0,i}$, $B_{0,i}$, $C_{0,i}$, $D_{0,i}$, $E_{0,i}$, a_i, b_i, c_i, d_i, α_i and γ_i for component i are calculated by using Eqs. (A.1) – (A.11), with A_j and B_j listed in Table A.3 [140].
PC-SAFT [141]	$\frac{\hat{a}^{\mathrm{res}}}{RT} = \frac{\hat{a}^{\mathrm{hc}}}{RT} + \frac{\hat{a}^{\mathrm{disp}}}{RT} + \frac{\hat{a}^{\mathrm{assoc}}}{RT} + \frac{\hat{a}^{\mathrm{polar}}}{RT}$	$\hat{a}^{\mathrm{hc}}/(RT) = \bar{m}\frac{\hat{a}^{\mathrm{hs}}}{RT} - \sum_i x_i(m_i - 1)\ln g_{ij}^{\mathrm{hs}}$, is the hard-chain term. $\hat{a}^{\mathrm{disp}}/(RT) = -2\pi\hat{\rho}I_1X - \pi\hat{\rho}\bar{m}C_1I_2Y$, is the dispersion term. $\hat{a}^{\mathrm{assoc}}/(RT) = \sum_i x_i \sum_A N_i\left(\ln X^{A_i} - \frac{X^{A_i}}{2} + \frac{1}{2}\right)$, is the association term. $\hat{a}^{\mathrm{polar}}/(RT) = \frac{[\hat{a}_2/(RT)]}{1-[\hat{a}_3/(RT)]/[\hat{a}_2/(RT)]}$, is the polar term. All the details for the calculation of the contribution terms and the formulation of the adjustable interaction parameters $\boldsymbol{k}_{ij}$ are provided in the Appendix A [141–143].
CPA [144], [61]	$p = \frac{RT}{\hat{v}-b} - \frac{a}{\hat{v}(\hat{v}+b)} - 0.5\frac{RT}{\hat{v}}\left(1 + \rho_m\frac{\partial \ln g}{\partial \rho_m}\right)\sum_i x_i \sum_{A_i}(1 - X^{A_i})$. The cubic (physical) term is calculated by the SRK EoS.	$a = \sum_i \sum_j x_i x_j (1-\boldsymbol{k}_{ij})\sqrt{a_i a_j}$; $b = \sum_i x_i b_i$; $k_{ij} = \boldsymbol{k}_{ij}^{(1)} + \boldsymbol{k}_{ij}^{(2)}\frac{T}{T_{\mathrm{ref}}}$, $T_{\mathrm{ref}} = 298.15$ K, $(k_{ij} = k_{ji})$; $a_i = \alpha_i 0.42748 \frac{R^2 T_{c,i}^2}{p_{c,i}}$; $b_i = 0.08664 \frac{RT_{c,i}}{p_{c,i}}$; $\alpha_i = \left[1 + (0.48 + 1.574\omega_i - 0.176\omega_i^2)(1 - T_r^{0.5})\right]^2$. $g = (1 - 1.9\eta)^{-1}$, where $\eta = (b\hat{\rho})/4$; $X^{A_i} = \left(1 + \hat{\rho}\sum_j x_j \sum_B X^{B_j}\Delta^{A_iB_j}\right)^{-1}$; $\Delta^{A_iB_j} = g\beta^{A_iB_j}b_{ij}\left[\exp\left(\frac{\varepsilon^{A_iB_j}}{RT}\right) - 1\right]$, with $b_{ij} = (b_i + b_j)/2$. b_i are defined as for the cubic term. Parameters β_i are given in Table A.1 [145].

3.1.2 Experimental data: pressure, temperature, and composition ranges

In the NET Power cycle, the most prominent real gas effects appear in the mixtures RE and OX (see Fig. 2.2) during the liquid-like compression stages. Consequently, the p, T ranges found in such compression, and the composition of the mixtures RE and OX, are the conditions under which the calibration procedure of the EoSs was performed. The mixtures RE and OX are compressed in the REP-1, REP-2 and OXP pumps (see Fig. 2.2) from 8 MPa to 30 MPa. During the compression, the temperature of the mixtures increases from about 299.15 K to 318.15 K, which is close to the critical temperature of CO_2. The composition of the RE and OX streams, which were obtained from the NET Power cycle numerical model developed in this work in Aspen Plus, are given in Table 3.2.

Table 3.2. Composition of the scCO_2-rich mixtures RE and OX (see Fig. 2.2 and Table 2.2).

Component	Mixture RE (% mol)	Mixture OX (% mol)
CO_2	97.9336	75.4445
H_2O	0.1195	0.0920
CO	0.0002	0.0001
H_2	0.0000	0.0000
O_2	0.1963	23.0000
N_2	1.1827	0.9571
Ar	0.5678	0.5063
CH_4	0.0000	0.0000

Table 3.3. $p, T, \bar{x}$ ranges and number of points of the density and VLE experimental data used for the EoSs numerical calibration.

Mixture	p (MPa)	T (K)	Mole fraction of the impurity	Number of points	References
CO_2 – H_2O (VLE)	1 – 17	298.18 – 423.15	–	197	[146–150]
CO_2 – H_2O (ρ)	5 – 45	307.00 – 398.15	0.002	51	[151–156]
CO_2 – CO (ρ)	2 – 49	303.15 – 373.15	0.050	120	[157]
CO_2 – H_2 (ρ)	2 – 22	303.15 – 333.15	0.020	122	[158,159]
CO_2 – O_2 (ρ)	1 – 20	293.18 – 373.46	0.274	180	[160]
CO_2 – N_2 (ρ)	2 – 30	293.15 – 330.00	0.018	60	[161–167]
CO_2 – Ar (ρ)	1 – 20	303.22 – 363.15	0.030	80	[167]
CO_2 – CH_4 (ρ)	1 – 20	304.15 – 353.00	0.004	955	[168,169]

Experimental density and VLE data for $scCO_2$-rich binary mixtures were used to perform the calibration of the binary interaction parameters of the EoSs mixing rules. Table 3.3 presents the p, T, $\bar{x}$ ranges, and the number of experimental data points used during the numerical fitting.

Experimental data were collected over the widest possible pressure range, covering the supercritical operating regime, 8 – 30 MPa, where the major real gas effects occur in the NET Power cycle. The temperature range was chosen close to the critical temperature of CO_2. For the CO_2 – O_2 system, the density regression was performed for an O_2 mole fraction of 0.274, which corresponds, approximately, with the typical composition of the oxidizing stream (mixture OX) of the NET Power cycle. For the remaining mixtures, small values of the impurity mole fractions were selected from the literature, with the aim of representing the composition of the $scCO_2$ recirculation stream (mixture RE) of the NET Power cycle.

3.1.3 Equations of state numerical fitting and performance assessment procedures

The softwares Aspen Plus V12.1 [170] and Matlab R2022b [171] were used to calibrate and evaluate the binary interaction parameters of the EoSs of Table 3.1, from the experimental density and VLE data of $scCO_2$-rich binary mixtures collected from the literature (Table 3.3). To this end, a communication between Matlab and Aspen Plus was established through an ActiveX server. A schematic diagram of the numerical procedure for calibration is presented in Fig. 3.1 [172].

In the first iteration ($l = 0$) a vector $\boldsymbol{k}_{ij}^{l}$, containing the interaction parameters of the EoS, is first initialized to 1 in Matlab. The experimental data of the binary mixture are stored in the Matlab code as vectors of pressure ($\boldsymbol{p}$), temperature ($\boldsymbol{T}$), composition ($\overline{\boldsymbol{x}}$), density ($\boldsymbol{\rho}$), equilibrium composition (**VLE**) and standard deviation ($\boldsymbol{\sigma}$). The $\boldsymbol{p}$, $\boldsymbol{T}$, $\overline{\boldsymbol{x}}$ vectors, together with $\boldsymbol{k}_{ij}^{l}$, are sent to Aspen Plus, which contains the formulation of the EoSs shown in Table 3.1, and calculates the density and equilibrium composition vectors. With the experimental and calculated data, Matlab executes the maximum-likelihood objective function [173], defined in Eq. (3.1), which is minimized by the optimization algorithm. In Eq. (3.1), the definition of the maximum-likelihood function is given for either density or VLE regression cases, with N denoting the number of experimental points. The regression convergence tolerance was set to 10^{-4}. Therefore, when the convergence criterion is satisfied, the optimization procedure is finished. Otherwise, the Britt-Luecke's generalized Least-Square method-based optimization algorithm generates a new vector of interaction parameters. For further details about the algorithm refer to [174]. The experimental data and the updated interaction parameters are sent to Aspen Plus and the optimization procedure is repeated until the convergence tolerance is achieved.

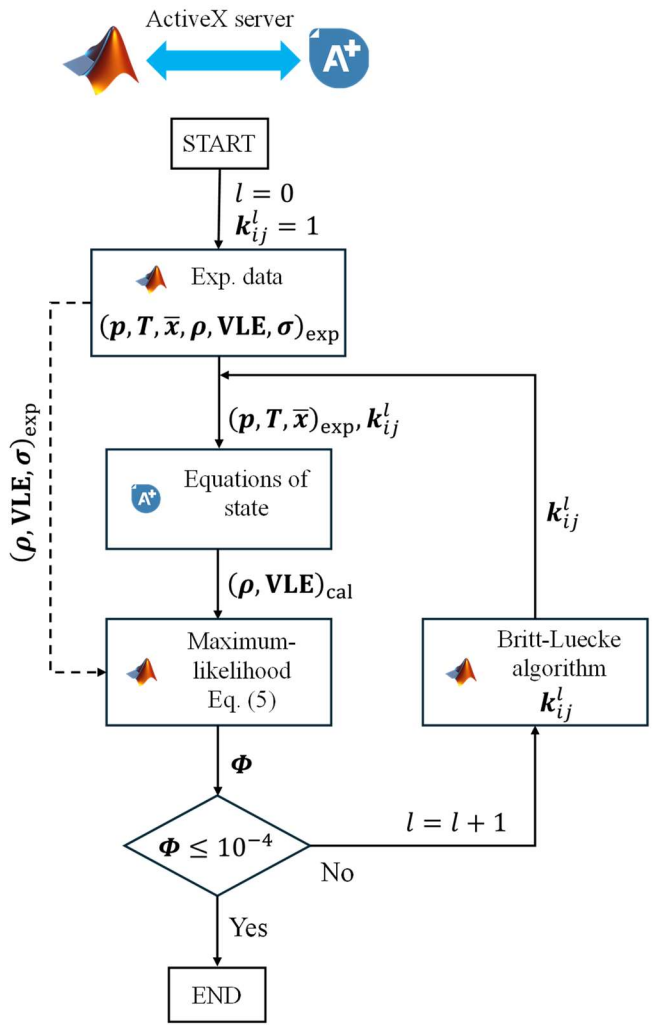

Fig. 3.1. Flow diagram of the numerical procedure for calibration of the interaction parameters of the EoSs presented in Table 3.1.

$$\Phi = \begin{cases} \frac{1}{N}\sum_{i=1}^{N}\left(\frac{\rho_{cal,i} - \rho_{exp,i}}{\sigma_{\rho,i}}\right)^2, \text{ for } \rho \text{ regression;} \\ \frac{1}{N}\sum_{i=1}^{N}\left[\left(\frac{x_{CO_2,cal,i} - x_{CO_2,exp,i}}{\sigma_{x_{CO_2,i}}}\right)^2 + \left(\frac{y_{CO_2,cal,i} - y_{CO_2,exp,i}}{\sigma_{y_{CO_2,i}}}\right)^2\right], \text{ for VLE regression.} \end{cases} \quad (3.1)$$

Once the calibrated interaction coefficients were found, they are introduced into the formulation of the EoSs in Aspen Plus. A quantitative comparison between the results provided by the EoSs and the experimental data was performed to determine the EoS that reproduces the experimental data most reliably. To perform this comparison, in the *Simulation* section of Aspen Plus, a material stream was created whose temperature, pressure and composition were established under the same conditions as the experimental data from a code implemented in Matlab. This code contains all the experimental source data and triggers the Aspen model to share the material stream results under the same operational conditions as the source data. As a result, the density and VLE compositions

response can be compared between the different EoSs as the deviation towards the source data. To quantify the deviations between the EoSs predictions and the data, the AARD, whose definition is presented in Eq. (3.2) for density and VLE in the liquid and gas phases cases, was used.

$$\text{AARD (\%)} = \begin{cases} \dfrac{100}{N}\displaystyle\sum_{i=1}^{N}\dfrac{\left|\rho_{cal,i}-\rho_{exp,i}\right|}{\rho_{exp,i}}, \text{ for } \rho; \\ \dfrac{100}{N}\displaystyle\sum_{i=1}^{N}\dfrac{\left|x_{CO_2,cal,i}-x_{CO_2,exp,i}\right|}{x_{CO_2,exp,i}}, \text{ for VLE in the liquid phase;} \\ \dfrac{100}{N}\displaystyle\sum_{i=1}^{N}\dfrac{\left|y_{CO_2,cal,i}-y_{CO_2,exp,i}\right|}{y_{CO_2,exp,i}}, \text{ for VLE in the gas phase.} \end{cases} \quad (3.2)$$

3.2 NET Power cycle off-design modeling and assumptions

Based on the optimal base cycle operating conditions presented in Table 2.1, the $scCO_2$ flowing through the microtubes and the CO_2 – H_2O mixture on the shell-side of the MSTHE operate at static pressures of 300 bar and 34 bar, respectively. Consequently, the design and analysis of the MSTHE should consider these pressure levels. However, these values were derived from an outdated NET Power cycle embodiment. For the updated embodiment considered in this study (Fig. 2.2), the optimal operating configuration under on-design conditions has not yet been determined. This implies that the nominal pressures within the MSTHE may deviate from the initially assumed 300 bar and 34 bar, potentially affecting the associated temperatures and mass flow rates.

Moreover, it is anticipated that these operating conditions will vary significantly depending on the cycle load level, which is influenced by the real-time demands of the electricity market. Therefore, it is essential to identify the new optimal on-design operating conditions, as well as the full range of expected variations in temperature, pressure, Reynolds number, and fluid composition within the MSTHE, across all potential part-load scenarios.

For this purpose, an off-design model of the NET Power cycle was developed in the process simulation software Aspen Plus V12.1. To optimize the cycle conditions, a novel derivative-free hybrid optimization algorithm, dedicated to accelerate the finding of the minimum of computationally expensive objective functions, was developed as a novelty and implemented in Matlab R2022b [171]. The modeling procedures of the off-design cycle components, and the development of the hybrid optimization algorithm, are explained in this section.

The power cycle and ASU models are based on the process flow diagram of the NET Power cycle of Fig. 2.2. The models of the process components (turbines, compressors, pumps, heat exchangers, …) were taken directly from the blocks available in Aspen Plus. A more detailed model of the cooled turbine, RHE, and gas- & dense- phase compressors at off-design conditions are explained in this section due to their complexity. The carbon purification unit was not modeled, as it has no direct influence on the power cycle performance.

Table 3.4 shows the input parameters for the model at nominal conditions, including the isentropic and mechanical efficiencies of all turbomachines, and the pressure drops in the heat exchangers and in the oxy-combustor. The fuel used is natural gas, which enters the cycle at a temperature and pressure of 15 ºC and 70 bar. The combustion process takes place with a percentage of O_2 excess of 3%. The minimum cycle temperature considered is 26 ºC. The purity of the O_2-enriched stream, supplied by the ASU to the power cycle at 18 ºC and 120 bar, is 99.5%.

Table 3.4. Input parameters and assumptions for the NET Power cycle + ASU models at nominal conditions.

Parameter	Unit	Value
Net Power cycle		
Fuel lower heating value (LHV) [89% CH_4, 7% C_2H_6, 1% C_3H_8, 0.1% C_4H_{10}, 0.01% C_5H_{12}, 2% CO_2, 0.89% N_2, (% vol)]	MJ kg^{-1}	46.502
Temperature and pressure of the fuel	°C/bar	15/70
Percentage of O_2 excess in combustion	%	3
O_2 mole fraction in the oxidizing stream	%	13.34
Minimum cycle temperature	°C	26
Bypass stream output temperature	°C	138
CO_2 gas-phase compressors isentropic efficiency	%	85
Fuel gas compressor isentropic efficiency	%	85
$ScCO_2$ dense-phase compressors hydraulic efficiency	%	85
Turbine stages isentropic efficiency	%	89
Mechanical efficiency of all turbomachinery	%	98
Recuperator high-pressure flows pressure drop	%	0.66
Recuperator low-pressure flows pressure drop	%	2.94
Combustor pressure drop	%	1
Condenser and intercoolers pressure drop	%	2
Air Separation Unit		
Ambient air temperature, pressure and relative humidity (ISO conditions)	°C/bar/%	15/1.013/60
O_2 purity of the O_2-enriched stream supplied by the ASU	% (mol)	99.5
Temperature and pressure of the O2-enriched stream supplied by the ASU	°C/bar	18/120
Air compressors isentropic efficiency (MAC and BAC)	%	85
Air turbines isentropic efficiency	%	85
Hydraulic efficiency of the liquid O_2 pump	%	80
Intercoolers pressure drop	%	1
HPC stages	-	45
HPC feed air inlet stage (starting from the top)	-	45
HPC reflux ratio (molar basis)	-	1.2
LPC stages	-	69
LPC N_2-enriched stream inlet stage	-	1
LPC O_2-enriched stream inlet stage	-	28
LPC feed air inlet stage	-	28
LPC reflux ratio (molar basis)	-	0.516

3.2.1 Equation of state selection

The strong variation of the thermo-physical properties of a supercritical fluid demands special attention to the selection of the EoS used in the thermodynamic model of the NET Power cycle. Accurately predicting the specific volume of the $scCO_2$-mixture is essential for modeling the gas- and dense-phase compression stages. Moreover, to be able to model the phase composition in thermodynamic equilibrium of the CO_2 – H_2O mixture, it is essential to predict the condensative heat transfer process that occurs in the recuperative heat exchanger of the NET Power cycle.

As discussed in Section 3.1, the binary interaction parameters of several EoSs were calibrated from experimental density and VLE data of $scCO_2$-rich binary mixtures, including components such as H_2O, CO, H_2, O_2, N_2, Ar and CH_4. The PR, SRK, LKP, BWRS, PC-SAFT and CPA EoSs were considered for the fitting process. In addition, the performance of these EoSs with respect to the experimental data was compared with the GERG-2008 EoS. As will be discussed in detail in Section 4.1, the thermodynamic model that proved to give the closest volumetric and phase predictions to the experimental data was a combination of GERG-2008 and LKP. Therefore, for the off-design NET Power cycle model developed in Aspen Plus, the GERG-2008 + LKP was adopted as the thermodynamic property method. The volumetric calculations are performed by the GERG-2008 EoS, and the phase behavior of the CO_2 – H_2O mixture is computed by the calibrated LKP EoS.

3.2.2 Supercritical CO_2 turbine

The cooled expansion model must provide the following features: (i) the ability to incorporate EoSs that reproduce the behavior of real gas mixtures; (ii) rely exclusively on several calibration parameters while not requiring turbine geometrical information. Haseli et al. [42] used the model adapted from [175] to determine the coolant mass flow, while other authors, [33,38,41,48,52] adopted the continuous expansion model proposed by El-Masri [176], and adapted by Scaccabarozzi et al. [38].

In the El-Masri model, the expansion process is divided into N + 1 stages. The first N stages correspond to the cooled section of the turbine (see Fig. 3.2), and the last expansion step (N + 1) represents the adiabatic section of the turbine. Each cooled expansion step is composed of an adiabatic expander, *EXP-I*; a mixer, *MIX-i*, mixing the coolant flow C_i associated with *EXP-i* with the main stream O_i; and a valve (*VALVE-i*). The isentropic efficiency of all expanders is assumed to be the same. The first N expanders have the same pressure ratio, which is iteratively adjusted to obtain $T_{I,N} = T_W$, where T_W is the maximum allowable material temperature of 860 °C. The pressure ratio of the adiabatic expansion section (N + 1) is automatically established to obtain the defined turbine outlet pressure. The number of turbine cooling stages N was fixed at 11 since, according to Zhao

et al. [52], a larger number of stages does not imply large differences in the total coolant flow calculation although it significantly increases the computational cost. The mass flow of each coolant stream $\dot{m}_{Ci}$ is calculated from the following expression:

$$\dot{m}_{Ci} = K_1 \frac{T_{Ii} - T_W}{T_W - T_{Ci}} \dot{W}_{EXP-i}, \tag{3.3}$$

where K_1 is a calibration parameter representing the turbine geometry and operating conditions, T_{Ii} is the inlet temperature of the *EXP-I*, T_{Ci} is the inlet temperature of the coolant and $\dot{W}_{EXP-i}$ is the power delivered by the expander i. The pressure drop caused by the addition of refrigerant, $p_{Oi} - p_{Ii+1}$, is calculated according to the following correlation:

$$p_{Oi} - p_{Ii+1} = K_2 \left(\frac{\dot{m}_{Ci}}{\dot{V}_{Hi}} \right)^{K_3}, \tag{3.4}$$

where K_2 and K_3, like K_1, are calibration parameters and $\dot{V}_{Hi}$ is the volumetric flow rate at the *VALVE-i* inlet. The parameters K_1, K_2 and K_3 were taken directly from [38].

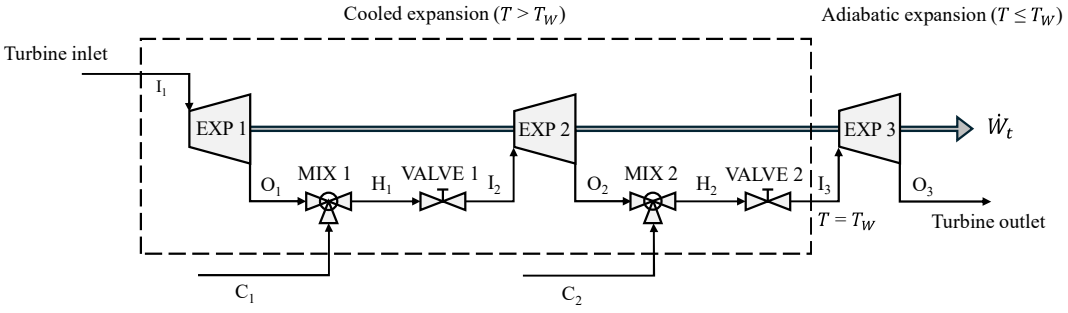

Fig. 3.2. Diagram of the adapted El-Masri cooled expansion model for $N = 2$.

In order to model the turbine at off-design conditions, it was assumed that the turbine corrected mass flow, CMF, is constant [177,178]. This condition conveniently approximates the performance map of a full admission turbine. The corrected mass flow is calculated by Eq. (3.5).

$$CMF = \frac{\dot{m}_{in} \sqrt{z_{in} R_g T_{in}}}{p_{in}} \tag{3.5}$$

It was assumed that the compressibility factor of the mixture is equal to one at nominal conditions, since the expansion process takes place at a high temperature. The value of the corrected mass flow constant, CMF, is calculated from the values of the inlet mass flow, $\dot{m}_{in}$, inlet temperature, T_{in}, inlet pressure, p_{in}, and gas constant, R_g, of the turbine

at nominal conditions. In addition, it was assumed that the isentropic efficiency of the expanders, which constitute the cooled turbine model, remains approximately constant over the entire operating partial load range [178]. Fig. 3.3 shows the cooled turbine model implemented in Aspen Plus.

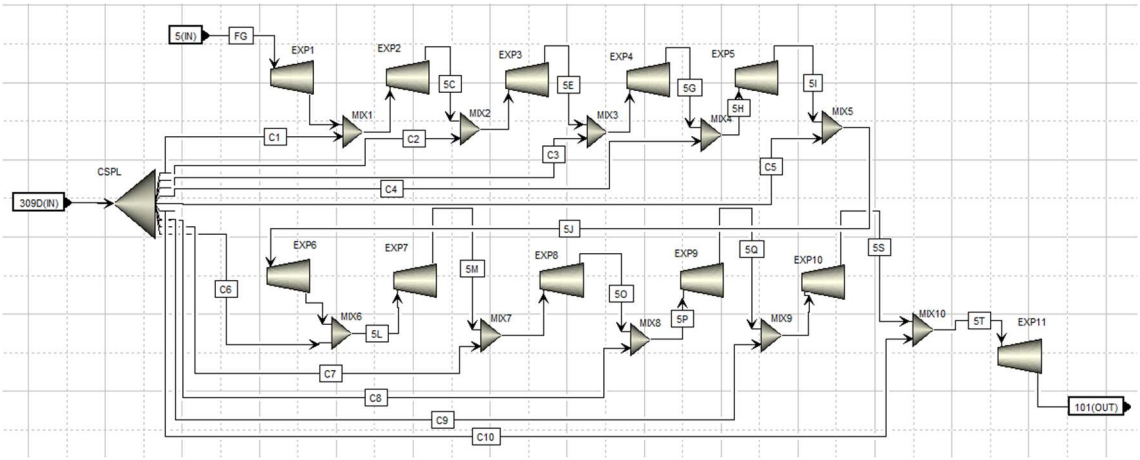

Fig. 3.3. Cooled turbine model implemented in Aspen Plus.

3.2.3 Recuperative heat exchanger (RHE)

The heat transfer process within the recuperator is strongly conditioned by the strong variations experienced by the thermo-physical properties of the fluid near the critical point [43]. Moreover, the addition of additive heating to the recuperator at different temperatures and the water condensation led to the occurrence of multiple pinch-points. To model the recuperator at nominal conditions, Allam et al. [29] employed three heat exchangers in series: two multi-stream ones, corresponding to the low- and medium-temperature sections, and another two-stream for the high-temperature section. Similarly, Mitchell et al. [41] and Colleoni et al. [43] used the approach of [29] by dividing the high-temperature exchanger into two, so that the turbine coolant is extracted in the intermediate section. They further discretized the resulting layout into a finite number of heat transfer stages to account for the non-linear variation of the heat capacities of the blended CO_2 streams. Excluding the additive heating by the bypass compressor, Scaccabarozzi et al. [38] and Chan et al. [47] divided the recuperator into two multi-stream heat exchangers, and Wimmer et al. [179] into three.

Under off-design conditions, fluid properties such as mass flow rate, temperature, pressure, and thermodynamic and transport properties change significantly, whereas the recuperator heat transfer area remains fixed. Therefore, it is essential to determine the heat exchange area based on nominal conditions prior to off-design modeling. For this purpose, a recuperator was first modeled at nominal conditions using a single multi-stream heat exchanger [180] discretized into 100 heat exchange stages. The outlet

temperatures of the CO_2 recirculation stream and the oxidizing stream were set equal and obtained from the constraint of maintaining an internal pinch-point of 5 °C. The pinch-point can occur on the cold side of the recuperator or at the dew point of the turbine exhaust gases. The *Complex* optimization algorithm (available in Aspen Plus V12.1) adjusts the turbine coolant outlet temperature to maximize the outlet temperature of the recycling streams, while the hot-side temperature difference (ΔT_h) must be greater than or equal to 10 °C. The bypass stream temperature at the recuperator extraction was set to 138 °C [29]. The outlet temperature of the hot streams are equal and derived from the energy balance within the heat exchanger. The thermal recuperator model at nominal conditions was run in Aspen Plus, allowing to obtain the hot and cold composite curves and thus the heat exchange area, as detailed in the following.

For off-design conditions, the recuperator was modeled using 10 multi-stream heat exchanger sections arranged in series. Fig. 3.4 shows a heat exchange section k, with two hot streams and two cold streams. H_K and C_K denote the number of hot and cold streams, respectively, in section k. Each hot stream i transfers a heat flow rate $\dot{Q}_{i,j,k}$ to each cold stream j, effectively converting each section k into a set of virtual two-stream heat exchangers. The inlet and outlet temperature of each stream, heat capacity flow, $(\dot{m}c_p)_{i,j,k}$, fluid properties, and heat flow rates $\dot{Q}_{i,j,k}$ are known for nominal conditions from the hot and cold composite curves.

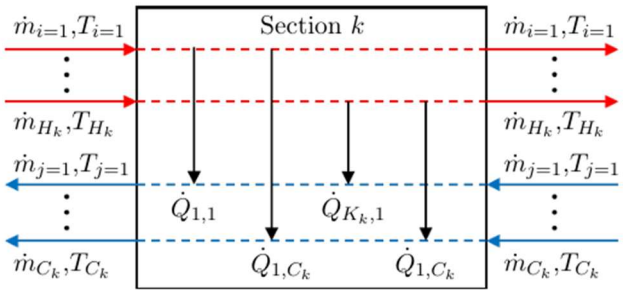

Fig. 3.4. Heat exchange section k. Subscripts i and j refer to the hot and cold streams, respectively.

The individual convective heat transfer coefficients for each hot and cold streams $\alpha_{i/j,on}$ in section k at design conditions were computed using the Gnielinski correlation [181]:

$$Nu_{i/j,on} = \frac{\alpha_{i/j,on} D_{i/j}}{\lambda_{i/j,on}} = \frac{(f_{i/j,on}/8)(Re_{i/j,on} - 1000)Pr_{i/j,on}}{1 + 12.7(f_{i/j,on}/8)^{0.5}\left(Pr_{i/j,on}^{2/3} - 1\right)}, \tag{3.6}$$

where $D_{i/j}$ is the diameter of the tubes and $f_{i/j} = \left(0.79 \ln Re_{i/j} - 1.64\right)^{-2}$ is the friction factor. Assuming negligible wall thermal resistance, the overall heat transfer coefficient for each virtual exchanger is:

$$U_{i,j,k,on} = \left(\frac{1}{\alpha_{i,on}} + \frac{1}{\alpha_{j,on}}\right)^{-1} \tag{3.7}$$

Therefore, the corresponding heat exchange area, which is held constant under off-design conditions, was derived via: $\dot{Q}_{i,j,k} = U_{i,j,k} A_{i,j,k} \Delta T_{lm,i,j,k}$. At off-design conditions, variations in fluid flow properties alter convective heat transfer coefficients. Following Hoopes et al. [182], the off-design heat transfer coefficients were computed using Eq. (3.8) by applying dimensionless similarity criteria, without knowing the detailed recuperator geometry.

$$\alpha_{off} = \alpha_{on} \frac{\lambda_{off}}{\lambda_{on}} \left(\frac{\dot{m}_{off}^2/\mu_{off}}{\dot{m}_{on}^2/\mu_{on}}\right)^{0.8} \left(\frac{Pr_{off}}{Pr_{on}}\right)^{0.33} \tag{3.8}$$

From the individual off-design heat transfer coefficients, the overall off-design heat transfer coefficient was calculated using Eq. (3.7). To update the outlet temperatures of the hot and cold streams in each section k, at off-design conditions, the effectiveness-number of transfer units (ε-NTU) method [183] was employed. Firstly, the NTU was calculated as follows:

$$NTU_{i,j,k} = \left[\frac{UA}{\left(\dot{m}c_p\right)_{min}}\right]_{i,j,k}, \tag{3.9}$$

where $A_{i,j,k}$ is known and constant. The ε for a counterflow disposition was calculated as follows:

$$\varepsilon_{i,j,k} = \frac{1 - e^{-(1-c_{i,j,k})NTU_{i,j,k}}}{1 - c_{i,j,k} e^{-(1-c_{i,j,k})NTU_{i,j,k}}}, \tag{3.10}$$

where $c_{i,j,k} = \left(\dot{m}c_p\right)_{min} / \left(\dot{m}c_p\right)_{max}$. So, the exchanged heat was computed by Eq. (3.11).

$$\dot{Q}_{i,j,k} = \varepsilon_{i,j,k} \left(\dot{m}c_p\right)_{min} \left(T_i^{in} - T_j^{in}\right). \tag{3.11}$$

The total heat delivered or absorbed by each stream in section k was then obtained as:

$$\dot{Q}_{i,k} = \sum_{j=1}^{C_K} \dot{Q}_{i,j,k}, \quad \dot{Q}_{j,k} = \sum_{i=1}^{H_K} \dot{Q}_{i,j,k}. \tag{3.12}$$

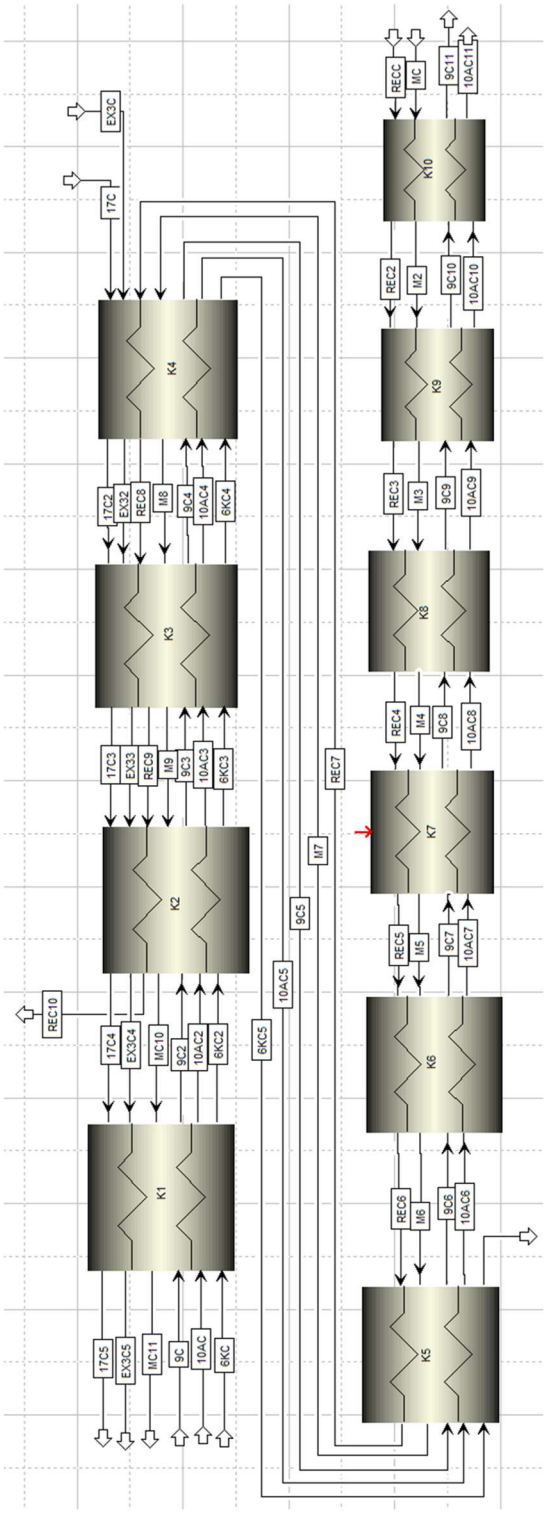

Fig. 3.5. Thermodynamic model of the RHE at off-design conditions implemented in Aspen Plus.

Finally, the outlet temperatures were determined by Eq. (3.13).

$$\dot{Q}_{i/j,k} = \left(\dot{m}c_p\right)_{i/j}\left(T_{i/j}^{in} - T_{i/j}^{out}\right). \tag{3.13}$$

The off-design pressure drops were calculated using Eq. (3.14), assuming smooth tubes, with the friction factors being an exclusive function of the Reynolds number [76].

$$\Delta p_{off} = \Delta p_{on}\frac{\dot{m}_{off}^2/\rho_{off}}{\dot{m}_{on}^2/\rho_{on}}. \tag{3.14}$$

The entire off design resolution, which requires iterative computation, was implemented in Aspen Plus via a custom Fortran block. An initial temperature profile across the 10 exchange sections is iteratively updated using the Broyden's method [184,185], achieving convergence when the temperature residual falls below 10^{-6}. Fig. 3.5 shows the final thermodynamic model of the recuperator operating under off-design conditions in Aspen Plus.

3.2.4 Gas-phase compressors

Compressor performance maps, which relate the relative pressure ratio, β_r, the angle of the compressor inlet guide vanes, α, and the relative isentropic efficiency, η_r, as a function of the relative volumetric flow, $\dot{V}_r$, were implemented in the Aspen Plus model. The compressor performance maps were those proposed by Alfani et al. [186], which are shown as blue dots in Fig. 3.6. Relative variables refer to the ratio between the value at off-design conditions and the value at on-design conditions of the compressor, i.e., $\beta_r = \beta_{off}/\beta_{on}$, $\eta_r = \eta_{off}/\eta_{on}$ and $\dot{V}_r = \dot{V}_{off}/\dot{V}_{on}$. To implement the performance maps in the Aspen Plus model, two 4th degree best-fit polynomials were fitted in Matlab to relate $\beta_r = \beta_r\left(\dot{V}_r, \alpha\right)$ and $\eta_r = \eta_r\left(\dot{V}_r, \alpha\right)$. These polynomials are shown in Eqs. (3.15) and (3.16).

$$\begin{aligned}\beta_r = {} & a_1 + a_2\alpha + a_3\dot{V}_r + a_4\alpha^2 + a_5\alpha\dot{V}_r + a_6\dot{V}_r^2 + a_7\alpha^3 \\ & + a_8\alpha^2\dot{V}_r + a_9\alpha\dot{V}_r^2 + a_{10}\dot{V}_r^3 + a_{11}\alpha^4 + a_{12}\alpha^3\dot{V}_r \\ & + a_{13}\alpha^2\dot{V}_r^2 + a_{14}\alpha\dot{V}_r^3 + a_{15}\dot{V}_r^4\end{aligned} \tag{3.15}$$

$$\begin{aligned}\eta_r = {} & b_1 + b_2\alpha + b_3\dot{V}_r + b_4\alpha^2 + b_5\alpha\dot{V}_r + b_6\dot{V}_r^2 + b_7\alpha^3 \\ & + b_8\alpha^2\dot{V}_r + b_9\alpha\dot{V}_r^2 + b_{10}\dot{V}_r^3 + b_{11}\alpha^4 + b_{12}\alpha^3\dot{V}_r \\ & + b_{13}\alpha^2\dot{V}_r^2 + b_{14}\alpha\dot{V}_r^3 + b_{15}\dot{V}_r^4\end{aligned} \tag{3.16}$$

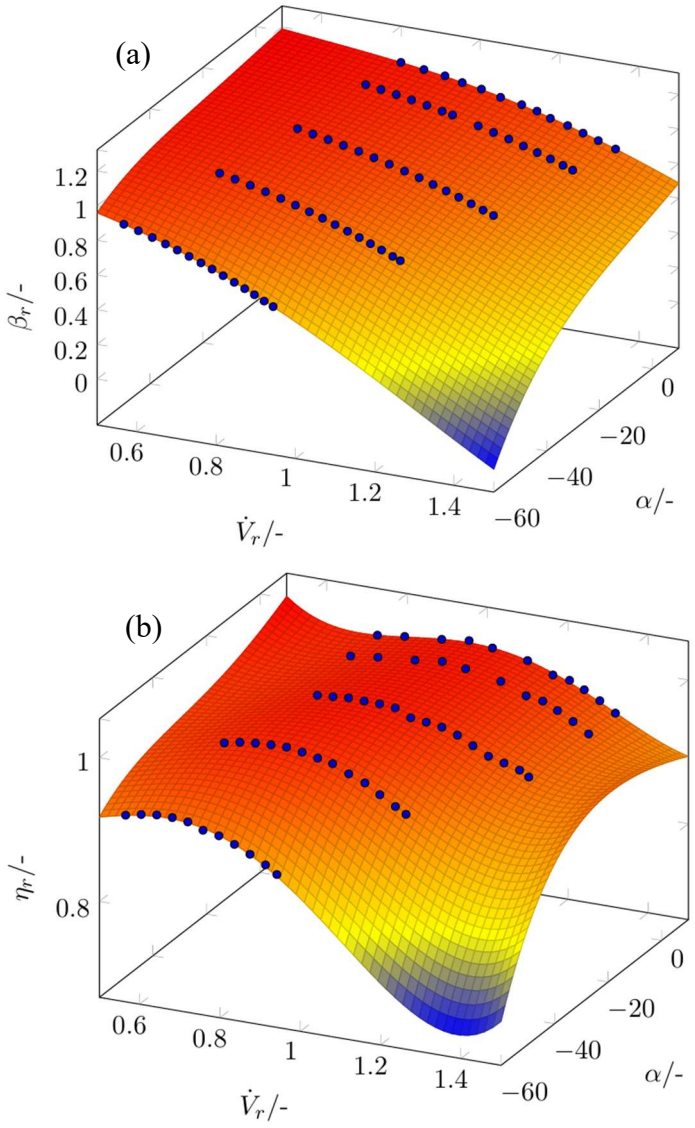

Fig. 3.6. Performance maps of the gas-phase compressors. (a) Relative pressure ratio (β_r) and (b) relative isentropic efficiency (η_r), as a function of the relative volumetric flow ($\dot{V}_r$) and the angle of the inlet guide vanes (α).

The fitting coefficients of the 4th degree polynomials of Eqs. (3.15) and (3.16) are presented in Table 3.5 and Table 3.6, respectively.

Table 3.5. Fitting coefficients of the 4th-degree best-fit polynomial $\beta_r = \beta_r(\dot{V}_r, \alpha)$ of Eq. (3.15).

a_1	1.407	a_6	1.484	a_{11}	$-1.659\cdot10^{-8}$
a_2	$6.857\cdot10^{-3}$	a_7	$-1.380\cdot10^{-6}$	a_{12}	$1.737\cdot10^{-6}$
a_3	-0.9458	a_8	$-2.907\cdot10^{-5}$	a_{13}	$2.160\cdot10^{-5}$
a_4	$1.422\cdot10^{-5}$	a_9	$2.291\cdot10^{-2}$	a_{14}	$-7.015\cdot10^{-3}$
a_5	$-1.928\cdot10^{-2}$	a_{10}	-1.236	a_{15}	0.291

Table 3.6. Fitting coefficients of the 4th-degree best-fit polynomial $\eta_r = \eta_r(\dot{V}_r, \alpha)$ of Eq. (3.16).

b_1	1.989	b_6	7.697	b_{11}	$-8.379 \cdot 10^{-9}$
b_2	$1.888 \cdot 10^{-2}$	b_7	$-5.578 \cdot 10^{-7}$	b_{12}	$6.162 \cdot 10^{-7}$
b_3	-4.651	b_8	$-8.640 \cdot 10^{-5}$	b_{13}	$1.978 \cdot 10^{-5}$
b_4	$6.038 \cdot 10^{-5}$	b_9	$6.094 \cdot 10^{-2}$	b_{14}	$-2.022 \cdot 10^{-2}$
b_5	$-5.954 \cdot 10^{-2}$	b_{10}	-5.341	b_{15}	1.305

The output pressure of the gas phase compression stage with intermediate cooling was fixed at 80 bar. In addition, all compression stages operate with the same pressure ratio, which was calculated by finding the root (β) of Eq. (3.17).

$$f(\beta) = -p_{in}\beta^4 + \Delta p_1 \beta^3 + \Delta p_2 \beta^2 + \Delta p_3 \beta + p_{out} = 0 \tag{3.17}$$

p_{in} is the inlet pressure, Δp_i are the pressure drops of the intercoolers, calculated by using the Eq. (3.14), and p_{out} is the outlet pressure, 80 bar. To calculate the isentropic efficiency of the gas phase compression at off-design conditions, first the compression ratio, β, was obtained from Eq. (3.17). Therefore, since β_r is known, and $\dot{V}_r$ is given by the output of the previous Aspen block, α was obtained by solving Eq. (3.15). Finally, knowing $\dot{V}_r$ and α, the isentropic efficiency η_r was determined from Eq. (3.16).

3.2.5 Dense-phase compressors

In the NET Power cycle there are three dense-phase compressors, which are assumed to be controlled by varying the rotational speed. To derive the behavior of the dense-phase compressors beyond the on-design conditions, the concept of similarity in hydraulic machines was used [187]. A hydraulic machine operating at different rotational speeds will operate with the same hydraulic efficiency if the flow coefficient, Θ, and the work coefficient, φ, defined in Eqs. (3.18) and (3.19), are kept constant under different operating conditions. The dimensionless characteristic curves, which relate the relative head and relative hydraulic efficiency with the relative volumetric flow, considered in the model, are shown in Fig. 3.7.

$$\Theta = \frac{\dot{V}}{\omega D^3} \tag{3.18}$$

$$\varphi = \frac{gH}{\omega^2 D^2} \tag{3.19}$$

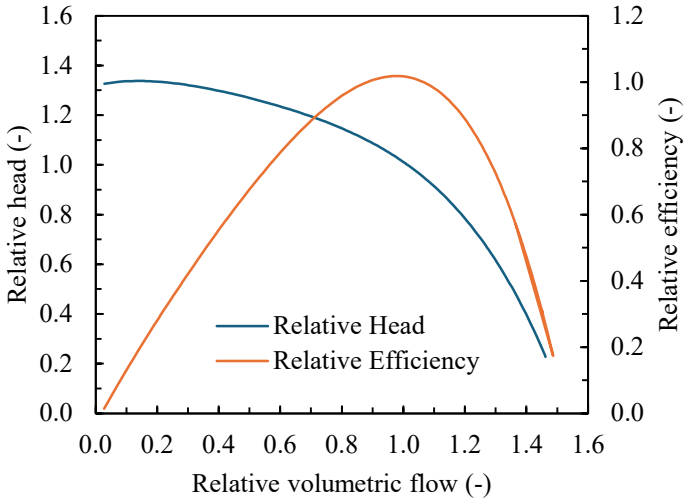

Fig. 3.7. Performance map of the dense-phase compressors.

To implement the characteristic curves in the Aspen Plus model, the curves were fitted in Matlab by the following polynomials:

$$H_r = c_1\dot{V}_r^4 + c_2\dot{V}_r^3 + c_3\dot{V}_r^2 + c_4\dot{V}_r + c_5 \tag{3.20}$$

$$\eta_r = d_1\dot{V}_r^4 + d_2\dot{V}_r^3 + d_3\dot{V}_r^2 + d_4\dot{V}_r + d_5, \tag{3.21}$$

where the fitting coefficients are shown in Table 3.7. The curves, presented in Eqs. (3.20) and (3.21), are given for a particular rotational speed. For a new operating point, at a different rotational speed, and by applying the concept of similarity in hydraulic machines, the following polynomials were obtained:

$$H_r = c_1\omega_r^{-2}\dot{V}_r^4 + c_2\omega_r^{-1}\dot{V}_r^3 + c_3\dot{V}_r^2 + c_4\omega_r\dot{V}_r + c_5\omega_r^2, \tag{3.22}$$

$$\eta_r = d_1\omega_r^{-4}\dot{V}_r^4 + d_2\omega_r^{-3}\dot{V}_r^3 + d_3\omega_r^{-2}\dot{V}_r^2 + d_4\omega_r^{-1}\dot{V}_r + d_5. \tag{3.23}$$

Table 3.7. Fitting coefficients of the polynomials $H_r = H_r(\dot{V}_r)$ and $\eta_r = \eta_r(\dot{V}_r)$.

c_1	-0.6156	d_1	-0.6532
c_2	1.267	d_2	0.7946
c_3	-1.2375	d_3	-0.781
c_4	0.2781	d_4	1.6872
c_5	1.3202	d_5	-0.0303

ω_r is the relative rotational speed. Therefore, in order to calculate the relative hydraulic efficiency at off-design conditions, first, the rotational speed at which the dense-phase compressor must operate to produce the required head was calculated by obtaining the root (ω_r) of Eq. (3.22). The required head that the dense-phase compressor must deliver was set from the desired discharge pressure, which was known and kept constant. Then, knowing $\dot{V}_r$ and ω_r, the relative hydraulic operating efficiency, η_r, was calculated using Eq. (3.23).

3.2.6 Air separation unit

The high- and low-pressure cryogenic distillation columns (HPC and LPC) of the ASU were modeled using the RadFrac block available in Aspen Plus. Table 3.4 shows the number of stages, stages at which feed is introduced and products are extracted, and the reflux ratios of the HPC and LPC distillation columns. The O_2-enriched stream is extracted at 18 ºC and 120 bar, with an O_2 mole fraction of 99.5%.

The ASU was also modeled at off-design conditions. For this purpose, the compressor performance maps of Fig. 3.6, were used for the ASU compressors. The dense-phase compressor performance curves in Fig. 3.7, were employed for the ASU pumps. Finally, the partial load heat exchanger model described in Section 3.2.3, was used to characterize the ASU heat exchanger. Fig. 3.8 shows the final thermodynamic model of the ASU implemented in Aspen Plus.

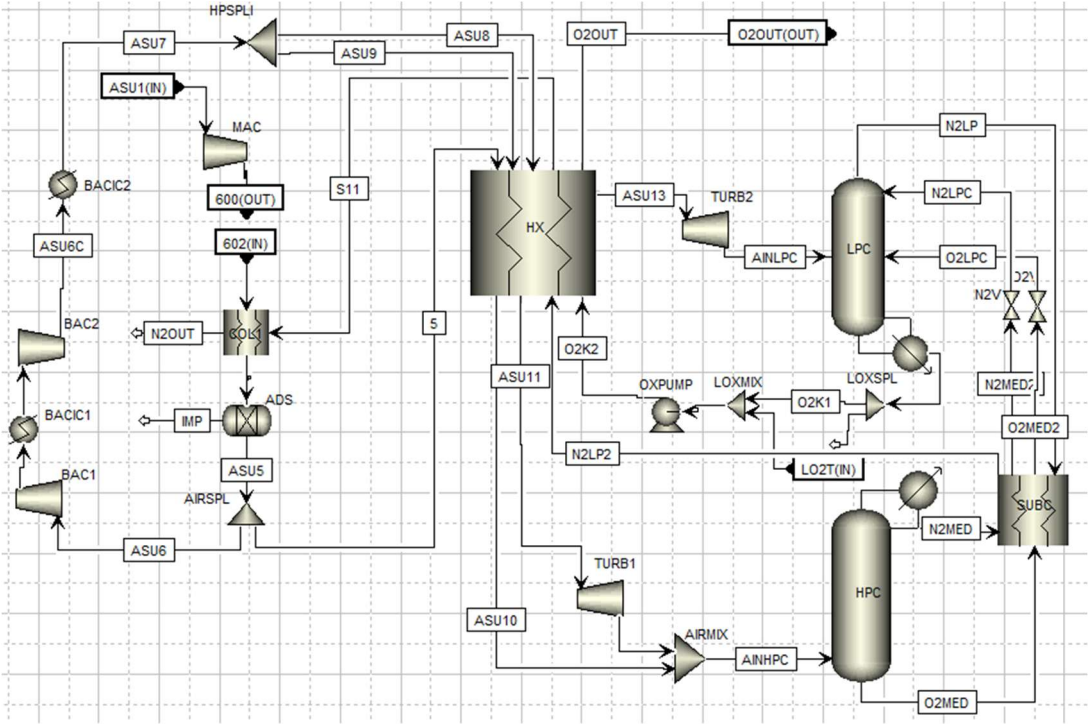

Fig. 3.8. Thermodynamic model of the ASU implemented in Aspen Plus.

3.2.7 Numerical process optimization algorithm methodology. The PSO + Complex optimization algorithm.

The numerical optimization problem was handled with the black-box approach. That is, the simulation model in Aspen Plus was considered as a black-box function, so that the direct search optimization method programmed in Matlab R2022b [171] generates the decision variable set and sends it to the Aspen Plus black-box function through an ActiveX server. Then, Aspen Plus computes the cycle performance and sends it back to the Matlab optimizer.

The objective function to be maximized was the net cycle efficiency. The decision variables, as well as their bounds and the (non-linear) design constraints, are shown in Table 3.8. The output of the process simulation model is non-smooth and presents noise [38]. Therefore, a hybrid derivative-free numerical optimization algorithm suitable to deal with this kind of objective functions, was implemented in Matlab. The optimization method is composed of two algorithms (whose solutions are shared) corresponding to a global search process, a particle swarm optimization (PSO); and a local search step, Complex algorithm modified by [188].

Table 3.8. Objective function, independent decision variables and (non-linear) design constraints involved in the numerical optimization process of the NET Power cycle.

	Parameters	Constraints
Objective function	Net cycle efficiency	Should be maximized
Independent decision variables	Recycle stream mass flow rate (which controls the combustor outlet temperature)	600 – 1800 (kg s^{-1})
	Turbine inlet pressure	200 – 400 (bar)
	Turbine outlet pressure	20 – 60 (bar)
	Recuperator outlet temperature of the recycle and oxidant streams	500 – 840 (°C)
	Recuperator outlet temperature of the turbine coolant flow	50 – 600 (°C)
	Bypass stream split fraction	0 – 15 (%)
Design (non-linear) constraints	ΔT_h	≥ 10 (°C)
	Pinch-point of the recuperator	≥ 5 (°C)

The PSO is a stochastic population-based optimization algorithm, which was proposed by Ebarhart et al. [189], based on the concept of "swarm intelligence". That is, the collective behavior of unsophisticated individuals interacting locally with each other, and with the environment, produces coherent global patterns [190]. The "swarm" in the PSO algorithm is a set of decision points (independent variables), named particles, which move in the *n*-dimensional space looking for the best solution. The new change of the particle i in the new iteration, $\Delta \boldsymbol{x}_{k+1}^{(i)}$, depends on the change that the particle i had in the previous iteration, $\Delta \boldsymbol{x}_{k}^{(i)}$ (inertial term), the position at which the particle i found the best result,

$\boldsymbol{x}_{best}^{(i)}$ (memory term), and the best point of the entire swarm, $\boldsymbol{x}_{best}$ (social term), according to Eq. (3.24).

$$\Delta \boldsymbol{x}_{k+1}^{(i)} = c_0 \cdot \Delta \boldsymbol{x}_k^{(i)} + c_1 \cdot r_1 \cdot \left(\boldsymbol{x}_{best}^{(i)} - \boldsymbol{x}_k^{(i)}\right) + c_2 \cdot r_2 \cdot \left(\boldsymbol{x}_{best} - \boldsymbol{x}_k^{(i)}\right) \tag{3.24}$$

Constants c_0, c_1 and c_2 control the degree of influence of the inertial, memory and social terms on the new movement of the particle, respectively. The values r_1 and r_2, which are random numbers between [0,2], introduce a degree of randomness to the search to handle the trend between local and global search.

Complex is a local search derivative-free optimization algorithm, which was proposed by Box [191]. The method was developed from the Simplex optimization algorithm of Nelder et al. [192] and Spendley et al. [193]. The working principle of the Complex algorithm is shown in Fig. 3.9. A set of decision variables, N_{pc}, in the n-dimensional space are taken. Then, the worst point is replaced by a new point obtained by reflecting the worst point through the centroid of the remaining points. The centroid, $\boldsymbol{x}_c$, of the points in the Complex (excluding the worst point) is calculated as follows:

$$\boldsymbol{x}_c = \frac{1}{N_{pc} - 1} \sum_{i=1, i \neq w}^{N_{pc}} \boldsymbol{x}_i. \tag{3.25}$$

Then, the new point, $\boldsymbol{x}_r$, is obtained by reflecting the worst point through the centroid:

$$\boldsymbol{x}_r = \boldsymbol{x}_c + \rho(\boldsymbol{x}_c - \boldsymbol{x}_r), \tag{3.26}$$

where ρ is the reflection coefficient, which usually takes a value of 1.3. If $\boldsymbol{x}_r$ is feasible and a better point than $\boldsymbol{x}_w$, $\boldsymbol{x}_w$ is replaced by $\boldsymbol{x}_r$ and the procedure is repeated, identifying the worst point in the new set. In the case that $\boldsymbol{x}_r$ is not feasible, or is a worse point than $\boldsymbol{x}_w$, $\boldsymbol{x}_r$ is recalculated by moving it towards the centroid. There is a possibility that a local minimum is located at the centroid of the Complex, causing the method to move all points towards the centroid and collapse to a point. To avoid this, $\boldsymbol{x}_r$ is gradually moved to the best value, $\boldsymbol{x}_b$. In addition, to make the method less prone to collapse or to stagnate at local minimum, a random component ϕ, which is uniformly distributed in the interval [0,1], is introduced as follows:

$$\boldsymbol{x}_r' = \frac{1}{2}[\boldsymbol{x}_r + \varepsilon \boldsymbol{x}_c + (1 - \varepsilon)\boldsymbol{x}_b] + (\boldsymbol{x}_c - \boldsymbol{x}_b)(1 - \varepsilon)(2\phi - 1). \tag{3.27}$$

ε is expressed in Eq. (3.28), with k_f denoting the number of times the solution repeated itself as lowest value.

$$\varepsilon = \left(\frac{4}{4 + k_f - 1}\right)^{4+k_f-1/4} \tag{3.28}$$

As can be seen in Fig. 3.10, the hybrid PSO + Complex algorithm firstly generates an initial population of random decision variables satisfying the design constraints [194]. Then, at each iteration, the algorithm executes the following two steps: (i) a global search consisting of an update (iteration) of the current set of decision variables according to the PSO algorithm; (ii) if the global search step fails to find a better value of the objective function, a local search consisting of two reflections is performed according to the Complex algorithm. If the global search step was successful, step (ii) is skipped. A population size of 50 and a complex of 12 vertices (twice the number of decision variables) was set. The set of decision variables that form the vertices of the complex are those closest to the global optimum in each iteration.

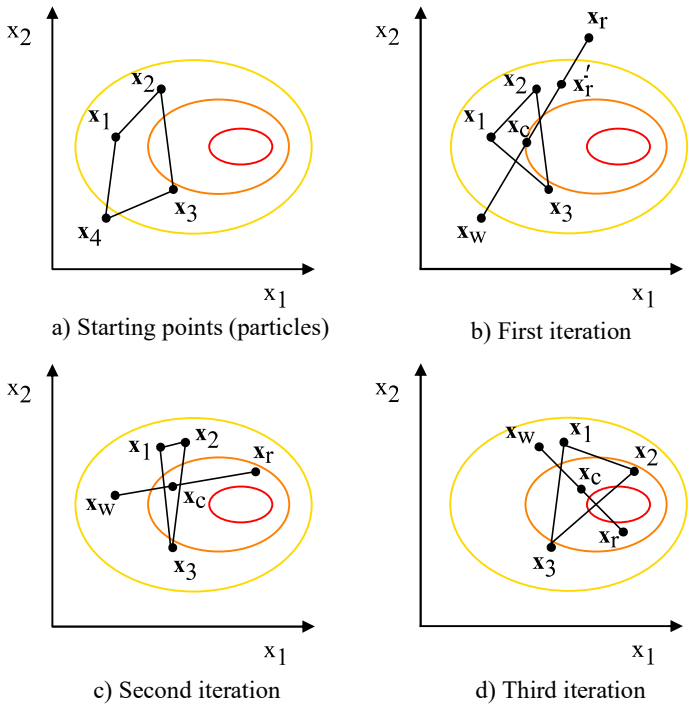

Fig. 3.9. Working principle of the optimization algorithm Complex with two independent variables and four vertices.

Non-linear design constraints and hidden constraints, which come from a numerical convergence failure of the process simulation software, were handled with a penalty function. That is, if any constraint is violated the objective function is set to infinity. The stopping criteria was set to 500 total iterations of the algorithm (steps i and ii). Because of the meta-heuristic nature of the optimization method, the algorithm was executed five

times to reach global optimum solutions, following a multi-start strategy. Therefore, by applying the PSO + Complex algorithm, the global optimum of computationally expensive objective functions is found in less time compared to conventional algorithms, without requiring surrogate models. The development of this algorithm, and its application for the optimization of the advanced NET Power cycle, represent novel contributions to the state of the art.

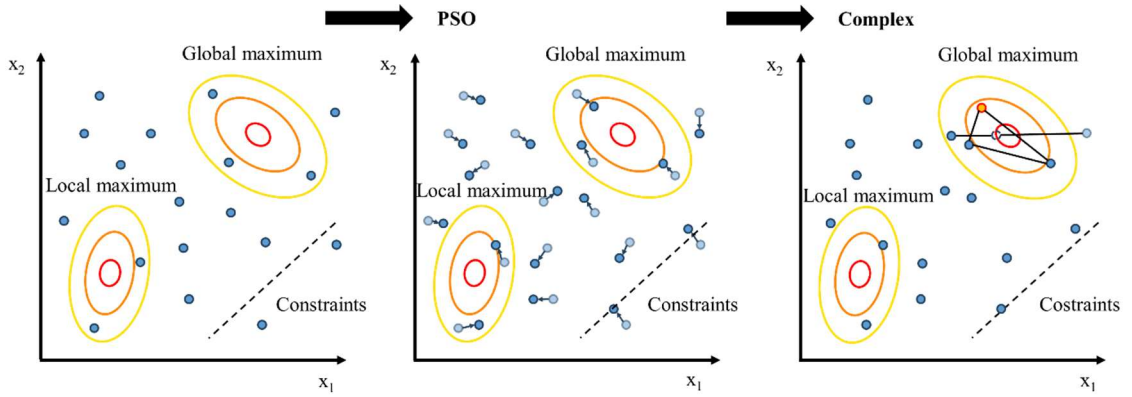

Fig. 3.10. Execution procedure of one iteration of the hybrid optimization algorithm PSO + Complex for a problem with 2 design variables, x_1 and x_2, a population size of 18, and a complex with 4 vertices.

3.2.8 Part-load control strategies

The NET Power cycle adjusts its power output in response to the demands of the electrical grid, operating over a load range from 100% (nominal design point) down to 20%. It is important to note that the cycle load percentage used during all of this study is based on the fuel mass flow rate entering the cycle, with 100% load corresponding to a fuel flow rate of 16.52 kg·s^{-1}.

Fig. 3.11 shows the thermodynamic model of the NET Power cycle under partial load conditions implemented in Aspen Plus. At partial load conditions, the turbine outlet temperature (TOT) and TOP are kept constant and equal to the values for maximum cycle efficiency at nominal conditions. This constraint ensures that the effectiveness of the RHE remains elevated at partial loads. Because decreasing fuel flow reduces the heat released during combustion, TOT would drop. To counteract this, the scCO$_2$ recirculation flow through the cycle is reduced by adjusting the variable inlet guide vanes of the gas-phase compressor. This regulation maintains TOP and adjusts COT such that TOT remains constant.

The discharge pressures of the gas phase compressor is held fixed at 80 bar by recirculating a portion of the partially compressed gases back to the compressor inlet. The intermediate pressure of 120 bar is maintained constant by varying the rotational speed of the dense-phase compressor. The maximum cycle pressure decreases as the

recirculation flow is reduced to match the turbine performance curve. This is accomplished by acting on the rotational speed of the CO_2 recycle and oxidizing dense-phase compressors. The minimum cycle temperature was kept constant at 26 ºC by adjusting the cooling water flow.

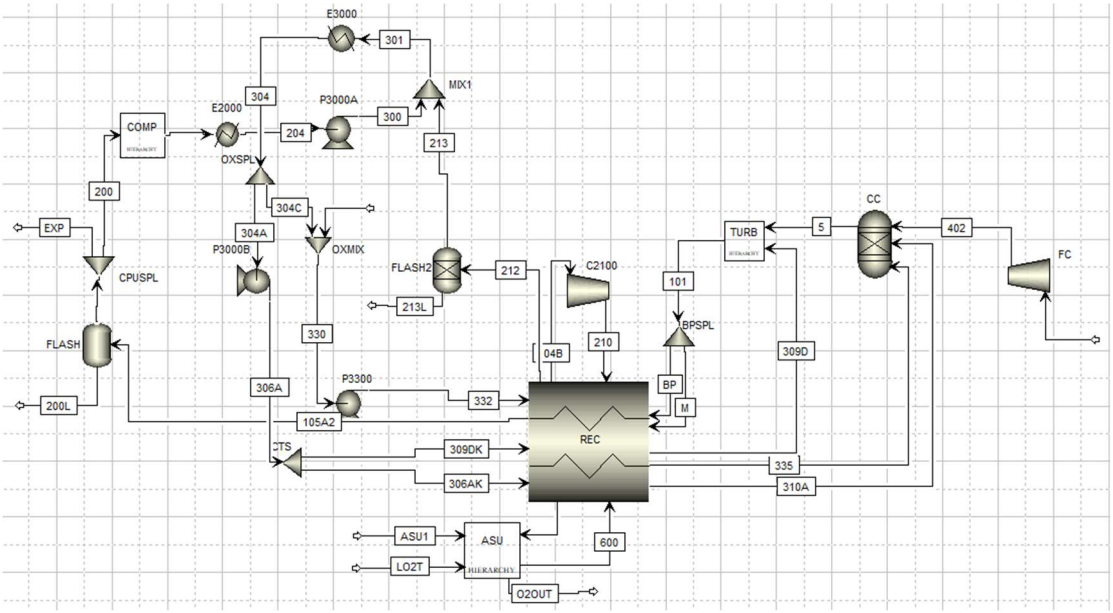

Fig. 3.11. Thermodynamic model of the NET Power cycle for partial loads (off-design conditions) implemented in Aspen Plus. The ASU, cooled turbine and gas-phase compression models were packed in hierarchy blocks.

The flow of O_2 supplied to the power cycle by the ASU is decreased in proportion to the fuel flow rate, ensuring that combustion takes place with a constant percentage of O_2 excess of 3%. This is managed by varying the air flow admitted into the ASU by acting on the MAC (see Fig. 2.2) variable inlet guide vanes. By varying the process air flow, the efficiency of the compressors and heat exchangers decreases, which causes a variation in the pressure and temperature of the feed streams to the distillation columns. This produces a variation in the purity of the produced O_2. To maintain a 99.5% O_2 purity in the O_2-rich product stream, the reflux ratios of the distillation columns are modified by acting on flow control valves. The variation of the reflux ratios causes the ratio of the introduced air flow, to the produced O_2 flow, to increase. Consequently, the ASU efficiency decreases as the processed air flow rate decreases.

3.2.9 Methodology for preliminary component design

In the results section, the influence of the used calibrated EoS on the NET Power cycle is also evaluated under nominal conditions. This serves to ensure that the results are independent from the EoS, deriving reliable outcomes. In addition to evaluating the influence of the EoS on the thermodynamic performance of the cycle, the effect on the

pre-dimensioning of the main components of the NET Power cycle is investigated. Accordingly, this section presents the methodology for the preliminary component design of the main turbomachines, recuperative heat exchanger, and distillation columns of the ASU.

The pre-design of the RHE is characterized by the thermal conductance, UA. The sizing of the turbomachines is defined by a magnitude representative of the geometry, D (i.e., the impeller diameter of a radial flow machine or the ratio between the length and the chord of a blade in an axial flow turbomachine). The diameter, Ω, sizes the distillation columns.

3.2.9.1 Recuperative heat exchanger

The conductance UA is a beneficial form to characterize the performance and size of a heat exchanger. The UA parameter can be obtained from the transferred heat flow rate $\dot{Q}$ and the log mean temperature difference ΔT_{lm}, which are process variables obtained from cycle simulation:

$$UA = \frac{\dot{Q}}{\Delta T_{lm}} = \frac{\dot{Q}}{\frac{\Delta T_c - \Delta T_h}{\ln(\Delta T_c / \Delta T_h)}}. \tag{3.29}$$

In Eq. (3.29), ΔT_c and ΔT_h denote the temperature difference on the cold- and hot- side of the RHE, respectively [195].

3.2.9.2 Turbomachinery

The similarity parameters specific speed (n_s) and specific diameter (d_s), defined in Eqs. (3.30) and (3.31), were used for the pre-design of the turbomachines [39,76].

$$n_s = \frac{\omega\sqrt{\dot{V}}}{(\Delta h)^{3/4}} \tag{3.30}$$

$$d_s = \frac{D(\Delta h)^{1/4}}{\sqrt{\dot{V}}} \tag{3.31}$$

ω is the angular shaft speed, Δh is the isentropic change of specific enthalpy, D is a representative geometric magnitude of the turbomachine (characteristic length). $\dot{V}$ is the volumetric flow rate at the inlet or outlet of the turbomachine depending on whether it is a compressor or a turbine, respectively [196]. $\dot{V}$ was estimated from the mass flow and the fluid density calculated by the EoS. ω was fixed such that n_s equals 1 for the REF

EoS [197]. Therefore, for each chosen EoS, n_s was first determined by Eq. (3.30). Then, d_s was estimated from a $n_s - d_s$ Balje diagram, which was fitted by polynomials in Eq. (3.32) by Du et al. [198]. Finally, D was obtained by Eq. (3.31). To quantify the impact on the turbomachine sizing of the EoS choice, the relative deviation in the prediction of D was used.

$$\log_{10} d_s = \begin{cases} -0.6433x + 0.7068, & x < -0.79 \\ 0.4890 - 0.4264x + 0.6387x^2 - 0.6370x^3 \\ -0.2498x^4 + 0.3800x^5 - 0.1965x^6, & -0.79 < x < 1.4' \\ 0.0764, & x > 1.4 \end{cases} \tag{3.32}$$

with $x = \log_{10} n_s$.

3.2.9.3 Distillation columns

The impact on the distillation columns sizing was quantified from the relative deviation of the calculated diameter, Ω. Ω can be obtained from the volumetric flow rate of gas rising through the column $\dot{V}_{reb}$ (process variable calculated in the ASU model) according to the following expression [199]:

$$\Omega = 0.87\dot{V}_{reb}{}^{0.5}. \tag{3.33}$$

3.2.10 Model validation

The performance of the numerical NET Power cycle model developed in this work was validated against previous results obtained by Mitchel et al. [41] and Scaccabarozzi et al. [38] in steady-state conditions. Mitchel at al. incorporated the bypass recompression loop and an ASU model. In contrast, Scaccabarozzi et al. did not consider the bypass loop and assumed that the ASU energy penalty is 1391 kJ·kgO_2^{-1}. Including in the validation process two data sources from slightly different cycle embodiments increases the reliability of the results derived from this study. The comparison of results was performed under the same cycle operating conditions as Scaccabarozzi et al., shown in Table 3.9. Moreover, the same EoS, the PR EoS, was employed.

Table 3.9. Key input parameters for model validation.

Key parameter	Unit	Value
Combustor outlet temperature	°C	1150
Turbine inlet pressure	bar	300
Turbine outlet pressure	bar	34
Recuperator hot side ΔT_h	°C	20
Recuperator pinch-point ΔT_c	°C	5
Minimum fluid temperature	°C	26

Table 3.10 presents the comparison of the major output variables with previous studies. The turbine output power was slightly higher in the Mitchel et al. study, as a result of a different expansion model than used in other works. The inclusion of the bypass compressor leads to a higher CO_2 compression power within this work, compared to Scaccabarozzi et al. The ASU energy penalty resulted similar in all studies. This ensures credible results from the ASU model developed in this study. The net cycle efficiency predicted in this work had a relative error of -1.56% versus the value estimated by Scaccabarozzi et al. The most significant difference between the Mitchel et al. study and this study, compared to Scaccabarozzi et al. study, was the turbine coolant temperature. The additional heat of compression, supplied to the recuperator by the bypass compressor, justifies the temperatures of 435.55 °C and 511.70 °C compared to 182.00 °C. Considering that the cycle embodiment considered in this study is different from those used by Mitchel et al. y Scaccabarozzi et al., the similarity between the results ensures the applicability and reliability of the model developed for this study.

Table 3.10. Comparison of the results with previous studies under the operating conditions shown in Table 3.9.

Output variable	Unit	This work	Mitchel et al. [41]	Rel. Dev. (%)	Scaccabarozzi et al. [38]	Rel. Dev. (%)
Fuel thermal input	MW_{th}	768.31	768.31	0.00	768.31	0.00
Turbine power output	MW_e	623.01	673.20	7.46	622.42	0.09
CO_2 compression	MW_e	121.98	126.71	3.73	111.15	9.74
Fuel compression	MW_e	4.26	4.29	0.70	4.18	1.91
ASU consumption	MW_e	81.08	83.30	2.67	85.54	5.21
Auxiliary penalties	MW_e	2.85	13.45	78.81	2.24	27.23
Net power output	MW_e	412.84	445.40	7.31	419.31	1.54
Net cycle efficiency	%	53.73	57.97	7.31	54.58	1.56
Turbine inlet mass flow	$kg\ s^{-1}$	1252.92	1203.00	4.15	1271.0	1.42
Turbine coolant mass flow	$kg\ s^{-1}$	157.207	190.30	17.39	99.40	58.16
Turbine coolant temperature	°C	435.55	511.70	14.88	182.00	139.31

Chapter 4

Results and discussion on the equations of state and modeling of the NET Power cycle

4 Results and discussion on the equations of state and modeling of the NET Power cycle

The results of the numerical calibration of the EoSs, and the modeling at off-design conditions of the NET Power cycle, are discussed in this section. The calibrated interaction parameters of the EoSs, and the performance assessment of the EoSs in volumetric and phase calculations of $scCO_2$-rich mixtures, are provided in Section 4.1. Next, the preliminary thermodynamic indexes of the NET Power cycle, while working at nominal conditions, and the influence of the EoS choice on the performance and preliminary sizing of the cycle and its components, are presented in Section 4.2. In addition, the maximum efficiency configuration of the NET Power cycle, obtained with the GERG-2008 + LKP thermodynamic model, is given. Finally, Section 4.3 presents the results of the NET Power cycle, and thermal recuperator performance maps, at partial loads from 100% (design point) to 20%.

4.1 Results of the numerical calibration of the binary interaction parameters of the EoSs

The adjustable binary interaction parameters of the selected EoSs (highlighted in bold in the Table 3.1), that resulted from the numerical calibration process, are presented in Table 4.1.

Table 4.1. Calibrated interaction parameters of the PR, SRK ,LKP, BWRS, PC-SAFT and CPA EoSs. These interaction parameters correspond to those highlighted in bold in the formulation of the EoSs given in Table 3.1.

		$CO_2 - H_2O$		$CO_2 - CO$	$CO_2 - H_2$	$CO_2 - O_2$	$CO_2 - N_2$	$CO_2 - Ar$	$CO_2 - CH_4$
		VLE	ρ	ρ	ρ	ρ	ρ	ρ	ρ
PR	$k_{ij}^{(1)}$	-0.4274	-0.0823492	0.0000	0.0000	-0.144269	0.0000	-0.128005	-0.229886
	$k_{ij}^{(2)}$	0.001	0.00130716	-0.00085152	-0.002656	0.00094759	-0.00109974	0.0000	-0.00093592
SRK	$k_{ij}^{(1)}$	-0.4614	0.0000	0.0000	0.0000	0.0603179	0.0000	-0.189057	0.0000
	$k_{ij}^{(2)}$	0.0011	-0.0010648	0.00149822	-0.021956	0.0000	-0.00087398	0.0000	-0.0789253
LKP	k_{ij}	0.0125	-0.278075	0.114011	0.916455	0.0253371	0.0901669	0.0200776	-0.489781
BWRS	k_{ij}	0.1053	0.0000	-0.181284	-0.681987	0.0130965	-0.476755	-0.033787	0.0531
PC-SAFT	$k_{ij}^{(1)}$	0.1565	0.0929834	-0.999539	-0.284113	0.205097	-0.96324	0.0000	0.0000
	$k_{ij}^{(2)}$	0.1449	0.116352	0.959316	-0.999873	-0.256288	0.996573	0.0732153	0.99997
	$k_{ij}^{(5)}$	0.0228	-0.0494549	-0.0147781	0.0000	0.0000	-0.576246	0.0000	0.998752
CPA	$k_{ij}^{(1)}$	0.168	0.285987	-0.211483	0.0000	0.503948	0.567561	0.0000	-0.412014
	$k_{ij}^{(2)}$	0.269	0.241135	-0.207193	0.0000	-0.455381	-0.011355	-0.037751	0.0000

The comparison between the composition of the equilibrium phases of the CO_2 – H_2O mixture calculated by the calibrated EoSs and the experimental VLE data is represented in Fig. 4.1. It can be seen in Fig. 4.1(a) that the EoSs predict the solubility of CO_2 in the H_2O-rich liquid phase with a deviation of less than 10%. All the EoSs predict the composition of the CO_2-rich gas phase within a deviation of 2% over the entire calibration range as found in Fig. 4.1(b).

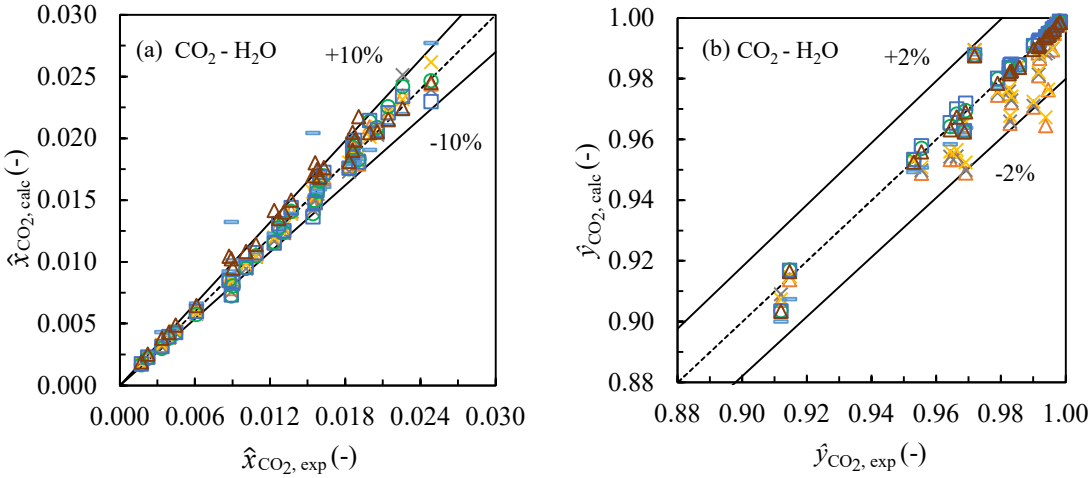

Fig. 4.1. Comparison between the CO_2 mole fraction in the (a) H_2O-rich liquid phase and (b) CO_2-rich vapor phase within the VLE calculated by the EoSs and the experimental data used for the interaction coefficient calibration. The temperature and pressure ranges are 298.15 – 423.15 K and 1 – 17 MPa. (△) PR, (×) SRK, (×) LKP, (–) BWRS, (○) PC-SAFT, (□) CPA, (△) GERG-2008.

Table 4.2. AARD (%) of the EoSs in the prediction of the VLE composition of CO_2 - H_2O mixtures in the $p, T, \bar{x}$ ranges shown in Table 3.3.

EoS	Bubble line	Dew line	**Average**
PR	3.83	1.92	**2.88**
SRK	4.30	1.78	**3.04**
LKP	2.23	1.83	**2.03**
BWRS	11.94	1.53	**6.74**
PC-SAFT	4.95	1.41	**3.18**
CPA	5.34	1.43	**3.39**
GERG-2008	8.51	0.25	**4.38**
Average	**15.56**	**1.45**	

Table 4.2 shows the AARD in the prediction of the bubble line and dew line by the EoSs with respect to the experimental data. The bubble point prediction, as a function of pressure, by the EoSs presents a larger deviation from the experimental data than the dew point prediction. The average AARD of the EoSs in the bubble line estimation is 15.56%, while it is 1.45% for the dew line. The calibrated LKP EoS reports the lowest AARD in the bubble line modeling, 2.03%, while the BWRS EoS gives the highest AARD, 11.94%.

Concerning the dew line prediction, the GERG-2008 EoS presents the lowest AARD, 0.25%. The EoS with the lowest average AARD in the prediction of both bubble and dew lines is the LKP, reporting an AARD of 2.03%. The results also reveal that the cubic PR and SRK EoSs, with an appropriate fitting of the binary interaction parameters, present a lower AARD than other thermodynamic models with more complex mathematical formulation within the pressure and temperature ranges considered in this study [200].

Regarding density predictions, Fig. 4.2 compares the prediction of the density of $scCO_2$-rich binary mixtures by the EoSs with respect to the experimental data points. Except for the CO_2 – H_2O and CO_2 – CH_4 mixtures, the EoSs predict the volumetric behavior of the binary mixtures with a deviation lower than 10% over the entire calibration range. For the CO_2 – CH_4 mixture, all EoSs show significant deviations, up to 126.4% for CPA, within the discontinuity band. This indicates that the experimental source data of the CO_2 – CH_4 mixture may have a larger uncertainty than expected.

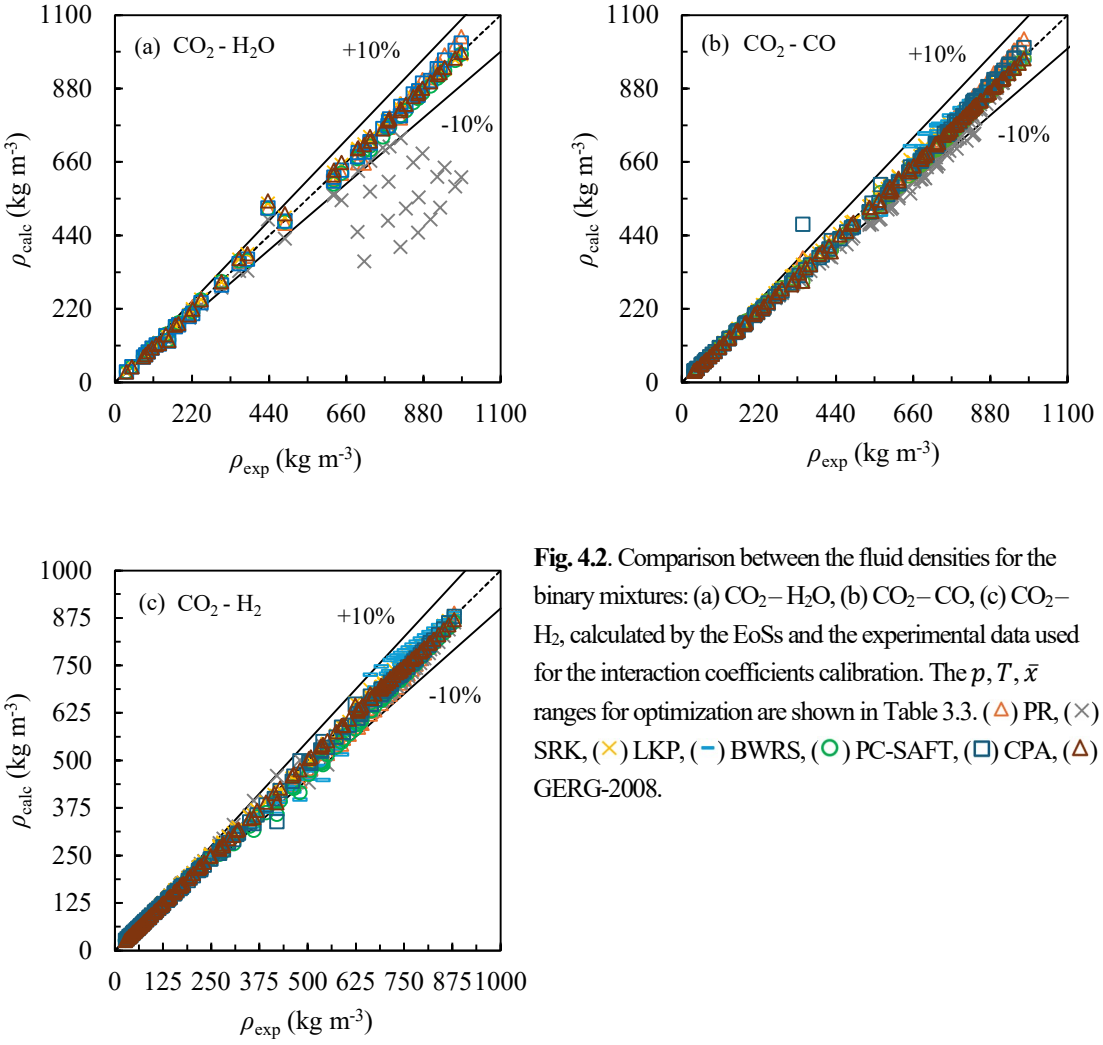

Fig. 4.2. Comparison between the fluid densities for the binary mixtures: (a) CO_2– H_2O, (b) CO_2– CO, (c) CO_2– H_2, calculated by the EoSs and the experimental data used for the interaction coefficients calibration. The $p, T, \bar{x}$ ranges for optimization are shown in Table 3.3. (△) PR, (×) SRK, (×) LKP, (–) BWRS, (○) PC-SAFT, (□) CPA, (△) GERG-2008.

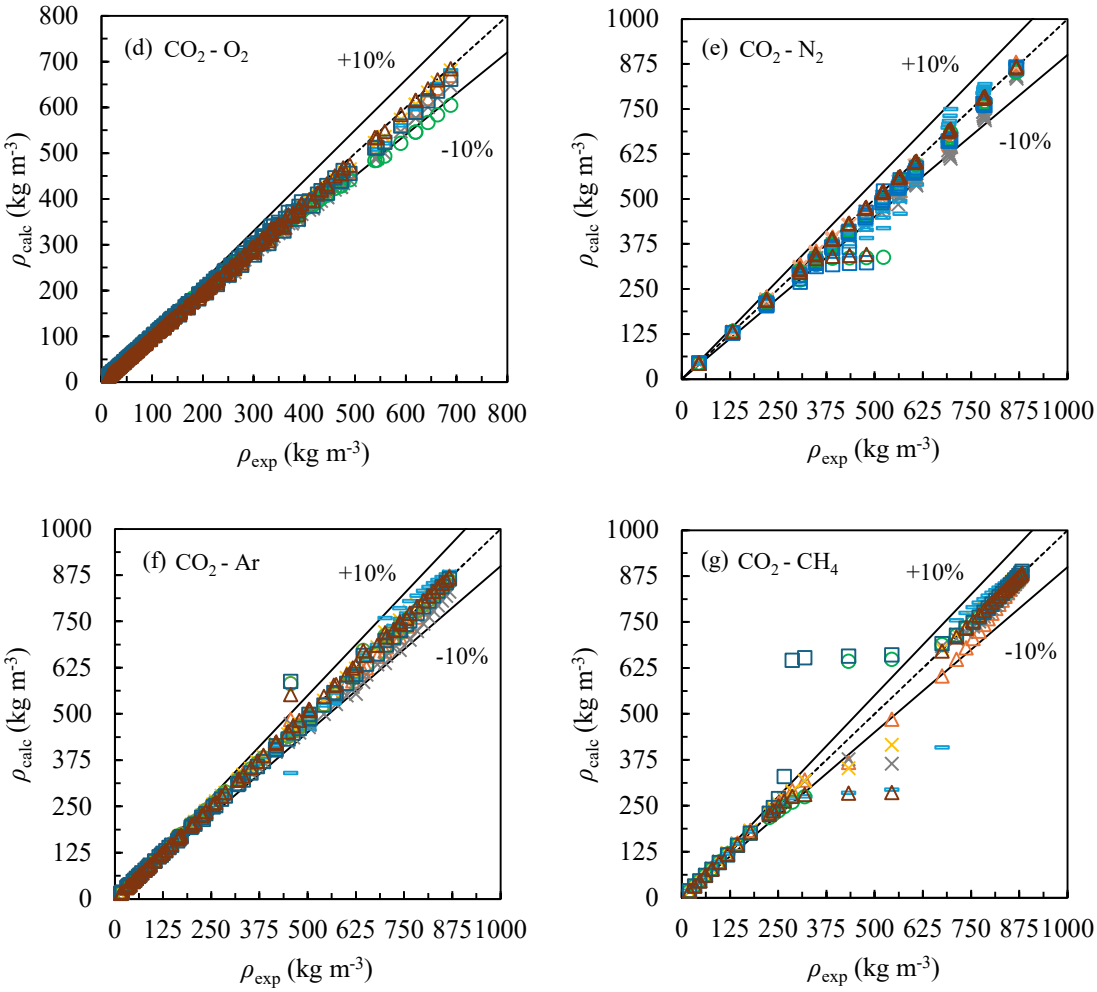

Fig. 4.2 (continued). Comparison between the fluid densities for the binary mixtures: (d) CO_2 – O_2, (e) CO_2 – N_2, (f) CO_2 – Ar, (g) CO_2 – CH_4, calculated by the EoSs and the experimental data used for the interaction coefficients calibration. The $p, T, \bar{x}$ ranges for optimization are shown in Table 3.3. (△) PR, (×) SRK, (×) LKP, (−) BWRS, (○) PC-SAFT, (□) CPA, (△) GERG-2008.

Table 4.3 reports the AARD in the prediction of the density of scCO_2-rich binary mixtures by the EoSs with respect to the experimental data. The volumetric behavior of the CO_2 – H_2O mixture is predicted by the EoSs with an AARD of about two times higher than for the rest of the binary mixtures. This is because the CO_2 – H_2O mixture is highly non-ideal due to the different polarity of the CO_2 and H_2O molecules [57,58]. The fact that the BWRS EoS is uncapable of predicting the density of the CO_2 – H_2O mixture was the reason for the retirement of its AARD results for this mixture. The results also pointed out that GERG-2008 is the model that, on average, matches the experimental data with the lowest deviation, presenting an average AARD for all considered mixtures of 1.34%. Therefore, the combination of GERG-2008 + LKP was used throughout this work for modeling purposes. GERG-2008 is used for volumetric calculations, and the calibrated LKP EoS for predicting the equilibrium phase behavior of the CO_2 – H_2O mixture.

Table 4.3. AARD (%) in the density prediction of scCO$_2$-rich binary mixtures in the $p, T, \bar{x}$ ranges shown in Table 3.3.

EoS	$CO_2 - H_2O$	$CO_2 - CO$	$CO_2 - H_2$	$CO_2 - O_2$	$CO_2 - N_2$	$CO_2 - Ar$	$CO_2 - CH_4$	**Average**
PR	3.03	2.30	3.10	1.49	3.17	2.16	3.21	**2.98**
SRK	18.28	5.65	2.72	3.33	3.50	2.82	2.05	**5.30**
LKP	2.29	0.62	1.02	1.79	1.82	0.65	0.97	**1.78**
BWRS	-	1.84	3.40	1.66	4.91	2.47	4.10	**2.96**
PC-SAFT	2.77	2.10	2.93	2.44	2.46	1.70	1.51	**2.33**
CPA	3.13	2.21	1.89	1.60	3.71	1.98	2.43	**2.44**
GERG-2008	2.37	1.51	0.58	1.37	1.10	0.94	0.93	**1.34**
Average	**4.89**	**2.22**	**2.03**	**1.88**	**2.72**	**1.71**	**2.02**	

4.1.1 Vapor-liquid equilibrium modeling trends

A pressure-composition diagram for the CO_2 – H_2O mixture, for a temperature of 298.15 K, is shown in Fig. 4.3. Fig. 4.3(a) presents the mole fraction of CO_2 in the H_2O-rich liquid phase, and Fig. 4.3(b) the CO_2 mole fraction in the CO_2-rich gas phase. All calibrated EoSs demonstrate an attenuation in their predictive capability as the temperature of the mixture increases.

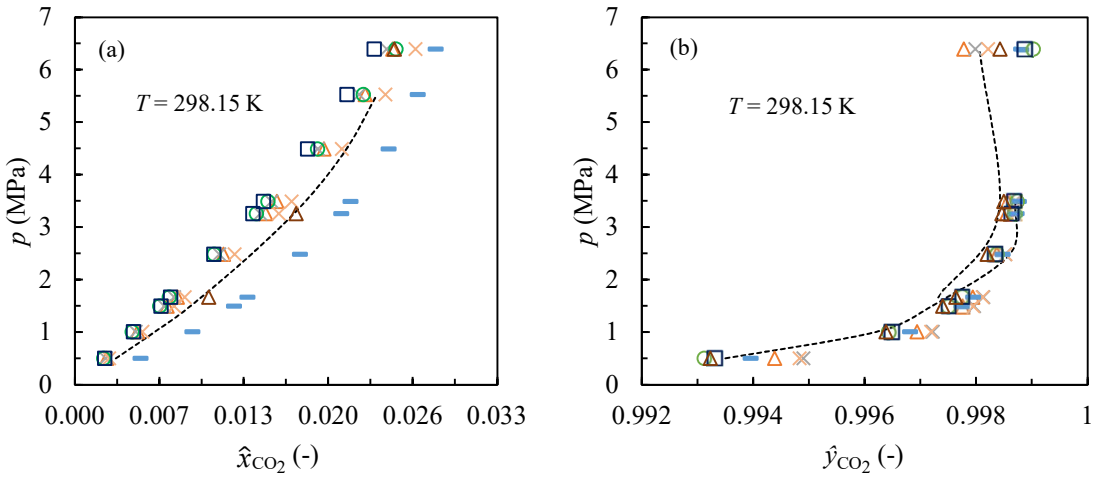

Fig. 4.3. Pressure-composition phase diagram for the CO_2 – H_2O mixture for a temperature of 298.15 K. (a) H_2O-rich liquid phase and (b) CO_2-rich liquid phase. (-------) Experimental data (△) PR, (×) SRK, (×) LKP, (–) BWRS, (○) PC-SAFT, (□) CPA, (△) GERG-2008.

PR and SRK EoSs tend to underestimate the mole fraction of CO_2 in the H_2O-rich liquid phase and the amount of water in the CO_2-rich gas phase. Although this deviation is reduced for high pressure. In general, both cubic EoSs were capable of accurate modeling the VLE of the CO_2 – H_2O mixture. The LKP EoS has fewer discrepancies than the other EoSs in comparison to the experimental data. BWRS EoS predicts a higher concentration of CO_2 in the aqueous phase. LKP and BWRS EoSs present a similar

pattern than PR and SRK EoSs in modeling the composition of the vapor phase. However, BWRS predicts a lower H_2O mole fraction in the CO_2 gas phase for pressures above 3.5 MPa. PC-SAFT and CPA EoSs accurately adjust the composition of the phases in equilibrium of the $CO_2 – H_2O$ mixture. However, CPA EoS tends to deviate towards lower values of the gas concentration because of the cubic term contained in its formulation. In addition, PC-SAFT and CPA EoSs underestimate the H_2O fraction in the CO_2-rich gas phase for high mixture pressures. GERG-2008 shows discrepancies in calculating the mole fraction of CO_2 in the aqueous phase for pressures below 2 MPa. This deviation is reduced as the mixture pressure increases.

4.1.2 Density modeling trends

Fig. 4.4 represents the evolution of the density of the binary mixtures (a) $CO_2 – H_2O$, (b) $CO_2 – CO$, (c) $CO_2 – H_2$, (d) $CO_2 – O_2$, (e) $CO_2 – N_2$, (f) $CO_2 – Ar$ and (g) $CO_2 – CH_4$, estimated by the calibrated EoSs, compared to the density experimental data, as a function of the pressure and temperature of the mixture. The density gradient becomes steeper as the mixture temperature decreases due to an increase of the isothermal compressibility factor, which intensifies the real gas effects. As a result, the deviation of the EoSs increases at low temperatures. For pressures far away from the corresponding ones in the discontinuity band, the deviation between the density estimated by the EoSs and the experimental data is reduced.

PR and SRK EoSs underestimated the density of the mixtures: $CO_2 – H_2O$, in the discontinuity band (as also stated by Ibrahim et al. [201]), although PR overestimated the density at pressures above 25 MPa; $CO_2 – CO$, in the pressure ranges between 7 – 27 MPa, although PR overestimates it at pressures higher than 25 MPa; $CO_2 – H_2$, in the liquid-like phase, with the deviation decreasing as the mixture pressure increases; $CO_2 – N_2$, for pressures above 8 MPa; $CO_2 – Ar$, in the liquid-like phase; and $CO_2 – CH_4$, from the critical pressure of the mixture up to 18 MPa. This periodic underestimation of the density by PR and SRK EoSs is relaxed as the mixture temperature augments. Beyond the calibration p, T, $\bar{x}$ ranges, results revealed that the deviation of PR and SRK EoSs, compared to the experimental data, increases more than the rest of EoSs, demonstrating that their performance is highly dependent on the binary interaction parameters [23,60].

LKP EoS is able to predict the density evolution within the discontinuity band close to the experimental data, without significant deviations. BWRS EoS yield erroneous densities for the $CO_2 – H_2O$ mixture. However, the rest of the binary mixtures are accurately predicted, tending to overestimate the density of the $CO_2 – N_2$, $CO_2 – Ar$ and $CO_2 – CH_4$ mixtures within the liquid-like phase region. PC-SAFT EoS underestimates the density of the $CO_2 – O_2$ mixture for pressures above 12 MPa. The rest of the EoSs model the density of the $CO_2 – O_2$ mixture accurately since the O_2 mole fraction used in

the numerical regression is high, tending to move the mixture away from the critical point. CPA EoS tends to underestimate the density of the $CO_2 - O_2$, $CO_2 - N_2$ and $CO_2 - Ar$ mixtures, although with less deviation than PR and SRK. This is because the physical term of the CPA EoS is precisely the SRK EoS [61]. GERG-2008 accurately matches the experimental data. The deviation of the EoSs decreases as the pressure and temperature increase, especially the former. This is because the deflection of the isotherm lines decreases as the mixture moves away from the critical point.

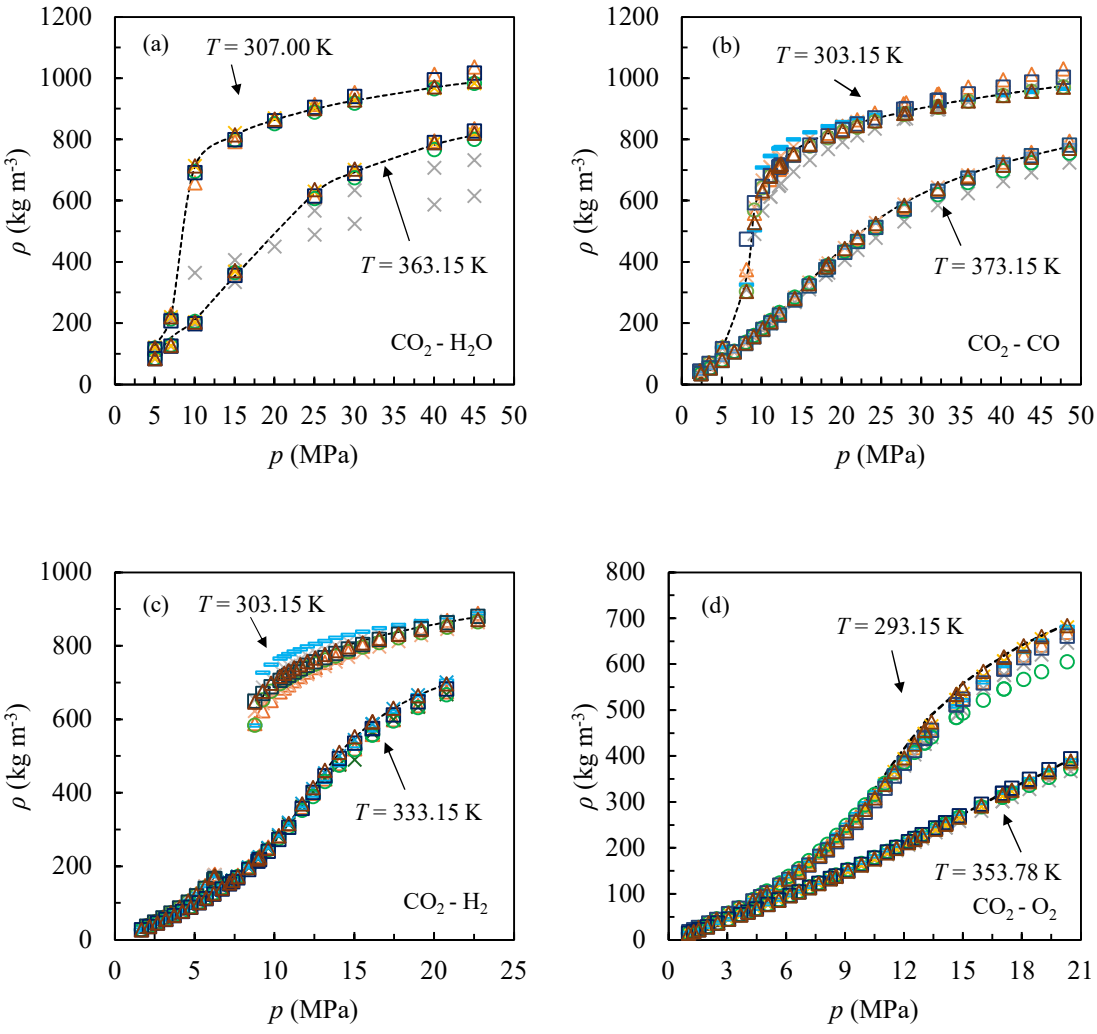

Fig. 4.4. Evolution of the density as a function of the pressure, for different temperatures, for the binary mixtures: (a) $CO_2 - H_2O$, (b) $CO_2 - CO$, (c) $CO_2 - H_2$, (d) $CO_2 - O_2$, calculated by the EoSs and the experimental data used for the interaction coefficient calibration. (-------) Experimental data (△) PR, (×) SRK, (×) LKP, (−) BWRS, (○) PC-SAFT, (□) CPA, (△) GERG-2008.

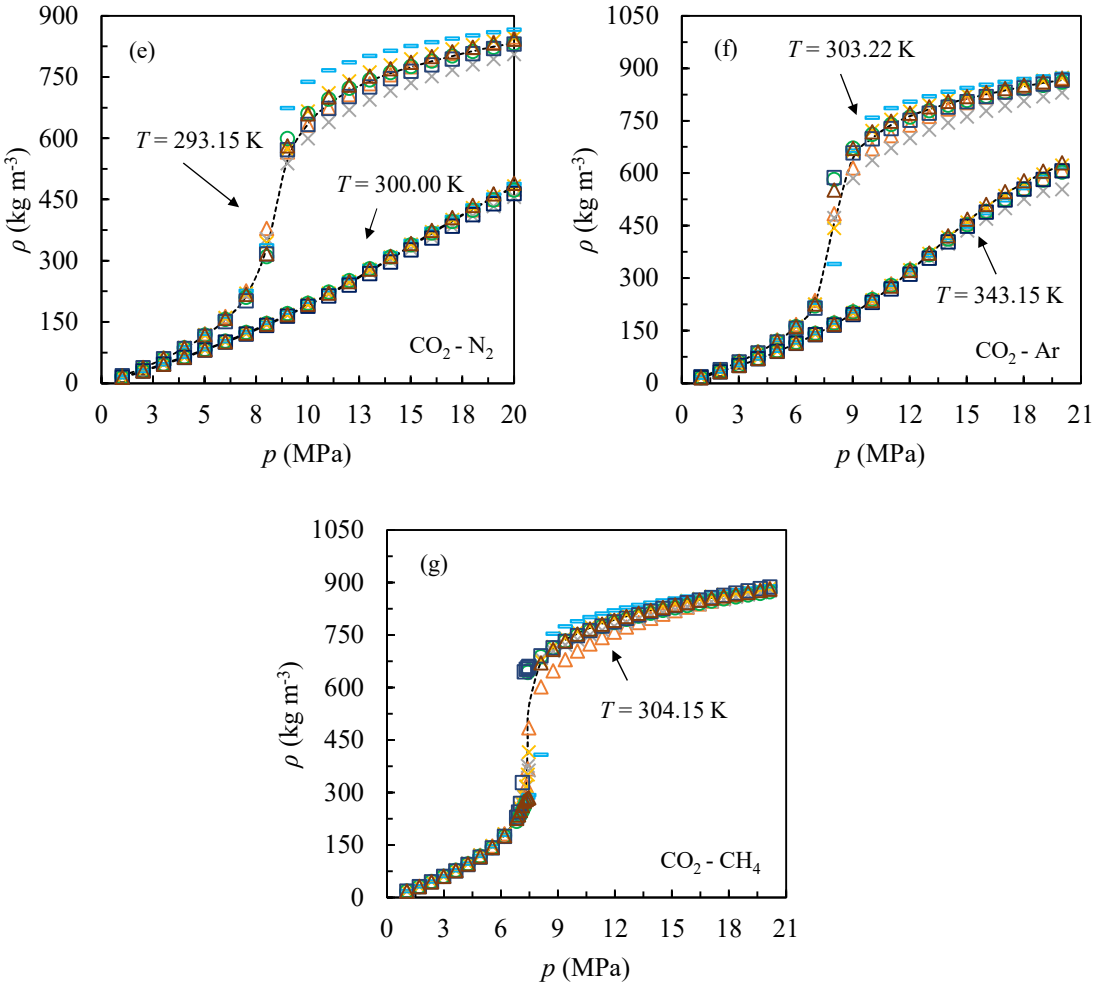

Fig. 4.4 (continued). Evolution of the density as a function of the pressure, for different temperatures, for the binary mixtures: (e) CO_2 – N_2, (f) CO_2 – Ar, (g) CO_2 – CH_4, calculated by the EoSs and the experimental data used for the interaction coefficient calibration. (-------) Experimental data (△) PR, (×) SRK, (×) LKP, (–) BWRS, (○) PC-SAFT, (□) CPA, (△) GERG-2008.

4.2 NET Power cycle at nominal conditions. Influence of the EoSs

The numerical model of the NET Power cycle, developed in Aspen Plus, was used to study the thermodynamic performance of the cycle at on- and off-design conditions, and to find the operating conditions of the RHE. First, this section evaluates the thermodynamic performance of the NET Power cycle at nominal conditions. Analysis were conducted for all calibrated EoSs, which were previously presented in Section 4.1. This allowed to evaluate the degree of influence of the EoS selection on the thermodynamic performance (Sections 4.2.1 and 0), component dimensioning (Section 4.2.3) and maximum efficiency operating conditions (Section 4.2.4) of the NET Power cycle. The methodology to perform this evaluation was presented in Section 3.2.9. The PR EoS, with the default binary interaction coefficients provided by Aspen Plus, is referred to as the REF EoS. The calibrated PR, SRK, BWRS, PC-SAFT and CPA EoS, as

well as the GERG-2008, and the combination of GERG-2008 + LKP, are referred to as EoSs. According to the findings of Section 4.1, GERG-2008 + LKP is the thermodynamic model, contained in Aspen Plus, that most accurately predicts the volumetric and phase properties of the working fluid of the NET Power cycle. Therefore, special consideration is given to the comparison between GERG-2008 + LKP and REF EoS. Streams and components of the NET Power cycle are referenced with the abbreviations of the process diagram of Fig. 2.2.

The interaction parameters of the binary mixtures involving CO_2 were calibrated and presented in Table 4.1. On the other hand, the interaction parameters for the rest of the binary systems, obtained from the database of Aspen Plus V12.1 [170], are shown in Table 4.4.

Table 4.4. Binary interaction parameters of the uncalibrated systems ($k_{ij} = k_{ji}$).

Component		PR		SRK		LKP	BWRS	PC-SAFT			CPA	
i	j	$k_{ij}^{(1)}$	$k_{ij}^{(2)}$	$k_{ij}^{(1)}$	$k_{ij}^{(2)}$	k_{ij}	k_{ij}	$k_{ij}^{(1)}$	$k_{ij}^{(2)}$	$k_{ij}^{(5)}$	$k_{ij}^{(1)}$	$k_{ij}^{(2)}$
CO	H_2	0.0919	0.0000	0.0000	0.0000	0.1285	0.0000	0.0000	0.0000	0.0000	0.0000	0.0000
CO	N_2	0.0307	0.0000	0.0000	0.0000	-0.0267	0.0000	0.0000	0.0000	0.0000	0.0000	0.0000
CO	CH_4	0.0300	0.0000	0.0000	0.0000	-0.0370	0.0000	0.0000	0.0000	0.0000	0.0000	0.0000
H_2	N_2	0.1030	0.0000	0.0000	0.0000	0.0837	0.0000	0.0000	0.0000	0.0000	0.0000	0.0000
H_2	CH_4	0.0156	0.0000	-0.0245	0.0000	0.2022	0.0000	0.0000	0.0000	0.0000	0.0000	0.0000
O_2	N_2	-0.0119	0.0000	0.0000	0.0000	-0.0089	0.0000	0.0000	0.0000	0.0000	0.0000	0.0000
O_2	Ar	0.0104	0.0000	0.0000	0.0000	-0.0144	0.0000	0.0000	0.0000	0.0000	0.0000	0.0000
N_2	Ar	-0.0026	0.0000	0.0000	0.0000	-0.0152	0.0000	0.0000	0.0000	0.0000	0.0000	0.0000
N_2	CH_4	0.0311	0.0000	0.0000	0.0000	-0.0256	0.0250	0.0000	0.0000	0.0000	0.0000	0.0000
Ar	CH_4	0.0230	0.0000	0.0000	0.0000	-0.0111	0.0000	0.0000	0.0000	0.0000	0.0000	0.0000

4.2.1 Thermodynamic performance of the NET Power cycle at base cycle conditions as a function of the equation of state

The thermodynamic performance of the NET Power cycle was studied at nominal base load conditions. The nominal conditions, given in Table 4.5, correspond to the original operating conditions for which the NET Power cycle was originally designed [10]. These conditions were used to perform most of the computational studies that can be found in the literature.

Table 4.5. Nominal base cycle conditions of the NET Power cycle.

Parameter	Unit	Value
Thermal energy of feedstock (LHV)	MW_{th}	768.19
Combustor outlet temperature	°C	1150
Turbine inlet pressure (TIP)	bar	300
Turbine outlet pressure (TOP)	bar	34
Bypass stream Split fraction	%	6
Recuperator hot-side temperature difference	°C	10
Recuperator pinch-point	°C	5
Minimum cycle temperature	°C	26
Multi-stage intercooled compressor outlet pressure	bar	80
Intermediate $scCO_2$ pump outlet pressure	bar	120

The thermodynamic performance of the NET Power cycle at the nominal conditions of Table 4.5, as a function of the EoS, is presented in Table 4.6. In addition, Fig. 4.5 presents the relative deviations in the prediction of the fluid density at the suction of the compressors and pumps.

Table 4.6. Thermodynamic performance of the NET Power cycle at base load cycle conditions shown in Table 4.5. Values of the thermodynamic indexes are only provided for the REF EoS, and the relative deviations for the rest of EoSs.

	REF EoS	PR (%)*	SRK (%)*	LKP (%)*	BWRS (%)*	PC-SAFT (%)*	CPA (%)*	GERG-2008 (%)*	GERG-2008 +LKP (%)*
Thermodynamic performance indexes									
Thermal energy of feedstock (LHV) (MW_{th})	*768.19*	0.00	0.00	0.00	0.00	0.00	0.00	0.00	0.00
Turbine power output (MW_e)	*624.84*	0.42	1.16	0.09	0.54	1.26	0.28	0.52	0.26
Gas-phase compressor train consumption (MW_e)	*55.14*	0.45	2.59	1.20	4.16	5.60	5.40	2.96	2.60
Dense-phase pumps consumption (MW_e)	*54.34*	0.50	-1.72	-1.27	0.95	-8.03	-10.71	-11.86	-11.57
Bypass compressor consumption (MW_e)	*12.03*	0.45	1.99	0.18	9.97	2.25	1.49	1.53	1.26
Fuel gas compressor consumption (MW_e)	*4.26*	-0.71	5.15	3.19	3.15	1.05	3.27	2.68	2.67
ASU consumption (MW_e)	*81.09*	0.00	0.00	0.00	0.17	0.00	0.00	0.00	0.00
Net cycle efficiency (%)	*54.41*	0.49	1.50	0.11	-0.21	2.11	1.03	1.86	1.48
Main dependent parameters									
Turbine outlet temperature (°C)	*737.95*	-0.03	0.28	-0.61	-0.48	-1.16	0.14	-0.76	-0.59
Flue gas to condenser temperature (°C)	*62.90*	-2.58	-0.52	-4.64	21.34	-15.92	-11.94	-12.82	-10.62
Turbine coolant temperature (°C)	*208.74*	33.89	14.25	5.63	85.39	113.15	-23.59	65.97	50.15
Turbine coolant flow rate (kg s^{-1})	*106.65*	11.98	6.74	0.46	33.62	50.35	-6.29	23.35	16.46
Turbine inlet flow rate (kg s^{-1})	*1290.58*	-0.33	0.06	-0.41	0.71	-1.54	0.46	-0.70	-0.47

$$*(\%) = \text{relative deviation} = \frac{\Phi_{TPM} - \Phi_{REF}}{\Phi_{REF}} \cdot 100$$

All EoSs predict a similar turbine power output of 625 MW_e since the behavior of the high temperature gas during expansion is close to the ideal gas behavior. The power consumption of the gas compressors estimated by the EoSs is higher than that estimated by the REF EoS. This is because the fluid density in the compressors estimated by the EoSs is lower than that by the REF EoS, as shown in Fig. 4.5. In the suction of the REP-1 and REP-2 pumps, the EoSs predict a fluid density notably higher than REF EoS. It can be seen in Fig. 4.5 that the PR and SRK cubic EoSs underestimate the density more than the other EoSs. Ibrahim et al. [201] also observed that the SRK EoS significantly underestimates the density of the $CO_2 – H_2O$ system at supercritical conditions. As the pumping specific work is inversely proportional to the fluid density, the power consumed by REP-1 and REP-2 is lower than that calculated by REF EoS. This leads to a total reduction of 11.57% in the pumping power consumption for GERG-2008 + LKP. As a result, the net cycle efficiency is higher than predicted by the REF EoS. In particular, GERG-2008 + LKP predicts a net cycle efficiency of 1.48% higher than the REF EoS. PR and LKP reported a different behavior, computing a similar density as the REF EoS

for the $scCO_2$ pumps, while underestimating the density of the oxidizing mixture by 25%. Considering GERG-2008 + LKP as the most reliable EoS in Aspen Plus, these findings suggest that the liquid-like pumping stages are not being adequately modeled in the NET Power cycle literature.

Fig. 4.6 shows the relative deviation in the prediction of the hot composite curve within the thermal recuperator. The exhaust gases leaving the recuperator, FG-3, are at a lower temperature than estimated by the REF EoS. This is because the fluid density in the REP-1 and REP-2 is higher than predicted by the REF EoS, as shown in Fig. 4.5. Thus, the fluid heating by viscous dissipation during compression diminishes and the CO_2 recirculation streams, RE-6 and TC-1, enter the recuperator at a lower temperature. As a result, for GERG-2008 + LKP, the exhaust gas temperature at the recuperator outlet is 10.62% lower than for the REF EoS. This leads to a noticeable reduction in the cooling energy demanded by the water separator. The discontinuities that appear in Fig. 4.6 are produced by the heat capacity flow (product of the mass flow and the specific heat at constant pressure $\dot{m}c_p$) change at the dew point, which coincides with the pinch-point of the recuperator, and by the addition of hot air from the ASU.

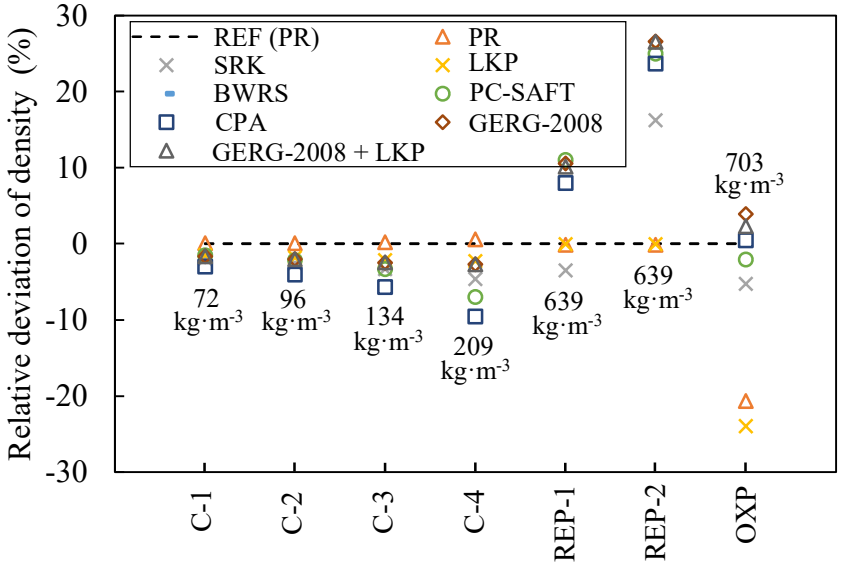

Fig. 4.5. Relative deviation in the calculation of the fluid density at the inlet of the four compression stages and pumps. The numerical density values were obtained with the REF EoS. The BWRS EoS has relative deviations lower than -30%. Density is overestimated by the REF EoS in the compressor, and underestimated by up to 25% in the REP-1 and REP.2 pumps suction.

Since the hot streams leave the recuperator at a lower temperature than estimated by the REF EoS, more heat is delivered by them. In addition, cold streams require more energy to reach the target hot-side temperature approach of 10 °C, since these streams are introduced into the recuperator at a lower temperature.

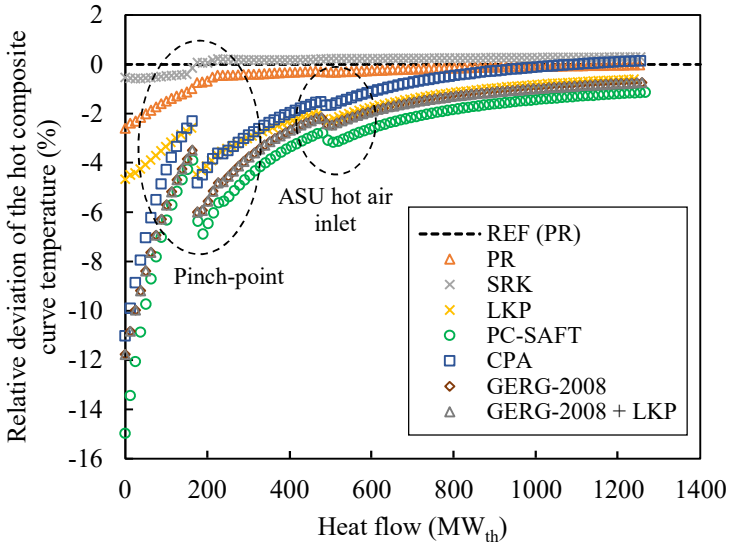

Fig. 4.6. Relative deviation in the calculation of the temperature of the hot composite curve within the thermal recuperator. EoSs predict an exhaust gas temperature leaving the recuperator significantly lower than REF EoS.

However, two effects occur that produce an excess of available heat in the recuperator for the EoSs, in comparison to the REF EoS: (i) the hot streams will deliver more latent heat of condensation as gradually cooled below the dew point, and (ii) the inlet temperature of the recirculation streams is further below the pseudo-critical temperature (i.e., the temperature at which c_p reaches its maximum value). This means that the heat capacity of the cold streams is lower in the low-temperature section of the recuperator. As a result, the temperature change of the cold streams in the recuperator is higher than predicted by the REF EoS. This leads to an overall increase in the recuperator effectiveness. This excess of available heat causes an increase of the turbine coolant temperature leaving the recuperator, as deduced from Table 4.6. This results in a turbine coolant mass flow rise according to Eq. (3.3). The higher the turbine coolant temperature, the higher the expansion power. However, the increase in coolant flow causes a higher circulative flow performing a thermodynamic cycle of lower maximum temperature, which results in a decrease in the overall cycle efficiency.

This excess of available heat was not addressed by most previous studies on the NET Power cycle that employed the REF EoS. Thus, this finding suggests that the recuperator design conditions should be updated to leverage the heat excess. For example, reducing the hot-side temperature approach, and the fraction of exhaust gas that goes towards the bypass compressor, could improve the recuperator effectiveness. The optimal cycle configuration, provided as a novelty in Section 4.2.4, fills this gap.

Table 4.7 shows the main thermodynamic performance indexes of the NET Power cycle for the base load cycle conditions, obtained with the GERG-2008 + LKP model. The expansion power was 626.44 MW$_e$ and the total compression power of the cycle was

121.18 MW_e. The ASU power consumption resulted in 81.09 MW_e, which represents about 40% of the total NET Power cycle power consumption. The air separation process turns out to be the main energy penalty of the oxy-combustion power plants [202]. The net cycle efficiency has a value of 55.22%.

Table 4.7. Thermodynamic performance of the NET Power cycle at base load cycle conditions for GERG-2008 + LKP.

Parameter	Unit	Value
Thermal energy of feedstock (LHV)	MW_{th}	768.19
Turbine power output	MW_e	626.44
Gas-phase compressor train consumption	MW_e	56.57
Dense-phase pumps consumption	MW_e	48.06
Bypass compressor consumption	MW_e	12.18
Fuel gas compressor consumption	MW_e	4.37
ASU consumption	MW_e	81.09
Net cycle efficiency	%	55.22
Turbine outlet temperature	ºC	733.59
Flue gas to condenser temperature	ºC	56.22
Turbine coolant temperature	ºC	313.42
Turbine coolant flow rate	kg s^{-1}	124.20
Turbine inlet flow rate	kg s^{-1}	1284.52

4.2.2 Sensitivity analysis of the NET Power cycle as a function of the combustor outlet temperature, turbine inlet pressure and turbine outlet pressure

The NET Power cycle efficiency, as a function of COT, TIP and TOP, for each EoS is shown in Fig. 4.7. Figs. 4.7(a), 4.7(c) and 4.7(e) present a comparison between the REF EoS and GERG-2008 + LKP, including the actual efficiency values; and Figs. 4.7(b), 4.7(d) and 4.7(f) depict the relative deviations of all EoSs with respect to the REF EoS. The COT was varied between 1050 °C and 1300 °C, by adjusting the recirculation mass flow; the TIP between 240 bar and 340 bar; and the TOP between 28 bar and 48 bar. The remaining parameters were kept constant and equal to those specified in Table 4.5.

In general, the EoSs predict higher efficiency for all COT, TIP and TOP ranges compared to the REF EoS because of the lower estimated compression work of the $scCO_2$ pumps. As can be noticed from Fig. 4.7, the maximum efficiency deviations are reported by PC-SAFT, which results in 2.81% for a COT of 1050 °C, 2.61% for a TIP of 340 bar and 2.37% for a TOP of 48 bar. LKP and BWRS notably underestimate the fluid density in the supercritical regime, which explains their different trend from the rest of EoSs.

GERG-2008 + LKP calculates a higher density of the recirculation streams in the pumping stage, as shown in Fig. 4.7. This leads to a reduction in the pumping work and a cycle efficiency between 1 – 3% higher than REF EoS over the entire COT range. The efficiency trend is similar, exhibiting a peak at 1150 °C. For GERG-2008 + LKP, the efficiency peak value is 55.22%, and for the REF EoS the value is 54.41%. Above this

temperature, the energy excess from the exhaust gases overheats the turbine coolant, deteriorating the efficiency. With the rest of EoSs, an efficiency of 0.5 – 3% higher than that for the REF EoS is obtained, as shown in Fig. 4.7(b). Below 1150 °C, the exhaust gases do not have enough thermal energy to preheat the recirculation streams up to the hot-side temperature specification of the recuperator. Thus, the efficiency decays. The excess of available heat in the recuperator predicted by the PR, PC-SAFT, GERG-2008 and GERG-2008 + LKP EoSs results in the recirculation streams leaving the recuperator at a higher temperature than expected by the REF EoS. This justifies the slight increase of efficiency difference obtained by the EoSs with respect to the REF EoS below 1150 °C shown in Fig. 4.7(b).

The efficiency calculated with GERG-2008 + LKP is between 0.5 – 2.5% higher than for the REF EoS over the entire TIP range considered; with a maximum efficiency at 280 bar as shown in Fig. 4.7(c). Below 280 bar, the efficiency decreases due to three factors: (i) the net power decay due to the lower advantage obtained from the low compression work of the $scCO_2$ pumps. (ii) The overheating of the turbine coolant due to the increase of the exhaust gases thermal energy. (iii) The increment of the heat capacity of the recirculation streams within the recuperator due to its approach to the critical point, which promotes the high temperature heat exchange and exergy destruction. An efficiency of up to 3% higher for the EoSs, with respect to the REF EoS, is observed in Fig. 4.7(d). Also, the higher the TIP, the higher the efficiency relative deviation. This fact is noticed in Fig. 4.7(c), where above 280 bar the efficiency for GERG-2008 + LKP remains approximately constant instead of decaying, as occurs for the REF EoS. This efficiency drop for the REF EoS is because as TIP increases, the thermal energy of the exhaust gases decreases. Thus, the recirculation streams leave the recuperator at a lower temperature and the total flow through the cycle is reduced to maintain a COT of 1150 °C. For PR, SRK, PC-SAFT, CPA, GERG-2008 and GERG-2008 + LKP, the net power is higher than for the REF EoS as the TIP increases because: (i) the compression work of the $scCO_2$ pumps is lower, and (ii) the excess of available heat in the recuperator produces an increase in the turbine coolant flow, and a minor reduction in the total flow.

As can be seen in Fig. 4.7(e), the efficiency calculated with GERG-2008 + LKP is between 0.5 – 2.5% higher than for the REF EoS over the entire TOP considered. However, the evolution of the efficiency as a function of the TOP presents differences. For the REF EoS, a maximum efficiency is found at a TOP of 44 bar, decreasing smoothly beyond this pressure. For GERG-2008 + LKP, the efficiency peak occurs at 40 bar. Below 40 bar, the efficiency decays smoothly with a similar slope as presented by the REF EoS. However, the efficiency drop becomes abrupt for pressures above 40 bar. This is because the fluid enters the vapor-liquid region at the suction of the last gas compression stage (C-4) for a minimum cycle temperature of 26 °C. Consequently, the fluid temperature should be increased to ensure that the mixture is at least in the saturated vapor state for

the proper compressor operation. This results in an increase in the fluid specific volume and an increment of the compression work. The compressor operation is close to the mixture dew point. Hence, using a EoS with high uncertainty on predicting saturation conditions of scCO$_2$-rich mixtures (such as REF EoS [73]) can drive the compressor to an operation within the biphasic region. This leads to a significant reduction of its lifetime. Okoro et al. [203] studied the effect of CH$_4$, O$_2$, Ar and N$_2$ on the saturation properties of CO$_2$-rich binary mixtures for temperatures between 228.15 – 273.15 K. They found that the presence of non-condensables, even at mole fractions as low as 0.5%, increase the risk of biphasic flow in CO$_2$-rich systems at high pressure, with N$_2$ having the most significant effect on bubble point pressures. The rest of the EoSs predict an efficiency of up to 2.5% higher than for the REF EoS, as deduced from Fig. 4.7(f).

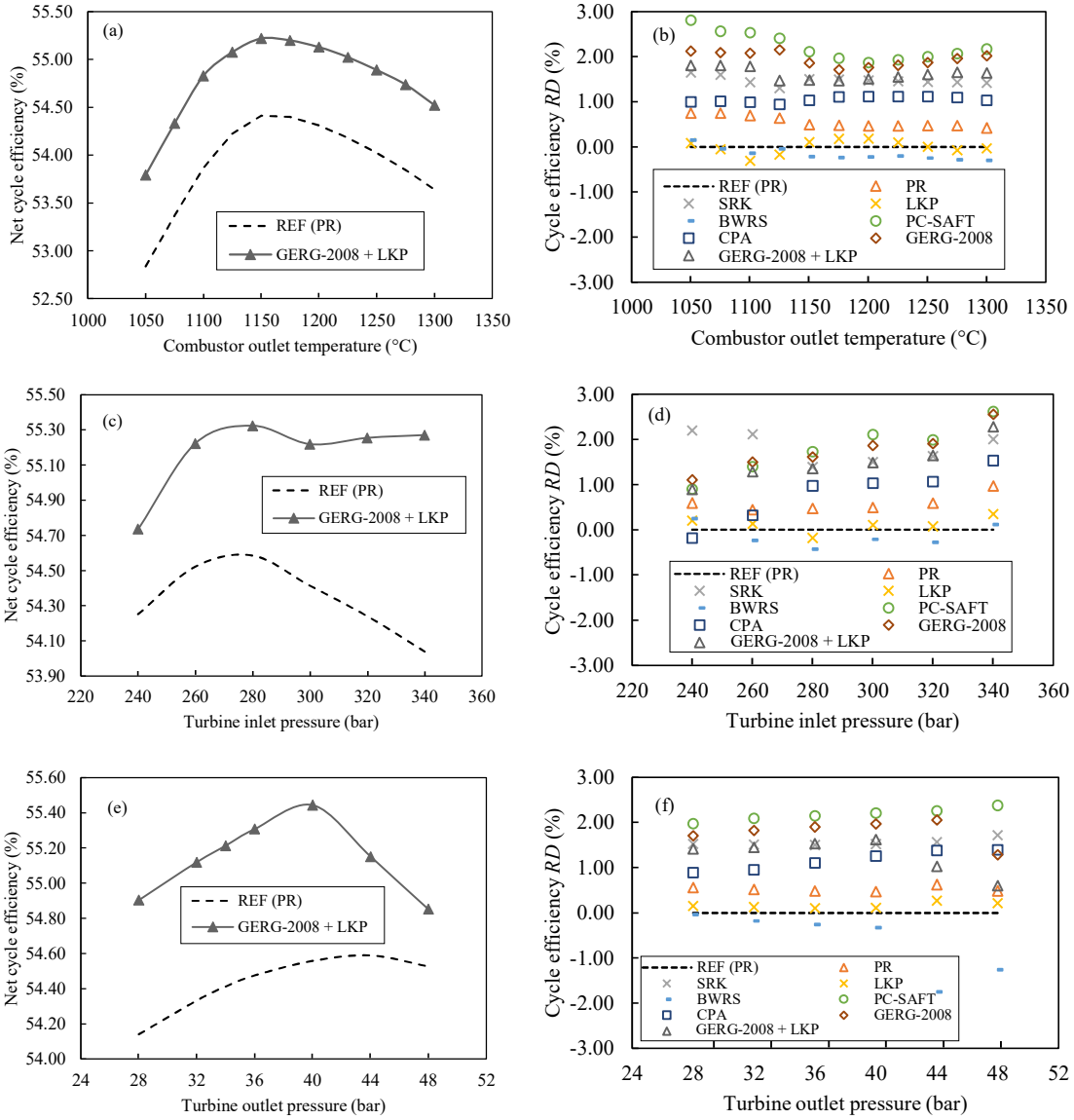

Fig. 4.7. NET Power cycle efficiency for the REF EoS and GERG-2008 + LKP, and efficiency relative deviation (*RD*) for all EoSs with respect to the REF EoS, as a function of COT (a and b), TIP (c and d), and TOP (e and f). EoSs estimate cycle efficiencies up to 3% higher than REF EoS.

4.2.3 Preliminary sizing of the main components of the NET Power cycle

4.2.3.1 Turbomachinery

Fig. 4.8 shows the relative deviation in the calculation of the characteristic length of the compressors and pumps, Fig. 4.8(a), and turbine, Fig. 4.8(b), as a function of the chosen EoS with respect to the REF EoS. On the *x*-axis the turbomachine is denoted by the abbreviations of the cycle process diagram of Fig. 2.2. In Fig. 4.8(b), the eleven expanders forming the cooled turbine are shown (based on the El-Masri model described in Section 3.2.2).

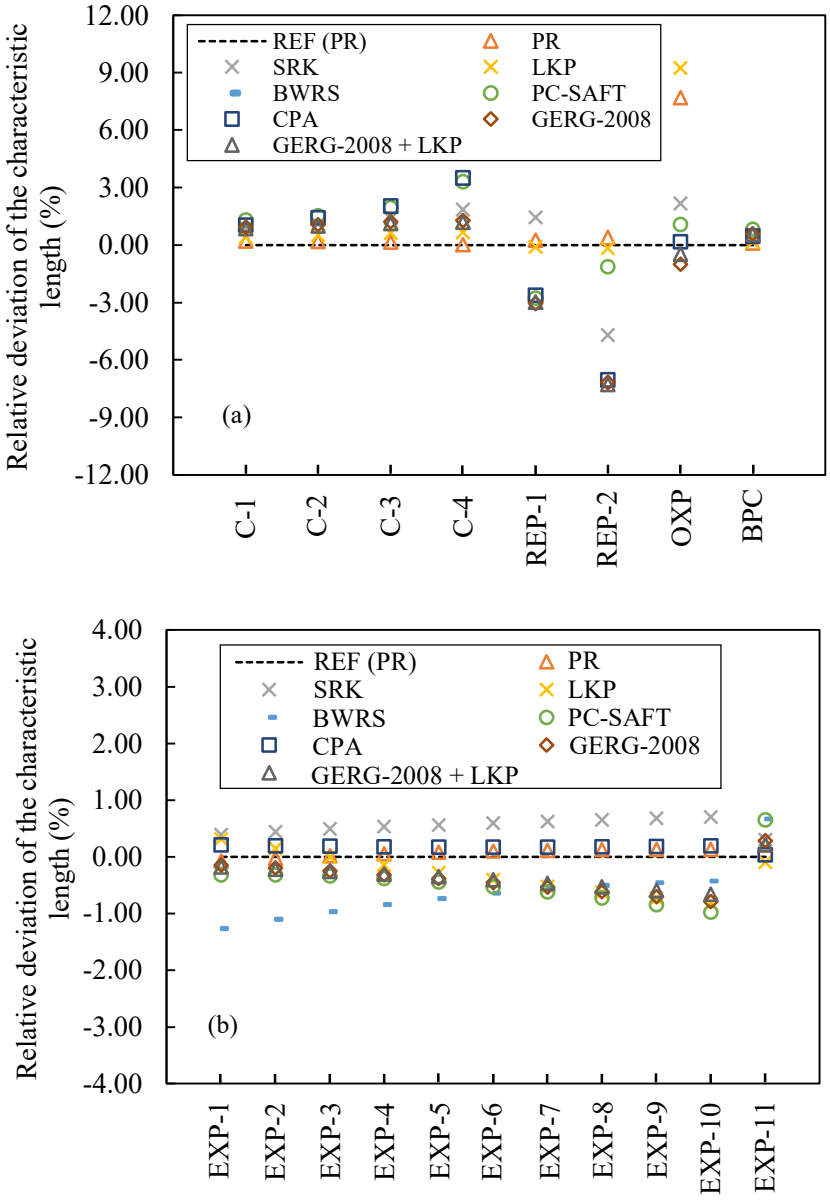

Fig. 4.8. Relative deviation in the calculation of the characteristic length of (a) the compressor and pumps, and (b) the expanders of the cooled turbine. The REP-2 pump is notably influenced by the EoS, with GERG-2008 + LKP predicting a 7.49% smaller characteristic length. Turbine is not significantly influenced by the EoS.

EoSs predict a larger characteristic length for the four gas-phase compression stages. The deviation increases progressively for each compression stage as the fluid approaches the critical point. EoSs predict a lower fluid density during compression (as depicted in Fig. 4.5), which leads to an increment of the volumetric flow and specific work. This results in a larger compressor. The maximum relative deviation in the characteristic length of the fourth compression stage, produced by the CPA EoS, is 3.49%. GERG-2008 + LKP reports only 1.19%. Therefore, it can be concluded that the compressor design is roughly insensitive to the EoS. Thus, for compressor modeling and design purposes, cubic EoSs are recommended, as they demand less CPU time.

Regarding the REP-1 and REP-2 pumps, the higher density predicted by the EoSs results in a lower volumetric flow and enthalpy change with respect to the REF EoS. Hence, the specific velocity increases and the specific diameter decreases, according to Eqs. (3.30) and (3.31). The decrease in volumetric flow and specific diameter causes a general reduction of the pumps size, as shown in Fig. 4.8(a). Assuming that the characteristic length represents the impeller diameter, GERG-2008 + LKP predicts an impeller diameter for the REP-2 pump that is 7.49% smaller than predicted by the REF EoS. This implies that a REP-2 design performed with the most widely used EoS in the NET Power cycle field, the REF EoS, would result in a significantly oversized pump. This would have major practical implications for pump operation. An oversized pump would operate outside the design point, at conditions of lower efficiency than projected. Also, achieving accurate flow control would become more challenging, which can deviate the combustion process from stoichiometric conditions and diminish the overall efficiency of the cycle. Vibration and noise issues, including potential overpressures in the downstream equipment, could appear [187]. CPA and GERG-2008, which are the most accurate models considered in this study, agree in estimating a REP-2 characteristic length of about -7.49%. Specifically, CPA and GERG-2008 estimated a reduction of 7.06% and 7.19%, respectively. Thus, a design of the recirculation pumps should be conducted with the aforementioned EoSs.

Concerning the OXP, the density of the oxidizing mixture estimated by the EoSs is similar to the density predicted by the REF EoS (except for PR and LKP). Thus, the volumetric flow and pump head are similar. This results in a similar pump size. However, the underestimation of the fluid density by the PR and LKP EoSs, with respect to the REF EoS, implies that the volumetric flow is higher and the pump size increases. The BPC compresses the mixture from the minimum cycle pressure up to 120 bar. The fluid at these discharge conditions is in a supercritical phase. However, fluid departs from the critical temperature, and the compressibility factor value approaches the unity due to the temperature increase during compression. Therefore, the EoSs compute a value of the characteristic length for the BPC similar to that predicted by the REF EoS. The

compressibility factor of the gas in the expansion process is close to unity, as a result of the elevated temperature. This implies that the gas behaves as an ideal gas, which means that the deficiencies of the EoSs predicting the fluid properties become negligible. This results in the turbine pre-sizing not being appreciably affected by the EoS, as deduced from Fig. 4.8(b). For modeling and design intents of the OXP, BPC and turbine, the REF EoS can be used with negligible deviations.

4.2.3.2 Recuperative heat exchanger

Table 4.8 shows the relative deviation in the calculation of the transferred heat flow, $\dot{Q}$, the log mean temperature difference, ΔT_{lm}, and the UA product of the RHE, as a function of the EoS.

The EoSs predict a higher heat flow compared with the REF EoS (except for LKP and BWRS). This is due to the excess of available heat, as discussed in Section 4.2.1. The EoSs compute a larger ΔT_{lm} than the REF EoS (except for CPA). With GERG-2008 + LKP, the log mean temperature difference is 8.08% higher than for the REF EoS. This results in a lower UA value than estimated by the REF EoS, as can be seen in Table 4.8. In the NET Power cycle recuperator, the heat transfer rate of the low-density exhaust gases is significantly lower than that of the high-pressure recirculating flows. As a result, it can be assumed that the overall heat transfer coefficient U becomes similar to the individual heat transfer coefficient of the hot gases.

The EoSs accurately predict the physical properties of the hot gases, as the gases have a pressure significantly lower than the critical pressure. Thus, it can be assumed that all EoSs predict a similar U value. This results in that, for GERG-2008 + LKP, the heat exchange area is 6.46% less than that predicted by the REF EoS. It is also important to note that the recuperator exchanges a heat flow of about 1 GW at nominal conditions, requiring a huge heat exchange area. Therefore, this finding has important practical consequences. A reduction in the amount of material reduces manufacturing costs. This is especially transcendent for the high-temperature heat exchange section, which is built from costly nickel-based superalloys [8,20].

Regarding the operation of the recuperator, a reduction of the total mass accelerates the transient response to operating point changes, start-ups and shutdowns. This means that, in general, the competing potential of the NET Power cycle is being underestimated in the literature. Therefore, particular emphasis should be given to the EoS used for modeling and design purposes of the recuperator, recommending the use of GERG-2008 + LKP.

Table 4.8. Relative deviation in the heat flow, log mean temperature difference and UA product of the RHE as a function of the EoS. EoSs predict a higher log mean temperature difference than REF EoS, resulting in a significantly lower UA value.

	REF (PR)	PR	SRK	LKP	BWRS	PC-SAFT	CPA	GERG-2008	GERG-2008 + LKP
$RD(\dot{Q})$	0.00	0.84	0.99	-0.30	-1.13	1.95	0.98	1.28	1.09
$RD(\Delta T_{lm})$	0.00	5.18	3.69	3.34	15.11	1.90	-5.05	8.87	8.08
$RD(UA)$	0.00	-4.12	-2.60	-3.52	-14.11	0.05	6.35	-6.97	-6.46

To explain the notable relative deviations in the ΔT_{lm}, that cause the deviations in the UA product, the evolutions of the heat capacity flows, as a function of the temperature for the hot and cold composite curves, are depicted in Fig. 4.9. The evolution of the heat capacity flow for the cold composite curve is only presented for GERG-2008 + LKP and the REF EoS in benefit of the explanation. The heat capacity flow was calculated as the inverse of the composite curves slope.

Three changes in the heat capacity flow slope for the hot composite curve appear: at approximately 112 °C, 138 °C, and 275 °C; corresponding to the exhaust gases dew point, the bypass gas extraction, and the hot air intake from the ASU. The EoSs compute an evolution of the heat capacity flow for the hot composite curve similar to the REF EoS, including the abrupt slope changes, since real gas effects are not relevant at the exhaust gas pressure. However, as can be seen in Fig. 4.9(b), the prediction of the heat capacity flow evolution for the cold composite curve by GERG-2008 + LKP presents discrepancies with respect to the REF EoS. For GERG-2008 + LKP, the turbine coolant is extracted from the recuperator at a higher temperature, 313.42 °C, than predicted by the REF EoS, 208.75 °C, due to the excess of available heat. This implies that the heat capacity flow drops (because of the extraction) at different temperatures. The decrease in the heat capacity flow causes an increase in the cold composite curve slope.

Fig. 4.10 shows the evolution of the hot and cold composite curves between 50 ºC and 500 °C. At low temperatures, the CCC predicted by the REF EoS and GERG-2008 + LKP are close and evolve with a similar slope. When reaching 208.75 °C, the cold composite curve slope for the REF EoS increases. However, the cold composite curve slope for GERG-2008 + LKP does not increase until a higher temperature of 313.42 °C is achieved. As a result, there is a larger separation between the cold composite curve and the hot composite curve for GERG-2008 + LKP than for the REF EoS. This justifies that the recuperator operated with a larger temperature difference for GERG-2008 + LKP than for the REF EoS.

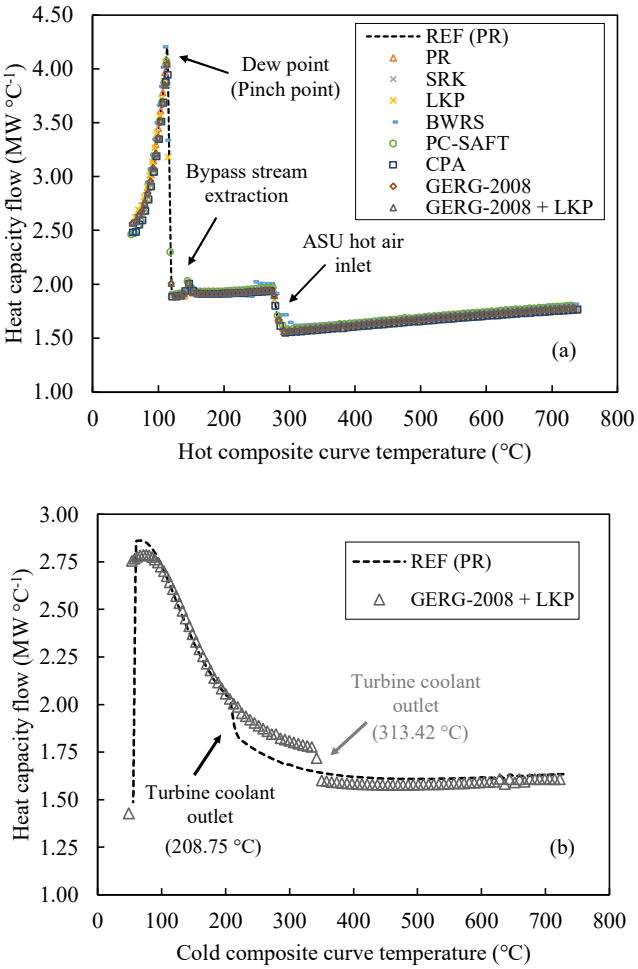

Fig. 4.9. Heat capacity flow evolution of (a) the hot composite curve for all EoSs, and (b) of the cold composite curve for the REF EoS and GERG-2008 + LKP. The heat capacity flow of the cold composite curve drops at a higher temperature (313.42 ºC) for GERG-2008 + LKP.

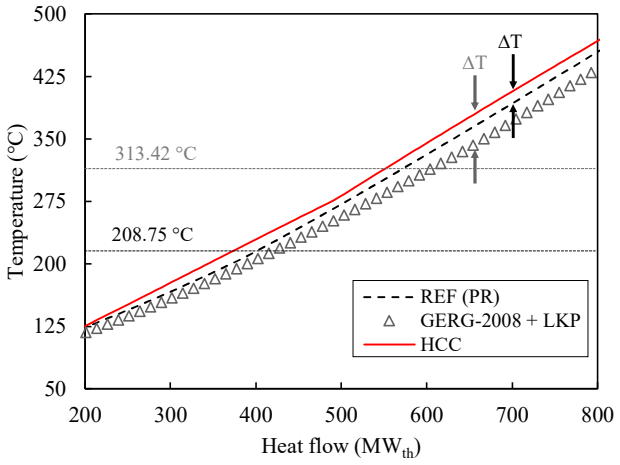

Fig. 4.10. Hot composite curve (in red) and cold composite curve (in black) for REF EoS and GERG-2008 + LKP. The heat capacity flow of the cold composite curve changes at higher temperature for GERG-2008 + LKP, which leads to a further separation of the composite curves.

4.2.3.3 Distillation columns of the air separation unit

The relative deviations in the calculation of the volumetric flow rate $\dot{V}$ and diameter Ω of the low and high pressure columns are presented in Table 4.9. Deviations do not exceed 2% (except for SRK), which means that the EoS employed does not substantially influence the ASU design. The discrepancies found for SRK lies in its periodic inaccuracy in predicting the partition coefficients in the vapor-liquid mixtures within the low-pressure distillation column.

Table 4.9. Relative deviation (RD) in the calculation of volumetric flow rates and diameters of the high and low pressure columns as a function of the EoS. The ASU is not significantly influenced by the TPM choice, unless SRK is used.

	REF(PR)	PR	SRK	LKP	BWRS	PC-SAFT	CPA	GERG-2008	GERG-2008 + LKP
$RD(\dot{V}_{\mathrm{LPC}})$	0.00	-1.48	33.80	-2.18	-2.19	-0.06	-3.52	-1.55	-1.55
$RD(\Omega_{\mathrm{LPC}})$	0.00	-0.74	15.67	-1.09	-1.10	-0.03	-1.78	-0.78	-0.78
$RD(\dot{V}_{\mathrm{HPC}})$	0.00	-0.72	27.97	-0.76	-0.57	-0.82	-0.16	-0.59	-0.59
$RD(\Omega_{\mathrm{HPC}})$	0.00	-0.36	13.12	-0.38	-0.28	-0.41	-0.08	-0.30	-0.30

4.2.4 Results of the numerical optimization process of the NET Power cycle

The configuration of the main operating parameters, that maximize the efficiency of the NET Power cycle, was found by conducting a numerical optimization process using the novel PSO + Complex optimization algorithm. Table 4.10 shows the thermodynamic performance of the NET Power cycle for the base case and the optimized case, resulting from the optimization process. The optimized cycle conditions were calculated with GERG-2008 + LKP, as it is the most reliable thermodynamic property method.

The optimum TIP found is 273.99 bar, instead of the 300 bar of the base load case. This is because the dense-phase compression work estimated by GERG-2008 + LKP is lower. This finding is relevant for the turbine design. A lower turbine inlet pressure causes a reduction of the mechanical stresses in the high-pressure blades, and a potential savings in the design.

The resulting optimum TOP is 44.83 bar, instead of 34 bar for the base case. This demonstrates that maximizing the effectiveness of the RHE is key to maximizing the efficiency. This conclusion also serves to justify the augment in the bypass stream split fraction from 6% to 11.37%, which also promotes heat transfer in the low/medium-temperature sections of the RHE, and reduces the exergy destruction. As a consequence, the temperature of the recycle and oxidant streams leaving the RHE increases, as represented in Table 4.10. As a result, the mass flow through the cycle is higher, with a value of 1410.67 $kg \cdot s^{-1}$. At the optimum conditions, the maximum cycle efficiency resulted in 55.94%, which is 1.53% higher than for the base conditions.

Table 4.10. Operating configuration for maximum efficiency of the NET Power cycle using the GERG-2008 + LKP EoS.

	Unit	Base case	Optimized
Turbine inlet pressure (TIP)	bar	300	273.99
Turbine outlet pressure (TOP)	bar	34	44.83
Total recycle flow rate	kg s^{-1}	1319.23	1410.67
Recuperator outlet temperature of recycle and oxidant streams	ºC	727.96	755.23
Recuperator outlet temperature of turbine coolant	ºC	208.74	242.40
Bypass stream split fraction	%	6.00	11.37
Thermal energy of feedstock (LHV)	MW_{th}	768.19	768.19
Turbine power output	MW_e	624.84	622.25
Power consumption	MW_e	206.86	192.50
Net cycle efficiency	%	54.41	55.94
Turbine pressure ratio (TIP/TOP)	-	8.82	6.11
Combustor outlet temperature	ºC	1150	1103.93
Turbine outlet temperature (TOT)	ºC	737.95	765.32
Turbine coolant flow rate	kg s^{-1}	106.65	98.94

4.3 NET Power cycle at part-load conditions. Operating ranges of the recuperative heat exchanger

The maximum efficiency operating configuration, obtained in Section 4.2.4, was used as an initial point in the present section to analyze the behavior of the NET Power cycle under part-load conditions. Section 4.3.1 discusses the trends of the efficiency and delivered power of the cycle as a function of the load degree. Then, the operating conditions of the RHE over the entire load levels spectrum are discussed in Section 4.3.2.

4.3.1 Efficiency and net power trends at partial loads

The performance of the NET Power cycle was analyzed under partial load conditions. For this purpose, the fuel flow introduced into the cycle was reduced from 100%, corresponding to the optimized nominal operating conditions, 16.52 kg·s^{-1}, to 20%.

Fig. 4.11 shows the evolution of the cycle efficiency and the net power delivered by the cycle, as the load degree is reduced. The cycle efficiency diminishes as the load degree decreases, reaching a maximum value of 55.94% at nominal conditions, and a minimum value of 14.26% for a load degree of 20%. When the load level is reduced from 100% to 50%, the cycle efficiency decays less steeply than when it is reduced from 50% to 20%. This result indicates that the NET Power cycle can be kept operating beyond on-design conditions with high efficiency over a wide load range. The delivered net power decays as the load degree decreases. Unlike efficiency, the decay of the net power occurs in an approximately linear fashion, ranging from a maximum value of 422 MW_e, at nominal conditions, to a minimum value of 20.4 MW_e, for a 20% load degree.

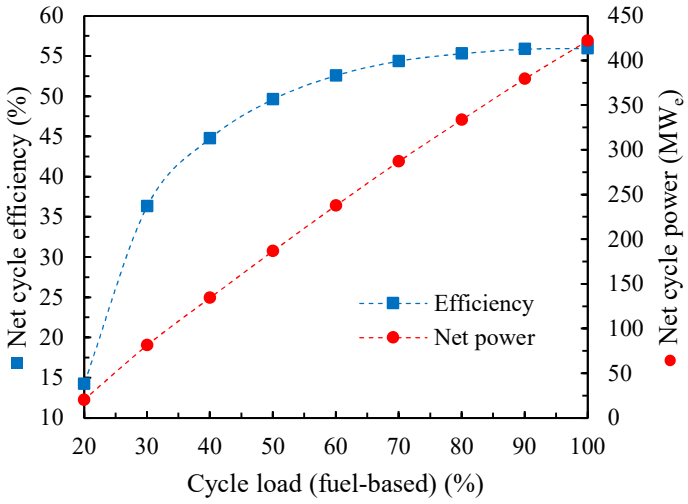

Fig. 4.11. Net cycle efficiency and net cycle power as a function of the cycle fuel-based load degree.

According to the control strategy of the NET Power cycle for partial loads described in Section 3.2.8, the CO_2 recirculation flow is adjusted to fix COT such that TOT remains constant for all load degrees. Thus, as the inlet fuel flow to the oxy-combustor is reduced, the released heat of combustion decreases, tending to decrease the COT and thus the TOT. To avoid the reduction of the TOT at partial loads, the recirculation flow throughout the cycle is reduced by closing the inlet guide vanes of the gas-phase compressor. This is shown in Fig. 4.12, which presents the evolution of the recirculation mass flow and the COT as a function of the load degree. The decrease of the recirculation flow explains the decay of the net power delivered by the cycle.

COT does not remain constant as the load degree decreases, but decreases from 1103.94 ºC to 875.14 ºC. This is due to the reduction in the temperature of the pressurized recirculation streams at the recuperator outlet. This temperature decrement is due to the deterioration of the heat transfer rates, which occur because of two reasons: (i) the decrease of the flow velocity, as a result of the recirculation mass flow reduction, and (ii) the reduction of the fluid density due to the decrease of the maximum pressure of the recirculation streams to satisfy the performance curve of the turbine. Both effects tend to decrease the Reynolds numbers of the pressurized fluid flows within the heat exchanger. The reduction of the COT and the recirculation flow, which causes also the decrease in the isentropic efficiency of the turbomachines, explains the decrease in cycle efficiency and the net power at partial loads.

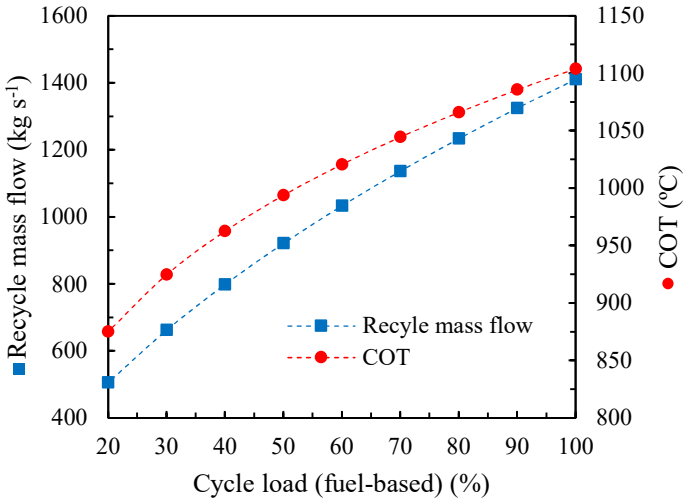

Fig. 4.12. Recycle mass flow and combustor outlet temperature as a function of the cycle fuel-based load degree.

4.3.2 Operating pressure, temperature and mass flows of the recuperative heat exchanger over the entire load range

The operating ranges of the RHE of the NET Power cycle for partial load conditions are analyzed in this section. To facilitate the interpretability of the results, a schematic of the inlet and outlet fluid streams to the RHE, which was divided into three heat exchange sections, is depicted in Fig. 4.13. A complete revision of the streams and components of the NET Power cycle was provided in Section 2.3.1. Fig. 4.14 shows the evolution of the key input parameters to the RHE as a function of the load degree of the NET Power cycle, and Table 4.11 presents the precise values at each evaluated load degree value.

The fluid pressure of the RE-6 stream decreases gradually from 279 bar, for the optimized nominal conditions (Table 4.10), to 95.6 bar for 20% of load, as depicted in Fig. 4.14(a). The temperature of the RE-6 stream decreases from 44.4 ºC to 23.9 ºC (Fig. 4.14(b)), and the mass flow from 949.1 kg·s^{-1} to 462.1 kg·s^{-1} (Fig. 4.14(c)). The pressure reduction is required to comply with the turbine performance curve. As discussed, the recirculation flow decreases, as the load degree is reduced, to maintain the TOT constant. Since the corrected mass flow in the turbine inlet is kept constant, according to Eq. (3.5), the pressure at the turbine inlet (i.e., the pressure of the recirculation streams) must decrease. Because of the reduction in the maximum cycle pressure, the pressure ratio of the dense-phase compressors decreases. Therefore, the temperature increase of the dense-phase CO_2, that takes place during compression, decreases justifying the reduction in temperature of the main recirculation CO_2 stream at the inlet of the heat exchanger.

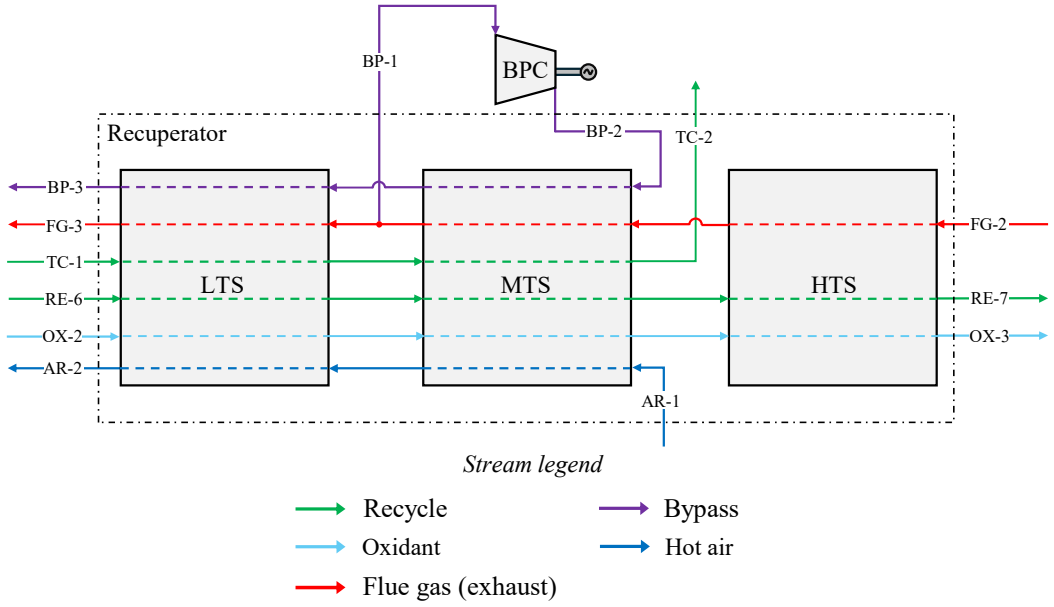

Fig. 4.13. Detailed view of the recuperative heat exchanger of the NET Power cycle divided into three heat exchange sections: high-temperature section (HTS), medium-temperature section (MTS) and low-temperature section (LTS).

Regarding the exhaust gas stream, FG-2, the H_2O mole fraction ($\hat{y}_{H_2O}$) and the mass flow, as a function of the cycle load degree, are shown in Figs. 4.14(d) and 4.14(e). $\hat{y}_{H_2O}$ decreases from 4.85%, for nominal conditions, to 2.86% for a cycle load degree of 20%. The reduction of fuel flow rate at partial loads causes a decrease in the amount of water generated in the combustion reactions. The mass flow rate of FG-2 decreases from 1484.75 kg·s^{-1} to 520.29 kg·s^{-1}. The temperature of FG-2 remains constant and equal to 765.32 ºC, in accordance with the control strategy of the cycle at partial loads. The evolution of the rest of the inlet flows to the RHE, shown in Fig. 4.13, are not discussed since the heat exchange study conducted in this work deals exclusively with the heat exchange that takes place between the RE-6 and FG-2 streams.

Table 4.11. Operating conditions of streams RE-6 and FG-2 for cycle part load (cycle fuel-based) conditions.

% Load (fuel-based)	Pressure RE-6 (bar)	Temperature RE-6 (ºC)	Mass flow RE-6 (kg s^{-1})	$\hat{y}_{H_2O}$ FG-2 (%)	Mass flow FG-2 (kg s^{-1})
100	278.99	44.40	949.14	4.85	1484.75
90	261.95	42.64	924.51	4.67	1291.20
80	243.79	40.74	893.21	4.48	1292.69
70	224.34	38.66	854.21	4.28	1188.45
60	203.39	36.36	805.97	4.05	1077.35
50	180.60	33.81	746.53	3.81	957.94
40	155.54	30.94	672.99	3.54	828.05
30	127.56	27.72	580.81	3.23	684.22
20	95.53	23.89	462.10	2.86	520.29

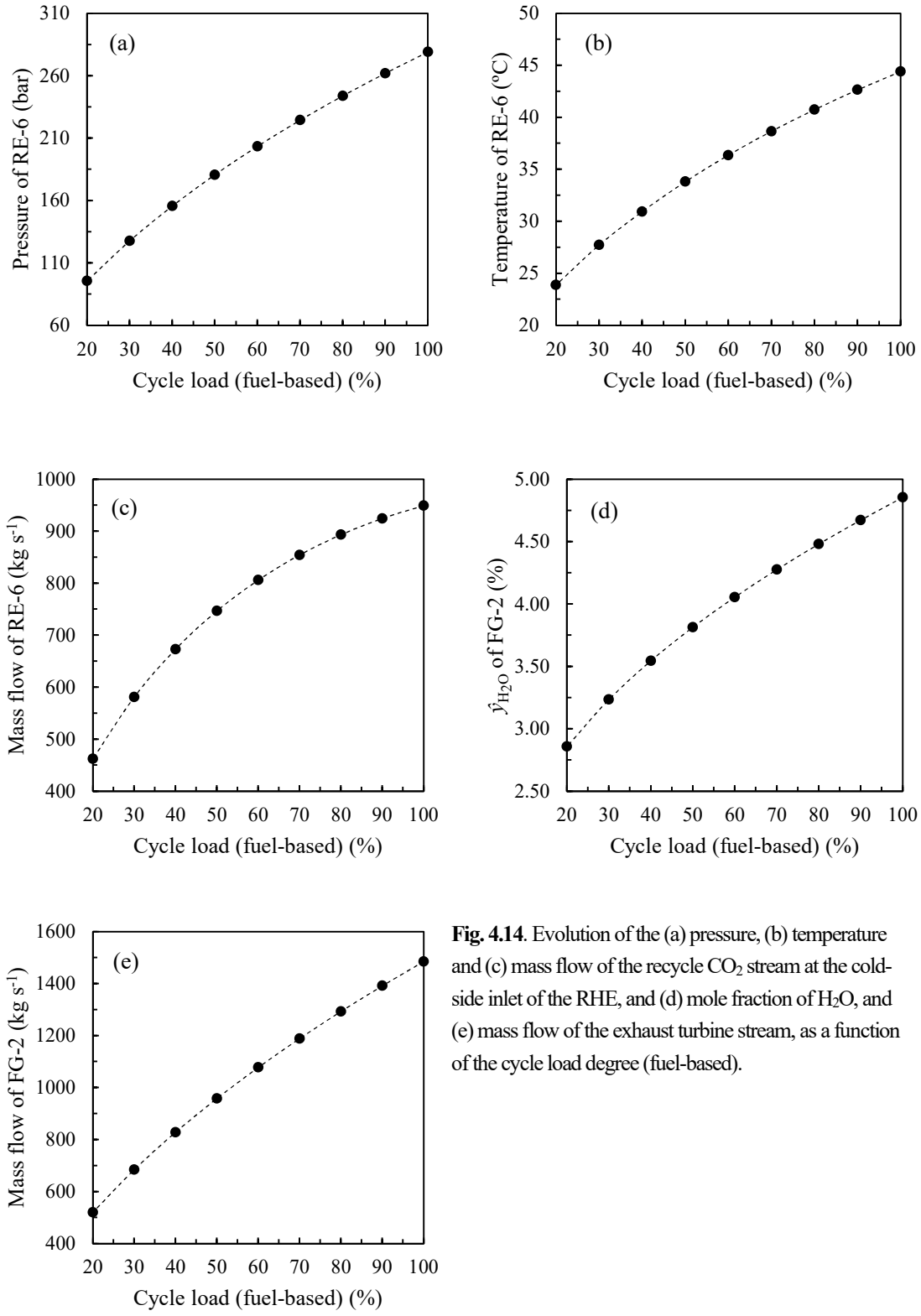

Fig. 4.14. Evolution of the (a) pressure, (b) temperature and (c) mass flow of the recycle CO_2 stream at the cold-side inlet of the RHE, and (d) mole fraction of H_2O, and (e) mass flow of the exhaust turbine stream, as a function of the cycle load degree (fuel-based).

Chapter 5

Methodology for the investigation of heat transfer in supercritical CO_2 microflows

5 Methodology for the investigation of heat transfer in supercritical CO_2 microflows

A major objective of this work is to investigate the heat transfer mechanisms of $scCO_2$ microflows for application in a MSTHE in the low-temperature section of the NET Power cycle thermal recuperator. In the previous Sections 3 and 4, the NET Power cycle was modeled at off-design conditions in Aspen Plus with the aim of deriving the full operating conditions of the MSTHE. In particular, the research focuses on the heat transfer between the humid expansion gases FG-2 (see Fig. 4.13) and the $scCO_2$-rich recirculating stream RE-6. As discussed in the previous sections, the RE-6 streams contains traces of components such as H_2O, N_2, Ar, H_2, CO, O_2, and CH_4. However, these impurities represent about 2% mol of the RE-6 stream composition, being 98% mol CO_2. Considering that the uncertainties of the experimental setup used in this work, that will be presented in the following sections, are higher than 2%, the investment and complexity resulting from including such impurities is not justified. Therefore, the heat transfer research was carried out assuming pure CO_2.

In the following, an experimental and computational investigation of the heat transfer characteristics of $scCO_2$ through a uniformly heated microtube is conducted under the operative conditions derived numerically in the previous sections. The methodology for conducting the experimental study is provided in Section 5.1. The CFD computational model, with the turbulence models validated against the experimental measurements, is presented in Section 5.2. Finally, based on an experimentally derived heat transfer model for $scCO_2$ through a microtube, a one-dimensional model of a MSTHE, for application in the low-temperature section of the NET Power cycle recuperator, was developed and implemented in Matlab. The geometrical and thermal-hydraulic modeling approach, the heat and mass transfer models, and the numerical procedures for model resolution, are discussed in Section 5.3.

5.1 Experimental investigation approach

The methodology to conduct the experimental investigation of heat transfer to $scCO_2$, flowing through a uniformly heated horizontal microtube, is presented in this Section. The complete experimental system is described in Section 5.1.1. Then, Section 5.1.2 details the design and construction of the test section for the measurement of the tube outer wall temperature profile. Data reduction and uncertainty analysis are outlined in Sections 5.1.3 and 5.1.4. Finally, the experimental ranges, test conditions, and operating procedure of the experimental setup, are discussed in Section 5.1.5.

5.1.1 Experimental setup

An experimental rig was constructed to measure convective heat transfer coefficients of CO_2 at supercritical pressures through a uniformly heated horizontal microtube. Fig. 5.1 shows the schematic process diagram, and Fig. 5.2 shows the physical diagram of the experimental system. The main parameters measured and controlled are the testing pressure, the mass flow, the fluid temperature at the inlet and outlet of the test section and the applied heat flux.

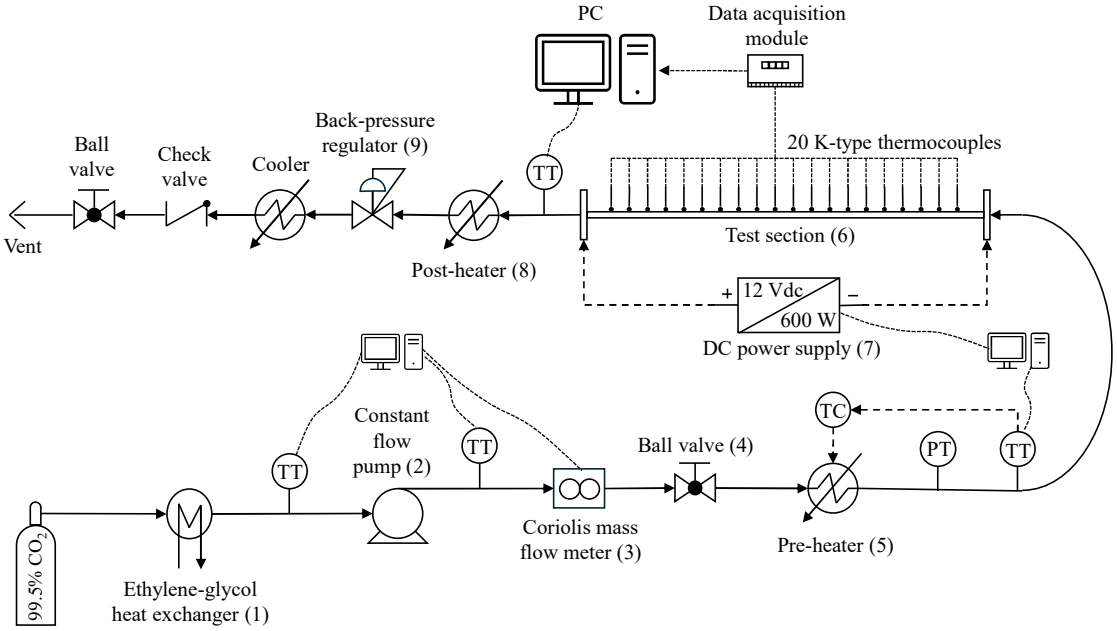

Fig. 5.1. Process flow diagram of the experimental system.

To obtain the fluid at supercritical conditions, CO_2 at a pressure of 45 - 70 bar, coming from a 99.5% purity cylinder, is cooled down to -2 ºC in a heat exchanger which uses ethylene-glycol at -12 ºC as coolant (Fig. 5.3(a)). The liquified CO_2 is pressurized to test pressure using a liquid pump (Milton Roy model MD 140 H6 M400), with a discharge pressure of up to 347 bar and a design volumetric flow of 4.17 $L \cdot h^{-1}$ (Fig. 5.3(b)). A ball valve allows flow through the experimental system.

The mass flow was adjusted by varying the pump stroke. A Coriolis-type digital mass flow meter, with a nominal range of 0 – 100 $kg \cdot h^{-1}$, was used to measure the mass flow with a measurement uncertainty of ± 1% (Fig. 5.3(c)). The CO_2 pressure at the inlet of the test section was monitored by a dial pressure gauge (Swagelok), with a range up to 400 bar. To adjust the fluid pressure at the inlet of the test section, a diaphragm back-pressure control valve (GO BP-66 series regulator), located after the test section, with a range up to 689.5 bar, was used (Fig. 5.3(d)). A thermostatically controlled wire heater

(Fig. 5.3(e)), coiled on the outer surface of the back-pressure valve inlet and outlet tubes, ensures that the fluid is heated to at least 120 ºC to prevent freezing during gas expansion.

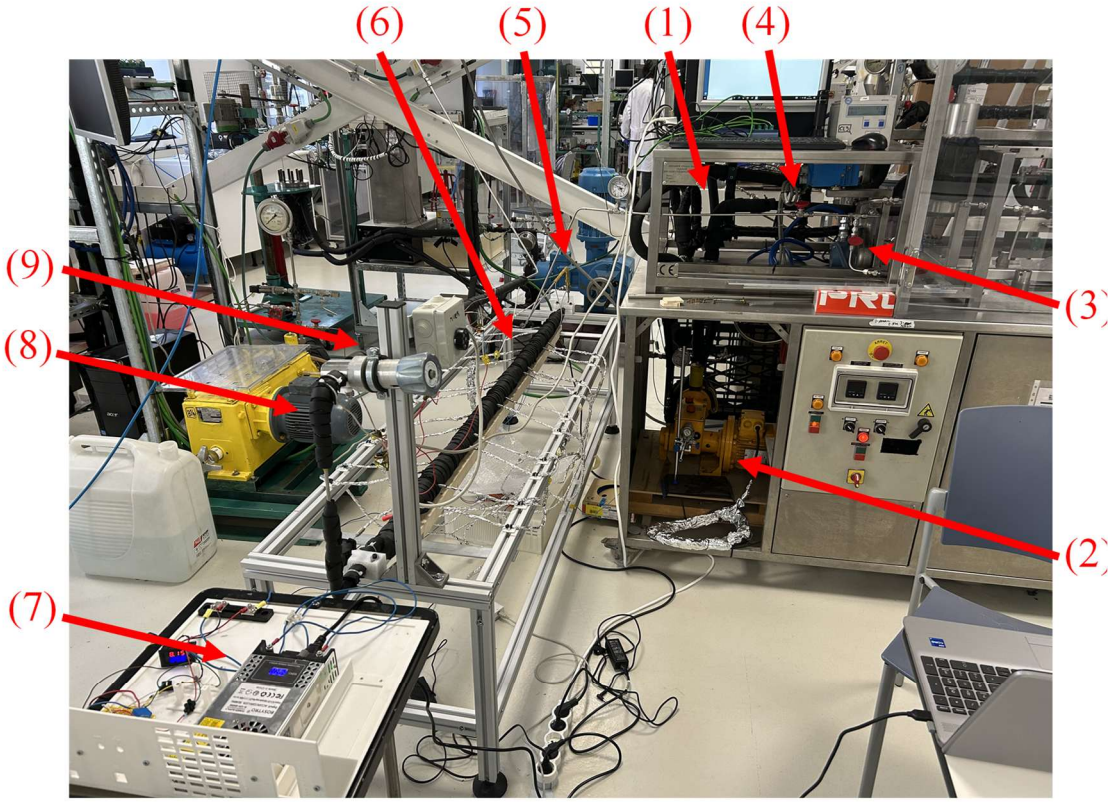

(1): Ethylene-glycol heat exchanger
(2): Constant flow pump
(3): Coriolis mass flow meter
(4): Ball valve
(5): Pre-heater
(6): Test section
(7): DC power supply
(8): Post-heater
(9): Back-pressure regulator

Fig. 5.2. Physical diagram of the experimental system.

The fluid temperature at each location of the test rig was measured by K-type thermocouples with ± 0.5 ºC of uncertainty. The fluid temperature at the inlet of the test section is a major parameter for calculating the enthalpy profile of the working fluid along the flow path. Then, the fluid supplied by the pump is preheated to the desired temperature, within ± 0.2 ºC, using a wire heater, coiled on the outer surface of the tube without thermal insultation (Fig. 5.3(f)), which is activated by a relay (SRD-05VDC-SL-C). The relay coil is excited by the digital signal of a microcontroller and a 2N2222A transistor. A 1 kΩ resistor limits the electric current through the digital pin of the microcontroller towards the base of the transistor and a 1N4007 diode protects the commutation transistor from transient voltage spikes that are induced when the relay coil is turned off.

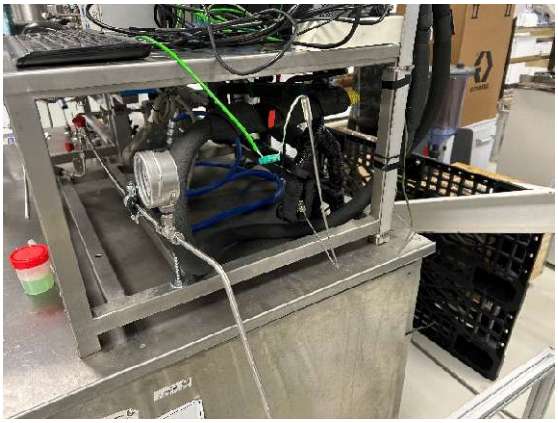

(a) Ethylene-glycol heat exchanger

(b) $scCO_2$ pump

(c) Coriolis mass flow meter

(d) Back-pressure control valve

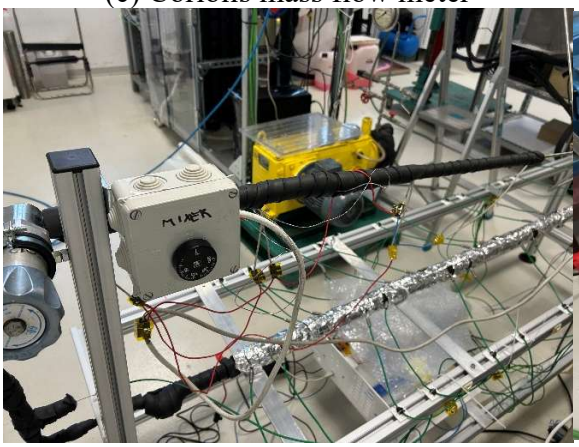

(e) Post heater

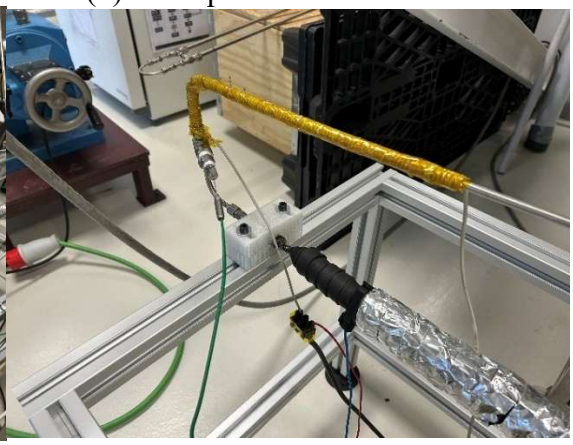

(f) Pre-heater

(g) Air-cooled helical heat exchanger

Fig. 5.3. Main components of the experimental system.

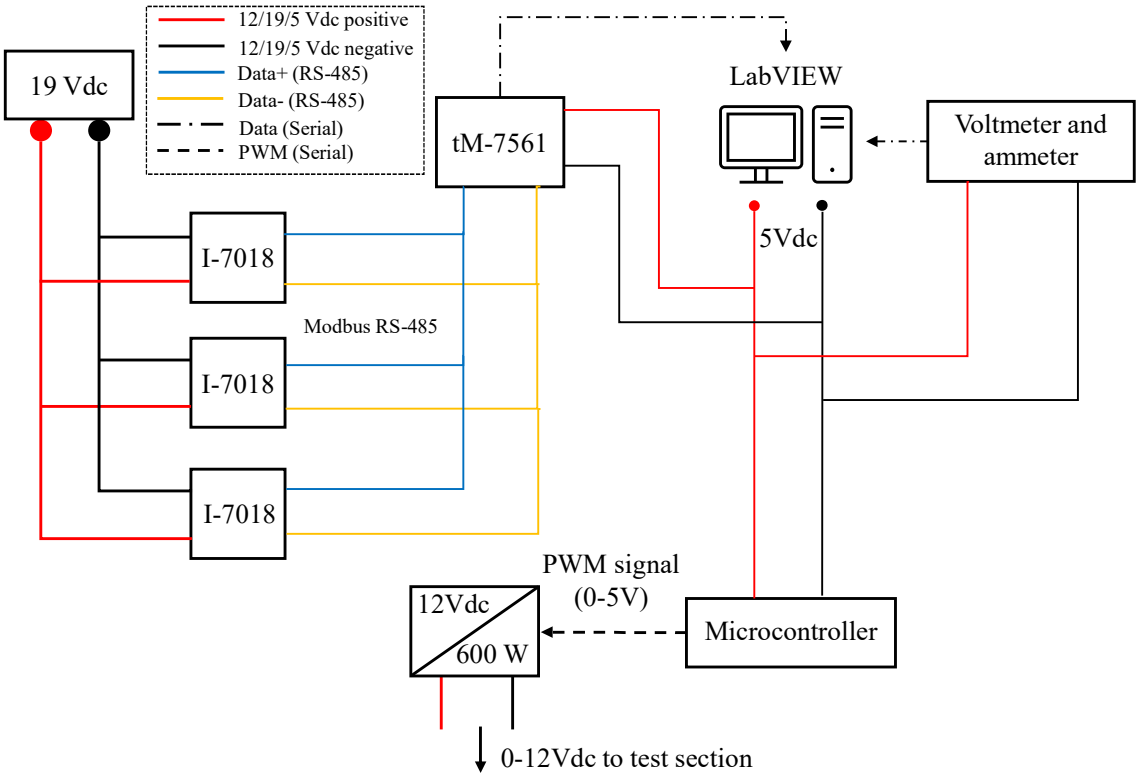

Fig. 5.4. Wiring diagram for data acquisition, DC power generation, and control of the testing section.

To provide the required uniform heat flux, the test section is heated by the passage of direct electric current (Joule effect), by applying voltage at the ends of the test tube with an adjustable DC power source (model BOSYTRO 0 – 12 Vdc, 50 A, 600 W), as shown in the electrical schematic of Fig. 5.4. To regulate the heat flux, the electric current is adjusted by controlling the output voltage of the power source through the duty cycle of a PWM signal coming from the same microcontroller that acts on the wire heater relay, which is power by the serial port of the computer. A voltmeter and ammeter measure (model ARCELI 200 A) the voltage and current applied to the test section with an uncertainty of 0.01 V and 0.01 A, and transmits data via serial port to the computer. Prior to venting, the fluid temperature is reduced in an air-cooled helical heat exchanger (Fig. 5.3(g)).

A *virtual instrument*, shown in Fig. 5.5, was developed in LabVIEW 2024 Q1 [204] to monitor and record real-time trends of the data captured by the sensors, and control the test rig during experiments.

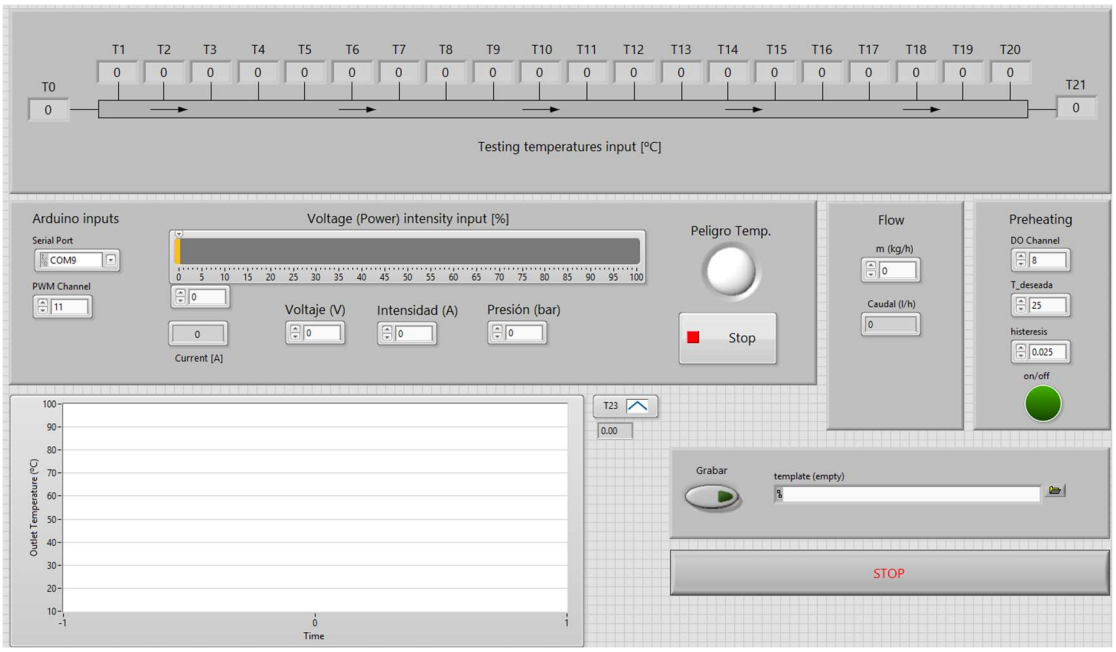

(a)

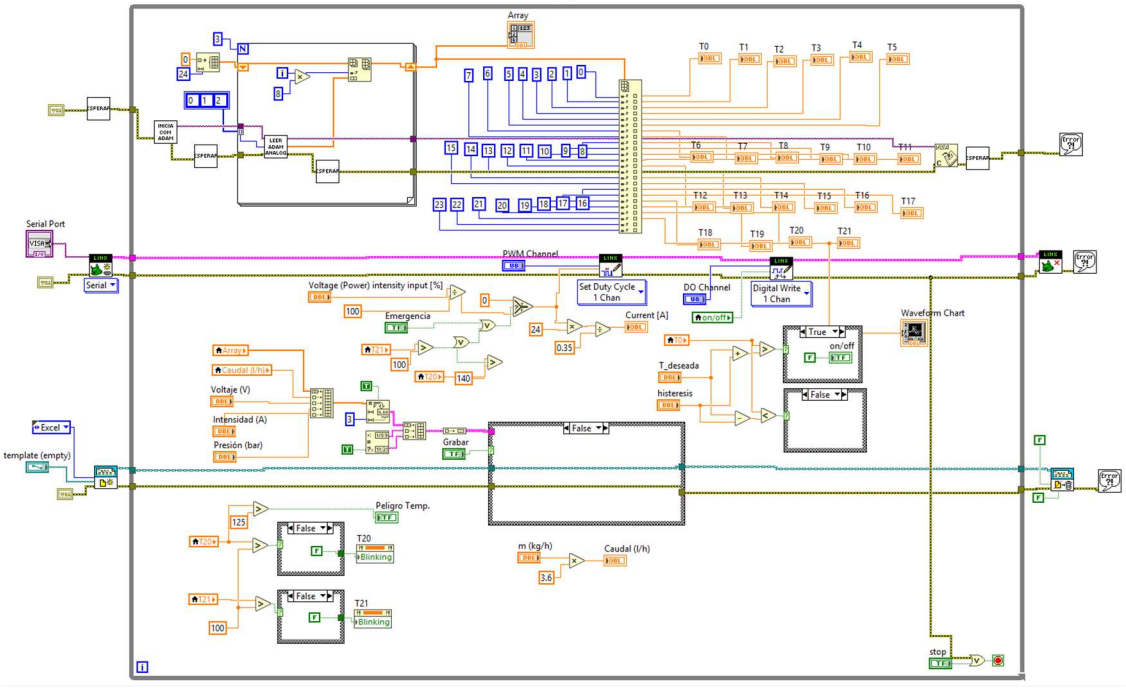

(b)

Fig. 5.5. *Virtual instrument* developed in LabVIEW. (a) Front panel and (b) block diagram.

5.1.2 Test section design

The test section consists of a 316L stainless steel circular microtube of length 1700 mm, and outer and inner diameters of 1.588 mm (1/16 ”) and 0.88 mm, as shown in Fig. 5.6. The heated length was 1600 mm, with 100 mm of unheated hydraulic inlet length. The tube length was chosen based on two criteria: (i) to represent the actual tube length in microtube heat exchangers, which ranges between 1 – 3 m [121,205], and (ii) to

increase the electrical resistance of the tube to minimize the electric current required for heating. The electrical resistance of the tube resulted in 1.03 Ω, considering the electrical resistivity of SS316L constant over the temperature range of the experiments and equal to 80 μΩ·cm [206]. A 3.175 mm (1/8 ”) helical-shaped stainless steel tube (Fig. 5.7) was placed at the end of the test section to gently pull the microtube and keep it straight, also allowing to absorb the stresses caused by the axial dilatation of the tube during heating and to avoid leakages at fittings. Moreover, to ensure perfect horizontality of the test tube, it rested (during experiments) on a wooden beam axially disposed in the direction of the tube, which supports the weight of the thermal insulator (Fig. 5.2). The voltage on the heated section was applied using two copper clamps. The test section was electrically isolated from the rest of the experimental system to avoid interference with the measurement systems, using two Swagelok dielectric fittings (Fig. 5.8). Two PETG fasteners, manufactured by 3D printing, fix the dielectric fittings at the end of the test section to the structure, preventing electrical current shunts.

Fig. 5.6. Test tube.

Fig. 5.7. 1/8 '' helical tube, used to maintain the test rube straight.

Fig. 5.8. Swagelok dielectric fittings.

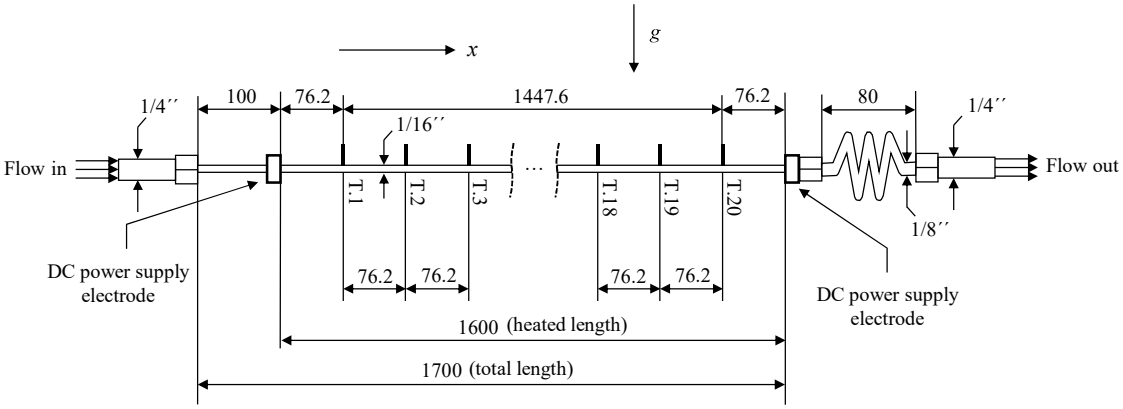

Fig. 5.9. (a) Distribution of the thermocouples along the outer wall of the test section. Units: mm, unless otherwise indicated.

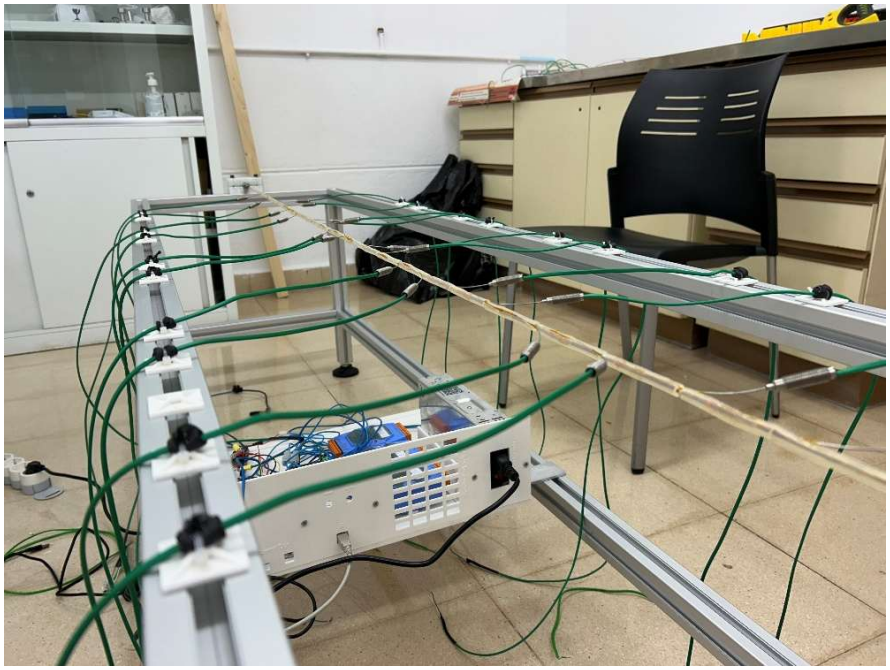

(a)

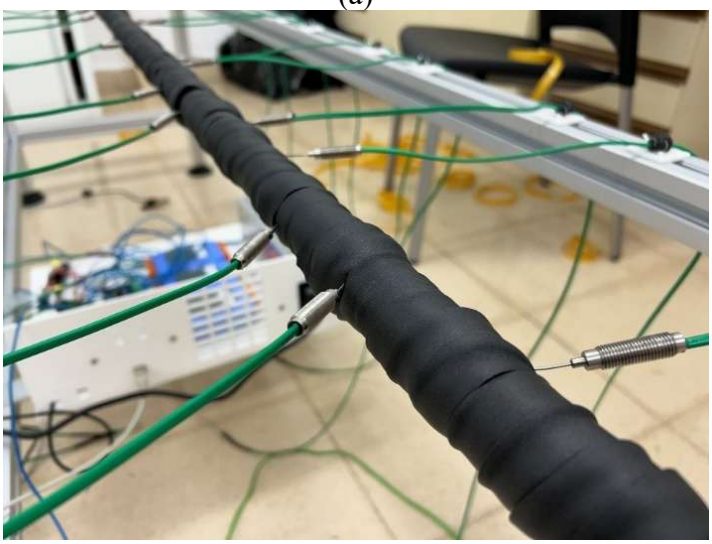

(b)

Fig. 5.10. (a) Internal thermal insultation layer of silicone, and (b) external thermal insulation of expanded elastomeric foam.

To measure the local outer wall temperature of the test tube, 20 K-type sheathed thermocouples (0.5 mm diameter, ungrounded junction) were uniformly distributed at 76.2 mm intervals along the top surface of the tube. Fig. 5.9 shows the distribution of the thermocouples along the outer wall of the test section. For attachment, the last 7 mm of the sheath were aligned longitudinally with tube axis. The thermocouple tip, where the sensing junction is located, was held in direct contact with the surface using a polyester knot to ensure a stable mechanical assembly. The remaining final section of the aligned sheath was affixed to the tube by applying a thin layer of thermally-conductive epoxy adhesive (MG Chemicals 8329TTF), ensuring proper alignment of the sensing junction with the tube surface. Then, the entire aligned length was further secured with Kapton

tape to reinforce its fixation. The surface-mounted thermocouples presented an uncertainty of 0.5 ºC after the application of the calibration function, provided by the manufacturer, in the surface temperature range covered in this work (up to 200 ºC).

To prevent high-frequency noise from the electric current signal through the tube from potentially inducing electromagnetic interference in the voltage signals of the thermocouples, the thermocouple wires were shielded with aluminum, and a cooper drain wire diverts stray currents to the installation ground. Three I-7018 8-channel thermocouple input modules, powered by an independent 19 Vdc power source, collect signals from the thermocouples. A tM-7561 module, powered by the serial port of the computer, converts the communication protocol Modbus RTU RS-485 to serial (USB) to establish communication with LabVIEW, as shown in Fig. 5.4.

Fig. 5.11. Validation of the thermal insulation by a thermographic camera.

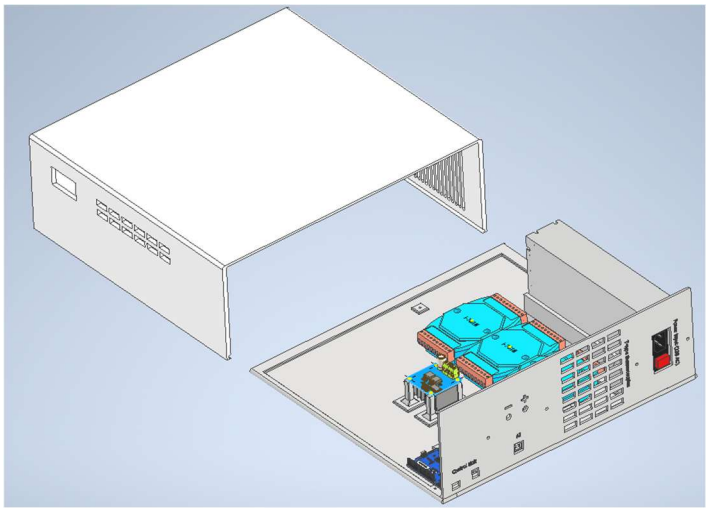

Fig. 5.12. PLA box, designed in Autodesk Inventor, to pack the electronic components.

The test section was thermally insulated to guarantee that the heat generated by the current passing through the tube is completely transferred to the fluid. For this purpose,

the microtube was firstly encased by a 10 mm diameter high thermal resistance silicone tube, Fig. 5.10(a), and a 80 mm diameter elastomeric foam outer layer, Fig. 5.10(b). The outer insultation layer was thickened, ensuring that the critical insulation radius was exceeded, until the temperature of the outer surface, captured by a thermographic camera, was no higher than the ambient temperature when the test section was heated at a temperature of 150 ºC, as shown in Fig. 5.11.

The DC power source, voltmeter, ammeter, I-7018 modules, tM-7561 module, microcontroller and relay were packed in a PLA box, manufactured by 3D printing, which was specifically designed for this purpose, as shown in Fig. 5.12.

5.1.3 Data reduction

Heat transfer in supercritical fluids is a local phenomenon due to the variation of the physical fluid properties. Hence, the data reduction analysis was based on local properties. For simplification in notation, the subscript x, which refers to the local property, was omitted. Fig. 5.13 represents the energy fluxes in the control volume considered during the data reduction.

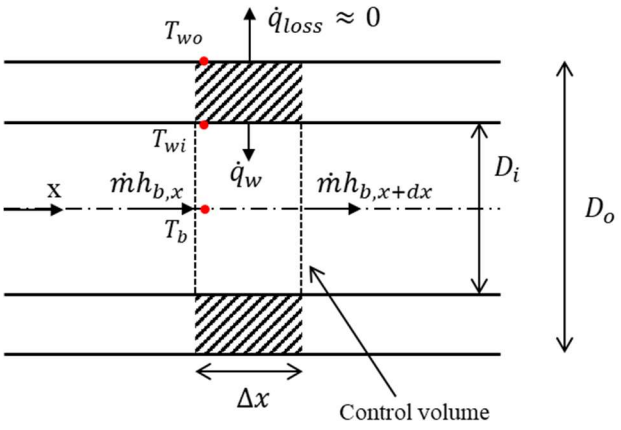

Fig. 5.13. Energy fluxes in the control volume considered for the data reduction.

The testing tube was heated by direct electrical heating, assuming that the volumetric heat generation rate is uniform,

$$\dot{q} = \frac{\mathcal{U}I}{\frac{\pi}{4}\left(D_o^2 - D_i^2\right)L_h}, \tag{5.1}$$

where $\mathcal{U}$ is the voltage, I is the intensity of current, and L_h is the heated length. The outer wall of the testing tube is insulated. However, heat losses due to conduction through the surface-mounted thermocouples occur. To account for these losses, an efficiency parameter, η, was defined as follows:

$$\eta = \frac{\dot{m}\left(h_{b,out} - h_{b,in}\right)}{\mathcal{U}I}. \tag{5.2}$$

The numerator in Eq. (5.2) represents the actual heat flow gained by the fluid, whilst the denominator denotes the heat flow supplied to the tube. In each experiment, the value of η was determined, which ranged from 0.93 to 0.98. Lower values of η were registered in tests conducted at higher heat fluxes and lower superficial flow velocities. Therefore, the effective heat flux imposed on the inner wall of the tube, which heats the fluid, is calculated as:

$$\dot{q}_w = \frac{\eta \mathcal{U}I}{\pi D_i L_h}. \tag{5.3}$$

The axial distribution of mean enthalpy through the flow path can be determined based on the convective heat balance equation in the control volume of Fig. 5.13 as:

$$h_{b,x+\Delta x} = h_{b,x} + \frac{\pi D_i \dot{q}_w}{\dot{m}} \Delta x, \tag{5.4}$$

where $\dot{m}$ is the mass flow rate and Δx is the distance between two thermocouple locations. From the mean enthalpy and inlet pressure (p_{in}), the corresponding bulk mean temperature is calculated using the Span & Wagner EoS [207], i.e., $T_b = f(h_b, p_{in})$. The temperature at the inner wall of the tube can be calculated from the outer wall temperature, measured by the thermocouples, based on the one-dimensional heat conduction equation, Eq. (5.5), and the boundary conditions of the experiments, Eq. (5.6).

$$\frac{1}{r}\frac{d}{dr}\left(r\frac{dT}{dr}\right) + \frac{\dot{q}}{\lambda} = 0 \tag{5.5}$$

$$\begin{aligned} &\text{i.} \quad \lambda \left.\frac{dT}{dr}\right|_{r=r_o} = 0 \\ &\text{ii.} \quad T(r_o) = T_{wo}. \end{aligned} \tag{5.6}$$

Integrating Eq. (5.5), the inner wall temperature was derived analytically:

$$T_{wi} = T_{wo} + \frac{\dot{q}}{16\lambda}\left(D_o^2 - D_i^2\right) - \frac{\dot{q} D_o^2}{8\lambda} \ln \frac{D_o}{D_i}. \tag{5.7}$$

The heat transfer coefficient was obtained based on the Newton's cooling law:

$$\alpha = \frac{\dot{q}_w}{T_{wi} - T_b} \tag{5.8}$$

5.1.4 Uncertainty analysis.

An analysis of the experimental uncertainties was performed based on the uncertainties of the measurement devices and McClintock method [208]. The experimental uncertainty of the heat transfer coefficient was calculated using Eq. (5.9).

$$\frac{\sigma_\alpha}{\alpha} = \sqrt{\left(\frac{\sigma_{\dot{q}_w}}{\dot{q}_w}\right)^2 + \left(\frac{\sigma_{T_{wi}}}{T_{wi} - T_b}\right)^2 + \left(\frac{\sigma_{T_b}}{T_{wi} - T_b}\right)^2} \tag{5.9}$$

The uncertainties of wall heat flux $\sigma_{\dot{q}_w}$ (Eq. (5.10)), inner wall temperature $\sigma_{T_{wi}}$ (Eq. (5.11)) and bulk mean temperature σ_{T_b} (Eq. (5.12)) were derived from Eqs. (5.3), (5.7) and (5.4), respectively.

$$\frac{\sigma_{\dot{q}_w}}{\dot{q}_w} = \sqrt{\left(\frac{\sigma_{\mathcal{U}}}{\mathcal{U}}\right)^2 + \left(\frac{\sigma_I}{I}\right)^2} \tag{5.10}$$

$$\sigma_{T_{wi}} = \sqrt{\left(\sigma_{T_{wo}}\right)^2 + \left[\left(\frac{D_o^2 - D_i^2}{16\lambda} - \frac{D_o^2}{8\lambda}\ln\frac{D_o}{D_i}\right)\sigma_{\dot{q}}\right]^2} \tag{5.11}$$

$$\sigma_{h_{b,x}} = \sqrt{\left(\sigma_{h_{b,x-\Delta x}}\right)^2 + \left(\frac{\pi D_i \Delta x}{\dot{m}}\sigma_{\dot{q}_w}\right)^2 + \left(\frac{\pi D_i \Delta x \dot{q}_w}{\dot{m}^2}\sigma_{\dot{m}}\right)^2} \tag{5.12}$$

The measurement uncertainties of the voltage $\sigma_{\mathcal{U}}$, electric current σ_I, mass flow rate $\sigma_{\dot{m}}$ and outer wall temperature $\sigma_{T_{wo}}$ are 0.1%, 0.1%, 0.5% and 0.5 ºC, respectively.

5.1.5 Experimental ranges and test conditions

The main experimental variables influencing the heat transfer mechanisms of $scCO_2$ are the pressure, mass flux, heat flux, and fluid temperature at the inlet of the test tube. In this work, the experimental design conducted in the software Statgraphics Centurion 19 [209], which is based on the fractional factorial model, covers the operational region of the low-temperature heat exchanger of the NET Power cycle with a reduced number of tests, without compromising statistical reliability, evaluating the influence of these experimental variables on the heat transfer coefficients.

The ranges of the influencing variables considered during the experiments are based on the study of the NET Power cycle at partial loads conducted in Section 4.3.2. In such study, the operating ranges of the MSTHE were found and presented in Table 4.11.

The experimental ranges of pressure, bulk enthalpy and bulk temperature are shown in Fig. 5.14 in the blue domain, while the blue dots represent the specific conditions where

the heat transfer coefficients were obtained. The pressure of the $scCO_2$ in the recuperative heat exchanger of the NET Power cycle varies between 9.5 – 28 MPa, depending on the load degree. Thus, the experimental range for the fluid pressure at the inlet of the test section was between 10 – 30 MPa. On the basis of the experimental design, tests were conducted for five equally distributed pressures, i.e.: 10, 15, 20, 25 and 30 MPa. The inlet temperature of the $scCO_2$ in the NET Power cycle heat exchanger ranges between 24 – 45 ºC, depending on the load degree. Hence, the experiments were performed for two levels of fluid temperature at the inlet of the test section, 20 ºC and 30 ºC. Then, heat transfer coefficients up to 45 ºC are measured along the tube length.

Real gas effects, which induce variations in the physical properties of $scCO_2$, appear essentially up to a temperature of around 100 ºC. Above 100 ºC, the fluid collapses to a single supercritical gas-like phase, with convective heat transfer being similar to that of a constant-property turbulent flow [96], resulting in a thermodynamic region lacking in research novelty. Consequently, the maximum test fluid temperature was assumed to be 100 ºC. In Fig. 5.14, the experimental region of pressure, enthalpy and temperature covered in the present study is presented in blue, as opposed to the red region representing the experimental domain covered in previous studies in the literature on heat transfer to $scCO_2$ in horizontal tubes, highlighting the novelty of this study.

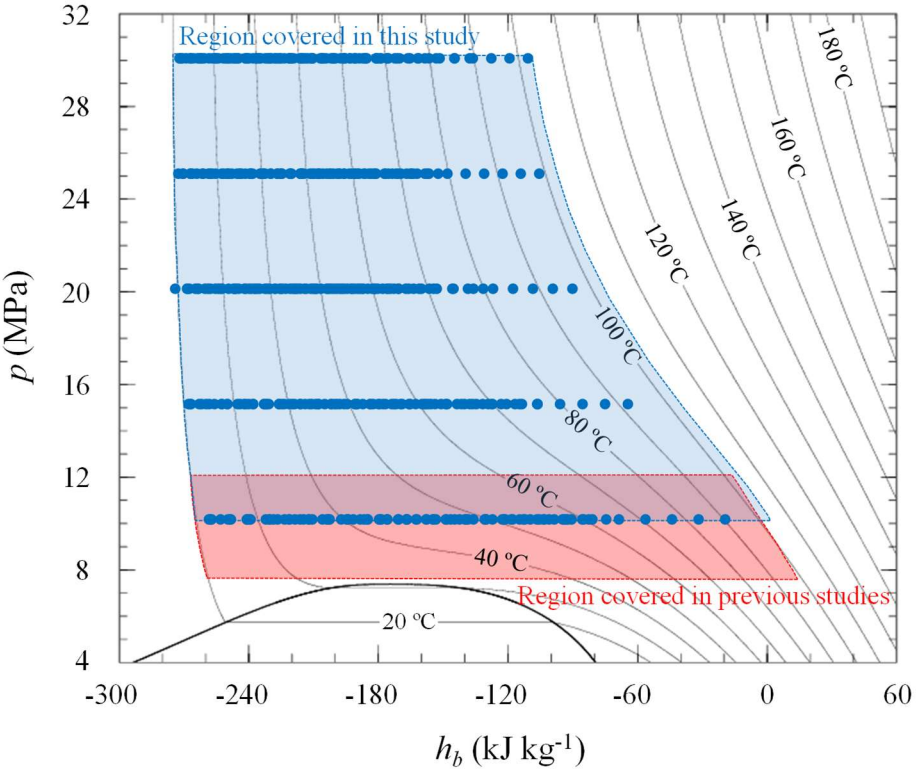

Fig. 5.14. Experimental ranges of pressure and bulk enthalpy (or bulk temperature) of this work in the blue domain, and of previous works (Table 2.4) in the red domain.

Fig. 5.15 shows the experimental ranges of Reynolds number (related to the mass flux) and heat flux as a function of the test pressure. Due to the reduction of the fluid viscosity with increasing temperature, the Reynolds number increases along the tube according to the fluid temperature profile, so that for each test, 20 heat transfer coefficients were measured (for having 20 thermocouples on the tube surface) at different Reynolds numbers. The design of experiments specified the maximum achievable Reynolds number, which depends on the capacity of the pump and the maximum assumed fluid temperature of 100 ºC. From the Reynolds number at the inlet of the test section, calculated for a temperature of 20 ºC or 30 ºC, to the Reynolds number at the outlet; intermediate values are progressively calculated along the heated tube due to the design of the experimental system itself. The Reynolds number varied in the experiments between 4100 and 23847, which allowed measuring heat transfer coefficients in the transitional and turbulent flow regimes, within flow velocity ranges compatible with the proper operation of MSTHEs [205].

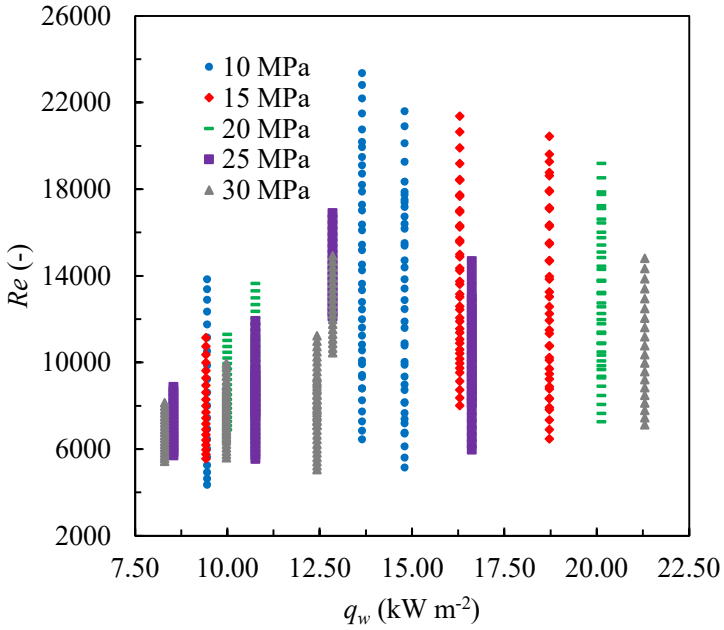

Fig. 5.15. Experimental ranges of wall heat flux $\dot{q}_w$ and Reynolds number Re.

Within the experimental domains of Fig. 5.14 and Fig. 5.15, a total of 28 tests were conducted, with the experimental variables shown in Table 5.1. In addition, the experimental design allowed parallel parametric studies to be performed as a function of the variables: pressure, p, heat flux, $\dot{q}_w$, mass flux, G, and the inlet fluid temperature, T_{in}. For pressure, five possible values were assumed, as previously explained, and for the rest of the influence variables two possible values were considered, attempting to optimize the total number of tests.

The experimental procedure is outlined in Fig. 5.16. At start-up, the CO_2 and ethylene-glycol inlet valves are opened to pressurize the system with the vent valve closed, allowing leak detection. Once verified, the vent valve is opened, and the system is preheated by activating the DC power supply (heating the test section to 100 ºC) and the post-heater (to prevent gas freezing at the back-pressure valve). With the system warmed, the pump is started, and operating conditions (pressure, mass flow, and heat input) are adjusted via the back-pressure regulator, pump stroke, and tube voltage. After setting the experimental conditions, the system is allowed to reach steady state, defined by fluid and surface temperature variations below 0.2 ºC. Data acquisition begins 5 minutes later. The data was recorded at a 10-minute interval with a frequency of 0.5 Hz. Therefore, the final results represent the arithmetic average over this time interval. After the experiment, the heat sources and pump are turned off, inlet valves are closed, and pressure is released by opening the vent and fully opening the back-pressure valve.

Table 5.1. Experimental conditions of the 28 tests.

Test code	p_{in} (MPa)	$\dot{q}_w$ (kW m^{-2})	G (kg m^{-2} s^{-1})	$T_{b,in}$ (ºC)	$T_{b,out}$ (ºC)	Re_{in}	Re_{out}
T1	10	9.5	447.4	20.1	58.2	4099.9	14243.5
T2	10	14.8	447.4	20.2	87.6	4750.6	17937.2
T3	10	14.8	604.9	19.9	58.4	6360.4	22222.1
T4	10	13.7	633.7	20.1	56.4	6090.0	20828.8
T5	10	13.7	633.7	30.1	61.3	8312.9	23847.4
T6	15	9.4	658.5	20.1	61.8	5368.8	11566.2
T7	15	18.7	658.5	19.8	90.5	6091.6	19894.5
T8	15	18.7	823.9	19.9	75.6	7544.3	21276.3
T9	15	16.3	821.6	20.0	69.8	7678.7	19158.4
T10	15	16.3	821.6	29.9	75.1	9350.0	22093.3
T11	20	10.0	804.4	20.2	61.8	6721.6	11591.9
T12	20	20.1	804.4	20.2	95.5	6907.5	18415.5
T13	20	20.1	1044.5	20.0	79.4	8932.0	19864.3
T14	20	10.8	821.6	20.1	64.7	6110.6	11388.4
T15	20	10.8	821.6	29.8	69.6	8199.0	13986.8
T16	25	8.5	717.3	20.0	63.5	5584.4	9077.9
T17	25	16.6	717.3	20.2	98.1	5719.0	13402.6
T18	25	16.6	994.2	20.1	77.7	7891.4	15108.2
T19	25	10.8	684.7	20.2	73.7	5377.1	9956.6
T20	25	10.8	684.7	30.1	75.1	7394.7	12193.6
T21	25	12.9	1355.2	34.2	66.8	12661.9	18270.5
T22	30	8.3	650.1	20.1	64.2	5328.8	8310.7
T23	30	12.4	650.1	19.8	88.7	4883.2	9565.1
T24	30	12.4	921.5	20.1	70.7	6926.4	11488.5
T25	30	10.0	754.9	20.2	70.6	5460.2	9108.7
T26	30	10.0	754.9	30.0	79.3	6334.8	10200.4
T27	30	21.3	921.5	20.1	101.8	6822.4	15302.2
T28	30	12.9	1176.4	34.6	74.6	10248.5	15214.0

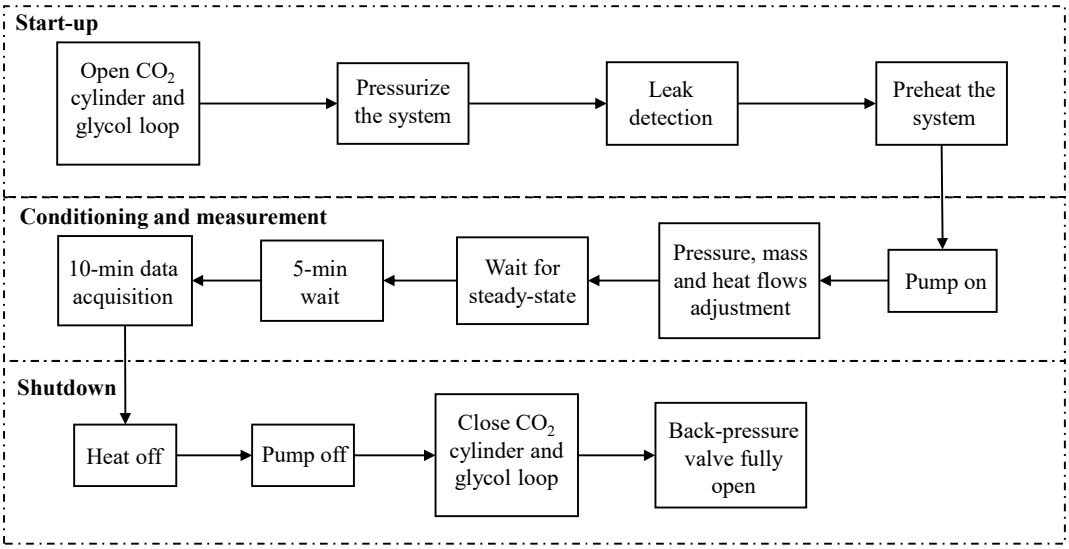

Fig. 5.16. Diagram of the experimental procedure.

5.2 Computational heat transfer model and validation of turbulence models

The testing microtube of 1700 mm length, 1/16 ” OD and 0.014 ” of thickness, used during the experimental work, was modeled in ANSYS Fluent R2023 [210] with the aim of:

- Validating the first-order RANS turbulence models from experimental results.
- Investigating the heat transfer mechanisms through flow field-based computational analysis.

In this section, the modeling approach of the CFD model is presented. The physical model and the procedure for calculating the inflation layers are outlined in Section 5.2.1. The governing equations and the turbulence modeling approach, based on the Favre averaging and first-order turbulence models, are presented in Section 5.2.2. Then, the numerical resolution strategies and boundary conditions are described in Section 5.2.3. Finally, to ensure that the results are independent of the mesh, a mesh sensitivity study is conducted in Section 5.2.4.

5.2.1 Physical model

A schematic of the computational model, which replicates the experimental test section, is shown in Fig. 5.17. The computational domain consists of a cylindrical channel of 1700 mm length and 0.88 mm inner diameter. The fluid enters uniformly at the inlet boundary ($z = 0$), and develops the boundary layer along the 100 mm adiabatic inflow length section. Heat is then applied through a uniform heat flux at the heated wall boundary, and the fluid exists the domain at the outlet boundary ($z = L$). Only the cylinder volume enclosed by the inner surface of the tube (fluid volume) was modeled, neglecting

the solid walls, since as the outer surface is perfectly insulated, all the volumetric heating generated by the electric current can be introduced directly into the model as a uniformly distributed heat flux boundary condition.

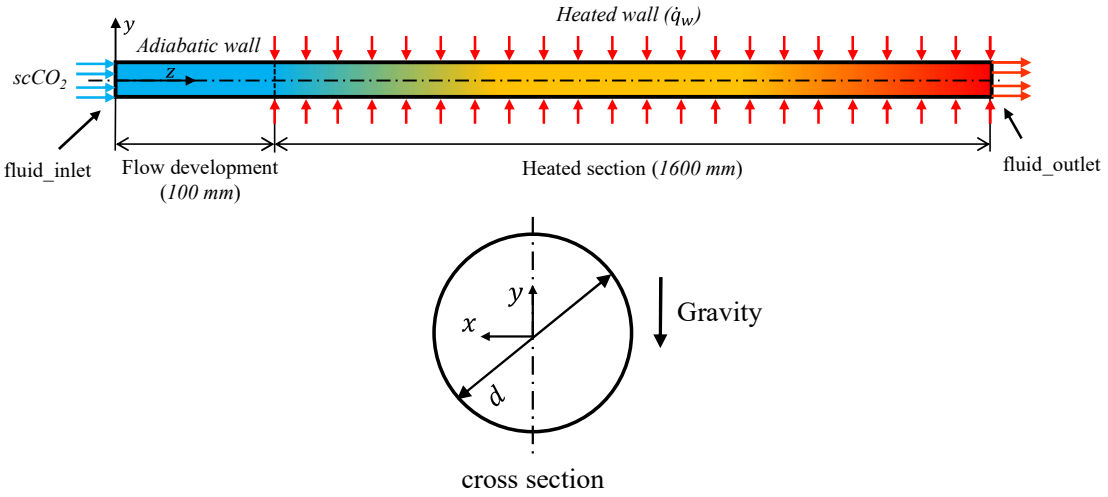

Fig. 5.17. Schematic of the computational model.

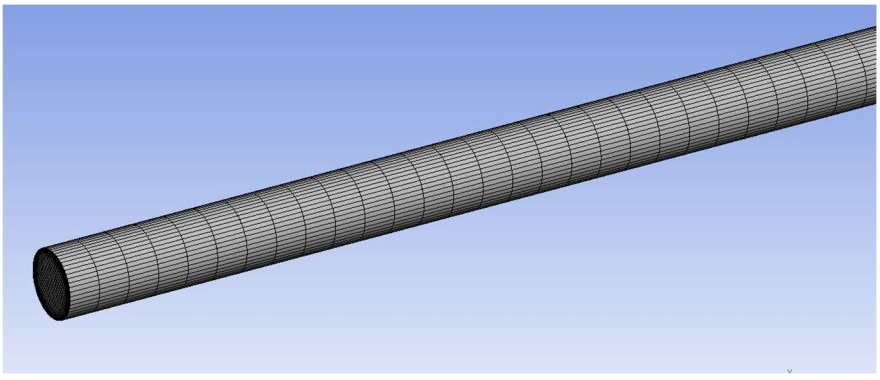

(a)

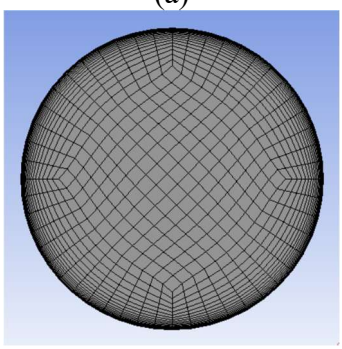

(b)

Fig. 5.18. (a) Meshed fluid domain and (b) cross-view of the computational bell-shaped 'O'-type mesh.

Fig. 5.18 shows the fluid volume and a cross-view of the computational mesh of the CFD computational model. The mesh consists of 1,242,582 hexahedral cells, which are thinner at the wall and coarser in the core section, with a bell-shaped 'O' configuration. Hexahedral cells allow efficient filling of the domain and alignment with the flow

direction to avoid numerical diffusion errors [211]. The turbulence models employed in this study demand well-refined meshes by inflation layers to properly capture the steep gradients near the wall, specifically, the dimensionless distance y^+ of the wall-adjacent nodes is < 0.5, and 5 grid layers fall within the viscous sublayer ($y^+ < 5$). For this purpose, the thickness of the first layer y_H, and the growth rate G of 20 inflation layers, were iteratively adjusted.

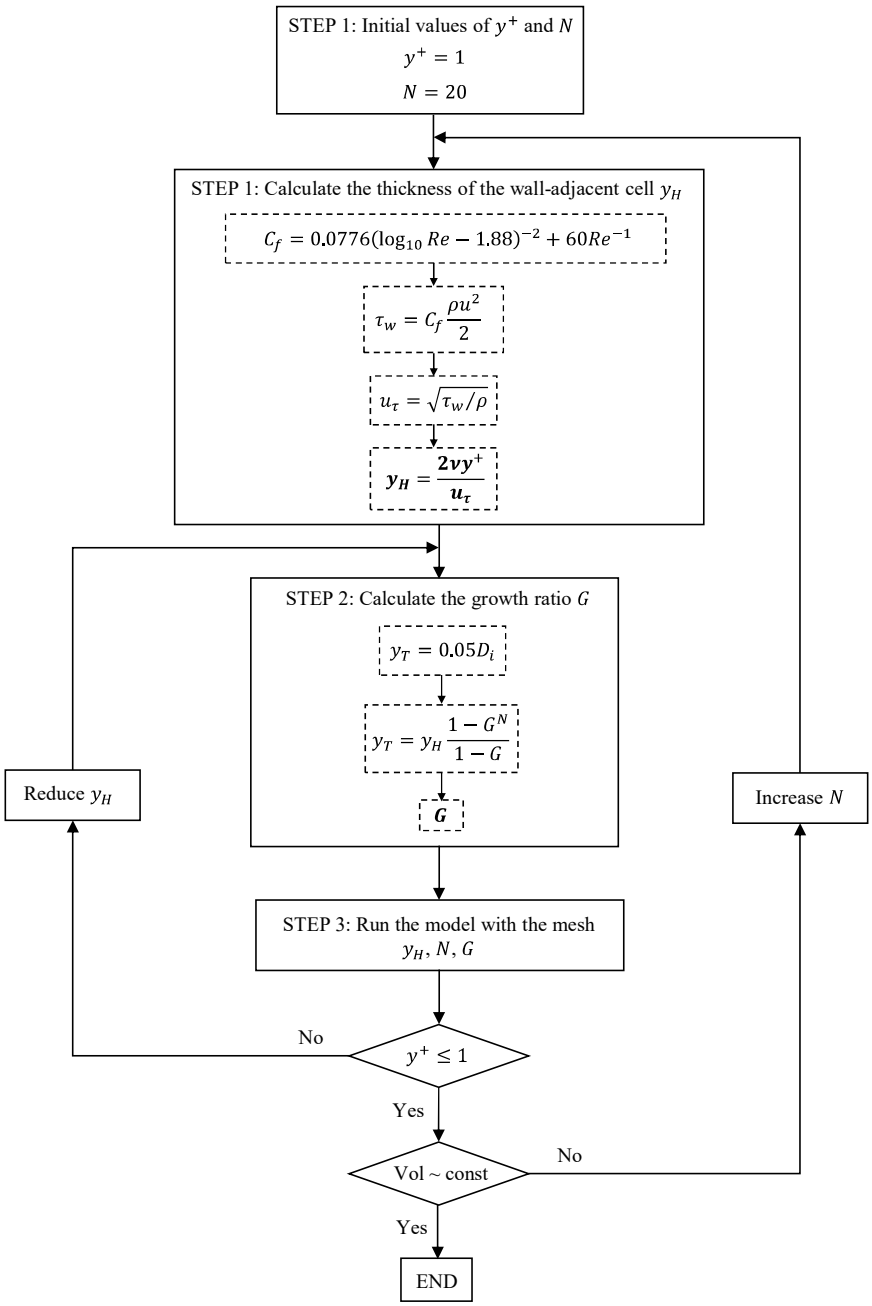

Fig. 5.19. Iterative procedure for the calculation of the wall inflation layers.

The iterative procedure for designing wall inflation layers is presented in Fig. 5.19. The method starts from the desired maximum value of $y^+$and the approximate total number of cells N; which is usually greater than or equal to 20 for y^+ values less than 30.

From the definition of y^+, an initial value of the first inflation layer thickness y_H is calculated, where the friction velocity, u_τ, may initially be estimated from the wall shear stress τ_w, which is calculated from the skin friction coefficient C_f by using an empirical correlation for turbulent flows [212]. The second step is to calculate the growth rate G, which denotes the constant ratio between the thickness of two adjacent inflation cells. For this, it was assumed that the total thickness of the N inflation layers y_T, defined as follows:

$$y_T = \sum_{k=0}^{N-1} y_H G^k = y_H \frac{1-G^N}{1-G}, \tag{5.13}$$

is greater than or equal to the boundary layer thickness. This ensures that the gradients within the boundary layer are captured by the inflation layers. To guarantee this condition, it was assumed that y_T is 5% of the inner diameter of the pipe. Once a first value of y_H, N and G was obtained, the model was executed to verify if: (i) $y^+ \leq 1$ and (ii) the volume of the last inflation cell is similar to that of the central section cells, and thus the volume transition between layers is smooth. If (i) is not satisfied, y_H is reduced, and if (ii) is not met, N is increased. This procedure was repeated until all requirements necessary to capture wall effects were fulfilled.

5.2.2 Governing equations and turbulence modeling

The computational model is based on the steady-state conservative differential Navier-Stokes equations of fluid motion [212], which expressed in mute subindex notation, result in:

continuity equation:

$$\frac{\partial}{\partial x_i}(\rho u_i) = 0 \tag{5.14}$$

momentum equation:

$$\frac{\partial}{\partial x_j}\left(\rho u_i u_j\right) = -\frac{\partial p}{\partial x_i} + \frac{\partial \tau_{ij}}{\partial x_j} + \rho g_i \tag{5.15}$$

with

$$\tau_{ij} = \mu\left(\frac{\partial u_i}{\partial x_j} + \frac{\partial u_j}{\partial x_i} - \frac{2}{3}\delta_{ij}\frac{\partial u_k}{\partial x_k}\right). \tag{5.16}$$

energy equation:

$$\frac{\partial}{\partial x_j}\left(\rho u_j H\right) = \frac{\partial}{\partial x_j}\left(\lambda \frac{\partial T}{\partial x_j}\right) + \frac{\partial}{\partial x_j}\left(u_i \tau_{ij}\right) \tag{5.17}$$

τ_{ij} in Eqs. (5.15) and (5.17) represents the viscous stress tensor, which is related to the strain rate tensor by the Stokes' hypothesis for Newtonian fluids, as shown in Eq. (5.16). Regarding body forces, only the force due to gravitational action was considered in the momentum equation. δ_{ij} is the Kronecker delta, which is $\delta_{ij} = 1$ if $i = j$, and $\delta_{ij} = 0$ if $i \neq j$. In the energy equation, H denotes the stagnation enthalpy, which represents the sum of the specific static enthalpy and the specific kinetic energy of the fluid. The first term on the right-hand side of the energy equation represents the diffusive heat transport, and the second term denotes heat transport by viscous dissipation.

Eqs. (5.14) - (5.17) describe the motion of a compressible fluid flow, both in laminar and turbulent regime. While laminar flows behave in a smooth and orderly fashion, turbulent flows (as is mainly the case) are characterized by the appearance of chaotic rotational flow structures, called eddies, which intensify the transport of momentum and energy by intensely mixing initially separated fluid regions. Those eddies are present over wide space and time scales, which may be extremely small, resulting in rapid fluctuations of the flow variables around an average value. To capture such small-scale fluctuations with the instantaneous equations of motion would demand too computationally expensive simulations. Instead, the governing equations are time-averaged to absent small scales, resulting in a set of equations that are much less expensive to solve.

For fluid flows in which density variations are significant, as is the case for heated supercritical fluid flows, Reynolds averaging [213] is employed for density and pressure, and Favre averaging [214] for all other variables such as velocity, temperature, enthalpy … . In Reynolds averaging, instantaneous variables are decomposed into a time-averaged component and a fluctuating component, which varies around the time-averaged value. For example, considering the density:

$$\rho = \bar{\rho} + \rho', \tag{5.18}$$

where ρ is the instantaneous density, $\bar{\rho}$ is the Reynolds time-averaged density component and ρ' is the fluctuating density component. The time-averaged density component $\bar{\rho}$ is calculated as follows:

$$\bar{\rho} = \lim_{T\to\infty} \frac{1}{T} \int_t^{t+T} \rho \, dt, \tag{5.19}$$

with $T \to \infty$, which means that the integration time interval, T, is larger compared to the typical time scales of turbulent fluctuations. Hence, the time-averaging of the

fluctuating component is zero. Favre's decomposition uses a density-weighted average, e.g. for the *x*-component of the velocity:

$$u_x = \tilde{u}_x + u_x'', \tag{5.20}$$

where $\tilde{u}_x$ is the Favre-averaged velocity component and u_x'' is the fluctuating velocity component. The time-averaged component is determined as:

$$\tilde{u}_x = \frac{\overline{\rho u_x}}{\bar{\rho}} \tag{5.21}$$

By decomposing the instantaneous magnitudes in the motion equations (Eqs. (5.14) - (5.17)) into their respective time-averaged and fluctuating components according to the Reynolds and Favre decompositions, and applying time-averaging to the resulting equations, the Favre- and Reynolds-averaged Navier-Stokes equations were obtained as follows [215]:

$$\begin{aligned} \frac{\partial}{\partial x_i}(\bar{\rho}\tilde{u}_i) &= 0 \\ \frac{\partial}{\partial x_j}(\bar{\rho}\tilde{u}_i\tilde{u}_j) &= -\frac{\partial \bar{p}}{\partial x_i} + \frac{\partial}{\partial x_j}\left(\tilde{\tau}_{ij} - \bar{\rho}\widetilde{u_i''u_j''}\right) + \bar{\rho}g_i \\ \frac{\partial}{\partial x_j}(\bar{\rho}\tilde{u}_j\tilde{H}) &= \frac{\partial}{\partial x_j}\left(\lambda\frac{\partial \tilde{T}}{\partial x_j} - \bar{\rho}\widetilde{u_j''h''}\right) + \frac{\partial}{\partial x_j}\left[\tilde{u}_i\left(\tilde{\tau}_{ij} - \bar{\rho}\widetilde{u_i''u_j''}\right)\right]. \end{aligned} \tag{5.22}$$

The components of the viscous stress tensor $\tilde{\tau}_{ij}$ are evaluated by Eq. (5.16) using the Favre-averaged velocity components. In the momentum and energy equations, $\tilde{\tau}_{ij}$ is extended by the turbulent stress tensor, $\bar{\rho}\widetilde{u_i''u_j''}$, which represents the additional momentum transport caused by turbulent fluctuations, and is modeled by the Boussinesq's turbulent viscosity hypothesis [216] as:

$$\bar{\rho}\widetilde{u_i''u_j''} = \mu_t\left(\frac{\partial \tilde{u}_i}{\partial x_j} + \frac{\partial \tilde{u}_j}{\partial x_i} - \frac{2}{3}\delta_{ij}\frac{\partial \tilde{u}_k}{\partial x_k}\right) - \frac{2}{3}\bar{\rho}\tilde{k}\delta_{ij}, \tag{5.23}$$

where μ_t is the turbulent viscosity and k is the turbulent kinetic energy. In (5.22), the term $\bar{\rho}\widetilde{u_j''h''}$ denotes the turbulent transport of heat, which is modeled by the Reynolds analogy [217] as follows:

$$\bar{\rho}\widetilde{u_j''h''} = -\lambda_t\frac{\partial \tilde{T}}{\partial x_j}, \tag{5.24}$$

with the turbulent thermal conductivity $\lambda_t = c_p\mu_t/Pr_t$. Pr_t represents the turbulent Prandtl number, which is constant within the flow field ($Pr_t = 0.85$).

In order to solve the averaged governing equations (Eqs. (5.22) - (5.24)), turbulence models are employed to capture the effects of turbulent fluctuations on the average flow. There are essentially three approaches: (i) first-order closures, (ii) large eddy simulation (LES) [218] and (iii) direct numerical simulation (DNS) [219]. First-order closures are based on the averaged Navier-Stokes equations and the Boussinesq's hypothesis, modeling the turbulent viscosity, μ_t, as a function of the averaged flow variables by adding scalar transport equations for turbulent quantities to the equations of motion. LES methods filter the Navier-Stokes equations to evaluate directly with the computational mesh the contributions to momentum and heat transfer from the large-scale high-energy transport eddies, employing models for the small-scale low-energy structures. The DNS technique refines the mesh sufficiently such that the instantaneous Navier-Stokes equations can be computed capturing the effects of both large- and small- scale turbulent structures. LES and DNS method are computationally expensive, so first-order closures are commonly employed in turbulent modeling of supercritical fluid flows in simple geometries.

The most well-known first-order turbulence models are the two equation k-ε and k-ω models, which include a transport equation for k, and for the turbulence dissipation rate ε, or the specific dissipation rate ω, respectively. These models, called high-Reynolds-number models, are valid exclusively in entirely turbulent flow regions, Near the wall, with viscous effect becoming dominant, these models do not lead to acceptable predictions. Thus, the following wall treatment strategies are used: (i) universal wall functions, or (ii) low-Reynolds-number models [220]. In the first case, the behavior of the fluid in the wall-adjacent cell, which may fall within the viscous or turbulent sublayer, is predicted on the basis of laws of the wall. In contrast, low-Reynolds-number models are integrated up to the wall, and use damping functions for turbulent quantities to account for the increasing importance of viscous effects as the wall is approached. Since the near-wall region is computed by the mesh, the resolution near the wall must be high to capture the strong gradients of the fluid variables. Very fine near-wall cells require small sizes in the axial direction to maintain low aspect ratios and mesh skewness, leading to significantly higher mesh density than when wall functions are used. However, this approach yields more accurate results, particularly for capturing buoyancy effects in turbulent supercritical fluid flows.

In this work, the following turbulence models were evaluated versus experimental heat transfer data to compare their performance: the high-Reynolds-number renormalization group (RNG) k-ε model [221], three low-Reynolds-number k-ε turbulence models of Launder-Sharma (LS) [222], Yang-Shih (YS) [223] and Abe-Kondoh-Nagano (AKN) [224], and the Shear Stress Transport k-ω turbulence model (SST k-ω) [225].

The k-ε turbulence equations for the various models can be expressed in a generic form:

Turbulent kinetic energy k:

$$\frac{\partial}{\partial x_i}\left[\bar{\rho}\tilde{k}\tilde{u}_i - \left(\mu + \frac{\mu_t}{\sigma_k}\right)\frac{\partial \tilde{k}}{\partial x_i}\right] = P_k + G_k - \bar{\rho}\tilde{\varepsilon} + \bar{\rho}D \tag{5.25}$$

Turbulent dissipation rate ε:

$$\frac{\partial}{\partial x_i}\left[\bar{\rho}\tilde{\varepsilon}\tilde{u}_i - \left(\mu + \frac{\mu_t}{\sigma_\varepsilon}\right)\frac{\partial \tilde{\varepsilon}}{\partial x_i}\right] = (C_{\varepsilon 1}f_1 P_k + C_{\varepsilon 1}C_{\varepsilon 3}G_k - C_{\varepsilon 2}f_2\bar{\rho}\tilde{\varepsilon})\frac{\tilde{\varepsilon}}{\tilde{k}} + \bar{\rho}E \tag{5.26}$$

where the term P_K represents the production of k,

$$P_k = \mu_t\left(\frac{\partial \tilde{u}_i}{\partial x_j} + \frac{\partial \tilde{u}_j}{\partial x_i}\right)\frac{\partial \tilde{u}_i}{\partial x_j}. \tag{5.27}$$

The simple Gradient Diffusion Hypothesis (SGDH) [226] is employed to account for the direct effect of buoyancy on turbulence G_k,

$$G_k = \beta g_i \frac{\mu_t}{Pr_t}\frac{\partial \tilde{T}}{\partial x_i}. \tag{5.28}$$

The turbulent viscosity is computed as:

$$\mu_t = \frac{C_\mu f_\mu \bar{\rho}\tilde{k}^2}{\tilde{\varepsilon}}. \tag{5.29}$$

Constants, expressions and damping functions are shown in Table 5.2.

Table 5.2. Coefficients and damping functions of the RNG k-ε model and LS, YS, AKN low-Re k-ε models.

Model	C_μ	$C_{\varepsilon 1}$	$C_{\varepsilon 2}$	σ_k	σ_ε	D	E
(a) Constants used in the turbulence models, D and E terms							
RNG k-ε	0.085	1.42 - $\frac{\eta(1-\eta/4.38)}{1+0.015\eta^3}$	1.68	0.7179	0.7179	0	0
LS	0.09	1.44	1.92	1.0	1.3	$2\nu\left(\frac{\partial\sqrt{\tilde{k}}}{\partial y}+\frac{\partial\sqrt{\tilde{k}}}{\partial x}\right)^2$	$2\nu\nu_t\left[\left(\frac{\partial^2\tilde{v}}{\partial x^2}\right)^2+\left(\frac{\partial^2\tilde{u}}{\partial y^2}\right)^2\right]$
YS	0.09	1.44	1.92	1.0	1.3	0	$2\nu\nu_t\left[\left(\frac{\partial^2\tilde{v}}{\partial x^2}\right)^2+\left(\frac{\partial^2\tilde{u}}{\partial y^2}\right)^2\right]$
AKN	0.09	1.50	1.90	1.4	1.4	0	0

Model	f_μ	f_1	f_2
(b) Functions used in the turbulence models			
RNG k-ε	1.0	1.0	1.0
LS	$\exp\left[\frac{-3.4}{(1+Re_t/50)^2}\right]$	1.0	1 - 0.3exp$(-Re_t^2)$
YS	$\left(1+\frac{1}{\sqrt{Re_t}}\right)\left[1-\exp\begin{pmatrix}-1.5\times10^{-4}Re_y\\-5.0\times10^{-7}Re_y^3\\-1.0\times10^{-10}Re_y^5\end{pmatrix}\right]^{0.5}$	$\frac{\sqrt{Re_t}}{1+\sqrt{Re_t}}$	$\frac{\sqrt{Re_t}}{1+\sqrt{Re_t}}$
AKN	$\left\{1-\frac{5}{Re_t^{0.75}}\exp\left[-\left(\frac{Re_t}{200}\right)^2\right]\right\}\left[1-\exp\left(-\frac{y^*}{14}\right)\right]^2$	1.0	$\left\{1-0.3\exp\left[-\left(\frac{Re_t}{6.5}\right)^2\right]\right\}\left[1-\exp\left(-\frac{y^*}{3.1}\right)\right]^2$

Note: $\eta = S\tilde{k}/\tilde{\varepsilon}$, $S = \left(2\tilde{S}_{ij}\tilde{S}_{ij}\right)^{0.5}$, $\tilde{S}_{ij} = \frac{1}{2}\left(\frac{\partial\tilde{u}_i}{\partial x_j}+\frac{\partial\tilde{u}_j}{\partial x_i}\right)$, $Re_t = \frac{\tilde{k}^2}{\nu\tilde{\varepsilon}}$, $Re_y = \frac{y\tilde{k}^{0.5}}{\nu}$, $y^* = \frac{y}{\nu}u_\varepsilon$, $u_\varepsilon = (\nu\tilde{\varepsilon})^{0.25}$.

The SST k-ω turbulence model includes the following transport equations:

Turbulent kinetic energy k:

$$\frac{\partial}{\partial x_i}\left[\bar{\rho}\tilde{k}\tilde{u}_i - \left(\mu + \frac{\mu_t}{\sigma_k}\right)\frac{\partial \tilde{k}}{\partial x_i}\right] = G_k - Y_k + S_k \tag{5.30}$$

Specific dissipation rate ω:

$$\frac{\partial}{\partial x_i}\left[\bar{\rho}\tilde{\omega}\tilde{u}_i - \left(\mu + \frac{\mu_t}{\sigma_\omega}\right)\frac{\partial \tilde{\omega}}{\partial x_i}\right] = G_\omega - Y_\omega + D_\omega + S_\omega \tag{5.31}$$

where the term P_k represents the production of k, the term P_ω represents the generation of ω, the term Y_k and Y_ω denotes the dissipation of k and ω due to turbulence, the term D_ω represents the cross-diffusion term, and the terms S_k and S_ω are user-defined source terms. Turbulent viscosity is computed as:

$$\mu_t = \frac{\rho k}{\omega}\frac{1}{\max\left[\frac{1}{\alpha^*}, \frac{SF_2}{a_1\omega}\right]}. \tag{5.32}$$

All constants and expressions of the SST k-ω model are shown in Table 5.3.

Table 5.3. Details of the SST k-ω turbulence model.

(a) Model parameters

G_k	G_ω	Y_k	Y_ω	D_ω
$\min\left[\mu_t\left(\frac{\partial \tilde{u}_i}{\partial x_j}+\frac{\partial \tilde{u}_j}{\partial x_i}\right)\frac{\partial \tilde{u}_i}{\partial x_j},\ 10\bar{\rho}\beta^*\tilde{k}\tilde{\omega}\right]$	$\frac{\alpha}{\nu_t}G_k$	$\bar{\rho}\beta^*\tilde{k}\tilde{\omega}$	$\bar{\rho}\beta\tilde{\omega}^2$	$2(1-F_1)\bar{\rho}\sigma_{\omega,2}\frac{1}{\tilde{\omega}}\frac{\partial \tilde{k}}{\partial x_j}\frac{\partial \tilde{\omega}}{\partial x_j}$

σ_k	σ_ω	F_1	F_2	Φ_1
$\left(\frac{F_1}{\sigma_{k,1}}+\frac{1-F_1}{\sigma_{k,2}}\right)^{-1}$	$\left(\frac{F_1}{\sigma_{\omega,1}}+\frac{1-F_1}{\sigma_{\omega,2}}\right)^{-1}$	$\tanh(\Phi_1^4)$	$\tanh(\Phi_2^4)$	$\min\left[\max\left(\frac{\sqrt{\tilde{k}}}{0.09\tilde{\omega}y}, \frac{500\mu}{\bar{\rho}y^2\tilde{\omega}}\right), \frac{4\bar{\rho}\tilde{k}}{\sigma_{\omega,2}D_\omega^+ y^2}\right]$

Φ_2	D_ω^+	α_∞	$\alpha_{\infty,1}$	$\alpha_{\infty,2}$
$\max\left(2\frac{\sqrt{\tilde{k}}}{0.09\tilde{\omega}y}, \frac{500\mu}{\bar{\rho}y^2\tilde{\omega}}\right)$	$\max\left(2\bar{\rho}\frac{1}{\sigma_{\omega,2}}\frac{1}{\tilde{\omega}}\frac{\partial \tilde{k}}{\partial x_j}\frac{\partial \tilde{\omega}}{\partial x_j}, 10^{-10}\right)$	$F_1\alpha_{\infty,1}+(1-F_1\alpha_{\infty,2})$	$\frac{\beta_{i,1}}{\beta_\infty^*}-\frac{\kappa^2}{\sigma_{\omega,1}\sqrt{\beta_\infty^*}}$	$\frac{\beta_{i,2}}{\beta_\infty^*}-\frac{\kappa^2}{\sigma_{\omega,2}\sqrt{\beta_\infty^*}}$

β_i
$F_1\beta_{i,1}+(1-F_1)\beta_{i,2}$

(b) Model constants

$\sigma_{k,1}$	$\sigma_{k,2}$	$\sigma_{\omega,1}$	$\sigma_{\omega,2}$	a_1	$\beta_{i,1}$	$\beta_{i,2}$	α_∞^*
1.176	1.0	2.0	1.168	0.31	0.075	0.0828	1
α_∞	α_0	β_∞^*	R_β	R_k	R_ω	ς^*	M_{t0}
0.52	1/9	0.09	8	6	2.95	1.5	0.25

5.2.3 Numeric strategies and boundary conditions

The finite volume-based commercial CFD software ANSYS Fluent 2023R1 [210] was used to computationally resolve the model. The finite volume method is based on three steps [227]: (i) discretization of the physical domain into discrete control volumes in a meshing procedure, (ii) integration of the fluid flow governing equations (Eqs. (5.22) - (5.24)) and turbulence equations over the control volumes and (iii) iterative resolution of

the resulting linear system of equations. Fig. 5.20 shows a generic hexahedral control volume that belongs to the three-dimensional mesh presented in section 5.2.1, in which the governing equations are discretized. The control volume is characterized by its centroid P, where the flow variables are stored, and the control surfaces north (n), south (s), west (w), east (e), top (t) and bottom (b). The centroids of the cells adjacent to P are called N, S, W, E, T and B, based on their relative positions x, y and z with respect to P.

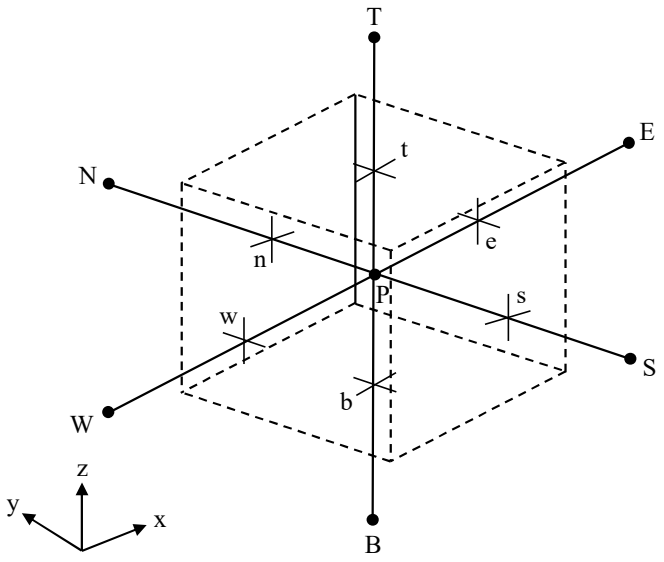

Fig. 5.20. Hexahedral control volume with centroid P. The centroids of the control volumes, adjacent to the control surfaces north (n), south (s), west (w), east (e), top (t) and bottom (b), are N, S, W, E, T and B, respectively.

The conservation equations can be written in a common form by introducing a generic intensive variable ϕ as follows:

$$\boldsymbol{\nabla} \cdot (\rho \phi \boldsymbol{u}) = \boldsymbol{\nabla} \cdot (\Gamma \boldsymbol{\nabla} \phi) + S_{\phi}, \tag{5.33}$$

where $\boldsymbol{\nabla}$ is the vectorial operator Nabla, which in a Cartesian coordinate system x, y, z is expressed as $\boldsymbol{\nabla} = \frac{\partial}{\partial x}\boldsymbol{e_x} + \frac{\partial}{\partial y}\boldsymbol{e_y} + \frac{\partial}{\partial z}\boldsymbol{e_z}$, and Γ is the diffusion coefficient. Substituting properly the terms ϕ and Γ results in the governing equations. The term $\boldsymbol{\nabla} \cdot (\rho \phi \boldsymbol{u})$ represents the net convective flux of ϕ (convective transport), the term $\boldsymbol{\nabla} \cdot (\Gamma \boldsymbol{\nabla} \phi)$ denotes the net diffusive flux of ϕ (diffusive transport), and the term S_{ϕ} represents the generation/destruction of quantity ϕ by sources/sinks. Integrating Eq. (5.33) over the control volume of Fig. 5.20, the following expression is obtained:

$$\sum_{\mathrm{f}=1}^{\mathrm{n_{faces}}} (\rho \phi \boldsymbol{u})_{\mathrm{f}} \boldsymbol{dA}_{\mathrm{f}} = \sum_{\mathrm{f}=1}^{\mathrm{n_{faces}}} (\Gamma \boldsymbol{\nabla} \phi)_{\mathrm{f}} \boldsymbol{dA}_{\mathrm{f}} + S_{\phi,P} \Delta V, \tag{5.34}$$

where the Gauss divergence theorem was applied, and surface integrals were substituted by sums over the control surfaces. Elaborating Eq. (5.34) over the six control surfaces of the control volume e, w, n, s, t and b:

$$\begin{gathered} F_e\phi_e - F_w\phi_w + F_n\phi_n - F_s\phi_s + F_t\phi_t - F_b\phi_b = \\ D_e(\phi_E - \phi_P) - D_w(\phi_P - \phi_W) + D_n(\phi_N - \phi_P) - \\ D_s(\phi_P - \phi_S) + D_t(\phi_T - \phi_P) - D_b(\phi_P - \phi_B) + S_{\phi,P}\Delta V. \end{gathered} \tag{5.35}$$

F represents the convective coefficient and D the diffusive coefficient. The gradients of the diffusive term, $(\boldsymbol{\nabla}\phi)_{\mathrm{f}}$, over the control volume faces are adequately discretized using the second-order centered differences. Nevertheless, the centered difference discretization scheme produces inconsistencies when applied to the convective terms over the control surfaces. This is because, while diffusion processes affect the distribution of the transported quantity in all directions along its gradients, convection spreads essentially in the flow direction. Then, assuming, for example, a fluid flow in the positive x-direction, the quantity ϕ_w would be more influenced by ϕ_W than ϕ_P. Therefore, the discretization schemes applied to the convective terms prioritize upstream flow quantities. In this work, the high-order discretization scheme by quadratic upward interpolation for convective kinetics (QUICK) [228] was employed for the convective terms in the momentum, energy, and turbulence equations. As shown in Fig. 5.21 for a one-dimensional domain, the QUICK scheme uses a three-point upward-weighted quadratic interpolation for the cell face values. The face value of ϕ is obtained from a quadratic function passing through two bracketing nodes (on each side of the face), and one node on the upstream side.

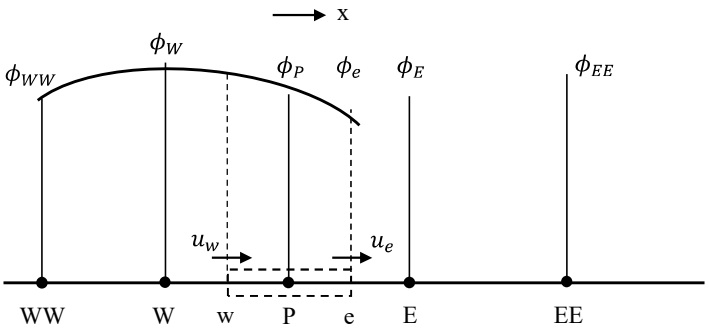

Fig. 5.21. Quadratic profiles used in the QUICK scheme in a one-dimensional domain

Hence, for a convective flux in the positive x-direction, the values of ϕ on surfaces w and e result in:

$$\phi_w = \frac{6}{8}\phi_W + \frac{3}{8}\phi_P - \frac{1}{8}\phi_{WW}, \tag{5.36}$$

$$\phi_e = \frac{6}{8}\phi_P + \frac{3}{8}\phi_E - \frac{1}{8}\phi_W. \tag{5.37}$$

The pressure gradient term was discretized with the 'body-force-weighted' scheme [229], which is especially appropriate when strong natural convective buoyancy forces are present. Applying the QUICK and 'body-force-weighted' discretization methods in Eq. (5.35), a linear expression, in the following format, was obtained:

$$a_P\phi_P = \sum_{nb} a_{nb}\phi_{nb} + b_P, \tag{5.38}$$

with nb denoting the centroids of the control volumes adjacent to P. The source term is normally evaluated at P. Therefore, a discretized linear equation, as presented in Eq. (5.38), was derived for each governing equation in each control volume in which the physical domain is discretized, resulting in a system of linear equations. Solving the system of equations should provide the velocity (u_x, u_y, u_z), temperature and pressure fields throughout the fluid domain.

Pressure is linked to the velocity components through the momentum equations in the x, y, z directions, however, it is not involved in a proper equation. Consequently, the coupling between pressure and velocity introduces an additional constraint to the flow field solving procedure: the applied pressure field should result, from the momentum equations, in the velocity field that satisfies continuity. Thus, the pressure-velocity coupling is solved by adopting an iterative solution strategy. There are several strategies for solving such a pressure-velocity linkage: SIMPLE, SIMPLER, SIMPLEC and PISO algorithms; although all of them are founded on the use of an equation for the correction pressure, that is derived from the continuity equation. These algorithms start by generating a guessed pressure field p^*, from which a guessed velocity field u_x^*, u_y^*, u_z^* is obtained from the discretized momentum equations $a_P u_{x,P}^* = \sum a_{nb}\, u_{x,nb}^* + (p_W^* - p_P^*)A_P + b_P$, $a_P u_{y,P}^* = \sum a_{nb}\, u_{y,nb}^* + (p_S^* - p_P^*)A_P + b_P$ and $a_P u_{z,P}^* = \sum a_{nb}\, u_{z,nb}^* + (p_B^* - p_P^*)A_P + b_P$. Similarly, the correct velocity field u_x, u_y, u_z can be found from the correct pressure field p using discretized momentum equations $a_P u_{x,P} = \sum a_{nb}\, u_{x,nb} + (p_W - p_P)A_P + b_P$, $a_P u_{y,P} = \sum a_{nb}\, u_{y,nb} + (p_S - p_P)A_P + b_P$ and $a_P u_{z,P} = \sum a_{nb}\, u_{z,nb} + (p_B - p_P)A_P + b_P$. Then, pressure and velocity correction terms p', u_x', u_y', u_z' are defined as the difference between the correct pressure and velocity fields and the guessed fields as follows:

$$p = p^* + p', \tag{5.39}$$

$$u_x = u_x^* + u_x', \tag{5.40}$$

$$u_y = u_y^* + u_y', \tag{5.41}$$

$$u_z = u_z^* + u_z'. \tag{5.42}$$

Subtracting the discretized momentum equations for the guessed "*" fields from those for the correct fields yields the discretized momentum equations for the correction fields $a_P u'_{x,P} = \sum a_{nb}\, u'_{x,nb} + (p'_W - p'_P)A_P + b_P$, $a_P u'_y = \sum a_{nb}\, u'_{y,nb} + (p'_S - p'_P)A_P + b_P$ and $a_P u'_{z,P} = \sum a_{nb}\, u'_{z,nb} + (p'_B - p'_P)A_P + b_P$; which substituted in Eqs. (5.40) - (5.42) derive expressions for the correct velocity field as a function of the guessed velocity field and the correction pressure. Finally, substituting these expressions into the discretized continuity equation results in a discretized equation for the pressure correction $a_P p'_P = \sum a_{nb} p'_{nb} + b_P$. The resolution of this equation provides the correction terms that are applied to the guessed velocity field to generate the updated correct velocity field, which is further employed as the starting point for the next iteration.

In this work, the SIMPLEC algorithm [230] was adopted for solving the system of linear equations of flow field to deal with the pressure-velocity coupling. Fig. 5.22 shows the SIMPLEC algorithm for a compressible flow and a k-ε turbulence model. First, guessed values of pressure, velocity, turbulent quantities and temperature fields are initialized in the whole domain. The discretized momentum equations and the pressure correction equation are solved to update the guessed velocity field and to generate the correction pressure. Then, the correct pressure and velocity fields are updated and used to solve the rest of discretized scalar transport equations corresponding to the conservation of energy (temperature), turbulent kinetic energy and turbulent dissipation rate. If the convergence is achieved, the iterative procedure is terminated, and the flow field is found. Otherwise, the correct quantities obtained in the current iteration are adopted as guessed quantities in the next iteration. The solutions of the systems of equations in steps 1, 2 and 4 are found using the under-relaxed Gauss-Seidel method in conjunction with an algebraic multigrid method (AGM) [231].

It was assumed that the convergence criterion for the termination of the calculations requires that the residuals of all monitored variables, corresponding to the continuity, momentum, energy, turbulent kinetic energy and turbulent dissipation rate to be less than 10^{-6}. The residual of a generic variable ϕ is defined as follows:

$$R_\phi = \frac{\sum_{cells\ P} |\sum_{nb} a_{nb}\phi_{nb} - b_P - a_P\phi_P|}{\sum_{cells\ P} |a_P\phi_P|} \tag{5.43}$$

In addition, it was verified that there were no observable changes in the fluid temperature at the outlet and at several surface locations, and that the mass flux at the outlet was identical to that at the inlet.

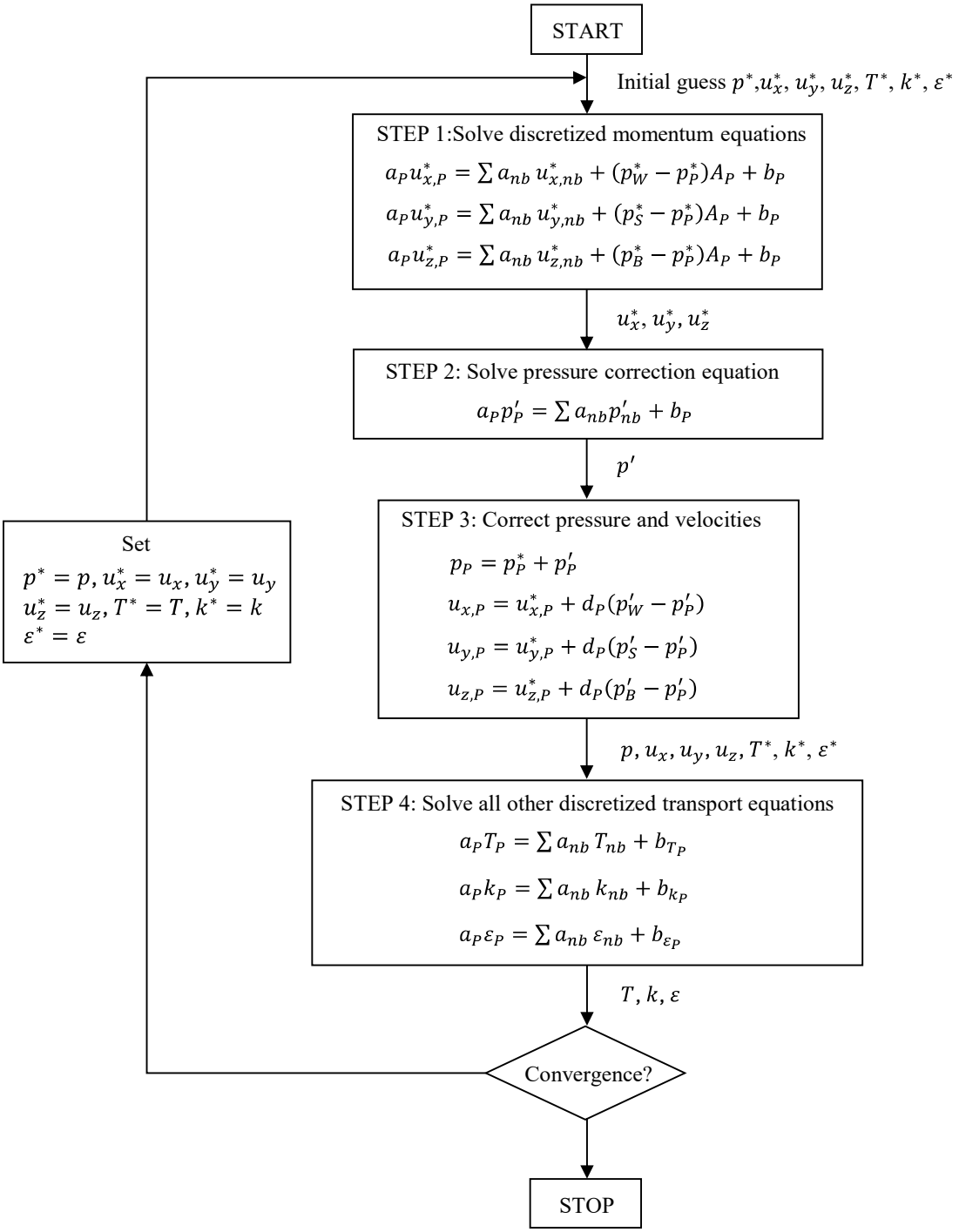

Fig. 5.22. The SIMPLEC algorithm.

The boundary conditions applied to solve the model are shown in Table 5.4. The mass flow and the distribution of temperature and turbulent quantities must be provided at the inlet mass flow boundary condition to the fluid domain. A uniform distribution of all fluid quantities was assumed, where the distributions of k, ε and ω are determined according to Eqs. (5.44) - (5.46), respectively [232].

$$k = \frac{3}{2}(U_{in}TI_{in})^2 \tag{5.44}$$

$$\varepsilon = C_{\mu}^{3/4}\frac{k^{3/2}}{0.07D_{ti}} \tag{5.45}$$

$$\omega = \frac{\sqrt{k}}{C_{\mu}^{1/4}0.07D_{ti}} \tag{5.46}$$

TI represents the turbulence intensity, which takes a value of 5% and U_{in} the inlet velocity, which is computed using the continuity integral equation and the tube internal diameter, D_{ti}, the fixed inlet mass flow and fluid density at the inlet temperature and operating pressure. At the outlet, the gauge pressure is specified and the gradient of the rest of fluid variables is assumed to be zero, i.e., $\partial\phi/\partial x|_{x=L} = 0$ (zero-gradient condition). On the symmetry boundary, the applying condition is that the velocity normal to the surface is zero. Moreover, the gradient of all other fluid quantities normal to the surface are zero. In the adiabatic and heated walls, the no-slip condition applies, so all velocity components are zero at the wall. When high-Reynolds number turbulence models are used, model equations are integrated right up to the near-wall region and universal laws of wall are used. Thus, if the centroid P of the wall-adjacent cell falls either in the viscous sublayer ($y_P^+ < 5$), or in the turbulent sublayer ($30 < y_P^+ < 200$), universal wall laws are applied to compute the wall-parallel velocity u_P^+, the temperature T_P^+, and turbulent quantities k_P^+, ε_P^+, ω_P^+ at the centroid P [233]. In the buffer sublayer, $5 < y_P^+ < 30$, it is not appropriate to place the wall-adjacent cell because the large uncertainty of the universal wall laws. y_P^+ represents the dimensionless distance to the centroid P of the wall-adjacent cell from the tube wall,

$$y_P^+ = \frac{y_P u_\tau}{\nu}, \tag{5.47}$$

where $u_\tau = \sqrt{\tau_w/\rho}$ denotes the friction velocity. In the case where low-Reynolds number turbulence models are used, model equations are integrated over the entire fluid domain, including the wall region. Thus, no universal wall laws are used. Instead, turbulent quantities are damped as $y_P^+ \to 0$ by using damping functions to denote the domain of viscous effects over turbulent effect in that region. In the adiabatic wall the heat flux is set at zero, while in the heated wall it is non-zero and positive (inward to the fluid flow). Since heat transport in the wall-adjacent fluid takes place mainly by diffusive action, the heat flux boundary condition is treated as a temperature gradient at wall.

The thermodynamic properties and transport coefficients of $scCO_2$ were taken from the NIST Refprop Standard Reference Database [207].

Table 5.4. Boundary conditions of the CFD model.

Boundary	B.C's
Fluid inlet	Mass flow inlet
Fluid outlet	Pressure outlet
Adiabatic wall	Wall (with zero heat flux)
Heated wall	Wall (with non-zero heat flux)

5.2.4 Mesh independence test

To check the mesh independence of the results, a mesh sensitivity study was carried out using five meshes. The inflation layer within the boundary layer, especially the thickness of the first layer, were adapted accordingly to respect the constraint of $y^+ < 0.5$. The pressure drop in the tube, and the outlet fluid temperature, were considered as output variables during the sensitivity study. Table 5.5 lists the size of the meshes and shows the pressure drop and outlet fluid temperature calculated with each mesh. Considering a deviation in both variables of less than 1% as a criterion for choosing the mesh size, the mesh with 1,242,582 elements was selected as the baseline for the rest of the numerical study.

Table 5.5. Mesh sensitivity study of the numerical CFD model based on the operating conditions of T3 (see Table 5.1).

Mesh	Number of cells	Pressure drop Δp (kPa)	Outlet fluid temperature T_{out} (ºC)	% Error Δp	% Error T_{out}
1	250,125	22.103	58.89	8.71	0.33
2	607,250	20.929	58.98	2.93	0.18
3	1,242,582	20.275	59.02	0.29	0.11
4	2,826,202	20.266	59.06	0.33	0.04
5	5,459,788	20.333	59.085	0.00	0.00

For the selected mesh size, the near-wall inflation layers were calculated according to the algorithm illustrated in Fig. 5.19. The skin friction coefficient, C_f, was calculated for the maximum Reynolds number that was experimentally attained in the T5 test (see Table 5.1), 23847.4. The higher the Reynolds number, the thinner the boundary layer. Thus, this Reynolds number selection ensures that the design constraints of the inflation layers are satisfied under all simulation scenarios. The algorithm resulted in 20 inflation layers with a first layer thickness y_H of $5.5 \cdot 10^{-4}$ mm and a growth rate G of 1.129. Fig. 5.23 proves, after the last model run, that the value of y^+ resulted lower than 0.24 for the adiabatic and heated tube walls of the physical model.

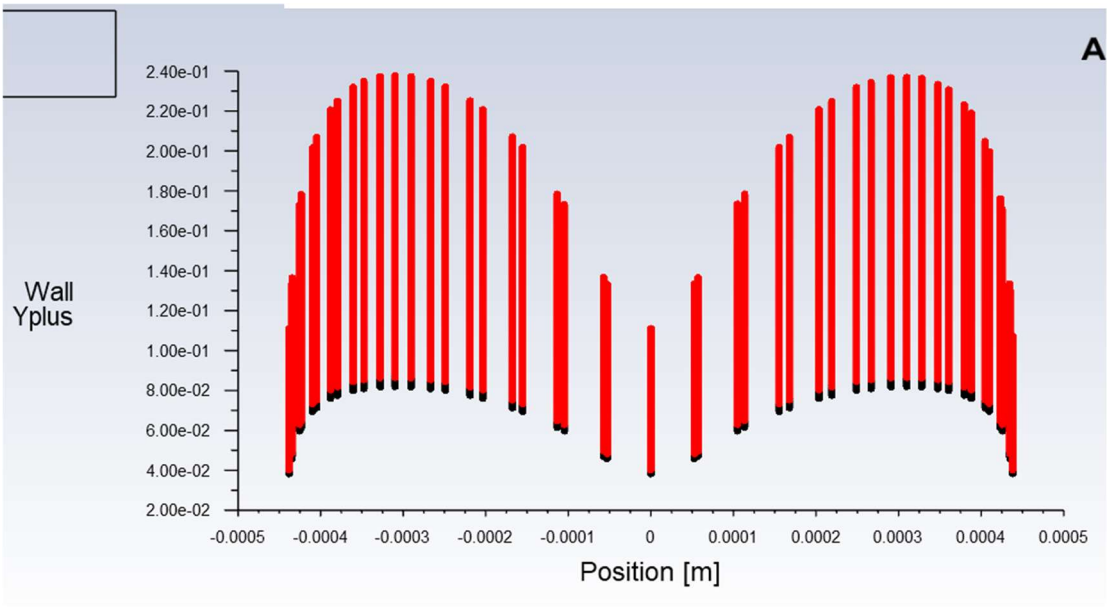

Fig. 5.23. Wall y+ in the adiabatic wall (●) and heated wall (●).

5.3 Correlational micro shell-and-tube heat exchanger modeling approach

In this chapter, the correlational thermal-hydraulic modeling of a MSTHE, for application in the condensative low-temperature section of the NET Power cycle recuperator, is presented. The operating conditions of the MSTHE are presented in Section 5.3.1. In Section 5.3.2, the geometric modeling, based on the base dimensional parameters of the MSTHE, is described. The governing equations of the thermal-hydraulic model are discussed in Section 5.3.3. Section 5.3.4 shows the iterative procedure for the numerical resolution of the model, and the applied boundary conditions.

To account for the variation of the supercritical fluid properties within the MSTHE, the exchanger was modeled in differential form. Therefore, the resulting system of ordinary differential equations was numerically integrated using an optimum discretization step. In Section 5.3.5, the optimal discretization step that balance between the computational error and computational time is found. Finally, Section 5.3.6 validates the heat and mass transfer models involved in the MSTHE modelling against global mass and energy balances performed in Aspen Plus.

5.3.1 Operating conditions

The basic configuration and cross-sectional view of the MSTHE, including its location within the low-temperature section of the RHE, is depicted in Fig. 5.24. In the low-temperature section, multiple streams exchange heat, as deduced from Fig. 5.24. In this

work, the heat exchange that takes place between the pressurized cold recirculation streams, RE-6, and the hot exhaust gases, FG-2b, was considered exclusively.

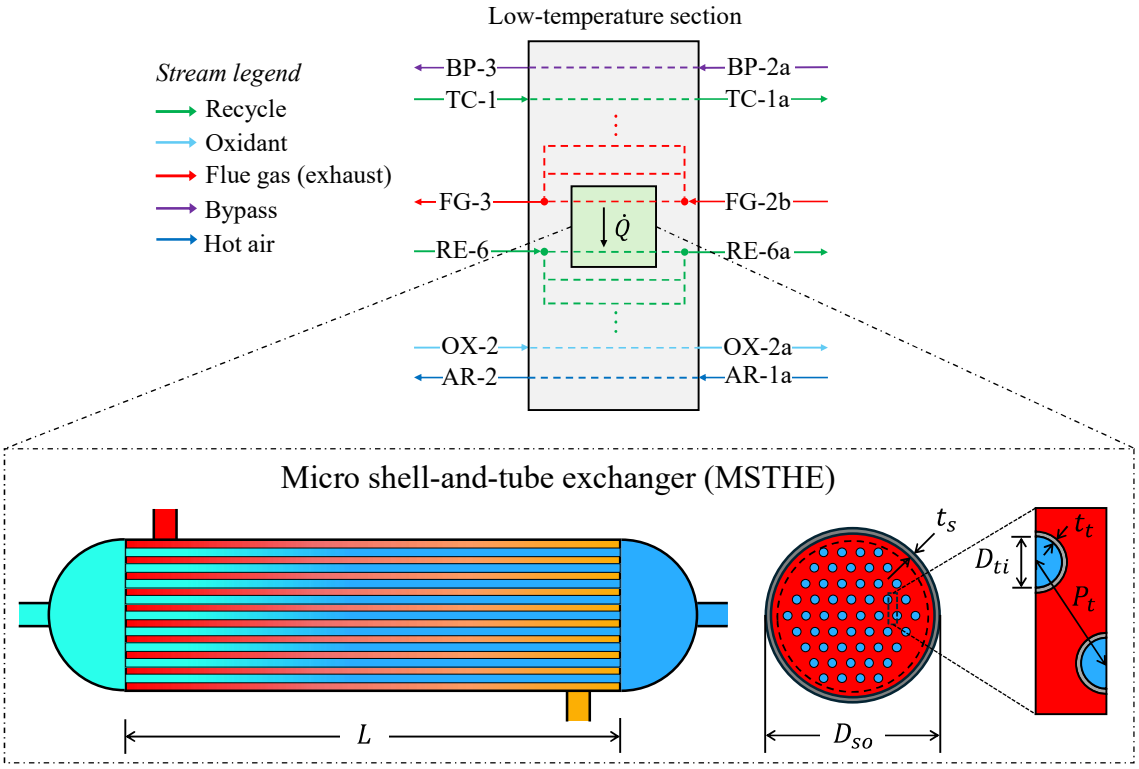

Fig. 5.24. Diagram of the base configuration and cross-sectional view of the MSTHE located in the low-temperature heat exchange section of the RHE.

According to the nominal operating conditions of the RHE of Table 4.11, the mass flow rates of FG-2b and RE-6 are 1315.93 kg·s^{-1} and 949.14 kg·s^{-1}, respectively [234]. The FG-2b flow rate was calculated as the FG-2 mass flow, 1484.75 kg·s^{-1} (Table 4.11), minus the percentage of the FG-2 flow that is recirculated to the bypass loop at the optimized nominal conditions, 11.37% (Table 4.10). A MSTHE of industrial standard dimensions, with a maximum number of tubes in a single bundle of ~ 80,000 [121], would not be able to transfer such mass flows, as it would incur unacceptably huge flow velocities and pressure drops. Therefore, FG-2b and RE-6 are split, and introduced into multiple parallel heat exchange trains, as noted from Fig. 5.24. To fix a basis for calculation, it was assumed that the maximum allowable flow velocity of a liquid through the exchanger tubes is 2.5 m·s^{-1} [235]. This limitation is also applicable to scCO$_2$ flows due to its liquid-like behavior within the supercritical regime. For an MSTHE of 65,000 microtubes of outer diameter 1.8 mm, and inner diameter 0.9 mm, a mass flow of 57.71 kg·s^{-1} of scCO$_2$, at 128 ºC and 278.49 bar, corresponds to a maximum velocity of about 2.5 m·s^{-1} through the tubes. Table 5.6 shows the nominal operating conditions of the MSTHE. T_h^{out}, T_c^{in}, p_h^{in}, p_c^{in} and $\hat{y}_{H_2O,h}^{in}$ were obtained in Table 4.11 from the simulation model in Aspen Plus for the optimized nominal conditions. The tube-side flow is assumed

to be pure scCO2 ($\hat{y}_{CO_2,c}$ = 1) Moreover, a MSTHE unit, exchanging a thermal power of 10 MW_{th}, was considered. This assumption resulted in a shell-side mass flow of 71.44 $kg \cdot s^{-1}$, as shown in Table 5.6.

Table 5.6. Nominal operating conditions of the MSTHE.

T_h^{in} (ºC)	138	T_h^{out} (ºC)	52.08
T_c^{in} (ºC)	44.40	T_c^{out} (ºC)	128
p_h^{in} (bar)	44.8	p_h^{out} (bar)	44.3
p_c^{in} (bar)	278.99	p_c^{out} (bar)	278.49
$\dot{m}_h^{in}$ (kg s^{-1})	71.44	$\dot{m}_c^{in}$ (kg s^{-1})	57.71
$\hat{y}_{H_2O,h}^{in}$ (%)	4.85	$\hat{y}_{CO_2,c}$	1

5.3.2 Base geometry parameters

A schematic diagram of the baseline configuration and cross-sectional view of the MSTHE are shown in Fig. 5.24. The MSTHE is composed by two inlet flanges, two outlet flanges, two headers, a straight single floating microtube bundle, and a perfectly insulated external shell. The floating tubesheet configuration allows axial expansion to avoid thermal loads. Since the thermal-hydraulic study of the MSTHE is focused on the low-temperature section of the RHE, the components are fabricated from SS316L [127,130]. Unlike conventional shell-and-tube heat exchangers, the MSTHE does not employ flow-guiding baffles, as the counterflow arrangement allows high heat transfer rates and prevents pressure drop from baffles [76]. The shell-side fluid enters and exists the exchanger perpendicular to the microtube bundle and flows in a counterflow direction relative to the tube-side flow, flowing along the MSTHE length through the remaining annular space between the shell and the tube bundle.

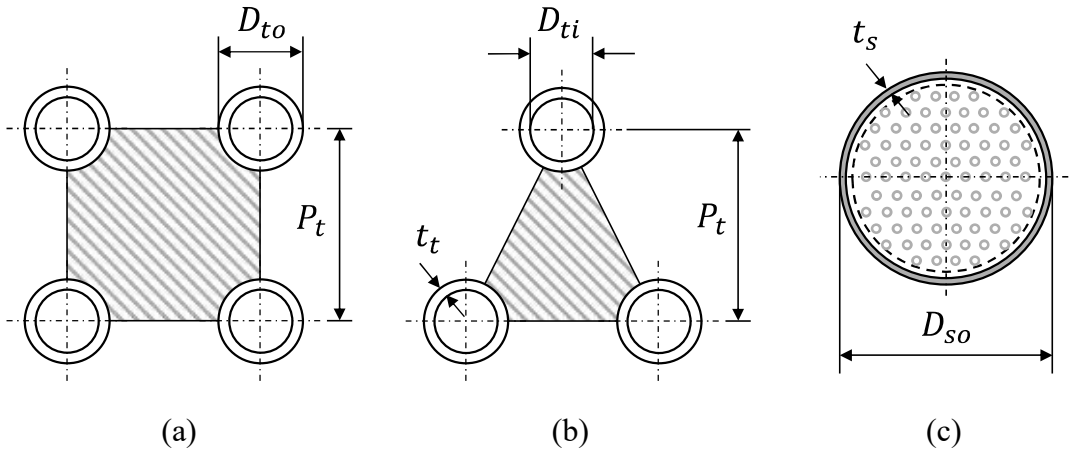

Fig. 5.25. Cross-sectional view of the MSTHE including square and triangle tube arrangements.

A cross-sectional view of the MSTHE showing a square and triangular tube arrangement is provided in Fig. 5.25. The key geometry parameters that characterize the MSTHE are: length of the tubes (L), number of tubes (N_t), inner diameter of the tubes (D_{ti}), tube wall thickness (t_t), outer diameter of tubes (D_{to}), distance between tubes (also known as "pitch", P_t), outer diameter of the shell (D_{so}), thickness of the shell (t_s), and inner diameter of the shell (D_{si}). Given N_t, D_{to}, P_t and the tube disposition (square or triangular), the geometry of the MSTHE is computed as follows [205]. D_{si} is calculated by Eq. (5.48); where CL is the tube layout constant, which is 1 for square layout and $\sqrt{3}/2$ for triangle layout; CTP is the constant (0.93 for a single pass) that considers the residual clearance space between the outer diameter of the tube bundle (represented by a dashed line in Fig. 5.25) and the inner diameter of the shell.

$$D_{si} = 2P_t \left[\frac{(CL)N_t}{\pi(CTP)}\right]^{0.5} \tag{5.48}$$

The hydraulic diameter, D_e, defined as 4 x free flow area / wetted perimeter, is the characteristic dimension used to compute the correlations for heat transfer, Eqs. (5.49) and (5.50), and pressure drop, Eqs. (5.51) and (5.52), for the non-circular cross-sectional shell-side flow [235].

$$D_{e,sq} = \frac{4(P_t^2 - \pi D_{to}^2/4)}{\pi D_{to}} \tag{5.49}$$

$$D_{e,tri} = \frac{4\left(\sqrt{3}\,P_t^2/4 - \pi D_{to}^2/8\right)}{\pi D_{to}/2} \tag{5.50}$$

$$D'_{e,sq} = \frac{4(P_t^2 - \pi D_{to}^2/4)}{\pi D_{to} + \pi D_{si}/N_t} \tag{5.51}$$

$$D'_{e,tri} = \frac{4\left(\sqrt{3}\,P_t^2/4 - \pi D_{to}^2/8\right)}{(\pi D_{to} + \pi D_{si}/N_t)/2} \tag{5.52}$$

The thickness of the tubes and the shell were evaluated by Eqs. (5.53) and (5.54), and the tubesheet thickness was calculated by Eqs. (5.55) - (5.57) employing the 11th TEMA Standard [236]. P_d is the design pressure; t_e, E, S, and Y are mechanical design parameters, for which values are shown in Table 5.7; F_{ts} = 1 for fixed and floating tubesheet; and k_e is the mean ligament efficiency.

$$t_t = t_{et} + \frac{P_{dt}D_{to}}{2(SE + P_{dt}Y)} \tag{5.53}$$

$$t_s = t_{es} + \frac{P_{ds} D_{si}}{2(SE + 0.6P_{ds})} \tag{5.54}$$

$$t_{ts} = \frac{F_{ts} D_{si}}{3} \left(\frac{P_d}{k_e S} \right)^{0.5} \tag{5.55}$$

$$k_{e,sq} = 1 - 0.785/(p_t/D_{to})^2 \tag{5.56}$$

$$k_{e,tri} = 1 - 0.907/(p_t/D_{to})^2 \tag{5.57}$$

Table 5.7. Mechanical design parameters of Eqs. (5.53) - (5.57).

	t_e (mm)	p_d (kPa)	S* (kPa)	E	Y	Reference
Tube	0.254	$1.05p_{c,in}$	$87.4 \cdot 10^3$	1.00	0.75	[237,238]
Shell	3.175	$p_{h,in}$+170 kPa	$87.4 \cdot 10^3$	0.85	-	[236]

* For a design temperature of 150 ºC.

5.3.3 Thermal-hydraulic modeling approach of the micro shell-and-tube heat exchanger

Fig. 5.26 presents the heat transfer model and control volumes, corresponding to the superheated and saturated regions, including the associated heat and mass fluxes, used in the derivation of the governing equations. The subscripts "c" and "h" refer to the tube-side cold scCO$_2$ and shell-side CO$_2$ – H$_2$O hot gas mixture, respectively. The hot gas mixture enters the shell side in a superheated vapor state. As it flows through the heat exchanger, the shell-side temperature, T_h, progressively decreases until the fluid in the near-wall region reaches the saturation temperature i.e., $T_{wo} = T_{sat}$. At this point, condensation of the vapor begins, along with small traces of dissolved CO$_2$, forming a H$_2$O-rich condensation film over the cooling tube walls [239,240], as illustrated in Fig. 5.26. The film thickness, δ, increases along the flow direction due to the continued condensation at the vapor-liquid interface. The inertia forces, resulting from the high velocity of the shell gas, are sufficient to: (i) prevent condensate droplets from falling due to gravitational action, and (ii) assume a constant film thickness in the tangential direction of the tube. Therefore, δ represents the circumferential average film thickness. This condensate layer introduces an additional thermal resistance, as the latent heat released during condensation must be conducted through the film before reaching the outer wall of the microtubes [241].

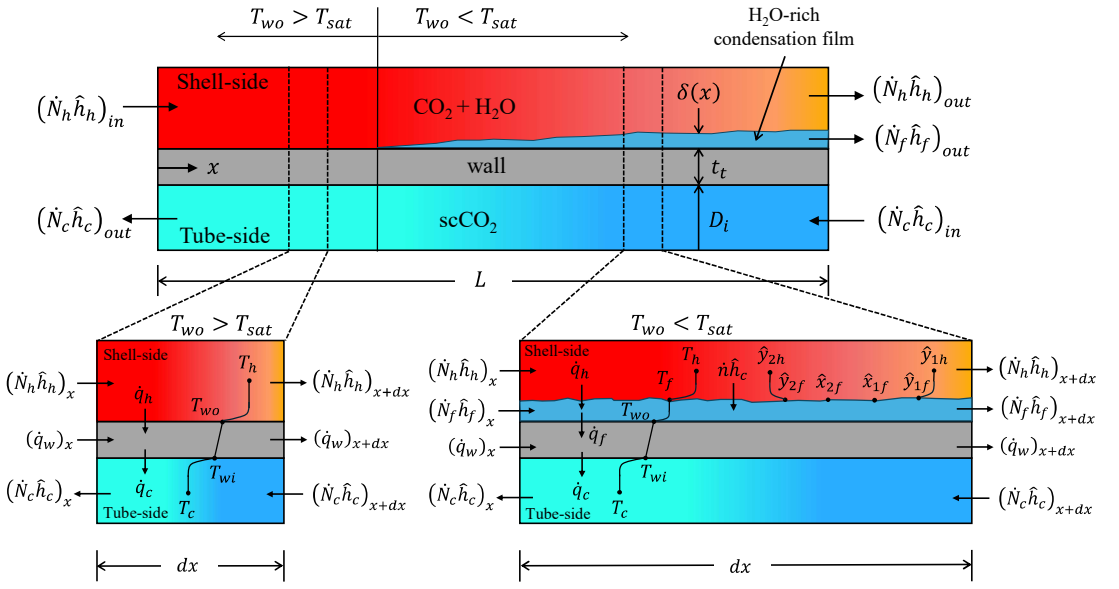

Fig. 5.26. Heat transfer model of the MSTHE and control volumes, including the energy and mass fluxes, for the deduction of the differential unidimensional governing equations for the superheated and saturated regions. Subscript "h" stands for hot-fluid (shell-side) and "c" for cold-fluid (tube-side). Subscript "1" refers to H_2O and "2" to CO_2.

The heat transfer mechanisms vary depending on whether the shell-side CO_2 – H_2O mixture is superheated or saturated. Consequently, the governing heat transfer equations are formulated separately for each condition. The following assumptions were adopted: (i) steady-state flow, (ii) Newtonian fluid behavior, (iii) negligible changes in kinetic and potential energy, and (iv) negligible axial heat conduction in the fluid phases (i.e., convection-dominated problem). This last assumption is justified despite the small hydraulic lengths, as the flow exhibits sufficiently high Peclet numbers. Due to the non-linear temperature and pressure dependence of the physical properties of the tube-side $scCO_2$, along with filmwise condensation occurring in the shell-side gas mixture, heat transfer in the MSTHE is inherently a local phenomenon. Therefore, the model equations were derived in differential form and numerically integrated along the flow path of the heat exchanger, following the shell-side flow direction (x-direction in Fig. 5.26). The discretized solution of the model requires local values of heat transfer coefficients, friction factors, and fluid properties. Local quantities are typically denoted using the subscript x, indicating their change along the axial direction of the heat exchanger. However, for notational simplicity, the subscript x was omitted in the expressions derived in the following sections.

5.3.3.1 Governing heat transfer equations

The mathematical modeling approach of the heat exchanger in the superheated region was derived from the mass and convective energy equations applied to the left-hand control volume plotted in Fig. 5.26.

Conservation of mass:

$$\frac{d\dot{N}_h}{dx} = 0, \tag{5.58}$$

$$\frac{d\dot{N}_c}{dx} = 0. \tag{5.59}$$

Conservation of energy in the shell-side fluid phase:

$$\dot{N}_h \frac{d\hat{h}_h}{dx} = -\alpha_h N_t \pi D_{to}(T_h - T_{wo}). \tag{5.60}$$

Conservation of energy in the microtube-side fluid phase:

$$\dot{N}_c \frac{d\hat{h}_c}{dx} = -\alpha_c N_t \pi D_{ti}(T_{wi} - T_c). \tag{5.61}$$

Conservation of energy in the solid phase:

$$\lambda_s A_c \frac{d^2 T_w}{dx^2} = \alpha_c \pi D_{ti}(T_{wi} - T_c) - \alpha_h \pi D_{to}(T_h - T_{wo}). \tag{5.62}$$

When the near-wall fluid reaches the saturation point (i.e., $T_{wo} < T_{sat}$), vapor begins to condense, forming a liquid film the envelops the outer surfaces of the microtubes. This new fluid phase, corresponding to the condensate layer, alters the heat and mass transfer mechanisms, and it was therefore incorporated into the governing equations. Equations describing the heat transfer between the condensing shell-side fluid and the tube-side scCO$_2$ were derived from the conservation of mass, chemical species (where subscript "1" denotes H$_2$O and "2" denotes CO$_2$), and energy applied to the right-hand control volume depicted in Fig. 5.26, These equations are complemented by kinetic theorems for heat and mass transfer.

Conservation of mass:

$$\frac{d\dot{N}_c}{dx} = 0, \tag{5.63}$$

$$\frac{d\dot{N}_f}{dx} = \dot{n} N_t \pi D_{to}, \tag{5.64}$$

$$\frac{d\dot{N}_h}{dx} = -\dot{n} N_t \pi D_{to}. \tag{5.65}$$

Conservation of chemical species:

$$\dot{N}_h = \dot{N}_{h1} + \dot{N}_{h2}, \tag{5.66}$$

$$\dot{n} = \dot{n}_1 + \dot{n}_2, \tag{5.67}$$

$$\frac{d\dot{N}_{f1}}{dx} = \dot{n}_1 N_t \pi D_{to}, \tag{5.68}$$

$$\frac{d\dot{N}_{h1}}{dx} = -\dot{n}_1 N_t \pi D_{to}. \tag{5.69}$$

Conservation of energy in the microtube-side fluid phase:

$$\dot{N}_c \frac{d\hat{h}_c}{dx} = -\alpha_c N_t \pi D_{ti}(T_{wi} - T_c). \tag{5.70}$$

Conservation of energy in the condensate film:

$$\dot{n} N_t \pi D_{to} \Delta\hat{h}_v(T_f) + \alpha_h E_T N_t \pi D_{to}(T_h - T_f) - \alpha_f N_t \pi D_{to}(T_f - T_{wo}) = 0. \tag{5.71}$$

Conservation of energy in the shell-side fluid phase:

$$\dot{N}_h \frac{d\hat{h}_h}{dx} = \dot{n} N_t \pi D_{to} \bar{\hat{c}}_{p,h}(T_h - T_f) - \alpha_h E_T N_t \pi D_{to}(T_h - T_f). \tag{5.72}$$

Conservation of energy in the solid phase:

$$\lambda_s A_c \frac{d^2 T_w}{dx^2} = \alpha_c \pi D_{ti}(T_{wi} - T_c) - \alpha_f \pi D_{to}(T_f - T_{wo}). \tag{5.73}$$

In Eqs. (5.58) - (5.72), $\dot{N}$ is the molar flow rate; $\hat{h}$ is the molar enthalpy; α_h, α_c and α_f are the individual convective heat transfer coefficients of the shell-side, tube-side and condensate film; T_h and T_c are the bulk temperatures of the shell- and tube- side fluids; T_f is the liquid film temperature; T_{wo} and T_{wi} are the shell-side and tube-side wall temperatures; λ_s is the thermal conductivity of SS316L, which was assumed to be constant and equal to 16 $W \cdot m^{-1} \cdot K^{-1}$; A_c is the cross-sectional area of the tube wall; $\dot{n}$ is the local condensing molar flux; $\Delta\hat{h}_v(T_F)$ is the molar latent heat of evaporation; δ is the condensate film thickness; and T_w is the bulk wall temperature. In the condensate film energy equation, expressed in Eq. (5.71), the molar enthalpy change of the liquid film was neglected. Hence, T_f was obtained from the iterative solution of Eq. (5.71). In Eqs. (5.63) - (5.73), δ was not considered to calculate the heat and mass transfer area because it is much smaller than the outer diameter of the tubes. The energy balance expressed in

Eq. (5.72) was used to calculate the bulk temperature of the shell-side gases, T_h, when it is above T_{sat}. Otherwise, T_h was set equal to T_{sat}. T_w was calculated by means of the wall thermal resistance network of Fig. 5.27 [120] by Eq. (5.74), where $r = (r_i + r_o)/2$. T_{wo} and T_{wi} were determined on the condition that, under steady-state conditions, the heat flow transported by convection in the fluid phases, and by conduction through the solid wall, must be equal.

$$T_w = \frac{\ln(r/r_i)\,T_{wo} + \ln(r_o/r)\,T_{wi}}{\ln(r_o/r_i)} \tag{5.74}$$

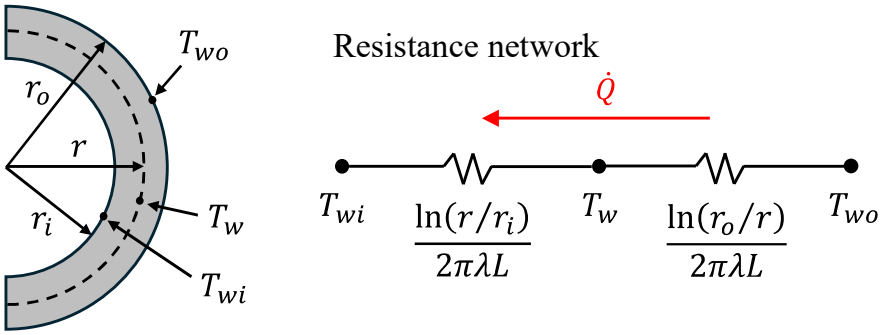

Fig. 5.27. Cross section of a half-tube and resistance network to determine the mean tube wall temperature T_w.

The condensate consists mainly of H_2O (subscript 1), because it is the only condensable molecule within the mixture. However, small traces of CO_2 (subscript 2) are dissolved in the aqueous liquid phase. The mole fraction of CO_2 in the H_2O-rich condensate phase is calculated at the vapor-liquid interface, at the temperature T_f, where the thermodynamic equilibrium was assumed to occur. For vapor-liquid equilibrium calculations, the LKP EoS, calibrated in Section 4.1, was employed.

Since the chemical equilibrium taking place between CO_2 and H_2O is of type iii [242], the mole fraction of CO_2 in the condensate is low [243]. As a result, CO_2 accumulates near the vapor-liquid interface, forming a concentration layer that acts as a mass transfer barrier. This accumulation hinders the direct contact between the vapor and the condensate surface, thereby reducing the efficiency of the condensation process. Before condensation can occur, water vapor must first diffuse through this gas-phase layer to reach the liquid film. Transport within the gas phase is predominantly convective, as indicated by high Peclet numbers characterizing the shell-side flow.

Based on the mole fraction gradients of H_2O and CO_2 in the gas phase (see Fig. 5.26), the local condensing molar flux was calculated using the following expression [244,245]:

$$\dot{n} = \hat{\rho}_h \theta_h \ln\left(\frac{\hat{x}_{1f} - \hat{y}_{1f}}{\hat{x}_{1f} - \hat{y}_{1h}}\right), \tag{5.75}$$

where θ_h is the convective mass transfer coefficient, whose calculation procedure is presented in the next section. Because of mass and heat transfer occurring in parallel in the shell-side fluid phase, the Ackermann correction factor E_T [246], defined in Eq. (5.76), was introduced into the Newton's cooling law for the shell-side convective heat transport (Eqs. (5.71) and (5.72)).

$$E_T = \frac{\phi_T}{1 - e^{-\phi_T}}, \text{ with } \phi_T = \frac{\dot{n}\hat{c}_{p,h}}{\alpha_h}. \tag{5.76}$$

5.3.3.2 Heat and mass transfer correlations

In the following, the correlations used to calculate the heat transfer coefficients of the shell-side, α_h, microtube-side, α_c, condensate film, α_f, mass transfer coefficient θ_h, and friction factors f_h and f_c [247], are presented.

α_h was computed using forced convection correlations, which depend on whether the flow regime through the shell is laminar, turbulent or transitional.

Laminar flow regime ($Re_{D_e} < 2300$) [248]:

$$\begin{gathered} Nu_{h,b,lam} = \\ \left[Nu_{h,b,lam\_1}^3 + 0.7^3 + \left(Nu_{h,b,lam\_2} - 0.7\right)^3 + Nu_{h,b,lam\_3}^3\right]^{1/3}, \\ Nu_{h,b,lam\_1} = 3.66, \\ Nu_{h,b,lam\_2} = 1.077\left(Re_{h,b,D_e} Pr_{h,b}\, D_e/x\right)^{1/3}, \\ Nu_{h,b,lam\_3} = \frac{1}{2}\left(\frac{2}{1 + 22Pr_{h,b}}\right)^{1/6} \left(Re_{h,b,De} Pr_{h,b}\, D_{he}/x\right)^{1/2}. \end{gathered} \tag{5.77}$$

Turbulent flow regime ($Re_{D_e} > 10^4$) [249,250]:

$$\begin{gathered} Nu_{h,b,tur} = \frac{(f_h/8)\left(Re_{h,b,D_e} - 1000\right)Pr_{h,b}}{1 + 12.7(f_h/8)^{1/2}\left(Pr_{h,b}^{2/3} - 1\right)}\left(\frac{Pr_{h,b}}{Pr_{h,w}}\right)^{0.11} C_A, \\ C_A = 1 + \frac{1}{3}(D_e/x)^{2/3}. \end{gathered} \tag{5.78}$$

Transitional flow regime ($2300 < Re_{D_e} < 10^4$):

$$Nu_{h,b,tra} = (1-\epsilon)Nu_{h,b,lam}\big|_{Re_{h,b,D_e}=2300} + \epsilon Nu_{h,b,tur}\big|_{Re_{h,b,D_e}=10^4}, \quad \epsilon = \frac{Re_{h,b,D_e}-2300}{10^4-2300}. \tag{5.79}$$

α_c was determined based on the experimentally derived correlation for mixed convection in $scCO_2$ through a uniformly heated horizontal microtube. The correlation is given in Eq. (5.80). Details about the derivation of this correlation will be provided in Section 6.2.1.

$$Nu_{c,b} = 0.0038 Re_{c,b}^{0.850} Pr_{c,b}^{2.038} Ri_{c,b}^{-0.028} \left(\frac{\rho_{c,w}}{\rho_{c,b}}\right)^{1.518} \left(\frac{\mu_{c,w}}{\mu_{c,b}}\right)^{4.690} \left(\frac{\lambda_{c,w}}{\lambda_{c,b}}\right)^{2.556} \left(\frac{\bar{c}_{p,c}}{c_{p,c,f}}\right)^{1.943}, \quad \bar{c}_{p,c} = \frac{h_{c,w}-h_{c,b}}{T_{c,w}-T_{c,b}}. \tag{5.80}$$

α_f was calculated, either for laminar or turbulent flow regimes, from the Nusselt [251] and Müller [252] correlations, respectively, as follows:

$$Nu_{f,lam} = \frac{\alpha_{f,lam}\mathcal{L}}{\lambda_f} = 0.693\left(\frac{1-\rho_h/\rho_f}{Re_f}\right)^{1/3}, \tag{5.81}$$

$$Nu_{f,tur} = \frac{\alpha_{f,tur}\mathcal{L}}{\lambda_f} = \frac{0.0283 Re_f^{7/24} Pr_f^{1/3}}{1+9.66 Re_f^{-3/8} Pr_f^{-1/6}}. \tag{5.82}$$

where $\mathcal{L}$ is the characteristic length of the film flow, and Re_f is the film Reynolds number, defined in Eqs. (5.83) and (5.84).

$$\mathcal{L} = \left(\frac{v_f^2}{g}\right)^{1/3} \tag{5.83}$$

$$Re_f = \frac{\dot{m}_f}{\pi D_{to}\mu_f}. \tag{5.84}$$

Although Eqs. (5.81) and (5.82) were derived for a film flow over vertical surfaces, they can be reasonably extended to horizontal tubes [181]. Nu_f, and thus α_f, was calculated by combining $Nu_{f,lam}$ and $Nu_{f,tur}$, through the following quadratic superimposition:

$$Nu_f = \frac{\alpha_f \mathcal{L}}{\lambda_f} = \sqrt{\left(K_{f,lam} K_\tau Nu_{f,lam}\right)^2 + \left(K_{f,tur} K_\tau Nu_{f,tur}\right)^2}. \quad (5.85)$$

Coefficients K_τ, $K_{f,lam}$ and $K_{f,tur}$, introduced in Eq. (5.85), account for the influence of the shell gas flow velocity on the heat transfer within the film. At the vapor-liquid interface, the axial velocity of the film and shell gas flows must coincide [253]. This generates a velocity gradient of the shell gas in the near-interface region and, thus, a shear stress at the interface, τ_{hf}. τ_{hf} increases the mean velocity of the film flow, leading to two effects: (i) film thinning, which reduces the thermal resistance; and (ii) amplification of turbulent fluctuations in the film, which intensifies heat diffusion by turbulent action. Effect (i) is accounted for by K_τ, which is valid for laminar and turbulent flow regimes [254]; and effect (ii) by $K_{f,lam}$ and $K_{f,tur}$, which depend on the flow regime [255]. The calculation procedure proposed in this work to determine K_τ; as well as the relationships for $K_{f,lam}$ and $K_{f,tur}$, extracted from the literature, are presented in the Appendix B. In addition, δ was calculated from the local volumetric vapor content, ϑ, according to Eq. (5.86). The calculation procedure of ϑ is also presented in Appendix B.

$$\delta = \frac{(1-\vartheta)}{4} D_{to}, \quad (5.86)$$

θ_h was calculated from α_h using the Chilton-Colburn analogy [244]:

$$\theta_h = \frac{\alpha_h}{\hat{\rho}_h \hat{c}_{ph} Le^{0.6}}, \quad (5.87)$$

where the Lewis number, Le, is defined as the ratio of thermal diffusivity to mass diffusivity,

$$Le = \frac{\lambda_h}{\hat{\rho}_h \hat{c}_{ph} \mathcal{X}_h}. \quad (5.88)$$

The binary diffusion coefficient of CO_2 and H_2O, $\mathcal{X}_h$, was estimated using the Fuller's correlation [256], at a pressure of 1 bar, as shown in Eq. (5.89).

$$\mathcal{X}_h{}^{id} = \frac{0.00143 T_h^{1.75}\left(M_1{}^{-1} + M_2{}^{-1}\right)^{1/2}}{p\sqrt{2}[(\sum \Delta_{v1})^{1/3} + (\sum \Delta_{v2})^{1/3}]^2}, \quad (5.89)$$

with Δ_{v1} = 13.1 and Δ_{v2} = 26.9.

To account for the effect of elevated pressures, $\mathcal{X}_h{}^{id}$ was corrected using the Riazi-Whitson correlation [257] of Eq. (5.90), which depend on the critical pressure of the mixture, p_{cr}, and the acentric factor, ω.

$$\frac{(\rho_h \mathcal{X}_h)}{(\rho_h \mathcal{X}_h)^{id}} = 1.07 \left(\frac{\mu_h}{\mu_h^{id}} \right)^{B+C\frac{p}{p_{cr}}}, \tag{5.90}$$

with $B = -0.27 - 0.38\omega$ and $C = -0.05 + 0.1\omega$.

The pressure drops for both the shell- and tube- sides were calculated for each discretized heat exchange section "dx" by using the Darcy equation [258]:

$$\frac{dp_i}{dx} = f_i \frac{\rho_i \bar{u}_i^2}{2D_e}, \tag{5.91}$$

where $i = h, c$, and D_e is the equivalent diameter, which is D_{ti} for the tube-side, and calculated by Eqs. (5.50) and (5.51) for the shell-side. The friction factor f_i for laminar flow regime is calculated as follows:

$$f_i = \frac{64}{Re_{i,D_e}} \tag{5.92}$$

For turbulent flow regime, f was calculated by using the high-accuracy explicit friction factor model of Romeo et al. [259], with the temperature correction factor of Musgrove et al. [260], as follows:

$$\begin{aligned} \frac{1}{\sqrt{f_{iso}}} = -2\ln\Bigg(& \frac{\varepsilon/D}{3.7065} \\ & - \frac{5.0272}{Re_{i,b,D_e}} \ln\left(\frac{\varepsilon/D}{3.827} \right. \\ & \left. - \frac{4.567}{Re_{i,b,D_e}} \ln\left(\left(\frac{\varepsilon/D}{7.7918} \right)^{0.9924} + \left(\frac{5.3326}{208.815 + Re_{i,b,D_e}} \right)^{0.9345} \right) \right) \Bigg) \end{aligned} \tag{5.93}$$

$$f_i = f_{iso} \left(\frac{T_b}{T_w} \right)^{0.1}.$$

5.3.4 Numerical procedures for model resolution

The thermal-hydraulic model of the MSTHE was implemented in Matlab R2022b [171]. The numerical procedure used to solve the model is illustrated in the flow diagram shown in Fig. 5.28. Since heat transfer in $scCO_2$ and filmwise condensation are local phenomena, the heat exchanger length was discretized into N_s heat exchange sections. The governing differential equations for heat transfer were then solved numerically along the direction of the shell-side flow, discretizing the convective transport terms of the governing equations using the first-order upwind discretization scheme [261].

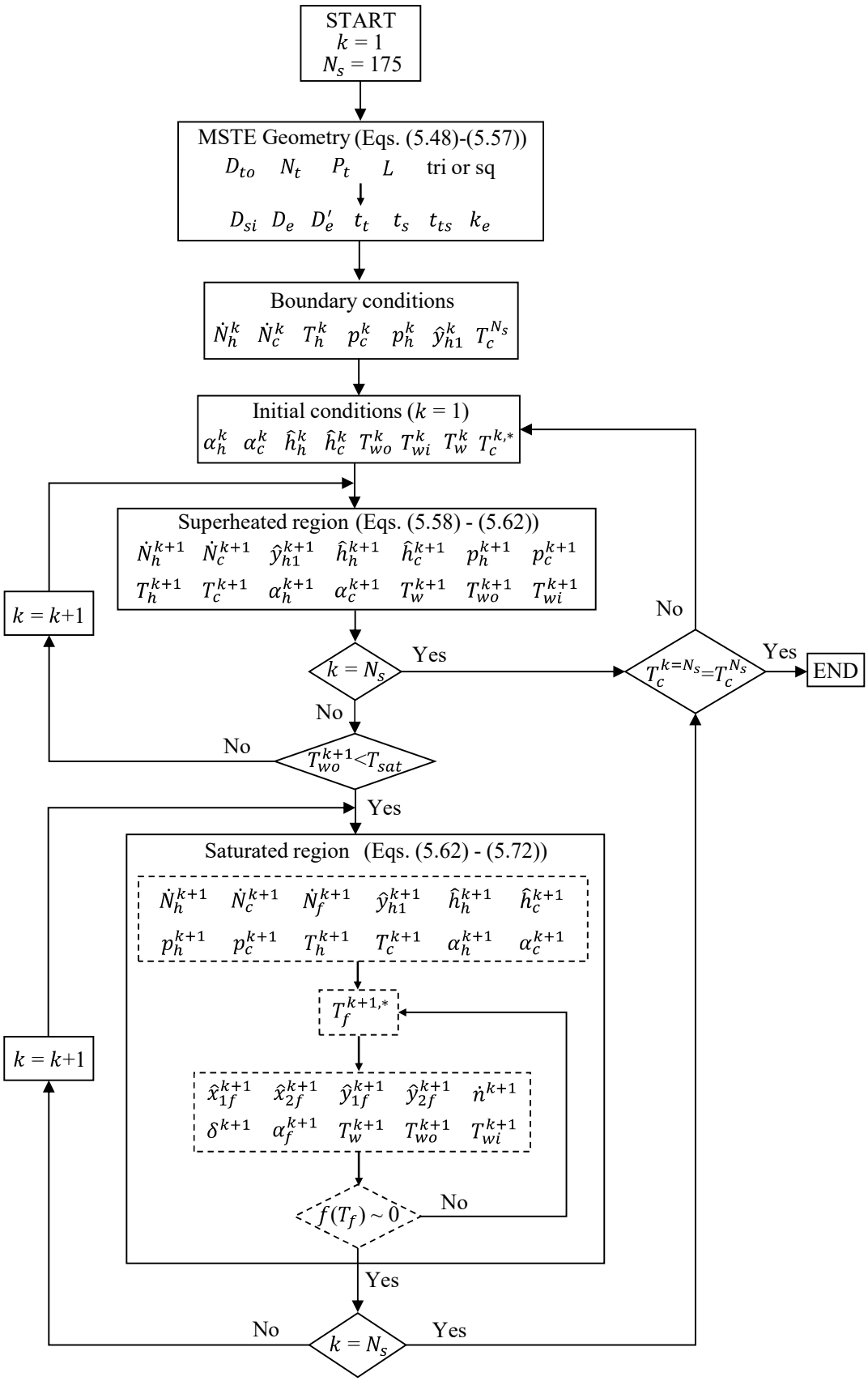

Fig. 5.28. Flow diagram of the numerical procedure for solving the thermal-hydraulic model of the MSTHE.

The procedure begins with the input of the independent geometric parameters. Eqs. (5.48) - (5.57) are used to define the complete geometry of the MSTHE. Next, boundary conditions are specified. Due to the countercurrent flow configuration, the boundary condition for the tube-side inlet temperature must be applied at $k = N_s$, even though the numerical integration begins at k = 1. Consequently, the initial temperature of the tube-side fluid at k = 1 must be estimated and subsequently adjusted iteratively until the calculated temperature at $k = N_s$ matches the specified boundary value $T_c^{N_s}$. At k = 1, additional initial values are set for the cold fluid temperature, heat transfer coefficients, molar enthalpies, and wall temperatures. The shell-side fluid enters the MSTHE in a superheated vapor state. The heat transfer model for this region is solved progressively until the fluid near the cooling tube wall reaches the saturation point, or until $k = N_s$ if saturation is not reached. Since enthalpy is pressure-dependent, especially for the tube-side $scCO_2$, fluid temperatures are obtained iteratively from the enthalpies and pressures.

Once the shell fluid in the near-wall region reaches the dew point, the condensation model for the saturated region is applied to the remaining sections. If the bulk temperature of the shell fluid at a given section k exceeds the dew point, T_h^{k+1} is calculated using Eq. (5.72); otherwise, it is set equal to T_{sat}. T_f is determined by iteratively solving Eq. (5.71). An initial guess for T_f^* is assumed, from which the thermodynamic equilibrium composition at the vapor-liquid interface ($\hat{y}_{1f}$ and $\hat{x}_{1f}$), $\dot{n}$, δ, α_f, and wall temperatures (T_{wo}, T_{wi} and T_w), are computed. These values are used to evaluate the function $f(T_f)$ in Eq. (5.71). If the root is found within a tolerance of 10^{-9}, the calculation proceeds to the next section $k = k + 1$. Otherwise, T_f is updated using the Newton-Raphson method until convergence is achieved. This process is repeated sequentially until the final section $k = N_s$ is reached. Finally, it is verified whether the calculated tube-side inlet temperature $T_c^{k=N_s}$ agrees with the specified boundary condition $T_c^{N_s}$ within a tolerance of 0.1 ºC. If the condition is met, the computation ends. If not, a new guess for T_c^{k*} is generated using a relaxation-based Newton-Raphson correction, and the entire model is recalculated until convergence is achieved.

5.3.5 Number of sections, N_s

The number of sections N_s into which the heat exchanger is discretized was determined by balancing computational accuracy and efficiency. Increasing N_s reduces the spatial discretization step, thereby improving the resolution of the varying thermophysical properties of the $scCO_2$ and the local condensation process along the MSTHE. However, a higher number of sections also leads to a considerable increase in computational time, since the full calculation procedure shown in Fig. 5.28 must be executed for each division. To determine the optimal value of N_s, the baseline MSTHE model was run under the

nominal boundary conditions listed in Table 5.6, with N_s varying from 50 to 1000. It was assumed that an optimal N_s would be the minimum value for which the relative error in key output variables (T_c^{out}, T_h^{out}, Δp_c, Δp_h and $\dot{N}_f$) did not exceed 0.1% compared to the results obtained with N_s = 1000.

Fig. 5.29 shows the variation of these output variables with respect to N_s on a logarithmic scale. As expected, the relative errors decrease with increasing N_s. However, for T_c^{out}, T_h^{out} and $\dot{N}_f^{out}$, minor fluctuations are observed rather than a monotonically decreasing trend. These fluctuations are attributed to local uncertainties in the calculation of T_f within each section, which propagate along the length of the MSTHE and slightly affect the final output value. Based on the analysis shown in Fig. 5.29, it was determined that for N_s = 175, the absolute error in all evaluated output variables remains below 0.1%. Therefore, the value of N_s = 175 was selected.

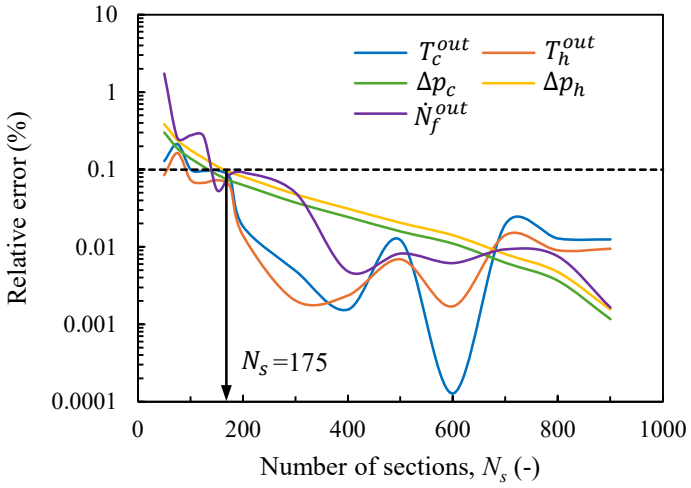

Fig. 5.29. Evolution of the output variables T_c^{out}, T_h^{out}, Δp_c, Δp_h and $\dot{N}_f^{out}$ as a function of the number of sections N_s.

5.3.6 *Model validation*

The reliability of the results produced by the baseline MSTHE model was assessed through a validation process. In the absence of experimental data, the primary output variables of the model were compared with the results obtained from overall mass and energy balances calculated using Aspen Plus. Fig. 5.30 shows the flow diagram of the simulation implemented in Aspen Plus. The cold inlet stream (MCI) is heated in a heat exchanger (H) by thermal energy transferred from the hot stream (MHI), which is cooled in a separate heat exchanger (C). The temperatures, pressures, and mass flow rates of the hot (MHI) and cold (MCI) streams entering the system were set according to the nominal operating conditions (100% cycle load) listed in Table 5.6. Additionally, the outlet temperature of the cold stream (MCO) was fixed at 128 ºC, as defined in Table 5.6. This

approach allows for a direct comparison between the output values obtained from the numerical integration of the MSTHE model and the resulting mass and energy balances resolved in Aspen Plus.

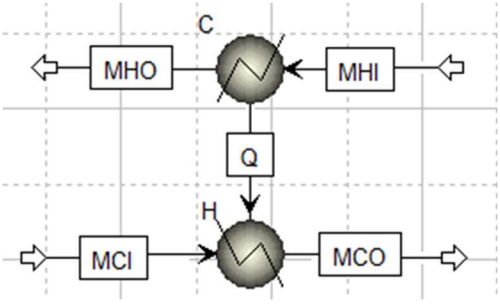

Fig. 5.30. Flow diagram of the model implemented in Aspen Plus to perform the MSTHE model validation.

Table 5.8 summarizes the comparison of the key output parameters obtained from both models. The outlet temperature of the cold stream predicted by the MSTHE model was 127.10 ºC, corresponding to a relative deviation of 0.71% from the imposed boundary value of 128 ºC. For the hot stream, the MSTHE model predicted an outlet temperature of 52.16 ºC, while Aspen Plus yielded a value of 52.09 ºC, resulting in a relative difference of 0.13%. The heat transfer rate calculated by the MSTHE model showed a deviation of 1.11% compared to the 10 MW_{th} specified in the boundary conditions. Regarding mass transfer, the molar flow rate of condensate predicted by the MSTHE model was 74.36 $mol{\cdot}s^{-1}$, in perfect agreement with the value obtained from Aspen Plus. This close match indicates that the mass transfer mechanisms implemented in the MSTHE model accurately describe the vapor condensation process. The predicted mole fraction of H_2O deviated by 4.44%. The mole fraction of dissolved CO_2 in the condensate, $\hat{x}_{CO_2,f}^{out}$, predicted by the MSTHE model was 6.51% higher than the one predicted by Aspen Plus. The agreement between the two modeling approaches confirms the accuracy and applicability of the thermal-hydraulic model developed for the MSTHE.

Table 5.8. Comparison of the main output parameters of the MSTHE model and the global mass and energy balances in Aspen Plus.

Output parameter	MSTHE model	Aspen Plus Mass & energy balances	AARD (%)
T_c^{out} (ºC)	127.10	128	0.71
T_h^{out} (ºC)	52.16	52.09	0.13
$\dot{Q}$ (MW_{th})	9.89	10	1.11
$\dot{N}_f^{out}$ ($mol\ s^{-1}$)	74.50	74.36	0.19
$\hat{y}_{H_2O,h}^{out}$ (%)	0.45	0.48	4.44
$\hat{x}_{CO_2,f}^{out}$ (%)	1.33	1.24	6.51

Chapter 6
Heat transfer results and discussion

6 Heat transfer results and discussion

The numerical optimization process and part load analysis of the NET Power cycle, presented in Section 4.2, enabled the determination of suitable operating conditions for a micro shell-and-tube heat exchanger (MSTHE) intended for application in the low-temperature section of the recuperative heat exchanger (RHE). The pressure and temperature of the $scCO_2$ on the tube side were found to range between 9.6 – 27.9 MPa and 25 – 100 ºC, respectively. Under these operating conditions, the experimental system, described in Section 5.1, was used to conduct an experimental study on heat transfer to $scCO_2$ flowing through a horizontal microtube. Findings from this investigation are presented in Section 6.1, where the influence of the mass flux, heat flux, inlet temperature, buoyancy and thermal acceleration on the heat transfer performance was assessed. In addition, novel empirical heat transfer models, developed from the experimental data points, are presented in Section 6.2.

The underlying heat transfer mechanisms, particularly those related to buoyancy and thermally-induced flow acceleration, are further analyzed in Section 6.3 by using the CFD model introduced in Section 5.2. Moreover, the effect of tube diameter on heat transfer was investigated, as this parameter could not be manipulated during the physical experiments. Prior to conducting this analysis, a CFD model, which replicates the geometry and conditions of the experimental test section, was used to validate RANS turbulence models.

In Section 6.4, the MSTHE numerical model, described in Section 5.3, was applied to conduct a comprehensive thermal-hydraulic performance study for integration into the low-temperature section of the NET Power cycle recuperator. Based on this study, the major thermodynamic performance indicators were evaluated as a function of the geometric design variables and the cycle load degree.

6.1 Experimental investigation on heat transfer in supercritical CO_2 microflows

Most of the experiments investigating the heat transfer process of $scCO_2$ in horizontal configurations focused on large diameter flow channels and pressure ranges close to the critical pressure of CO_2 [262]. Nevertheless, these conditions are distant from the actual operating conditions of the compact recuperative heat exchanger of the NET Power cycle. To fill this gap, this first section of results presents the outcomes derived from the experimental parametric study, which considers the effect of mass flux ($447.4 \leq G \leq 1044.5$ kg·m^{-2}·s^{-1}), heat flux ($8.3 \leq \dot{q}_w \leq 21.3$ kW·m^{-2}), inlet temperature ($19.8 \leq T_{in} \leq 30.1$ ºC), buoyancy and thermal acceleration on the heat transfer performance of $scCO_2$ through a microtube of 0.88 mm inner diameter and 1700 mm length, for the test pressures of 10, 15, 20, 25 and 30 MPa.

In total 28 experiments were conducted, and 560 data points were collected in combinations of these experimental variables. From the total amount of tests, 25 were selected, from a fractional factorial experiment design model, to conduct the sensitivity analysis; while the remaining 3 test (T21, T27 and T28 in Table 5.1) were used to validate the RANS turbulence models, and to develop the empirical heat transfer models. The maximum uncertainties of the resulting heat transfer coefficients are located in the inflow length, where the heat transfer coefficients are high during the thermal boundary layer development, and in the region near the pseudo-critical point, where a minimum change in temperature causes a significant change in the thermo-physical properties of the fluid. The maximum uncertainty recorded was 18.18%, although for most of the experiments the maximum range of relative deviation of the heat transfer coefficient was below 6%.

An experimental repeatability study was conducted to ensure the reliability of the test rig and to avoid the influence of unforeseen factors. To this end, the T4 test (see Table 5.1) at 10 MPa, and the T24 test at 30 MPa, were repeated twice and the deviations in the measurements of the tube outer-wall temperatures by the thermocouples were evaluated. Results are shown in Fig. 6.1. For the T4 test, the maximum deviation recorded was 6.8% near the pseudo-critical conditions, while for the T24 test was 3.6% at the entry region. It is important to note that these deviations do not originate solely from the thermocouples uncertainty. Uncertainties in the measurement and control of mass flux, pressure, inlet temperature, and heat input also play a significant role. Furthermore, conditions near the pseudo-critical point and inflow length are particularly sensitive to such uncertainties. Hence, these findings suggest that the experimental data are consistent, validating the repeatability of the experimental apparatus.

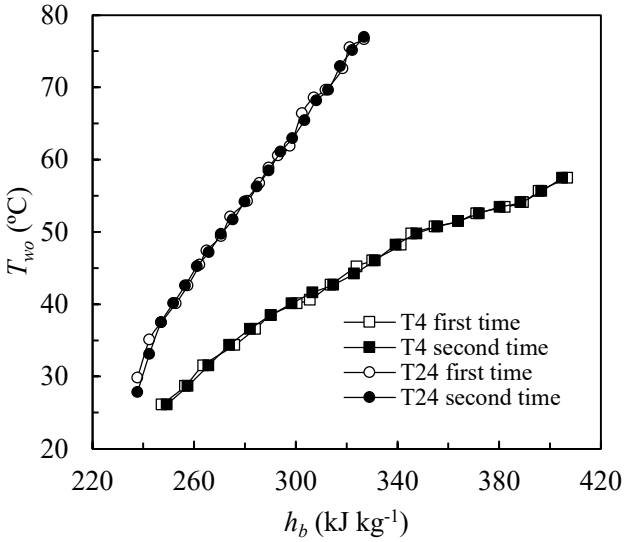

Fig. 6.1. Results of the repeatability analysis of the T4 and T24 tests. For T4 the maximum deviation is 6.8% near the pseudo-critical point, while for T24 it was 3.6% in the thermal inflow region.

6.1.1 Effect of mass flux

Using the mass flux as an independent parameter, Fig. 6.2 shows the distributions of the inner-wall temperature (left graph) and local heat transfer coefficient (right graph), as a function of bulk enthalpy and inlet distance from the heated section, respectively. The heat flux and fluid temperature at the inlet of the test section were kept constant for each test pressure. Heat transfer rates are enhanced with increasing mass flow rates for all tested points. Increasing the mass flux increases the Reynolds number, which enhances the heat transport by turbulent action and, therefore, the heat transfer.

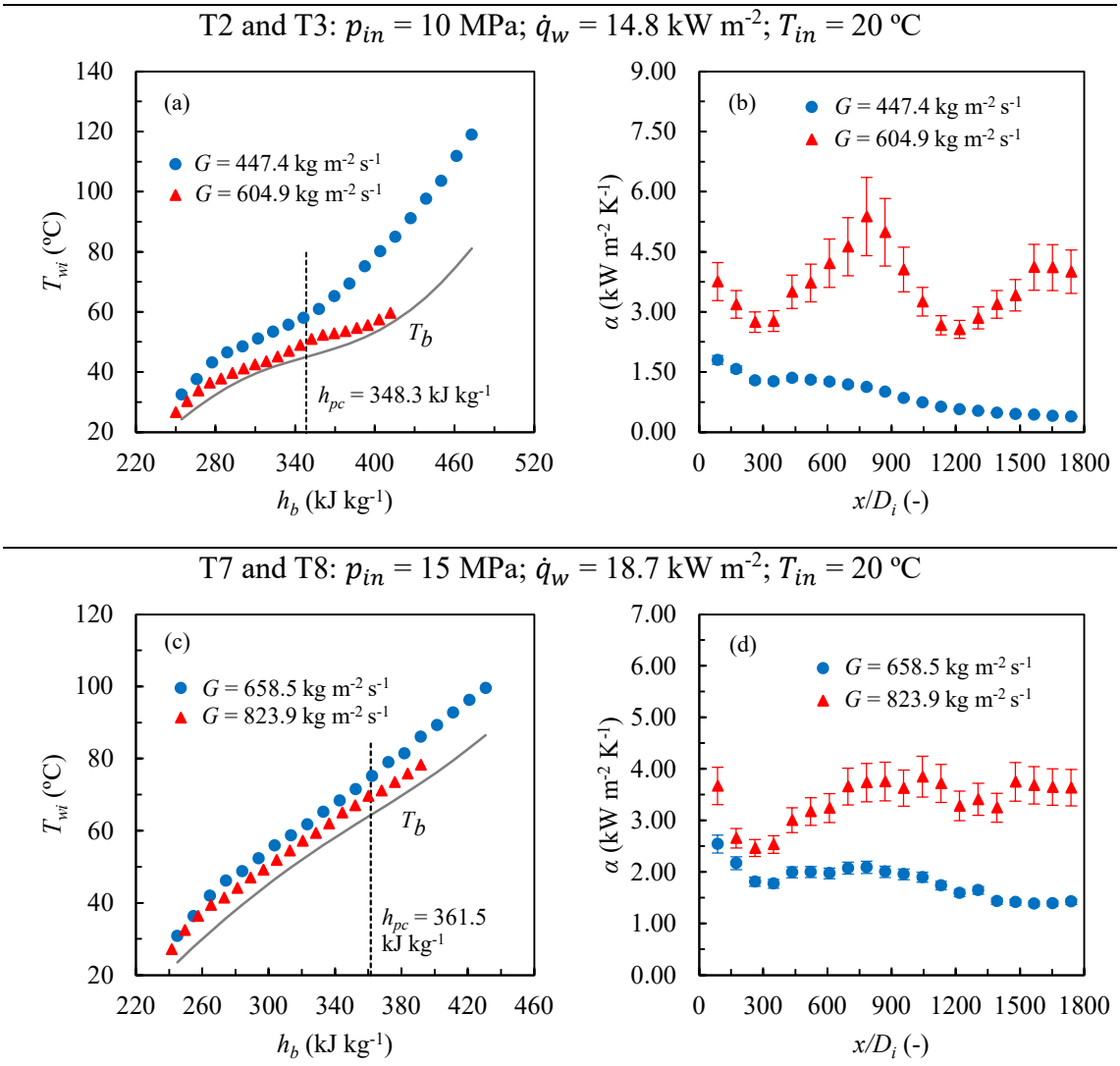

Fig. 6.2. Effect of mass flux on inner-wall temperature and local heat transfer coefficient for tests T2, T3, T7, T8, T12, T13, T17, T18, T23 and T24 (see Table 5.1). The higher the mass flux, the higher the heat transfer coefficients.

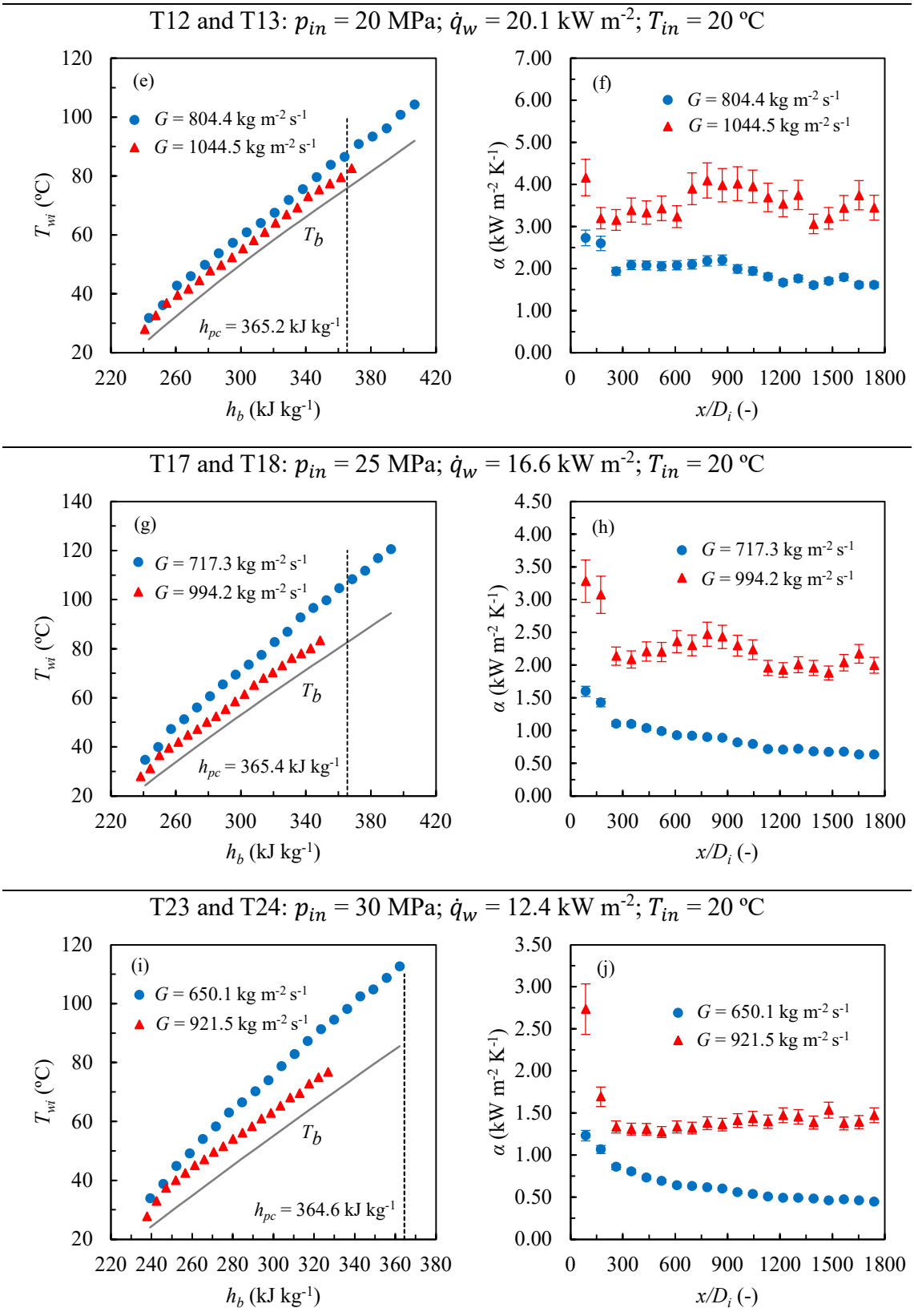

Fig. 6.2 (continued). Effect of mass flux on inner-wall temperature and local heat transfer coefficient for tests T2, T3, T7, T8, T12, T13, T17, T18, T23 and T24 (see Table 5.1). The higher the mass flux, the higher the heat transfer coefficients

For a test pressure of 10 MPa, and a mass flux of 604.9 $kg \cdot m^{-2} \cdot s^{-1}$, Fig. 6.2(b) shows that the heat transfer coefficient initially decreases along the thermal inflow length due to the gradual thickening of the thermal boundary layer. Thereafter, it increases as the bulk fluid temperature rises, reaching a peak value just before the pseudo-critical enthalpy. This peak is attributed to the rapid increase in specific heat capacity and Prandtl number near the pseudo-critical point. As the bulk fluid temperature rises beyond the pseudo-critical temperature, the heat transfer coefficient declines, followed by a recovery to a constant value, forming a deteriorative valley region. Experiments conducted by Wang et al. [109] also demonstrated the appearance of the deteriorative valley region after the pseudo-critical point in miniature tubes.

The heat transfer coefficient drop within the valley region can be attributed to buoyancy-induced secondary cross-flows, which accumulate low-density fluid in the upper part of the tube. This results in thermal stratification and a suppression of turbulent quantities. In contrast, the subsequent recovery of the heat transfer coefficient is driven by axial flow acceleration, which enhances the production of turbulent kinetic energy. This physical explanation resulted from the numerical (CFD) study conducted in Section 6.3.2. Temperature stratification in the microtube leads to asymmetric thermal expansion between the top and bottom tube walls, potentially inducing thermal fatigue and promoting crack propagation issues.

When the mass flux was reduced to 447.4 $kg \cdot m^{-2} \cdot s^{-1}$, the valley region disappears and there is a monotonic decrease of the heat transfer coefficient after reaching the pseudo-critical point, as can be found in Fig. 6.2(b). This trend has been reported in several previous studies [86,93,110,263]. Since axial flow acceleration decreases with the mass flow, the recovery effect of the heat transfer coefficient in the valley region vanishes as the mass flow decreases. This is further discussed in Section 6.3.2.2. Moreover, under constant heating power and inlet temperature, a reduction in mass flow leads to an increase in the fluid outlet temperature. As a result, the region downstream of the pseudo-critical enthalpy is extended, attenuating the heat transfer rates.

For 15, 20, 25 and 30 MPa, the peak values of the fluid properties near the pseudo-critical point are significantly lower than for 10 MPa. Therefore, as shown in Figs. 6.2(c-j), the trends of the heat transfer coefficient become flatter, with similarity to constant-property flows. For the lower values of mass flux used in the experiments, the heat transfer coefficients decrease smoothly along the flow path to a constant value, as deduced from the progressive separation of the inner-wall and bulk temperatures. This is a result of a larger thermal inflow length and a thick thermal boundary layer, which is a consequence of low Reynolds numbers. The higher the mass flux, the shorter the thermal inflow length.

6.1.2 Effect of heat flux

The effect of the heat flux applied to the test section in the evolution of the inner-wall temperature as a function of the bulk enthalpy (left graph), and the local heat transfer coefficient as a function of the bulk fluid temperature (right graph), are represented by Fig. 6.3. For this case, more meaningful insights were found by plotting the heat transfer coefficient as a function of the bulk temperature rather than heating distance. For each test pressure, the mass flux and inlet temperature were maintained constant.

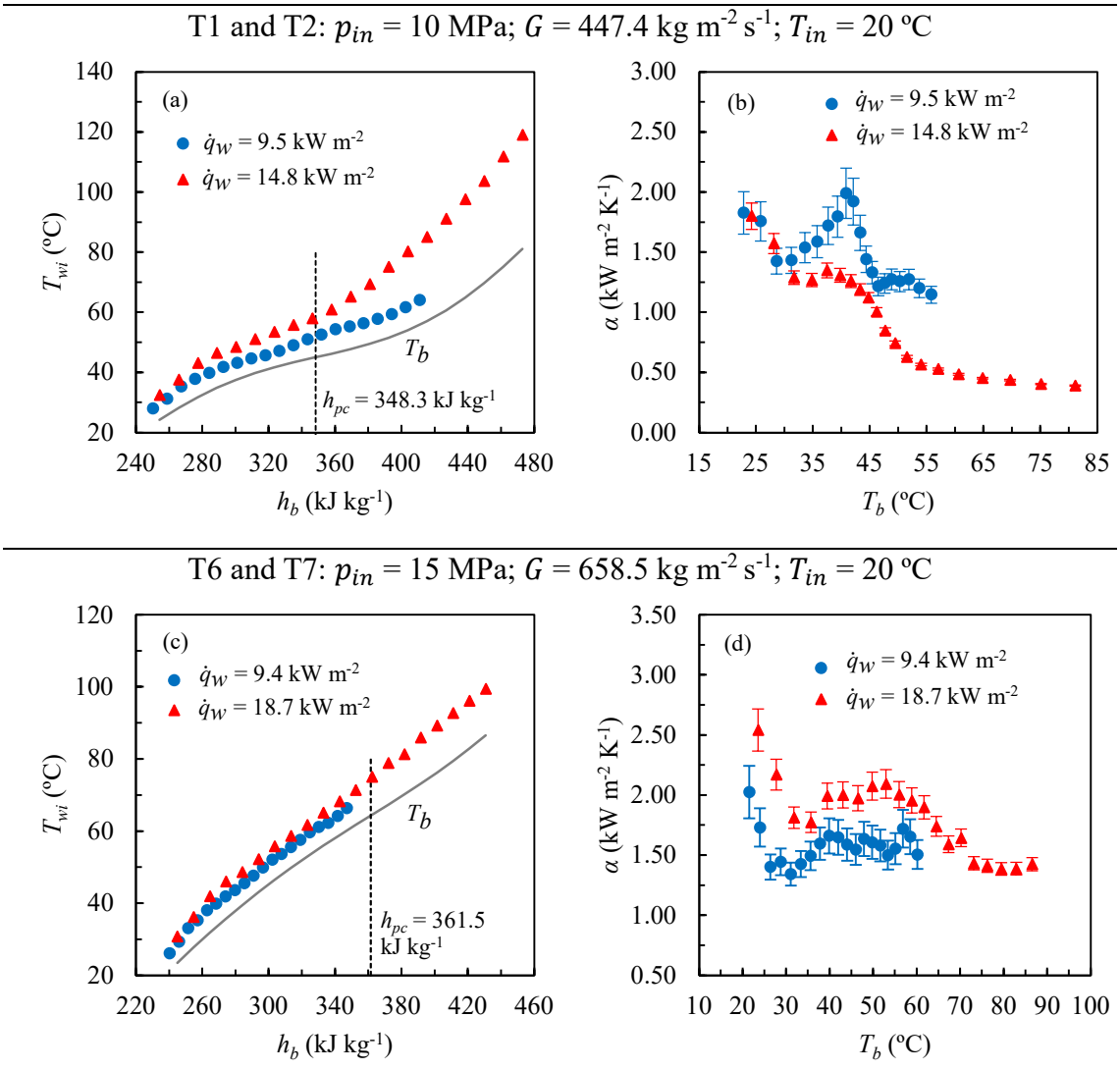

Fig. 6.3. Effect of heat flux on inner-wall temperature and local heat transfer coefficient for tests T1, T2, T6, T7, T11, T12, T16, T17, T22 and T23 (see Table 5.1). At 10 MPa the heat transfer coefficients decrease with increasing heat flux, whereas at higher pressures they increase.

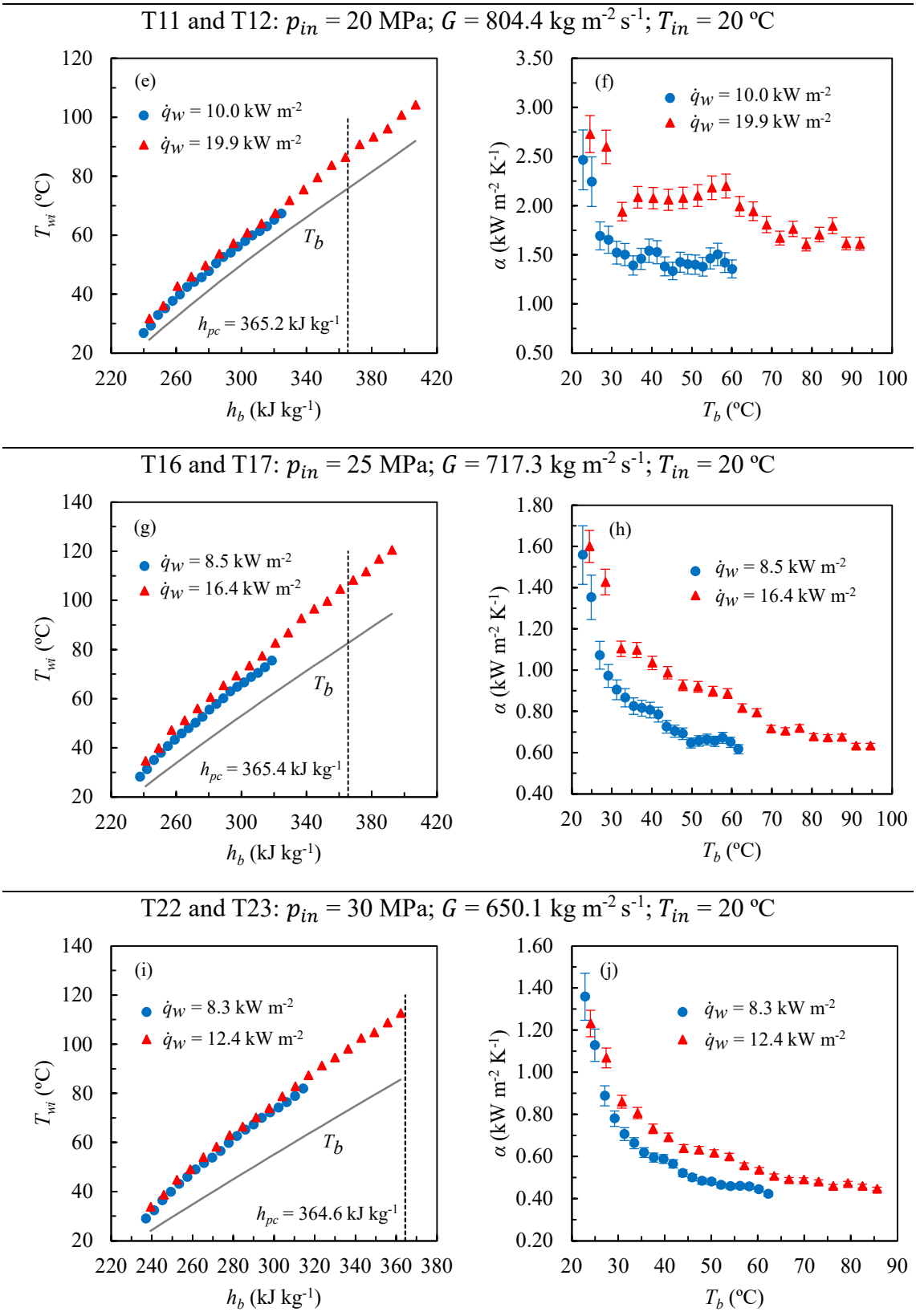

Fig. 6.3 (continued). Effect of heat flux on inner-wall temperature and local heat transfer coefficient for tests T1, T2, T6, T7, T11, T12, T16, T17, T22 and T23 (see Table 5.1). At 10 MPa the heat transfer coefficients decrease with increasing mass flux, whereas at higher pressures they increase.

It can be seen in Fig. 6.3(b) that, when the pressure was fixed at 10 MPa, increasing the heat flux causes an attenuation of the heat transfer coefficient peak value, while the bulk fluid temperature at which peak occurs decreases. Increasing the heat flux causes an increase in the temperature difference between the near-wall and bulk fluid regions, intensifying the buoyancy effects, as deduced from the Grashof number definition (expressed in terms of $\dot{q}_w$) in Eq. (6.1).

$$Gr_q = \frac{g\bar{\beta}\dot{q}_w D_i^4}{\nu_b^2 \lambda_b} \tag{6.1}$$

$\bar{\beta}$ denotes the coefficient of volumetric expansivity $\bar{\beta} = \left(1/\rho_f\right) \cdot (\rho_b - \rho_w)/(T_w - T_b)$, with the density ρ_f evaluated at the film temperature $T_f = (T_w + T_b)/2$. Therefore, flow stratification, with accumulation of low-density fluid in the upper half of the tube, is accentuated, with a significant heat transfer impairment. Wang et al. [114] reported that, when buoyancy forces are sufficiently dominant, part of the low-density fluid, that ascends by natural circulation in the cross-section of the tube, counteracts the high-density flow descending along the centerline, mitigating the turbulent quantities. Both phenomena account for the reduction in the heat transfer coefficient peak. For bulk enthalpy values below the pseudo-critical point, the heat transfer coefficient tendency during the thermal boundary layer development remains insensitive to variations in heat flux. However, for a constant mass flow and inlet temperature, increasing the heat flux rises the fluid outlet temperature and expands the enthalpy region beyond the pseudo-critical point, resulting in a reduction of heat transfer rates.

The improvement of the $scCO_2$ heat transfer process at 10 MPa with the reduction of the heat flux is advantageous when considering the actual operating conditions of a compact microtube heat exchanger within the NET Power cycle. Under minimum load conditions, the pressure of the recirculating $scCO_2$ flowing through the microtubes approaches 10 MPa, while the heat flux delivered by the exhaust gases decreases due to a reduction in the recirculating mass flow. Thus, the improvement of the heat transfer coefficient under these conditions helps to sustain high heat transfer effectiveness in the low-temperature section, compensating for the diminished heat transfer rates caused by the mass flow reduction.

Figs. 6.3(c-j) show that, for pressures of 15, 20, 25 and 30 MPa, the heat transfer coefficients increase with rising thermal load. This is attributed to the reduction in fluid viscosity as temperature increases, which causes the Reynolds number to rise, under constant mass flux conditions. Consequently, as the thermal input increases, the average fluid temperature in the tube increases, resulting in higher average Reynolds numbers and enhanced turbulent diffusivity. This finding supports high heat transfer effectiveness in

the NET Power cycle MSTHE at nominal conditions, when the heat flux is at its maximum value.

6.1.3 Effect of inlet temperature

To clarify the effect of the fluid temperature at the inlet of the test tube, Fig. 6.4 depicts the trends of the inner-wall temperature and the local heat transfer coefficient, as a function of the bulk fluid enthalpy and distance from the heated section, respectively. The mass flux and heat flux were kept constant for the five tested pressures, 10, 15, 20, 25 and 30 MPa. The inlet temperature adopted the values of 20 and 30 ºC, within an accuracy of ± 0.2 ºC.

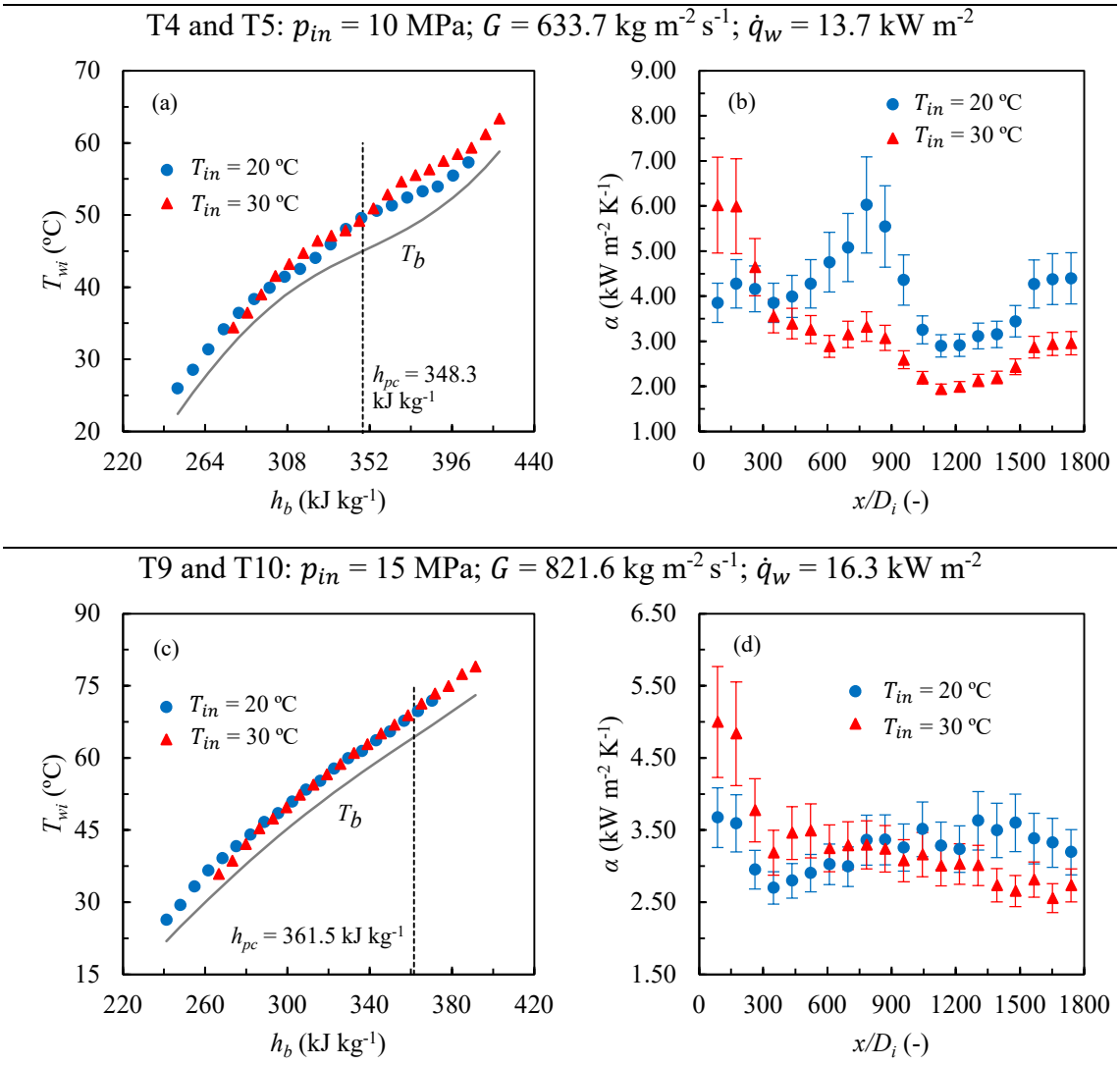

Fig. 6.4. Effect of inlet temperature on inner-wall temperature and local heat transfer coefficient for tests T4, T5, T9, T10, T14, T15, T19, T20, T25 and T26 (see Table 5.1). The higher the fluid inlet temperature, the higher the heat transfer coefficients in the inlet region.

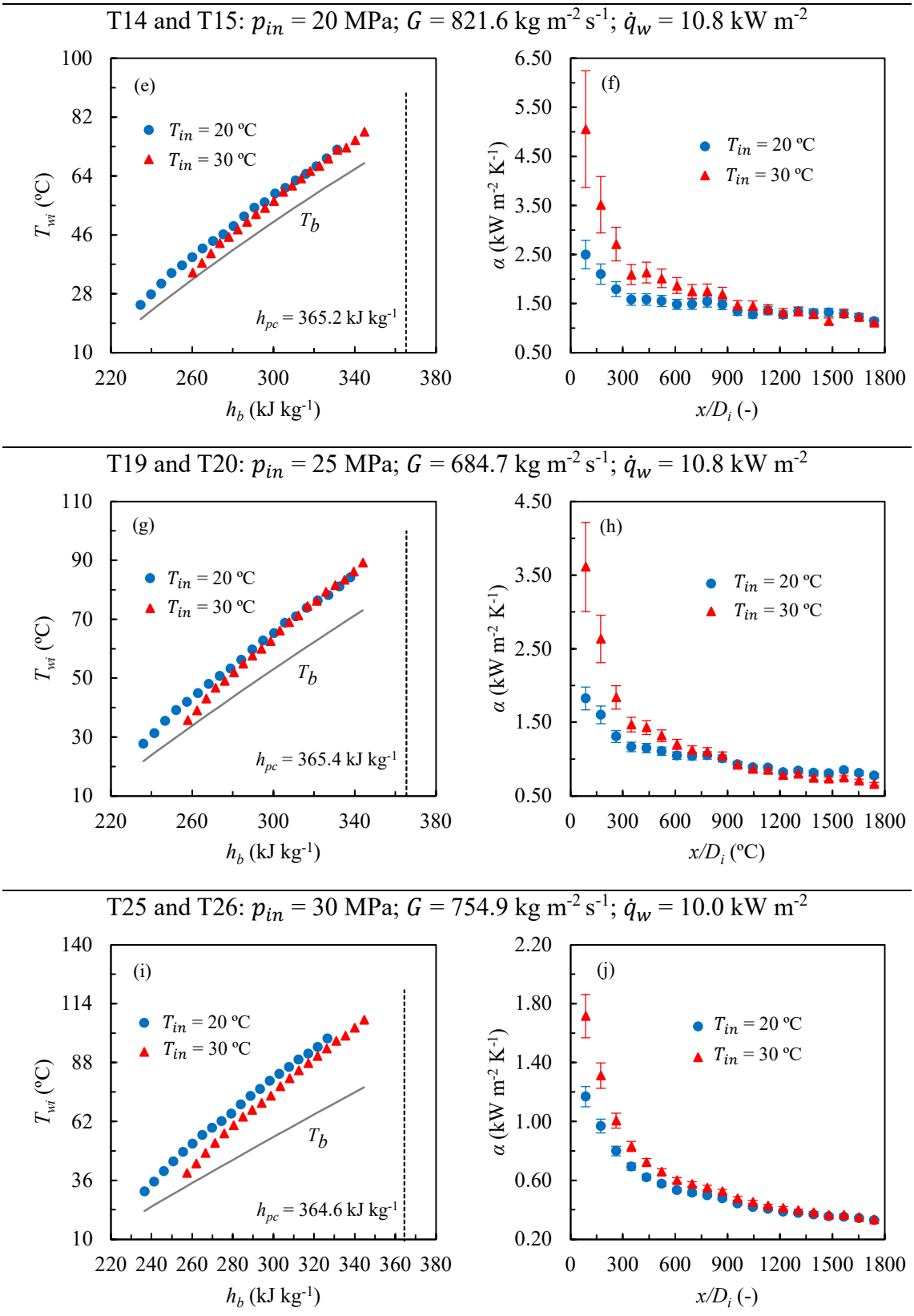

Fig. 6.4 (continued). Effect of inlet temperature on inner-wall temperature and local heat transfer coefficient for tests T4, T5, T9, T10, T14, T15, T19, T20, T25 and T26 (see Table 5.1). The higher the fluid inlet temperature, the higher the heat transfer coefficients in the inlet region.

Increasing the inlet fluid temperature results in an increase of the heat transfer coefficient within the thermal inflow length for all tested pressures. Given a constant mass flow, the Reynolds number increases with the bulk fluid temperature as a result of the decrease in viscosity. Thus, a higher inlet temperature implies that the Reynolds number and turbulence intensity are higher during the first heating interval, with a consequent heat transfer improvement. Nevertheless, downstream of the inflow region, heat transfer trends resulted qualitatively different based on the tested pressure.

As depicted in Fig. 6.4(b) for 10 MPa, the heat transfer coefficient decreases with increasing inlet temperature. For a fixed mass flow and heat input, an elevated inlet temperature results in a higher fluid outlet temperature, which expands the gas-like enthalpy region beyond the pseudo-critical point, while reducing the liquid-like region below it. This leads to a deterioration in heat transfer performance. Notably, the bulk fluid temperature corresponding to the peak heat transfer coefficient remains insensitive to variations in inlet temperature. For the inlet temperatures examined (20 and 30 ºC), a degradative valley region immediately follows the peak. Similar trends were reported in previous studies [109,110,263].

When the NET Power cycle operates at minimum load conditions, the inlet pressure and temperature of the $scCO_2$ flow to the RHE are at minimum values. Hence, these results reveal a heat transfer enhancement in the low-temperature section of the RHE under such conditions.

When the pressure was set at 15 MPa, Fig. 6.4(c) reveals an overlapping of the inner-wall temperatures after a certain length, indicative of a thermal fully developed flow [110]. However, for an inlet temperature of 30 ºC, the widening of the pseudo-critical region, originated by the increase of the fluid outlet temperature, leads to a slight reduction of the heat transfer coefficient near the end of the flow path, beyond the pseudo-critical point. This decline is less intense at 15 MPa than at 10 MPa.

It can be found in Figs. 6.4(e-j) that the local heat transfer coefficients exhibit a similar pattern as a function of the inlet temperature when the pressures were set at 20, 25 and 30 MPa. In the thermal inflow region, heat transfer is enhanced with increasing inlet temperature. Afterwards, the temperatures in the near-wall region overlap, leveling the heat transfer coefficients. Regarding the NET Power cycle working at nominal load, the $scCO_2$ pressure and temperature are at maximum values. Hence, this experimental study concludes that higher heat transfer rates may be expected within the thermal inflow region, slightly enhancing the overall effectiveness of the heat transfer process.

6.1.4 Effect of buoyancy

A temperature profile is developed in the fluid in the radial direction of the tube during fluid heating. The temperature in the near-wall region is higher than in the bulk, with a

steep gradient close to the wall. As a result, near-wall fluid packets reach the pseudo-critical point earlier than the bulk fluid. After heating above the pseudo-critical temperature, the near wall fluid experiences a sharp decrease in density. Meanwhile, the bulk fluid, which remains below the pseudo-critical temperature, stills exhibiting high density. This radial density gradient induces buoyancy forces that transport low-density fluid portions toward the top region of the tube along the walls. High density fluid flows downward through the centerline of the tube, transferring momentum. These induced secondary flow patterns intensify the turbulent mixing and the turbulent kinetic energy production. This leads to an enhancement of the average heat transfer rates. However, low-momentum fluid can accumulate at the top wall. This can eventually disrupt the secondary flow patterns, decrease heat transport by turbulent action, and thicken the thermal boundary layer. This causes a heat transfer deterioration in the top region of the tube. At the bottom region, the high-density fluid accumulates, which promotes kinetic energy production and enhanced heat transfer. These conclusions are further justified by flow field simulations in Section 6.3.

As the pressure of the supercritical fluid approaches the critical pressure, the density gradient between the liquid-like and gas-like fluid phases augments. As a result, buoyancy effects intensify. Thus, buoyancy-induced natural convection can significantly intervene on heat transport, especially for the tests conducted at 10 MPa. Consequently, quantifying the influence of buoyancy forces on heat transfer becomes essential. For turbulent mixed convection in horizontal flows, the best-known criterion to describe the influence of buoyancy on heat transfer is the Richardson number, Ri [241]. It has been previously applied by numerous authors to study supercritical fluid flows [95,99,100,109,110] presenting acceptable results. This criterion states that when natural convection, caused by buoyancy effects, significantly influences the heat transfer, the Ri number is higher than 10^{-3}, as it is stated in Eq. (6.2).

$$Ri = \frac{Gr_b}{Re_b^2} > 10^{-3}. \tag{6.2}$$

The Grashof number, Gr_b, defined in Eq. (6.3), relates the buoyancy and viscous forces,

$$Gr_b = \frac{g\beta(T_w - T_b)D_i^3}{v_b^2}. \tag{6.3}$$

Other authors [108,110,113] have employed the criterion built by Petukhov and Polyakov [264], which proposes a threshold Grashof number, Gr_{th}, defined in Eq. (6.4), that quantifies the strength of the buoyancy forces.

$$Gr_{th} = 3 \cdot 10^{-5} \overline{Pr}^{0.5} Re_b^{2.75} \left[1 + 2.4 Re_b^{-1/8} \left(\overline{Pr}^{2/3} - 1\right)\right] \tag{6.4}$$

The Prandtl number, $\overline{Pr}$, results from the integration of the specific heat to $\overline{Pr} = (\mu_b/\lambda_b) \cdot (h_w - h_b)/(T_w - T_b)$. Then, the Petukhov and Polyakov criterion states that when the effect of buoyancy-induced secondary flow does not significantly influence the heat transfer, the ratio Gr_q/Gr_{th} should be lower than the unity. Gr_q was previously defined in Eq. (6.1). Adebiyi et al. [97] and Tanimizu et al. [265] studied the criterion proposed by Jackson, which includes the thermal inflow length as an indication of the onset of buoyancy effects. The Jackson criterion establishes that in horizontal pipe flows, buoyancy effects cannot be neglected when

$$Ja = Ri \left(\frac{\rho_b}{\rho_w}\right) \left(\frac{x}{D_i}\right)^2 > 10. \tag{6.5}$$

Fig. 6.5 shows the buoyancy criterions of (a) Richardson, (b) Petukhov and (c) Jackson, plotted on a logarithmic scale, as a function of the distance from the heating onset, applied to the 560 experimental data points obtained in this work, for pressures of 10, 15, 20, 25 and 30 MPa.

As can be seen in Fig. 6.5(a), the Richardson criterion states that, for 10 MPa, convective heat transfer is affected by buoyancy, especially in the tube regions where the bulk enthalpy approaches the pseudo-critical enthalpy. For higher system pressures, the radial density gradient decreases, leading to a reduction in buoyancy effects. However, for experimental cases with a high $\dot{q}_w/G$ ratio, mixed convection is found for all tested pressures.

According to the Petukhov criterion, depicted in Fig. 6.5(b), only a few data points at 10 MPa are influenced by buoyancy. For pressures above 10 MPa, the Gr_q/Gr_{th} ratio remains below unity, indicating that buoyancy effects can be neglected. It can be seen in Fig. 6.5(b) that, for the tests conducted at 10 and 15 MPa, Gr_q/Gr_{th} increases along the tube to a peak before decreasing monotonically. This behavior results from the approximation of the inner-wall and bulk fluid temperatures in the vicinity of the pseudo-critical point, which causes a sharp increase in volumetric expansivity, and decrease in both kinematic viscosity and thermal conductivity. As the fluid is further heated beyond the pseudo-critical temperature, Gr_q/Gr_{th} decreases. The peak value of Gr_q/Gr_{th} increases with higher $\dot{q}_w/G$ values. For pressures above 15 MPa, the axial trend of Gr_q/Gr_{th} becomes flatter.

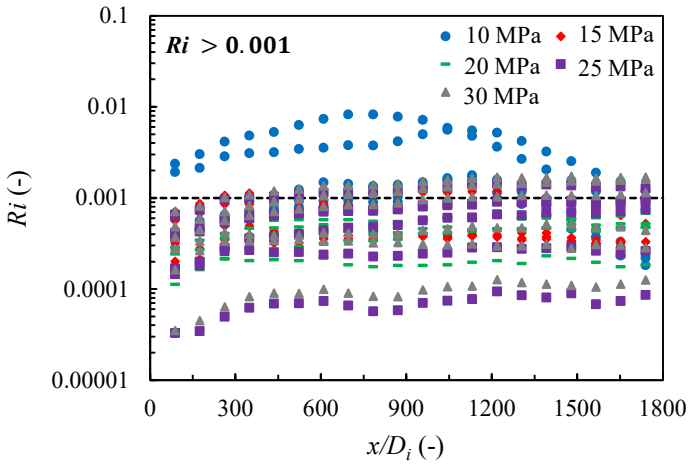

(a) Richardson criterion [241].

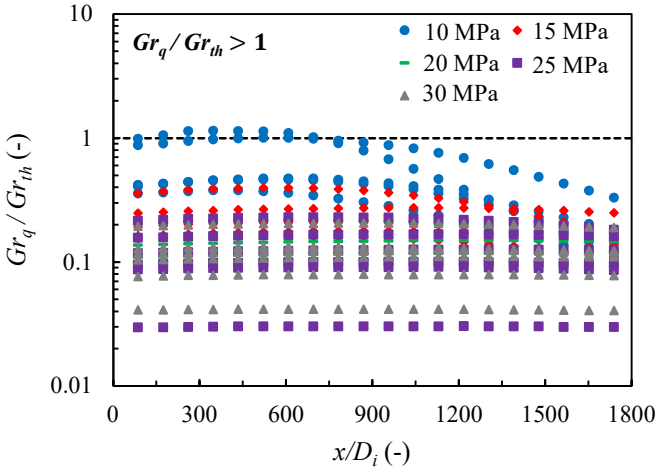

(b) Petukhov and Polyakov criterion [264].

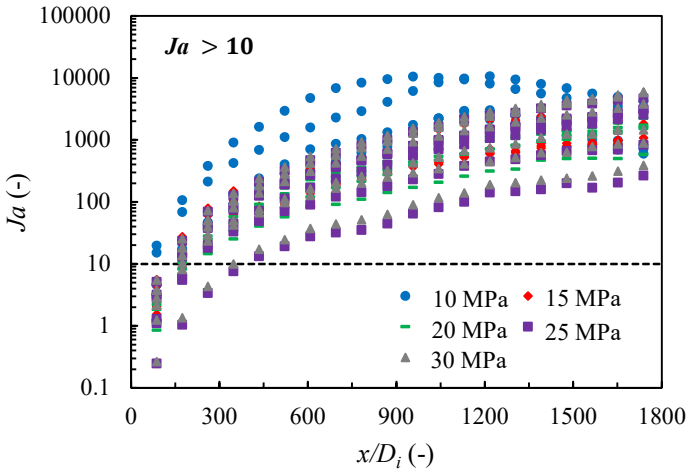

(c) Jackson criterion [97].

Fig. 6.5. (a) Richardson, (b) Petukhov and (c) Jackson criterions for buoyancy as a function of the inlet pressure. Buoyancy significantly affects convective heat transfer at 10 MPa, but its influence decreases with increasing pressure, although mixed convection can still occur when the heat-to-mass flux ratio is high.

Fig. 6.5(c) shows that, for most experimental conditions and tested pressures, the Jackson number, *Ja*, is greater than 10, indicating the presence of mixed convection. Jackson introduces the thermal inflow length, so that values at the tube inlet depart from a low buoyancy influence and increase along the tube. The local *Ja* number for 10 MPa increases to a maximum value, which is close to 10000, and then decreases. Similar tendencies were reported in previous studies [110]. For pressures above 10 MPa, all *Ja* values increase continuously throughout the tube. Moreover, Jackson criterion proves that the distance for which buoyancy effects start to become significant increases as the system pressure increases. Buoyancy effects cause low-momentum fluid to accumulate along the top wall of the tube, thickening the boundary layer and inducing a re-laminarization effect. At low mass fluxes, this effect counteracts the development of the turbulent boundary layer on the upper wall in the tests at 25 and 30 MPa, which explains the longer thermal inflow length observed in Figs. 6.4(h) and 6.4(j).

It is worth noting that, based on the definition of the Grashof number given in Eq. (6.3), the inner diameter of the flow channel appears in the numerator to the third power. This implies that a reduction of the tube diameter towards the microscale would lead to a notable decrease in buoyancy forces, which are usually neglected under constant-property gas flow conditions. However, the results derived in this work, which are in good agreement with previous research [97,108–110], demonstrated that, although the intensity of buoyancy decreases, it remains significant in microconfined CO_2 flows at supercritical pressures. Therefore, heterogeneous expansion in the microtubes of the NET Power cycle MSTHE, caused by buoyancy-induced thermal stratification, may appear. A potential solution to this adverse mechanical reaction would be to orient the microtubes vertically, with the $scCO_2$ flowing downward [93]. Anyway, this finding points out an additional advantage of MSTHEs over PCHEs. While the floating head of the MSTHEs allows absorbing the thermal stresses generated by the uneven expansion of the microtubes, the compact PCHEs block is susceptible to mechanical fatigue.

To clarify the effect of heat flux, mass flux and fluid inlet temperature on the strength of the buoyancy, Fig. 6.6 plots the mean Richardson number against: (a) heat flux, (b) mass flux and (c) inlet temperature, as a function of the investigated pressures. The codes of the employed tests, details of which were given in Table 5.1, are also provided in Fig. 6.6. For all tested pressures, the influence of buoyancy on heat transfer is accentuated as the thermal input is increased, which is in concordance with the definition of the Grashof number in Eq. (6.3). The increase of the inertia forces, derived from a mass flow augment, reduces the Richardson number, since it is inversely proportional to the Reynolds number. The influence of inlet temperature is found to be dependent on the tested pressure. For 10 MPa, the higher the inlet temperature, the higher the average Richardson number, which causes heat transfer deterioration in the upper half of the tube. For higher pressures, the buoyancy strength is diminished as the inlet temperature is increased.

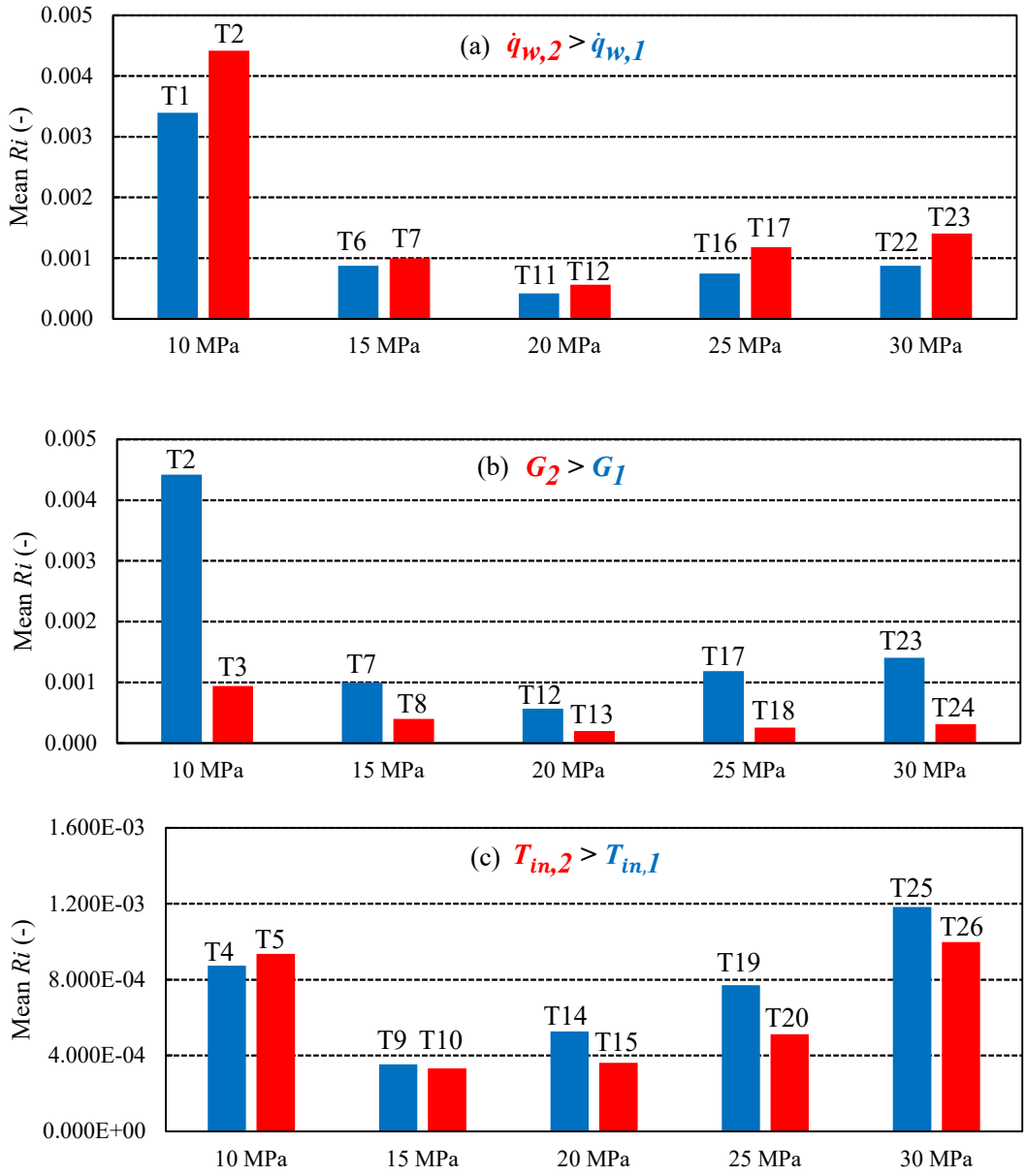

Fig. 6.6. Effect of (a) heat flux, (b) mass flux and (c) inlet fluid temperature on the mean Richardson number *Ri,* as a function of the tested pressure. The experimental tests employed are indicated in Table 5.1.

6.1.5 Effect of flow acceleration

The fluid density decreases in the axial direction of the tube as a result of the applied heat flux on the tube wall. This leads to an axial increase in flow velocity to satisfy mass conservation. To promote such acceleration, a favorable pressure gradient is imposed on the turbulent boundary layer. This intensifies the radial velocity gradient in the near-wall region, which enhances the turbulent kinetic energy. However, according to the literature, under large-scale flow channels, the axial pressure gradient can cause a re-adjustment of

the shear stress distribution across the boundary layer. As a consequence, the shear stress at the outer edge of the viscous sublayer decreases and this sublayer thickens. This phenomenon is commonly referred to as *re-laminarization*. As a result, less turbulence could be produced, and the heat transfer could be impaired.

Several criteria have been proposed to predict the potential heat transfer deterioration due to the thermally-induced flow acceleration effect. The criterion built by Jackson et al. [94], which defines the thermal acceleration parameter ψ as follows:

$$\psi = 10^4 \left(\frac{\beta_b \dot{q}_w D_i}{\lambda_b Re_b^{1.625} Pr_b}\right)\left(\frac{\mu_{ave}}{\mu_b}\right)\left(\frac{\rho_{ave}}{\rho_b}\right)^{-0.5}, \tag{6.6}$$

states that when the value of ψ is lower than 0.385, the heat transfer impairment due to thermal acceleration can be neglected. For heat transfer studies of $scCO_2$ in either vertical or horizontal flow configurations, numerous authors [93,95,266] employed the dimensionless thermal acceleration parameter K_v proposed by McEligot et al. [267], which is defined as:

$$K_v = \frac{4\dot{q}_w D_i \beta_b}{Re_b^2 c_{p,b} \mu_b}. \tag{6.7}$$

For values of K_v less than $3 \cdot 10^{-6}$ the flow remains turbulent and the effect of flow *re-laminarization* caused by thermal acceleration can be ignored. Theologou et al. [110] used the criterion of Petukhov et al. [268], which predicts the heat transfer deterioration using the coefficients of acceleration resistance, ξ_{ac}, and friction resistance, ξ_{Pe}, given in Eqs. (6.8) and (6.9).

$$\xi_{ac} = 8q_b^+ \tag{6.8}$$

$$\xi_{Pe} = \left(\frac{\rho_w}{\rho_b}\right)^{0.4} \left[1.8\log\left(\frac{Re_b}{8}\right)\right]^2 \tag{6.9}$$

In Eq. (6.8), the dimensionless heat flux is expressed as $q_b^+ = (\beta_b \dot{q}_w)/(c_{p,b} G)$. Thus, when the ratio ξ_{ac}/ξ_{Pe} is lower than 1 – 1.3, the influence of flow acceleration on heat transfer is negligible.

Fig. 6.7 represents the thermal flow acceleration criterions proposed by (a) Jackson, (b) McEligot and (c) Petukhov, in logarithmic scale, against the distance from the heating onset for the 28 experiments conducted in this study. According to the criterions, all experimental points lie below the respective threshold values. This means that the potential heat transfer impairment, caused by the thermal expansion-induced boundary layer *re-laminarization*, is negligible.

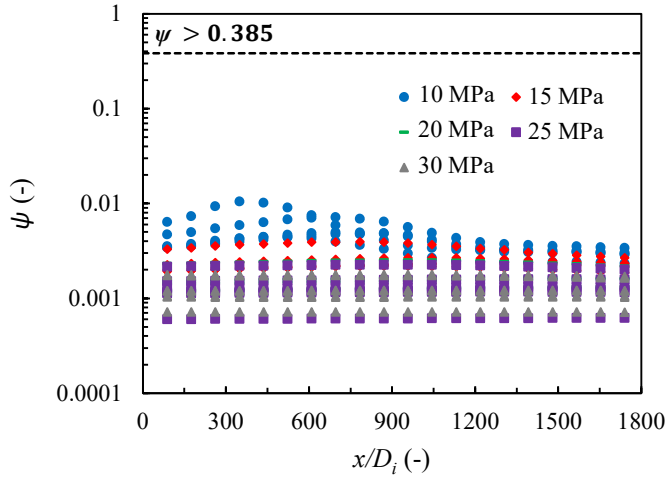

(a) Jackson criterion [269].

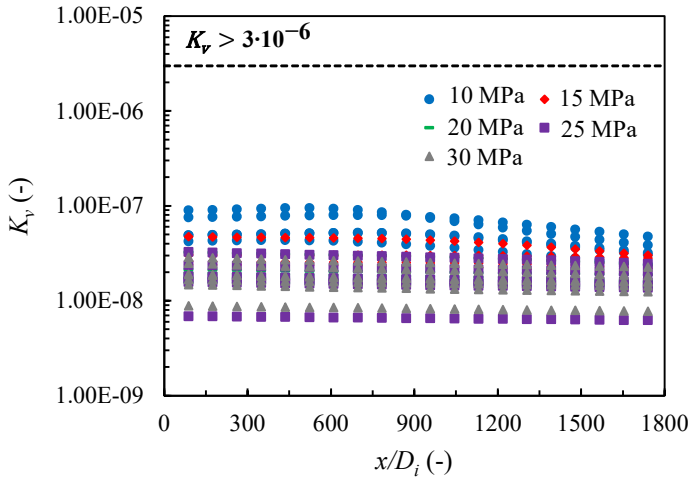

(b) McEligot criterion [267].

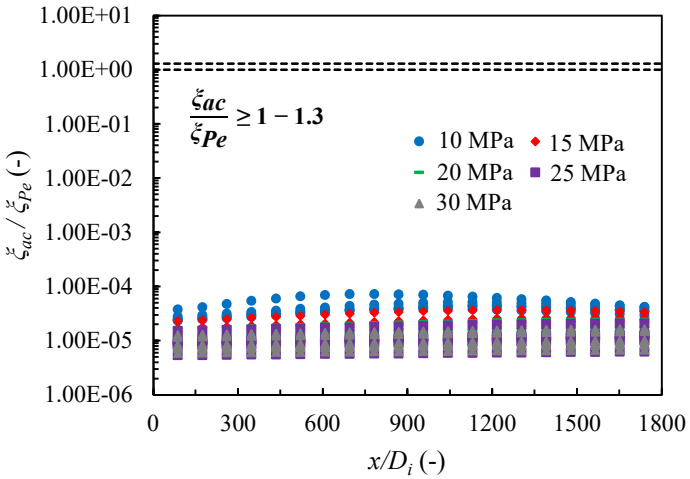

(c) Petukhov criterion [268].

Fig. 6.7. (a) Jackson, (b) McEligot and (c) Petukhov criterions for flow acceleration along the heating length as a function of the inlet pressure. According to the criterions, the effect of *re-laminarization* of the boundary layer by flow acceleration can be neglected.

Nonetheless, it is relevant to point out that the threshold value of the Petukhov criterion, ξ_{ac}/ξ_{Pe}, was found on the basis of experiments carried out with 8 mm inner diameter tubes in horizontal and vertical flow configurations. Therefore, there is uncertainty whether this threshold value can be extrapolated to the microscale.

6.2 Development of a new heat transfer model

Numerous empirical correlations for the prediction of heat transfer coefficients for supercritical fluid flows have been developed. A complete survey of them, with their application ranges, are available in [84,270]. Most of the correlations were derived for $scCO_2$ or scH_2O through large-diameter vertical tubes. Regarding $scCO_2$ through horizontal tubes, the number of correlations available is significantly smaller, which is explained by the reduced amount of experimental data. This data gap is further intensified when considering microtubes, with inner diameters of less than 1 mm.

Table 6.1 lists the most widely employed heat transfer correlations in literature for $scCO_2$. Although some of them were derived for a vertical flow orientation, they have proven to yield acceptable results for the horizontal configuration.

These correlations are founded on the well-known constant property turbulent flow Dittus-Boelter correlation [274], given in Eq. (6.10), and incorporate terms of property ratios to account for the large variation of fluid properties at bulk and wall temperatures.

$$Nu_b = 0.023 Re_b^{0.8} Pr_b^{0.4}, \tag{6.10}$$

The correlations of Liao et al. [100] and Wang et al. [109] were developed for microtubes, and include the Richardson number Ri to account for the heat transfer by buoyancy-induced natural convection. The model of Kim et al. [98] superimposes a correlation for forced convection heat transfer affected by flow acceleration Nu_{fc}, and a correlation for buoyancy-induced natural convection, Nu_{nc} [241]. The effect of the thermally-induced flow acceleration on forced heat transfer convection is considered on the basis of the two-layer heat transfer model [275–277].

The Bishop correlation [271] demonstrated to predict heat transfer coefficients for $scCO_2$, in large diameter horizontal tubes, with acceptable accuracy [110], despite it was fitted from experiments with upward flowing scH_2O. Moreover, the Bishop correlation considers the thermal inflow length as a parameter. The correlations of Swenson et al. [272] and Preda et al. [273] were evaluated by Kim et al. for horizontal flows.

Table 6.1. Heat transfer correlations for $scCO_2$ and scH_2O, under heating conditions, in horizontal and vertical flow configurations.

Authors	Correlation	Fluid and flow orientation	Application ranges
Liao et al. [100]	$Nu = 0.124 Re_b^{0.8} Pr_b^{0.4} (Ri_b)^{0.203} \left(\frac{\rho_w}{\rho_b}\right)^{0.842} \left(\frac{\bar{c_p}}{c_{p,f}}\right)^{0.384}$ $Gr = \frac{(\rho_b - \rho_w)\rho_b g D_i^3}{\mu_b^2}, \bar{c_p} = \frac{h_w - h_b}{T_w - T_b}$	$ScCO_2$, horizontal	D_i = 0.7-2.16 mm p = 74-120 bar T_b= 20-110 ºC $\dot{m}$ = 0.02-0.2 kg s^{-1} Ri = 10^{-5}-10^{-2}
Kim et al. [98]	$Nu = \left(Nu_{\mathrm{fc}}^2 + Nu_{\mathrm{nc}}^2\right)^{1/2}$ $Nu_{\mathrm{fc}} = a_1 Re_b^{0.8} Pr_b^{0.4} \frac{Q_b^{a_2}}{Re_b^{a_3} Pr_b^{a_4}} \left(\frac{\rho_{ave}}{\rho_b}\right)^{a_5} \left(\frac{\mu_{ave}}{\mu_b}\right)^{a_6} \left(\frac{\lambda_{ave}}{\lambda_b}\right)^{a_7}$ $\frac{1}{Nu_{\mathrm{nc}}} = b_1 Gr_q^{b_2} Pr_b^{b_3} \left(\frac{\rho_{ave}}{\rho_b}\right)^{b_4} \left(\frac{\mu_{ave}}{\mu_b}\right)^{b_5} \left(\frac{c_{p,ave}}{c_{p,b}}\right)^{b_6} \left(\frac{\lambda_{ave}}{\lambda_b}\right)^{b_7}$ $Q_b = \frac{\beta_b \dot{q}_w D_i}{\lambda_b}$ a_1 1.14; a_2 0.54; a_3 -0.50; a_4 -0.36; a_5 0.83; a_6 -3.48E-14; a_7 0.52 b_1 7.05; b_2 -0.30; b_3 -0.55; b_4 -14.64; b_5 3.52E-6; b_6 -8.23E-11; b_7 -5.35	$ScCO_2$, horizontal	D_i = 7.75-22.14 mm p = 73.83-77.35 bar T_{in}=13.8-30.1 ºC G = 52.1-391.9 kg m^{-2} s^{-1} $\dot{q}_w$= 1.2-26.9 kW m^{-2}
Wang et al. [109]	$Nu = 0.225 Re_f^{0.423} Pr_f^{0.229} (Ri_f)^{-0.156} (T^+)^{0.055} \left(\frac{\bar{c_p}}{c_{p,f}}\right)^{0.401}$ $T^+ = \frac{T_{pc} - T_{f,in}}{T_{f,out} - T_{f,in}}, \ \bar{c_p} = \frac{h_w - h_f}{T_w - T_f}$	$ScCO_2$, horizontal	D_i = 0.5-1.0 mm p = 76.6-90.0 bar T_{in}=30.8-37.3 ºC G = 672-4810 kg m^{-2} s^{-1} $\dot{q}_w$= 70.7-344.2 kW m^{-2}
Bishop [271]	$Nu = 0.0069 Re_b^{0.9} \overline{Pr_b}^{0.66} \left(\frac{\rho_w}{\rho_b}\right)^{0.43} \left(1 + 2.4\frac{D_i}{x}\right)$ $\overline{Pr_b} = \frac{\bar{c}_p \mu_b}{\lambda_b}, \ \bar{c}_p = \frac{h_w - h_b}{T_w - T_b}$	ScH_2O, vertical (upward)	p = 228-276 bar T_b = 282-527 ºC G = 651-3662 kg m^{-2} s^{-1} $\dot{q}_w$= 0.31-3.46 MW m^{-2}
Swenson et al. [272]	$Nu = 0.00459 Re_w^{0.923} \overline{Pr_w}^{0.613} \left(\frac{\rho_w}{\rho_b}\right)^{0.231}$	ScH_2O, vertical (upward)	D_i = 9.42 mm p = 227.5–413.7 bar T_b = 75-576 ºC G = 543-2150 kg m^{-2} s^{-1} $\dot{q}_w$ = 0.2–1.82 MW m^{-2}
Preda et al. [273]	$Nu = 0.0015 Re_w^{1.03} \overline{Pr_w}^{0.76} \left(\frac{\rho_w}{\rho_b}\right)^{0.46} \left(\frac{\mu_w}{\mu_b}\right)^{0.53} \left(\frac{\lambda_w}{\lambda_b}\right)^{-0.43}$	$ScCO_2$, vertical (upward)	p = 81.2 bar T_b = 25-125 ºC G = 430-1200 kg m^{-2} s^{-1} $\dot{q}_w$= 49.2-134.9 MW m^{-2}

In addition to the heat transfer models listed in Table 6.1, the Gnielinski correlation [181] for constant property turbulent flows at subcritical conditions, defined in Eq. (6.11), is commonly employed in literature.

$$Nu = \frac{(f/8)(Re_b - 1000)Pr_b}{1 + 12.7(f/8)^{0.5}\left(Pr_b^{2/3} - 1\right)}\left[1 + \left(\frac{D_i}{x}\right)^{2/3}\right], \tag{6.11}$$

$$\text{with } f = (1.82 \log_{10} Re_b - 1.64)^{-2}.$$

Predictions of these correlations are compared against the experimental data, derived in this study, using the average of absolute relative deviation (AARD), defined as follows:

$$\text{AARD (\%)} = \frac{100}{N}\sum_{i=1}^{N}\left|\frac{\alpha_{cal,i} - \alpha_{exp,i}}{\alpha_{exp,i}}\right|. \quad (6.12)$$

Comparisons between the experimental and calculated Nusselt numbers from the correlations of Table 6.1, including the Gnielinski correlation, are depicted in Fig. 6.8. The correlation of Kim et al. constantly yielded unreasonable Nusselt number values, so it was excluded during the comparison. An incorrect typing of a fitting coefficient in the original publication is a possible explanation. To quantitatively compare the performance of the correlations, the AARD for all data points, as well as the percentage of predicted data within a range of 30%, 40% and 60%, are shown in Table 6.2.

Table 6.2. Comparison of the prediction accuracy among the evaluated heat transfer correlations. The heat transfer models developed in this work (i.e., the empirical correlation and the DNN) are highlighted in bold.

		Percentage of data predicted within		
Heat transfer model	AARD (%)	30%	40%	60%
Liao et al. [100]	164.49	8.59	12.11	24.89
Wang et al. [109]	114.01	20.70	28.19	40.31
Bishop et al. [271]	113.51	11.01	16.08	30.18
Gnielinski [181]	148.34	8.15	9.91	20.48
Preda et al. [273]	66.53	31.72	41.19	57.27
Swenson et al. [272]	76.82	28.41	33.92	49.56
Correlation (present work)	**18.73**	**86.82**	**94.29**	**99.90**
DNN (present work)	**6.74**	**98.68**	**99.78**	**100.00**

It can be found in Fig. 6.8 that the correlations overestimate the Nusselt numbers. The correlations of Liao et al. and Gnielinski reported the highest AARD values; 164.49% and 148.34%, respectively. The correlation of Preda et al. proves to be the most accurate, with an AARD of 66.53%, followed by the correlation of Swenson et al., with an AARD of 76.82%. The overestimations can be explained by different reasons depending on the operating pressure.

Near the critical point (i.e., 10 MPa), the correlations for supercritical fluid flows in Table 6.1 were fitted for a narrow application range. Outside that range, the predictions become inaccurate. Kim at al. [98] and Theologou et al. [110] also reported significant overestimates of the Nusselt numbers when challenging various correlations against their experimental data. This suggests that the strength of buoyancy forces is not properly captured by the correlations. Kim et al. [98] tested the correlations of Lei et al. [278], Swenson et al., Mokry et al. [279], and Preda et al. The comparison was conducted for the Nusselt numbers of the top and bottom tube walls, in which the heat transfer is deteriorated and enhanced under heating conditions, respectively. Figs. 6.9(a) and 6.9(b) show the overestimation of the Nusselt numbers by the correlations, especially in the top wall.

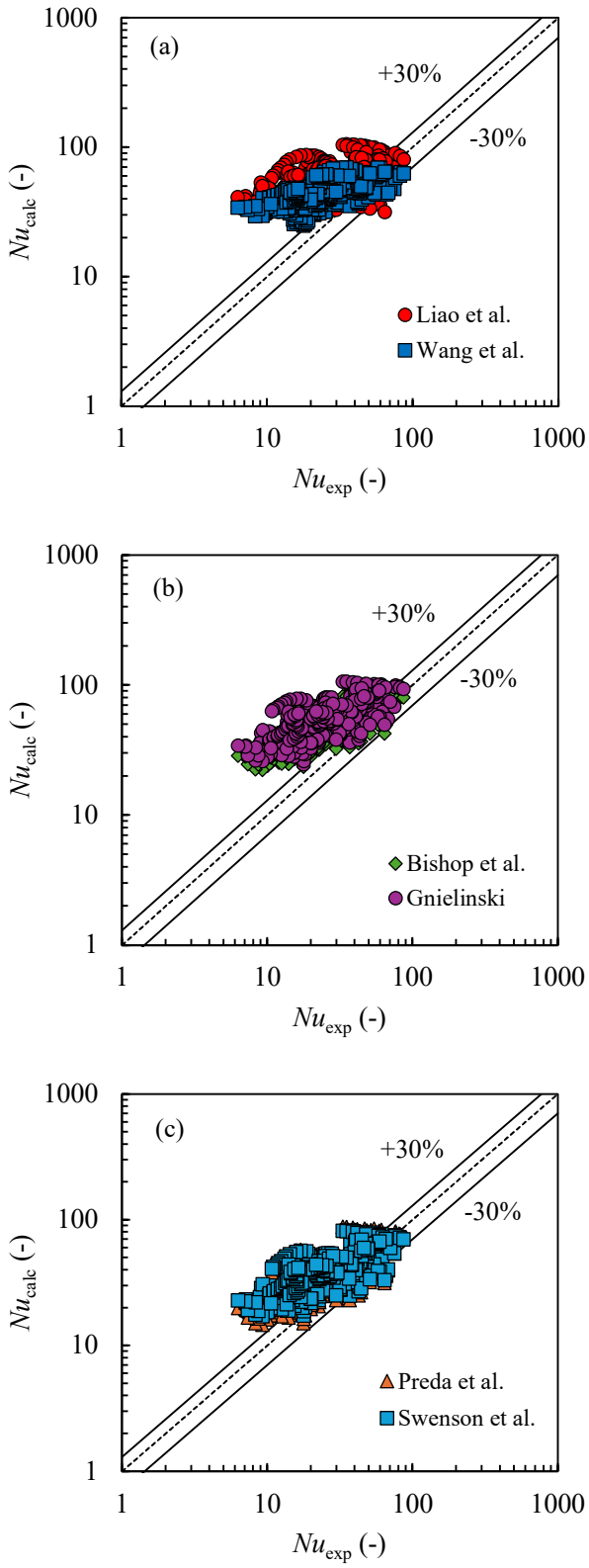

Fig. 6.8. Comparison of experimental and calculated data in terms of the Nusselt number. The considered correlations were: (a) Liao et al. [100] and Wang et al. [109], (b) Bishop et al. [271] and Gnielinski [181], (c) Preda et al. [273] and Swenson et al. [272]. Correlations overestimate the Nusselt numbers mainly due to the low experimental Reynolds numbers.

Theologou et al. [110] tested the correlations of Gnielinski, Bishop et al., Liao et al., and Lei et al., reporting AARD values of 308%, 89%, 248%, and 213%, respectively. In the process of computationally deriving a heat transfer correlation, Wang et al. [280] found, after a thorough literature survey, permanent overestimations of the heat transfer rates of $scCO_2$ through horizontal flow channels by the Gnielinski correlation.

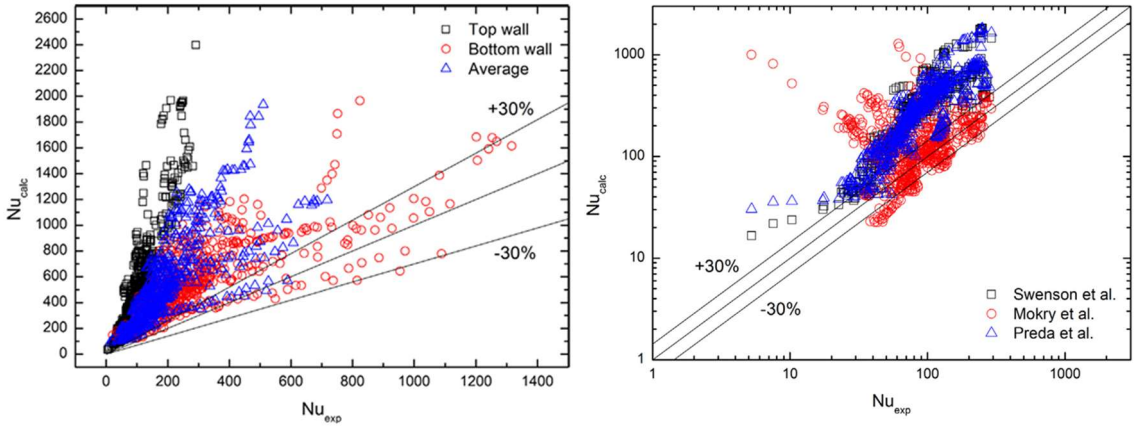

(a) Kim et al. [98] (b) Kim et al. [98]

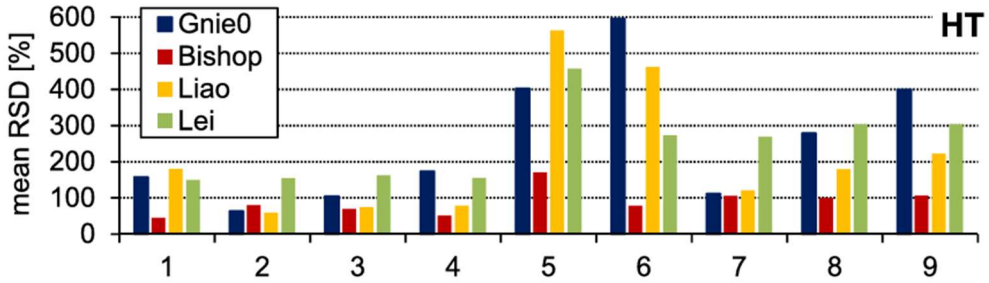

(c) Theologou et al. [110]

Fig. 6.9. Comparison of experimental and calculated data by various correlations in the works of (a and b) Kim et al. [98], and (c) Theologou et al. [110]. The correlation of Lei et al. [278] was used for (a) and (c) in green color.

As the test pressure increases (between 15 and 30 MPa), the fluid viscosity rises, leading to a significant reduction in Reynolds numbers, as shown in Table 5.1. In fact, 56% of the heat transfer coefficients were acquired at Reynolds numbers below 10^4. Under the controlled conditions of the experiments, this implies that certain flow regions likely remain in the transitional regime, where viscosity limits efficient transverse fluid mixing. This is manifested by the progressive separation between the wall and bulk fluid temperature profiles shown, for example, in Fig. 6.4(i). On the other hand, the conventional Gnielinski correlation is valid for Reynolds numbers between 10^4 and 10^6, under the assumption of fully developed turbulence. In this flow regime, heat transfer rates are considerably higher than in transitional flow, which explains the observed overestimation of the Nusselt numbers in Fig. 6.8. Furthermore, it is noticeable from Fig. 6.8 that the higher the Nusselt number (i.e., higher Reynolds), the more accurate the

predictions are, reinforcing this physical interpretation. Additionally, the flow laminarization effect is accentuated at high pressures due to the reduced axial flow acceleration, which increases de residence time. This favors the accumulation of low-momentum fluid on the top wall, delaying the flow development towards the turbulent regime.

6.2.1 Empirical heat transfer correlation

Discrepancies of existing correlations suggest that a suitable correlation for predicting heat transfer coefficients of $scCO_2$ in horizontal microtubes, for pressures up to 30 MPa and the Reynolds number ranges of Table 5.1, still needs to be developed. For this purpose, the Dittus-Boelter heat transfer correlation, previously expressed in Eq. (6.10), was used as a baseline model. Preda et al. [273] and Mokry et al. [279] identified the main dimensionless groups governing mixed convective heat transfer in $scCO_2$ flows on the basis of a dimensional analysis. As a result, the new correlation should have the generic functional form presented in Eq. (6.13):

$$Nu_x = C_1 Re_{b,x}^{m_1} Pr_{b,x}^{m_2} Ri_{b,x}^{m_3} \left(\frac{\rho_w}{\rho_b}\right)_x^{m_4} \left(\frac{\mu_w}{\mu_b}\right)_x^{m_5} \left(\frac{\lambda_w}{\lambda_b}\right)_x^{m_6} \left(\frac{\bar{c}_p}{c_{p,f}}\right)_x^{m_7} \left(1 + C_2 \frac{D_h}{x}\right)^{m_8}$$
$$\bar{c}_{p,x} = \frac{h_{w,x} - h_{b,x}}{T_{w,x} - T_{b,x}} \tag{6.13}$$

The property ratios account for the variation in fluid properties between the near-wall region and the bulk of the tube. The last term on the right-hand side of the correlation represents the thermal inflow length, which increases the heat transfer rates during the development region of the thermal boundary layer. The subscripts *b*, *w* and *f* refer to a fluid property calculated at bulk, wall and film temperature, respectively. The subscript *x* stands for the axial position along the heated length. The correlation expression, together with the experimentally derived Nusselt numbers, were entered into Matlab R2022b [171]. The C_1 - C_2 and m_1 - m_8 coefficients were fitted using a non-linear regression method from the Matlab Optimization Toolbox. All data points, 560, that were acquired in this work from the 28 performed experiments (see Table 5.1), were used for the correlation adjustment. The regression method optimized the fitting coefficients to minimize an objective function, which is the sum of squares of the residual values:

$$\text{objective function} = \sum_{i=1}^{N} \left(Nu_{\text{calc},i} - Nu_{\text{exp},i}\right)^2, \tag{6.14}$$

where N is the total number of points, 560. The resulting correlation is given in Eq. (6.15).

$$Nu_x = 0.0038 Re_{b,x}^{0.850} Pr_{b,x}^{2.038} Ri_{b,x}^{-0.028} \left(\frac{\rho_w}{\rho_b}\right)_x^{1.518} \left(\frac{\mu_w}{\mu_b}\right)_x^{4.690} \left(\frac{\lambda_w}{\lambda_b}\right)_x^{2.556} \left(\frac{\bar{c}_p}{c_{p,f}}\right)_x^{1.943} \quad (6.15)$$

No improvement was found in the predictions including the thermal inflow length term in Eq. (6.15); therefore, it was excluded from the correlation. The new empirical correlation, given in Eq. (6.15), is valid for a microtube of D_i = 0.88 mm in the range of $10 \leq p_{in} \leq 30$ MPa, $4099.9 \leq Re_b \leq 23847.4$, $19.8 \leq T_b \leq 101.8$ ºC, $447.4 \leq G \leq 1355.2$ kg·m^{-2}·s^{-1}, and $8.3 \leq \dot{q}_w \leq 21.3$ kW·m^{-2}.

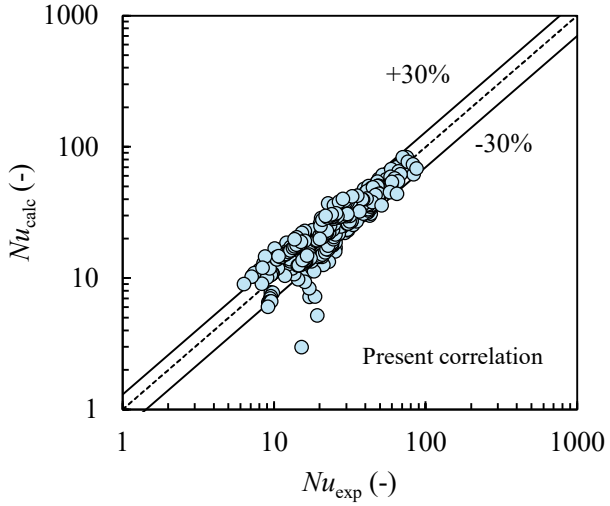

Fig. 6.10. Comparison of the experimental and calculated data in terms of the Nusselt number for the empirical heat transfer correlation developed in this work. 86.8% of the data satisfies a relative deviation of less than 30%.

The comparisons between the experimental results of the local Nusselt number and predicted values, based on the present empirical correlation of Eq. (6.15), are illustrated in Fig. 6.10. It can be seen that the present correlation improves the predictions with respect to the other correlations. The results demonstrate that the AARD is 18.95%, with a 86.6% of the data satisfying a relative deviation of less than 30%, as depicted in Table 6.2. This indicates that the new correlation can reasonably predict the local Nusselt numbers in the wide pressure range considered.

6.2.2 Artificial deep neural network-based heat transfer model

The accuracy of the predictions given by the correlation of Eq. (6.15) can be improved by using an artificial deep neural network (DNN) as a heat transfer model of $scCO_2$, $Nu_{DNN} = DNN(\boldsymbol{x})$ [86].

To propose a more feasible heat transfer model, the DNN, with the structure presented in Fig. 6.11, was developed for the 560 experimental Nusselt number data points acquired in this work. A DNN-based heat transfer model can capture the experimental data with less deviation compared to a conventional heat transfer correlation. This is especially important in this study, in which the experimental pressure range is wide. The DNN includes four layers: an input layer; two hidden layers with 15 and 10 units, respectively; and an output layer. The inputs to the DNN are expressed in Eq. (6.16) by the input vector $\boldsymbol{x}$.

$$Nu_{b,DNN} = DNN(\boldsymbol{x}), \text{ with } \boldsymbol{x} = \left\{ Re_b, Pr_b, \frac{\rho_w}{\rho_b}, \frac{\mu_w}{\mu_b}, \frac{\lambda_w}{\lambda_b}, \frac{\bar{c_p}}{c_{p,f}}, \frac{x}{D_i}, \frac{p_{in}}{p_{cr}} \right\} \tag{6.16}$$

The property ratios account for the variation of the fluid properties between the near-wall region and the bulk of the tube. The x/D_i ratio allows modeling local heat transfer coefficients, including the thermal inflow effects. The heat transfer performance of $scCO_2$ is strongly affected by the pressure, as concluded in the previous sections. Although the influence of the pressure is embedded in the physical properties of the fluid, a significant improvement in the predictive capability of the model was found when the term p_{in}/p_{cr} was included as an input. p_{cr} denotes the critical pressure of CO_2 (~ 73.8 bar).

The hyperbolic sigmoid function (tansig) [281], defined in Eq. (6.17), was used as the activation function for the hidden layer neurons.

$$\text{tansig}(x) = \frac{e^x - e^{-x}}{e^x + e^{-1}} \tag{6.17}$$

Then, the output of the j^{th} hidden unit (HU), of the first hidden layer, can be computed as follows:

$$HU_{1j} = \text{tansig}\left(\sum_{i=1}^{N_{in}} w_{1ji} x_i + b_{1j} \right), \tag{6.18}$$

where i is the i^{th} input, w are the synaptic weights, b the bias, and N_{in} the total number of inputs. In general, the output of the j^{th} HU of the k^{th} layer is calculated according to Eq. (6.19).

$$HU_{kj} = \text{tansig}\left(\sum_{i=1}^{N_{HU_{k-1}}} w_{kji} HU_{k-1,i} + b_{kj} \right). \tag{6.19}$$

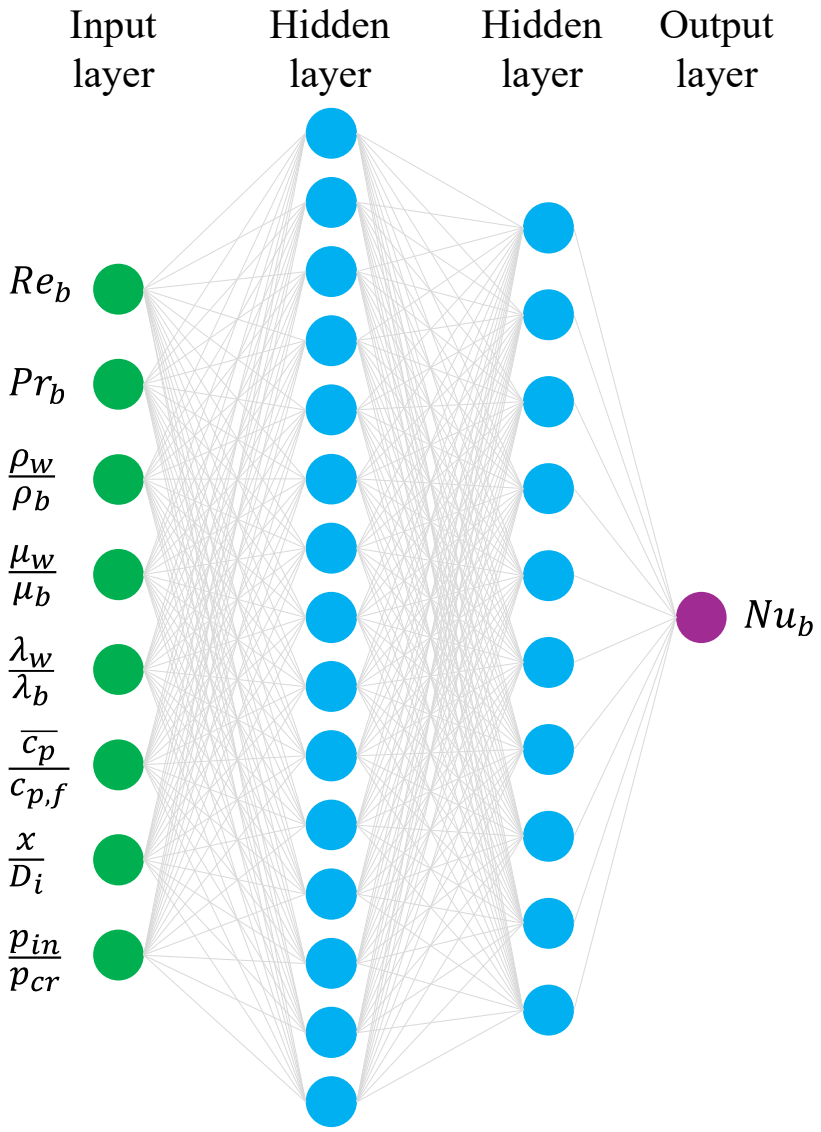

Fig. 6.11. Structure of the artificial deep neural network based heat transfer model. The DNN consists of four layers: an input layer, two hidden layers, and an output layer.

N_{HUk} denotes the total number of HU in the k^{th} layer. Then, the output results:

$$DNN(\boldsymbol{x}) = \sum_{i=1}^{N_{HU_{M-1}}} w_{o,i} HU_{M-1,i} + b_o, \tag{6.20}$$

where M is the number of layers. The DNN model, together with the experimental Nusselt numbers, were entered in Matlab R2022b. The weights and bias were trained to minimize the mean square error using the 70% of the experimental data points, while the remaining were used for validation (15%) and testing (15%). The resulting weights and bias are given in Table 6.3.

Table 6.3. Weights and bias of the artificial deep neural network.

w_1							
-0.61	-0.11	1.12	-0.84	0.71	0.91	0.03	-0.56
-0.43	-0.62	-0.94	0.32	0.51	-0.29	-1.22	0.98
0.66	-0.81	0.16	-1.01	0.42	1.05	0.43	1.40
1.98	0.71	1.25	0.51	0.26	-0.24	-1.01	-0.10
1.28	-0.38	-0.21	0.93	1.18	0.35	1.38	-0.80
-0.10	-0.79	0.62	-0.54	0.44	0.61	-0.70	-0.37
-1.52	-1.47	1.02	-0.92	-0.57	0.07	-0.51	-0.84
2.56	-0.33	-0.52	0.14	0.17	0.08	-2.71	0.75
0.14	0.52	-2.30	-2.38	-0.62	-0.31	-0.13	0.08
2.10	0.09	-0.95	0.64	-0.88	1.28	0.51	0.12
-1.07	-0.89	-1.59	-0.40	0.10	-0.32	0.24	2.21
0.40	1.11	0.98	-1.52	0.31	-0.08	0.63	-0.69
0.50	0.29	0.50	0.49	1.28	-1.05	-0.14	-0.61
-0.05	0.09	0.48	-1.06	-0.42	-0.12	2.16	0.00
0.15	-0.58	0.22	0.82	0.61	0.19	-1.05	-1.46
w_2							
-0.32	-0.87	0.34	1.07	0.12	-0.97	-0.19	-1.39	0.10	-0.60	-0.17	1.14	-0.40	-0.51	-0.42
0.19	0.18	-0.26	1.21	0.41	0.26	0.46	-0.66	0.35	0.01	0.52	-0.61	-0.24	0.80	-0.60
0.21	-0.56	0.71	1.43	-0.63	-1.14	-0.62	0.60	0.22	-1.32	-0.25	0.15	-0.88	-0.86	-0.33
0.14	-0.22	0.17	-2.32	0.63	0.36	-0.32	1.02	-0.42	0.60	-0.07	-0.16	0.08	-0.69	-0.05
-0.07	0.55	0.38	-0.14	0.03	0.00	-0.27	-0.31	0.15	0.10	0.29	0.95	-0.21	1.15	0.30
-0.28	0.67	-0.25	-0.88	0.62	-0.39	0.04	-0.62	0.76	-0.13	0.86	0.41	0.15	-0.12	-1.09
-0.02	-0.52	0.23	0.99	0.05	-0.57	1.44	0.02	-0.27	-0.13	0.32	1.09	-0.45	0.49	-0.17
-0.42	0.34	-0.85	-0.53	0.32	0.10	0.51	-1.73	0.33	-0.88	0.77	-1.13	-0.48	0.32	0.60
-0.72	-0.97	-0.19	2.13	-0.21	-0.04	0.24	-1.26	-0.35	-0.58	0.29	-0.24	0.25	-1.15	0.37
-0.38	-0.49	0.89	-0.10	-0.05	-0.71	0.69	0.17	-0.08	0.36	-0.37	0.43	-0.07	0.27	-0.64
w_3														
0.21	0.48	0.65	-0.24	0.05	0.00	0.13	-0.21	0.96	-0.80					
b_1														
1.95	1.78	-1.39	-0.69	-0.27	1.61	0.34	0.62	0.18	1.12	-1.59	0.98	2.47	1.90	2.59
b_2														
1.39	-1.14	-1.09	0.72	0.53	-0.26	0.00	-0.75	-1.50	-1.91					
b_3														
0.96														

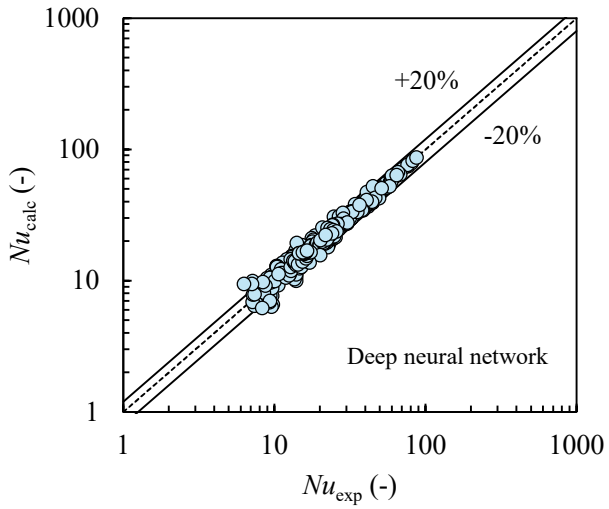

Fig. 6.12. Comparison of the experimental and calculated data in terms of the Nusselt number for the artificial deep neural network heat transfer model developed in this work. 94.5% of the data shows a relative deviation under 20%.

The comparison between the experimental and the DNN predicted Nusselt number values are illustrated in Fig. 6.12. It can be clearly concluded that the DNN-based heat transfer model improves the predictions with respect to the existing correlations, including Eq. (6.15). As can be seen in Table 6.2, the DNN captures the experimental data with an AARD of 6.74%, with 94.49% of the data satisfying a relative deviation of less than 20%. This indicates that the new heat transfer model can be used for MSTHE design purposes for the low-temperature section of the NET Power cycle recuperator.

6.3 Computational research on the heat transfer mechanisms

In this section, the fundamental mechanisms governing heat transfer in $scCO_2$ flowing through horizontal flow channels are investigated using the CFD model described in Section 5.2. To this end, the RANS turbulence models, introduced in Section 5.2.2, are validated in Section 6.3.1 against the experimental data acquired in this work. This validation ensures that the turbulence characteristics are properly captured, providing confidence in the applicability and reliability of the simulation outcomes. Subsequently, in Section 6.3.2, the influence of buoyancy and flow acceleration on the heat transfer process in $scCO_2$ are analyzed as a function of the tube diameter, fluid pressure and wall heat flux.

6.3.1 Validation of the numerical solution

The CFD numerical model, presented in Section 5.2, was validated against the experimental results obtained in this work. To this end, the geometry of the CFD model was generated to reproduce the exact dimensions of the microtube section used during the experimental tests.

The output variable used during the validation was the temperature of the inner-wall of the tube. To ensure that the results of the CFD model are applicable and reliable over the entire operating range of the NET Power cycle, it was validated against the experimental conditions T3, T8, T13, T21 and T28, each corresponding to a tested pressure of 10, 15, 20, 25 and 30 MPa. The aforementioned tests were selected because they were conducted at high Reynolds numbers, which assures a fully developed turbulent flow regime. Fig. 6.13 compares the CFD model results using the SST k-ω, RNG k-ε, LS, YS and AKN turbulence models (see Section 5.2.2) versus experimental measurements. To quantitatively compare the closeness of the numerical model predictions with the experimental data, the AARDs are shown in Table 6.4.

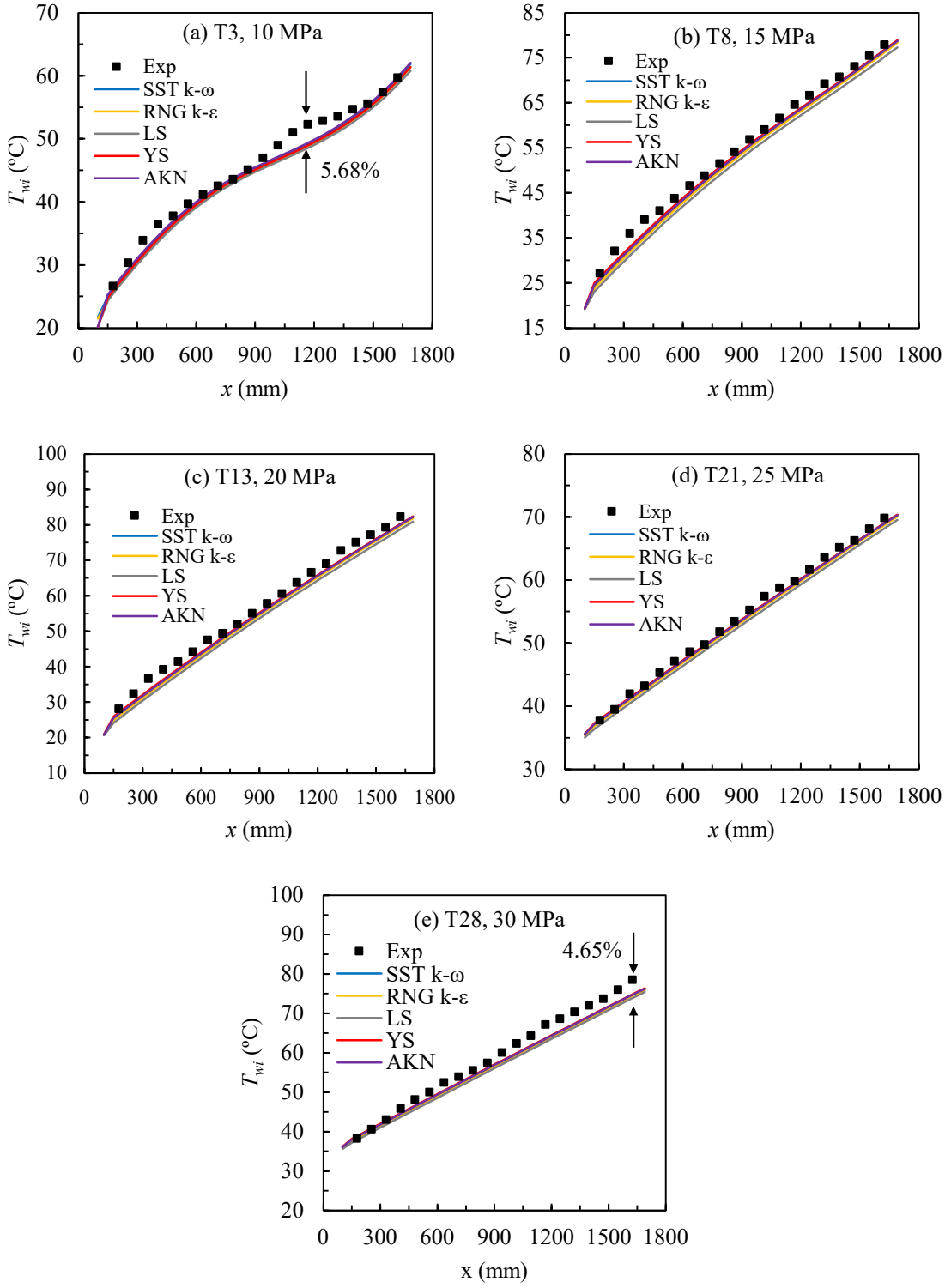

Fig. 6.13. Comparison of the inner-wall temperatures calculated by the CFD model versus the experimental data for validation of the first-order RANS turbulence models. The test conditions used for the comparison can be found in Table 5.1.

Table 6.4. Comparison of the predicted accuracy in terms of the AARD of the evaluated first-order RANS turbulence model as a function of the tested pressure.

Turbulence model	AARD (%)					**Average**
	T3 10 MPa	T8 15 MPa	T13 20 MPa	T21 25 MPa	T28 30 MPa	
SST k-ω	3.00	3.96	4.32	1.23	4.04	**3.31**
RNG k-ε	4.08	5.03	5.28	1.74	4.49	**4.12**
LS	4.47	6.67	6.89	2.69	5.40	**5.22**
YS	3.43	3.19	3.78	1.08	3.85	**3.07**
AKN	2.43	3.89	4.34	1.26	4.05	**3.19**
Average	**3.48**	**4.55**	**4.92**	**1.60**	**4.37**	

It can be seen that all the considered turbulence models are able to qualitatively reproduce the evolution of the wall temperature for the five tests. Other authors have also found, in general, an acceptable agreement between numerical predictions and the experimental data [89,90,114,280,282,283]. For a pressure of 10 MPa, the wall temperature peak, which arises due to buoyancy-induced heat transfer deterioration, is not accurately captured by the turbulence models. However, the relative deviation within the deterioration regime was not exceed 5.68%, as illustrated in Fig. 6.13(a). This suggests that the strength of buoyancy forces is underestimated by the turbulence models.

In the computational investigations of heat transfer to $scCO_2$ in horizontal tubes conducted by Wang et al. [280], the authors also arrived to a similar conclusion. They validated a CFD model of a heated tube, with an inner diameter of 22.14 mm and heated length of 2.44 m, using the experimental measurements obtained by Adebiyi et al. [97]. The results of their validation are shown in Fig. 6.14. As can be deduced, the CFD model predicts a lower temperature than the experimental one at the top wall of the tube. Manda et al. [284] found that this deviation, at the top wall of the tube, intensifies with increasing the heat flux, as a result of increasing the buoyancy forces.

For a pressure of 30 MPa, the turbulence models reported a slight deviation increase at high temperature, as plotted in Fig. 6.13(e). The observed error is 4.65% for the YS turbulence model. In addition, Wang et al. [280] found that the AKN and YS turbulence models perform better than the rest.

According to Table 6.4, in this work, it was found that the turbulence model with predictions closest to the experiments is the YS, which reports an AARD of 3.07%. Followed, the models AKN, SST k-ω, RNG k-ε and, with larger deviation, the LS. These models reported AARD values of 3.19%, 3.31%, 4.12% and 5.22%, respectively. Therefore, the YS low-Reynolds number turbulence model is selected for the subsequent computational study of this work.

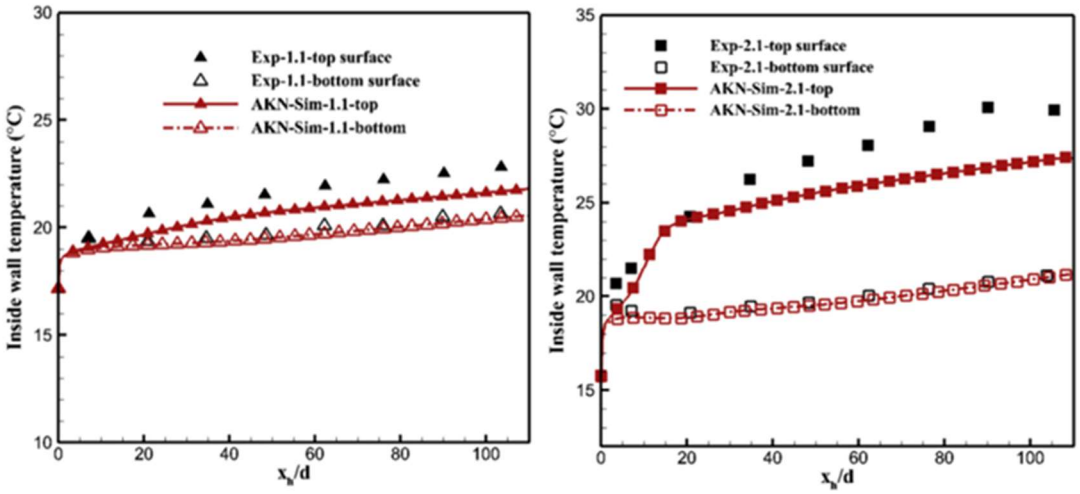

Fig. 6.14. Validation of the numerical CFD model of Wang et al., adapted from [280].

6.3.2 Heat transfer mechanisms

The influence of buoyancy and thermal acceleration on the $scCO_2$ flow and heat transfer was numerically investigated in this section. Two horizontal tubes, with internal diameters of 1 mm and 4 mm, were considered under uniform heating conditions. Unlike the simulations performed in the previous section, where a 1700 mm long tube was used to validate RANS turbulence models against experimental data, the present simulations employed tubes of 1000 mm length, with 100 mm adiabatic thermal inflow length. This reduction in length was aimed at decreasing the computational cost. The analysis of buoyancy and flow acceleration effects was primarily focused on the 4 mm diameter tube, as the influence of buoyancy, according to the Grashof number defined in Eq. (6.3), becomes more significant with increasing tube diameter.

The influence of heat flux and fluid pressure boundary conditions on heat transfer mechanisms was evaluated for heat flux values of 26 $kW \cdot m^{-2}$ and 30 $kW \cdot m^{-2}$, and pressure values of 8 MPa and 28 MPa. The fluid inlet temperature was fixed at 20 ºC for all simulations. In total, five simulation cases were conducted, with the exact boundary conditions summarized in Table 6.5. All simulations were performed assuming an inlet Reynolds number of 8000. To achieve this, the mass flux was adjusted for each case based on the tube diameter, applied heat flux, and static fluid pressure.

Table 6.5. Boundary conditions of the computational cases.

Simulation code	G (kg m^{-2} s^{-1})	D_i (mm)	$\dot{q}_w$ (kW m^{-2})	p (MPa)
S1	620	1	26	8
S2	920	1	26	28
S3	155	4	26	8
S4	155	4	30	8
S5	230	4	26	28

6.3.2.1 *Buoyancy effects*

Fig. 6.15 illustrates the evolution of the radial velocity profile of $scCO_2$ along the tube as a function of the temperature ratio T_b/T_{pc} for simulation S3.

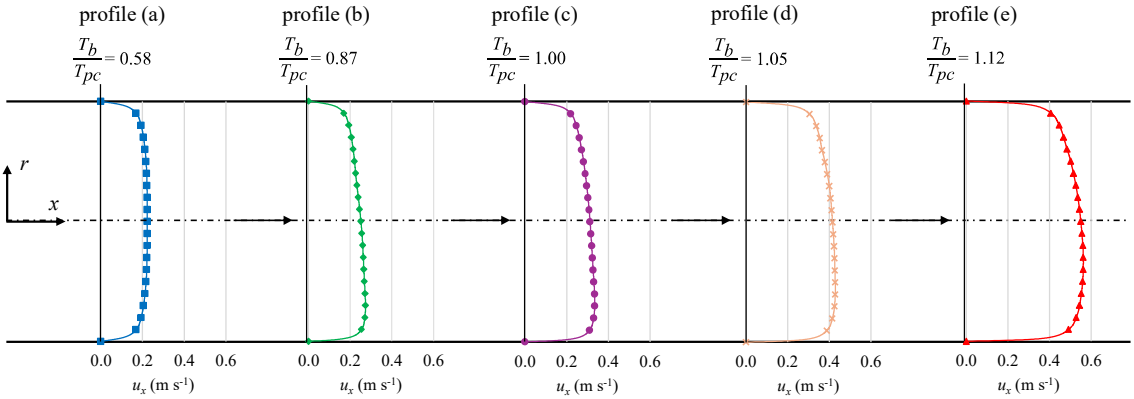

Fig. 6.15. Radial flow velocity profile along the tube, as a function of T_b/T_{pc}, for the simulation S3 (see conditions in Table 6.5).

Initially, at the entrance of the heated region (profile (a)), the flow exhibits a fully axisymmetric radial velocity distribution with a uniform temperature profile. As the fluid is heated from the wall, a radial temperature gradient develops, which is more pronounced near the wall due to the damping of the turbulent quantities in this region. Consequently, the near-wall fluid eventually reaches T_{pc}, while the bulk fluid remains below T_{pc} (T_b/T_{pc} < 1). This leads to a rapid decrease in the fluid density near the wall, generating a steep radial density gradient.

The buoyancy forces drive low-density fluid packets upward along the tube walls, while high-momentum fluid flows downward through the centerline, transferring momentum to the bottom region of the tube. Therefore, a buoyancy-induced transverse secondary flow circulation is gradually formed. Fig. 6.16 presents streamlines, derived from the velocity field for simulation S3, underlining the development of the secondary transverse flow along the heated tube. This flow pattern enhances turbulent mixing and, consequently, improves the average heat transfer rates.

The buoyancy-induced secondary flow causes an accumulation of low-momentum fluid in the upper half of the tube, while high-momentum fluid concentrates in the lower half. As a result, the turbulent boundary layer becomes thicker at the top wall, and thinner at the bottom wall. This asymmetry leads to a progressive downward shift of the velocity peak as the $scCO_2$ is heated. This phenomenon can be seen in the velocity profiles (b), (c), (d) and (e) in Fig. 6.15, where the velocity maximum progressively moves toward the region adjacent to the bottom wall.

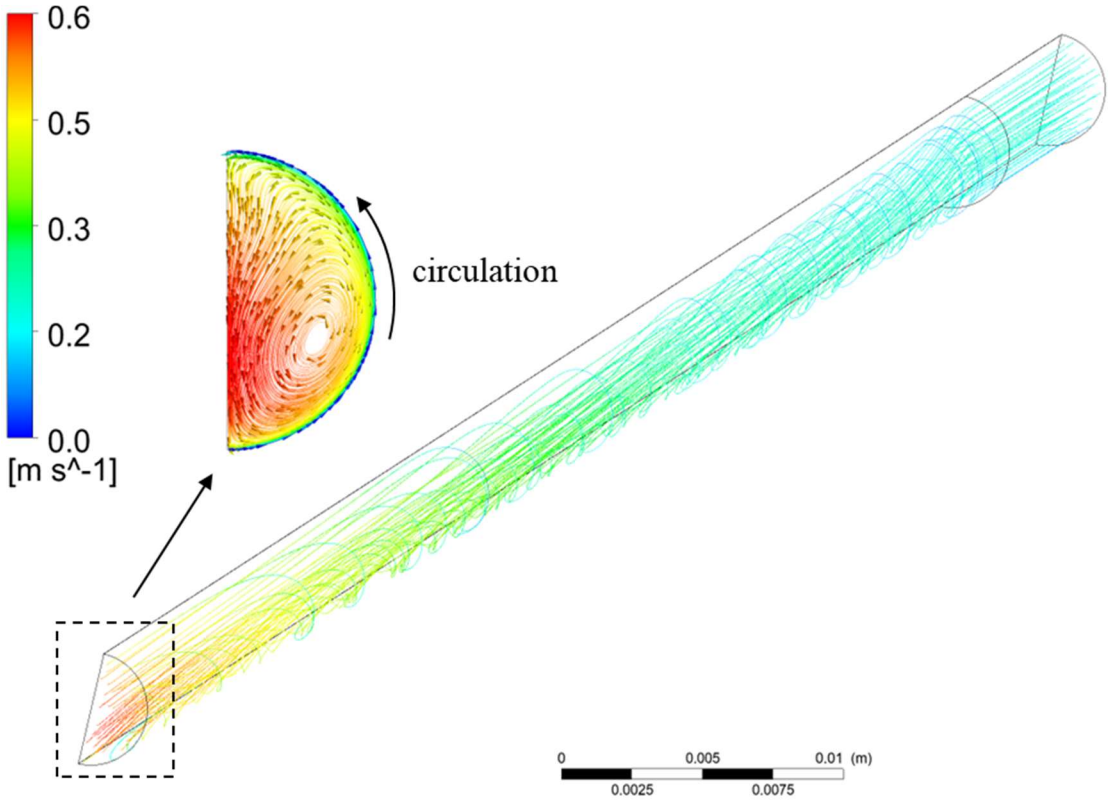

Fig. 6.16. Buoyancy-induced secondary flow pattern along the heated tube. D_i = 4 mm, $\dot{q}_w$ = 26 kW·m^{-2}, and p = 8 MPa.

Fig. 6.17 plots the radial velocity contours at axial positions of 100 mm, 300 mm, 600 mm and 900 mm, outlining the effects of tube diameter and fluid pressure. For the 4 mm tube, the velocity peak is located in the lower part of the tube for both 8 MPa and 28 MPa cases. The asymmetry in the velocity profile is more pronounced at 8 MPa. This is attributed to the steeper density gradient within the pseudo-critical region at lower pressures, which enhances buoyancy effects. For the 1 mm tube, buoyancy effects are weaker due to the smaller hydraulic length scale. As a result, the asymmetry in the radial velocity profiles is less discernible in Fig. 6.17. Nevertheless, experimental results, discussed in Section 6.1, confirm the presence of mixed convection in the microtube scale.

The intensity of the transverse secondary flow, quantified by Eq. (6.21) [113], is depicted in Fig. 6.18 for simulations S1, S3 and S5, as a function of the inner diameter and pressure. In the 4 mm tube, the secondary flow is stronger at 8 MPa than at 28 MPa, consistent with the greater buoyance strength close to the critical pressure. Regardless of the pressure, the secondary flow is significantly more intense in the 4 mm tube than in the 1 mm tube, which supports the limited velocity profile asymmetry observed for the smaller diameter case in Fig. 6.17.

$$\text{intensity of secondary flow} = \frac{\sqrt{u_y^2 + u_z^2}}{|u_x|} \tag{6.21}$$

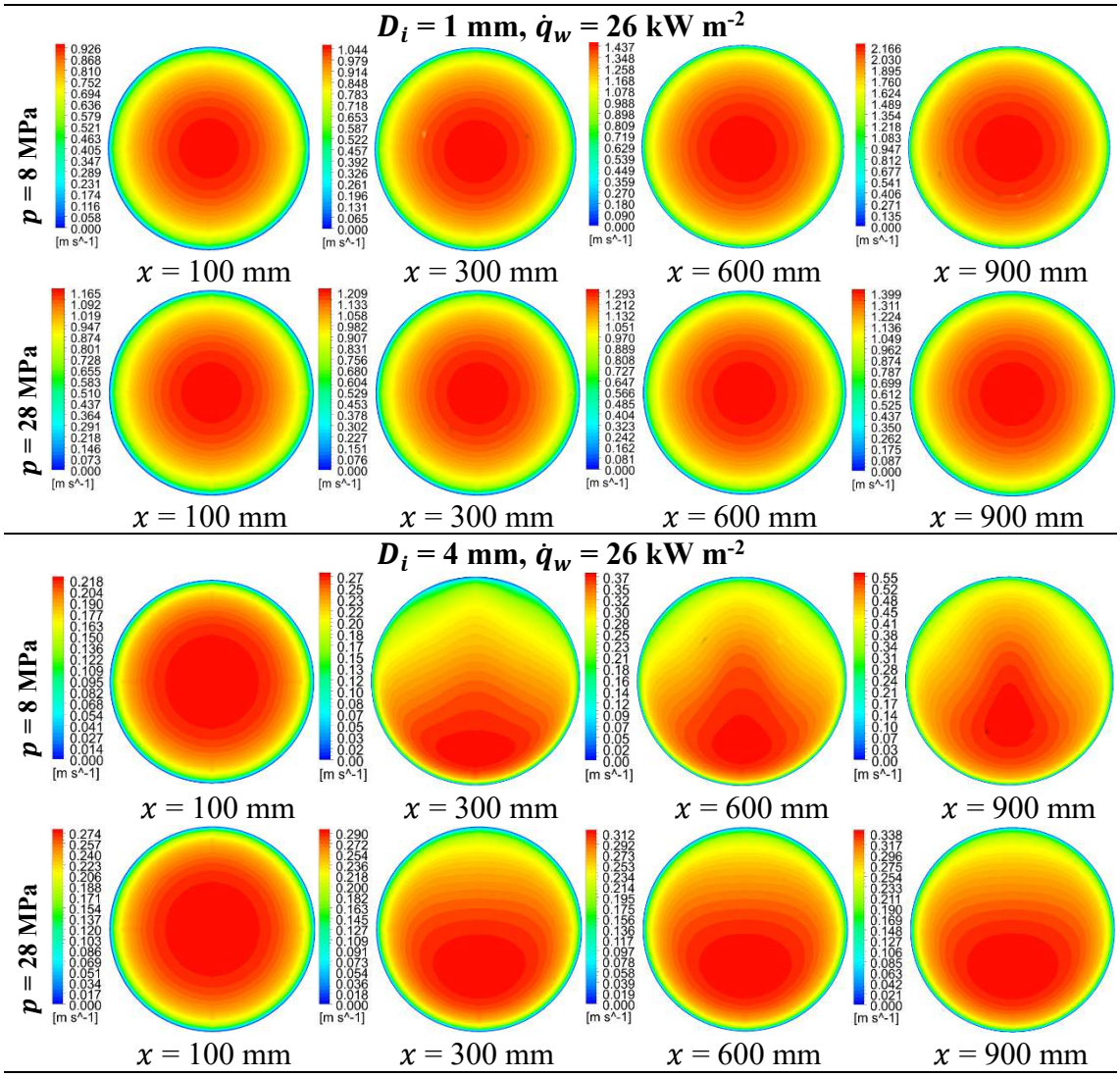

Fig. 6.17. Contours of velocity magnitude at different axial positions, as a function of the inner diameter and pressure, along the heated tube.

As previously discussed, the formation of a buoyancy-induced secondary flow leads to an asymmetric velocity profile. To assess how this asymmetry influences turbulent heat diffusion on the scCO$_2$-side, the production of k, P_k, defined in Eq. (6.22), is employed.

$$P_k = \bar{\rho}\widetilde{u_i'' u_j''}\frac{\partial \tilde{u}_i}{\partial x_j} \tag{6.22}$$

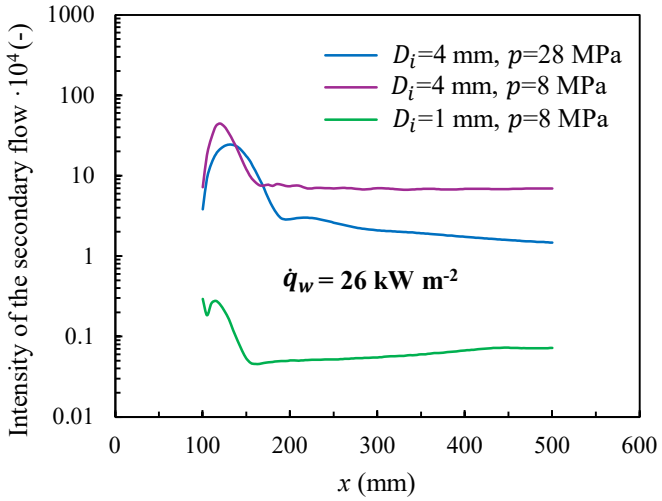

Fig. 6.18. Intensity of the secondary flow along the heated tube, as a function of the tube diameter and pressure. $\dot{q}_w$ = 26 kW·m^{-2}.

$\bar{\rho}\widetilde{u_i''u_j''}$ represents the turbulent shear stresses, which are proportional to the velocity gradients, with the turbulent viscosity being the proportionality factor. Accordingly, P_k is directly related to the local velocity gradients. By comparing velocity profiles (b), (c), (d), and (e) in Fig. 6.15 to the initial, fully developed profile (a), it can be observed that the velocity gradients increase across the radial extent of the tube core as the flow evolves along the heated tube. This results in a general increase in the average P_k, indicating enhanced turbulence production due to the secondary flow formation.

This behavior can be confirmed in Fig. 6.19, which shows radial profiles of P_k for the 4 mm tube under a thermal load of 26 kW·m^{-2}, for pressures of 8 MPa and 28 MPa. As the velocity peak shifts downward, the location of minimum P_k also moves toward the bottom wall (i.e., y < 0 mm), aligning with the point of zero shear stress. It can be seen in Fig. 6.19(a) that the minimum P_k value in the heated region is higher than in the adiabatic inflow section at x = 100 mm. This indicates that, as the velocity peaks near the bottom wall, the local velocity gradient (and hence P_k) increases in that region. Consequently, this higher P_k value leads to an increase of k, as shown in Fig. 6.20.

These intensified radial velocity gradients facilitate energy transfer from the mean flow to turbulent structures, enhancing turbulence levels in the lower half of the tube. For the 28 MPa case in Fig. 6.19(b), the aforementioned effect is less pronounced.

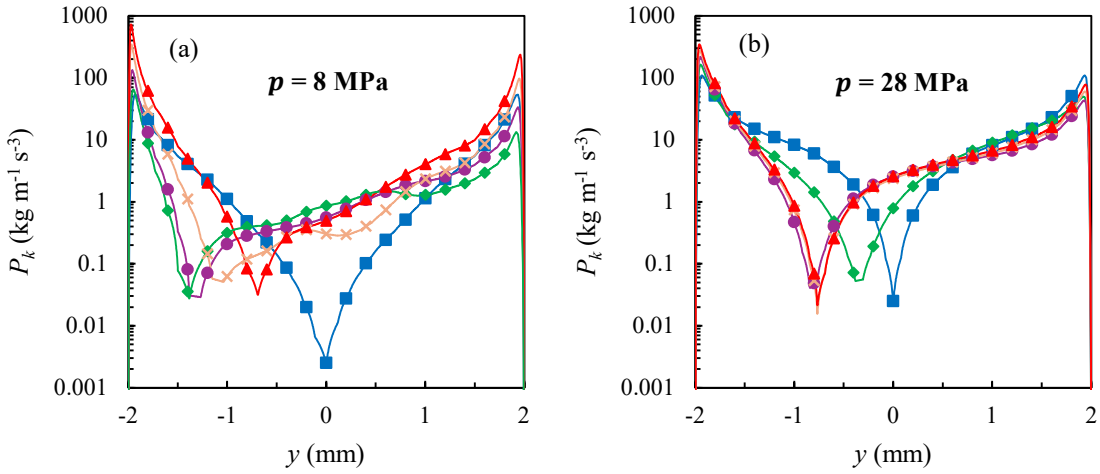

Fig. 6.19. Production of turbulent kinetic energy, P_k, at (—■—) $\frac{T_b}{T_{pc}} = 0.58$, (—◆—) $\frac{T_b}{T_{pc}} = 0.87$, (—●—) $\frac{T_b}{T_{pc}} = 1.00$, (—×—) $\frac{T_b}{T_{pc}} = 1.05$, and (—▲—) $\frac{T_b}{T_{pc}} = 1.12$. $D_i = 4$ mm, $\dot{q}_w = 26$ kW·m^{-2}, and (a) $p = 8$ MPa and (b) $p = 28$ MPa.

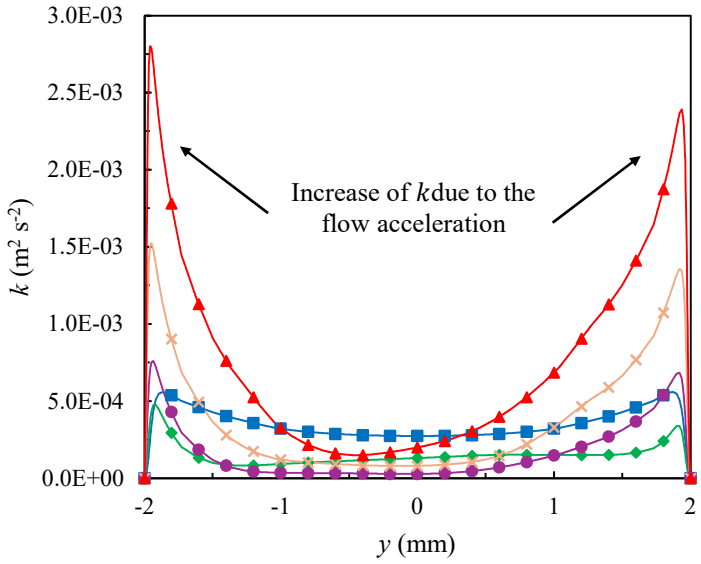

Fig. 6.20. Turbulent kinetic energy, k, profile at (—■—) $\frac{T_b}{T_{pc}} = 0.58$, (—◆—) $\frac{T_b}{T_{pc}} = 0.87$, (—●—) $\frac{T_b}{T_{pc}} = 1.00$, (—×—) $\frac{T_b}{T_{pc}} = 1.05$, and (—▲—) $\frac{T_b}{T_{pc}} = 1.12$. $D_i = 4$ mm, $\dot{q}_w = 26$ kW·m^{-2}, and $p = 8$ MPa.

In the upper half of the tube, the accumulation of low-momentum fluid leads to a thickening of the boundary layer and a reduction in turbulence production. This attenuation is evident in Fig. 6.19(a): for y values between 1 mm and 2 mm, including the near-wall region, the values of P_k at x-distances of 150 mm ($T_b/T_{pc} = 0.87$), 300 mm ($T_b/T_{pc} = 1.00$) and 600 mm ($T_b/T_{pc} = 1.05$), are lower than those at $x = 100$ mm ($T_b/T_{pc} = 0.58$). This behavior indicates a localized *re-laminarization* effect in the top wall of the

tube. Fig. 6.20 further supports this interpretation, showing reduced k values in the top wall compared to the bottom. The suppression of turbulent heat diffusion in the upper region of the tube explains the experimentally observed decline in scCO$_2$ heat transfer coefficients within the valley region for a pressure of 10 MPa.

As a result, on the basis of the Newton's cooling law, the temperature at the top wall increases to maintain the imposed uniform heat flux condition. This thermal behavior is illustrated in Fig. 6.21, which displays temperature contours at the tube cross section for the 4 mm tube under a heat flux of 26 kW·m^{-2} at 8 MPa and 28 MPa. It can be observed that the temperature at the top wall is higher than at the bottom, resulting in a thermally stratified flow. This stratification may have implications for the mechanical integrity of the tube material, particularly under prolonged thermal loading. Moreover, Fig. 6.21 also reveals that the radial temperature gradient becomes less pronounced as the operating pressure increases, indicating a mitigation of buoyancy-driven stratification at higher pressures. This temperature rise due to buoyancy effects has also been observed experimentally, as shown in Figs. 6.2(a), 6.3(a) and 6.4(a).

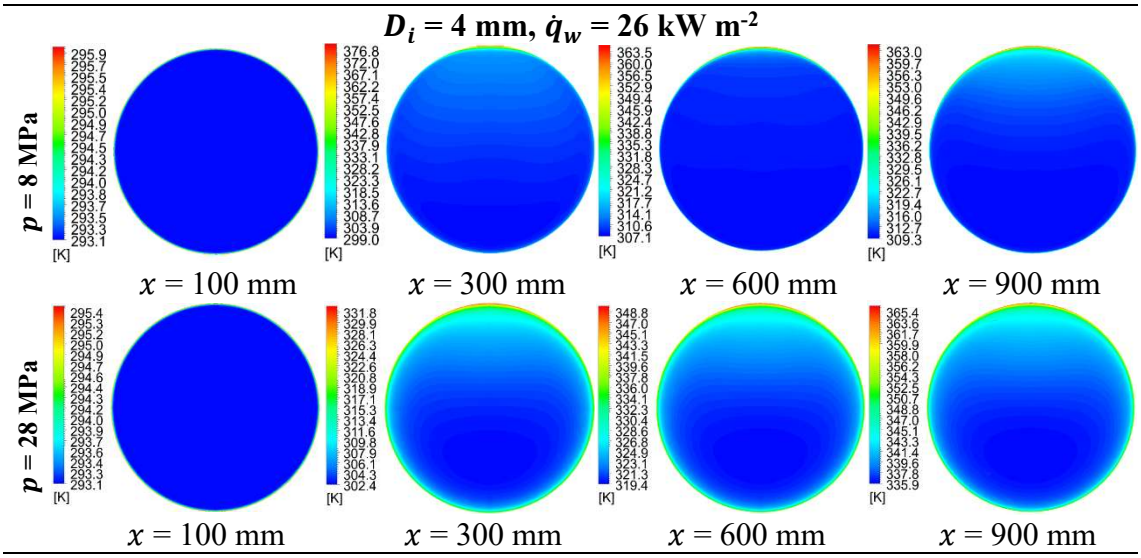

Fig. 6.21. Contours of temperature magnitude at different axial positions along the heated tube, as a function of the pressure. D_i = 4 mm and $\dot{q}_w$ = 26 kW·m^{-2}.

Fig. 6.22 shows the velocity streamlines as a function of the ratio T_b/T_{pc}. For all values of T_b/T_{pc}, the formation of two symmetric vortices in the lower half of the tube is observed, arising from buoyancy-induced secondary circulations. Notably, at T_b/T_{pc} = 0.87 and T_b/T_{pc} = 1.05 (i.e., in the vicinity of the pseudo-critical point), two additional intense symmetric microvortices emerge near the tube centerline. These convective structures originate from flow instabilities, induced by steep radial density gradients and the strong temperature-dependence of the scCO$_2$ thermophysical properties in the pseudo-critical region. In particular, the sharp variations in volumetric expansivity can lead to

localized buoyancy forces that trigger Rayleigh–bénard-type thermal instabilities [285]. As illustrated in Figs. 6.22(a) and 6.22(c), these microvortices interact with the downward flow of high-density fluid along the centerline, attenuating its momentum transport. This flow disruption contributes to the deterioration of heat transfer performance at the upper wall of the tube, where the thermal boundary layer thickens, and turbulence is suppressed.

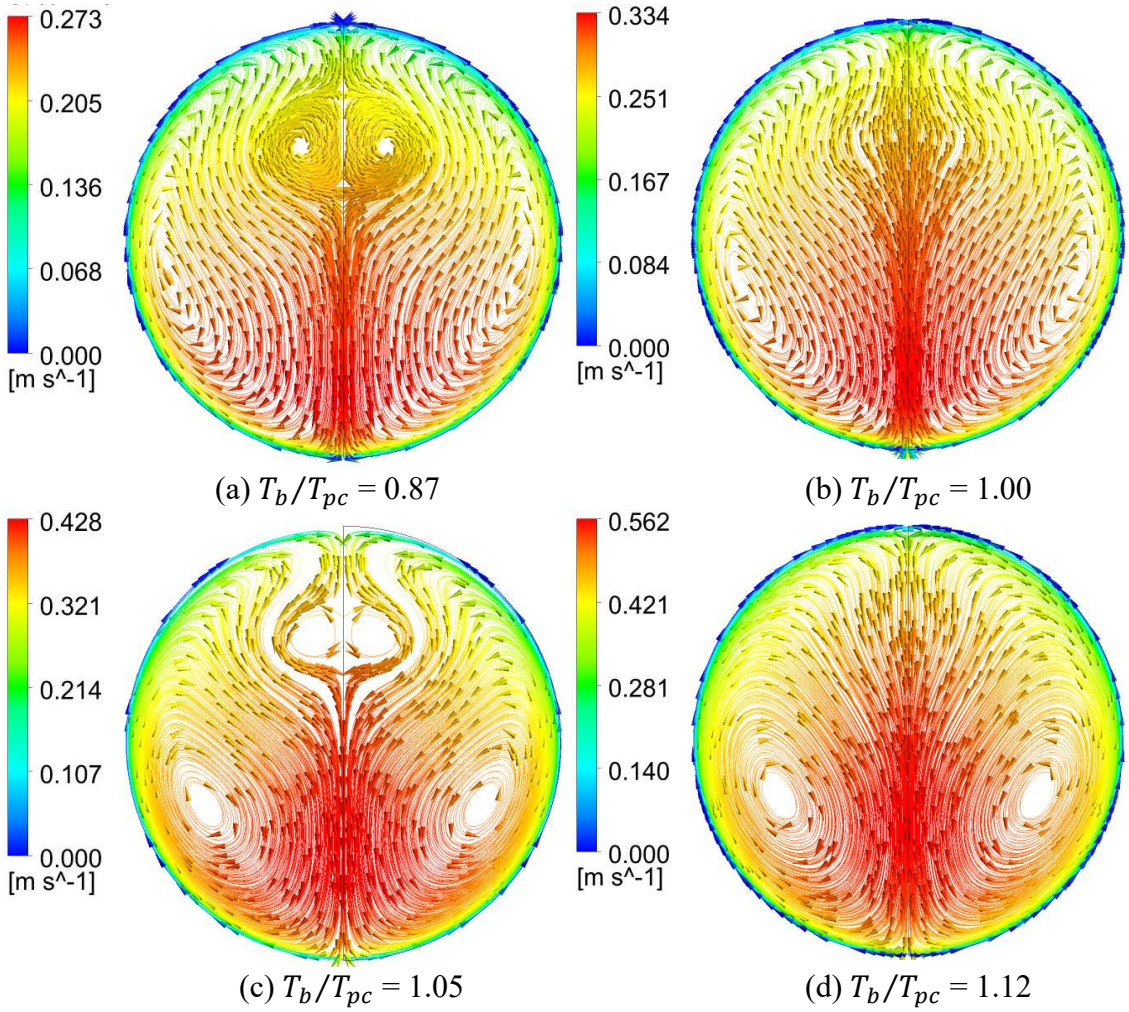

Fig. 6.22. Streamlines of the velocity magnitude along the heated tube, as a function of the ratio T_b/T_{pc}. $D_i = 4$, $\dot{q}_w$ = 26 kW·m^{-2}, p = 8 MPa.

6.3.2.2 Thermal flow acceleration effects

The decrease of the $scCO_2$ density along the axial direction of the tube induces a flow acceleration to satisfy mass conservation. This acceleration is reflected in the velocity profiles along the tube shown in Fig. 6.15, and is more clearly illustrated in Fig. 6.23, which presents velocity profiles for the 4 mm tube under a thermal load of 26 kW·m^{-2} at 8 MPa and 28 MPa. The axial flow acceleration increases the velocity gradients near the walls, as depicted in Fig. 6.23(a). Consequently, as seen in Fig. 6.19, P_k increases in the

near-wall region, leading to the significant rise of k shown in Fig. 6.20. This amplification in turbulent quantities results in an increase of the heat transfer coefficients at both the top and bottom walls of the tube. This may explain the recovery effect of the heat transfer coefficient in the valley region, found in the experiments conducted at a pressure of 10 MPa.

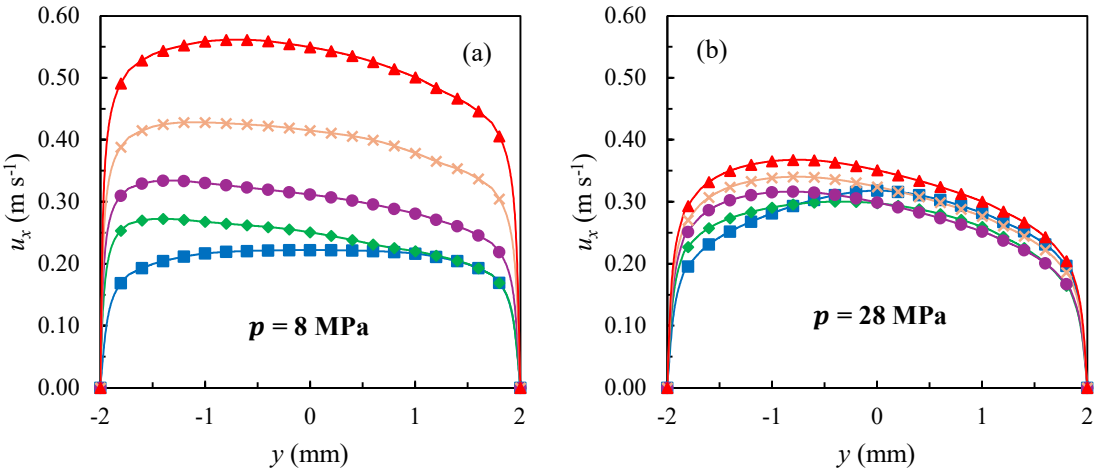

Fig. 6.23. Radial velocity profile at (—■—) $\frac{T_b}{T_{pc}} = 0.58$, (—◆—) $\frac{T_b}{T_{pc}} = 0.87$, (—●—) $\frac{T_b}{T_{pc}} = 1.00$, (—×—) $\frac{T_b}{T_{pc}} = 1.05$, and (—▲—) $\frac{T_b}{T_{pc}} = 1.12$. $D_i = 4$ mm, $\dot{q}_w = 26$ kW·m^{-2}, and (a) $p = 8$ MPa and (b) $p = 28$ MPa.

Fig. 6.24 represents the convective axial flow acceleration along the tube for simulations S1, S3, S4 and S5, calculated using Eq. (6.23). It can be observed that the flow acceleration is greater in the 1 mm tube compared to the 4 mm tube. This difference contributed to explaining why the recovery of the heat transfer coefficients, within the valley region, is predominantly observed in experiments using microtubes, rather than in large diameter tubes.

$$a_x = u_x \frac{\partial u_x}{\partial x} + u_y \frac{\partial u_x}{\partial y} + u_z \frac{\partial u_x}{\partial z} \tag{6.23}$$

The influence of heat flux and pressure on flow acceleration can also be analyzed in Fig. 6.24 for the 4 mm tube. Higher heat fluxes produce greater flow acceleration because, under constant mass flux and inlet temperature, a higher heat input raises the outlet fluid temperature. This leads to steeper axial velocity gradients and, thus, a stronger flow acceleration. Conversely, increasing the pressure reduces flow acceleration; this is consistent with the velocity profiles shown in Fig. 6.23(b). This inverse relationship arises from the diminished density variation at higher pressures, which reduces the axial velocity gradients.

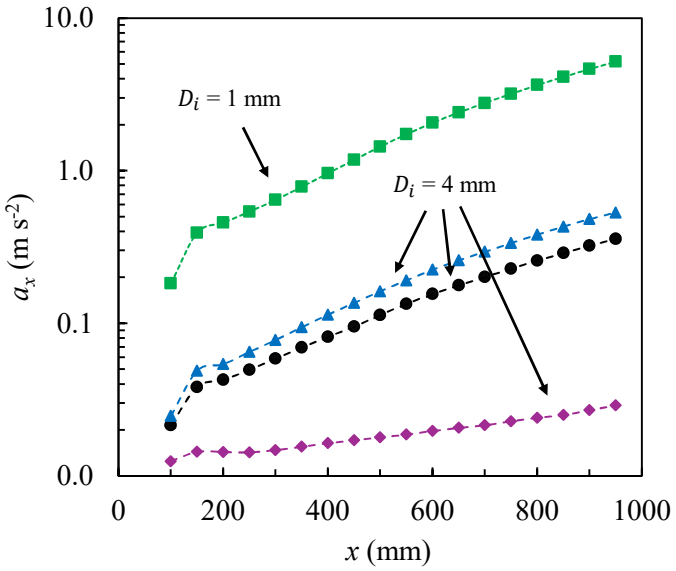

Fig. 6.24. Axial flow acceleration. (----■----) D_i = 1 mm, p = 8 MPa, $\dot{q}_w$ = 26 kW·m^{-2}, (- - ▲ - -) D_i = 4 mm, p = 8 MPa, $\dot{q}_w$ = 30 kW·m^{-2}, (- - ● - -) D_i = 4 mm, p = 8 MPa, $\dot{q}_w$ = 26 kW·m^{-2}, (- - ◆ - -) D_i = 4 mm, p = 28 MPa, $\dot{q}_w$ = 26 kW·m^{-2}.

An interesting experimental observation was presented in Fig. 6.2(b), where a recovery in the heat transfer coefficient was observed in the valley region when the mass flux was 604.9 kg·m^{-2}·s^{-1}. This behavior was not observed when the mass flux was reduced to 447.4 kg·m^{-2}·s^{-1}. This effect can be explained based on Eq. (6.23), assuming that the transverse velocity components (u_y and u_z) are negligible compared to the axial component (u_x). From the continuity equation, the axial velocity gradient can be expressed as:

$$\frac{du_x}{dx} = -\frac{u_x}{\rho}\frac{d\rho}{dx} \tag{6.24}$$

Assuming that the axial pressure gradient is much smaller than the temperature gradient, the density gradient can be approximated as:

$$\frac{d\rho}{dx} = -\rho\beta\frac{dT}{dx} \tag{6.25}$$

The axial temperature gradient can, in turn, be obtained from the convective energy balance:

$$\frac{dT}{dx} = \frac{4\dot{q}_w}{\rho u_x c_p D_i} \tag{6.26}$$

Substituting Eqs. (6.25) and (6.26) into Eq. (6.24), and using the definition of mass flux $G = \rho u_x$, the convective acceleration in the axial direction is given by:

$$a_x \approx \frac{4G\beta\dot{q}_w}{\rho^2 c_p D_i} \tag{6.27}$$

Eq. (6.27) justifies the increase in flow acceleration under conditions of small inner diameter, high heat flux, and pressures near the critical point. Moreover, it shows that flow acceleration is directly proportional to the mass flux G, which explains the experimentally observed recovery in heat transfer rates at high mass flux conditions.

6.4 Micro shell-and-tube heat exchanger for application in the NET Power cycle

This section presents a computational investigation of the heat transfer process in a MSTHE, intended for use in the low-temperature section of the NET Power cycle recuperator. To this end, the one-dimensional MSTHE model, presented in Section 5.3, was implemented in Matlab, under the operating conditions of the NET Power cycle derived in Section 4.3. The convective heat transfer correlation, fitted from experimental heat transfer data in Section 6.2.1, was used to determine the convective heat transfer coefficients of the tube-side $scCO_2$ flow. Local heat and mass transfer models for the shell-side hot gas, including the filmwise partial condensation, were included and validated against mass and energy balances conducted in Aspen Plus.

First, a baseline geometrical configuration of the MSTHE was established to comply with the nominal operating conditions given in Table 5.6. To this end, the design constraints for MSTHEs given in Table 6.6, proposed by Jiang et al. [205], were considered.

Based on these constraints, a heat exchanger configuration consisting of 65,000 tubes with an outer diameter of 1.8 mm, arranged in a triangular pattern with a pitch of $1.25D_{to}$, was adopted. The exchanger length was determined through trial-and-error to achieve a thermal power of 10 MW_{th} under nominal conditions, resulting in a length of 3.5 m. The resulting baseline MSTHE configuration is shown in Table 6.7.

Table 6.6. Design constraints of a MSTHE [205].

Variable	Unit	Lower limit	Upper limit
N_t	-	47,000	80,000
D_{so}	m	-	2.3
L	m	-	8
P_t/D_{to}	-	1.25	1.5
D_{to}	mm	1.0	3.5

Table 6.7. Baseline geometry configuration of the MSTHE.

Parameter	Unit	Value
N_t	-	65,000
D_{so}	m	0.6
L	m	3.5
P_t/D_{to}	-	1.25
D_{to}	mm	1.8
Tube arrangement	-	Triangle

In order to arrive to an optimized geometrical layout of the MSTHE, it would be necessary to first know the network of heat exchangers that make up the NET Power cycle recuperator. Although such exercise is beyond the scope of this study, the MSTHE model, and the hybrid optimization algorithm developed in this work, can be used to perform the design subject to the constraints presented in Table 6.6. However, with the aim of investigating the influence of the main geometric variables and load level on the thermal-hydraulic performance of the MSTHE, the baseline geometry given in Table 6.7 can be used.

Firstly, a sensitivity study of the thermal-hydraulic performance of the MSTHE, as a function of the geometrical variables: tube diameter D_{to}, distance between tubes (pitch) P_t, and number of tubes per shell N_t is performed in Section 6.4.1. Then, the thermal-hydraulic behavior of the baseline MSTHE for the partial load conditions of the NET Power cycle is assessed in Section 6.4.2. This allows deriving a complete performance map of the MSTHE for all operative load ranges of the NET Power cycle.

6.4.1 Sensitivity study of geometrical variables

This section evaluates how the major geometric parameters of the MSTHE influence its thermal-hydraulic performance. The analysis is based on the baseline MSTHE design presented in Table 6.7, with the boundary conditions fixed at the nominal values listed in Table 5.6.

Fig. 6.25 shows the performance maps of the MSTHE as a function of the number of tubes N_t and the outer tube diameter D_{to}, for two pitch values: $P_t = 1.25D_{to}$ and $P_t = 1.45D_{to}$. The performance maps include the thermal power (a and b), overall heat transfer coefficient (c and d), effectiveness (e and f), and pressure drops on the cold-side (g and h), and hot-side (i and j). The effectiveness, defined in Eq. (6.28), represents the ratio between the actual heat flow exchanged and the theoretical maximum. The number of tubes considered ranges from 50,000 to 80,000, and the tube diameters from 1.5 mm to 3 mm; values commonly reported in the MSTHE literature [121,205].

$$\varepsilon = \frac{\dot{Q}}{\left(\dot{m}\bar{c}_p\right)_{min}\left(T_{h,in} - T_{c,in}\right)} \tag{6.28}$$

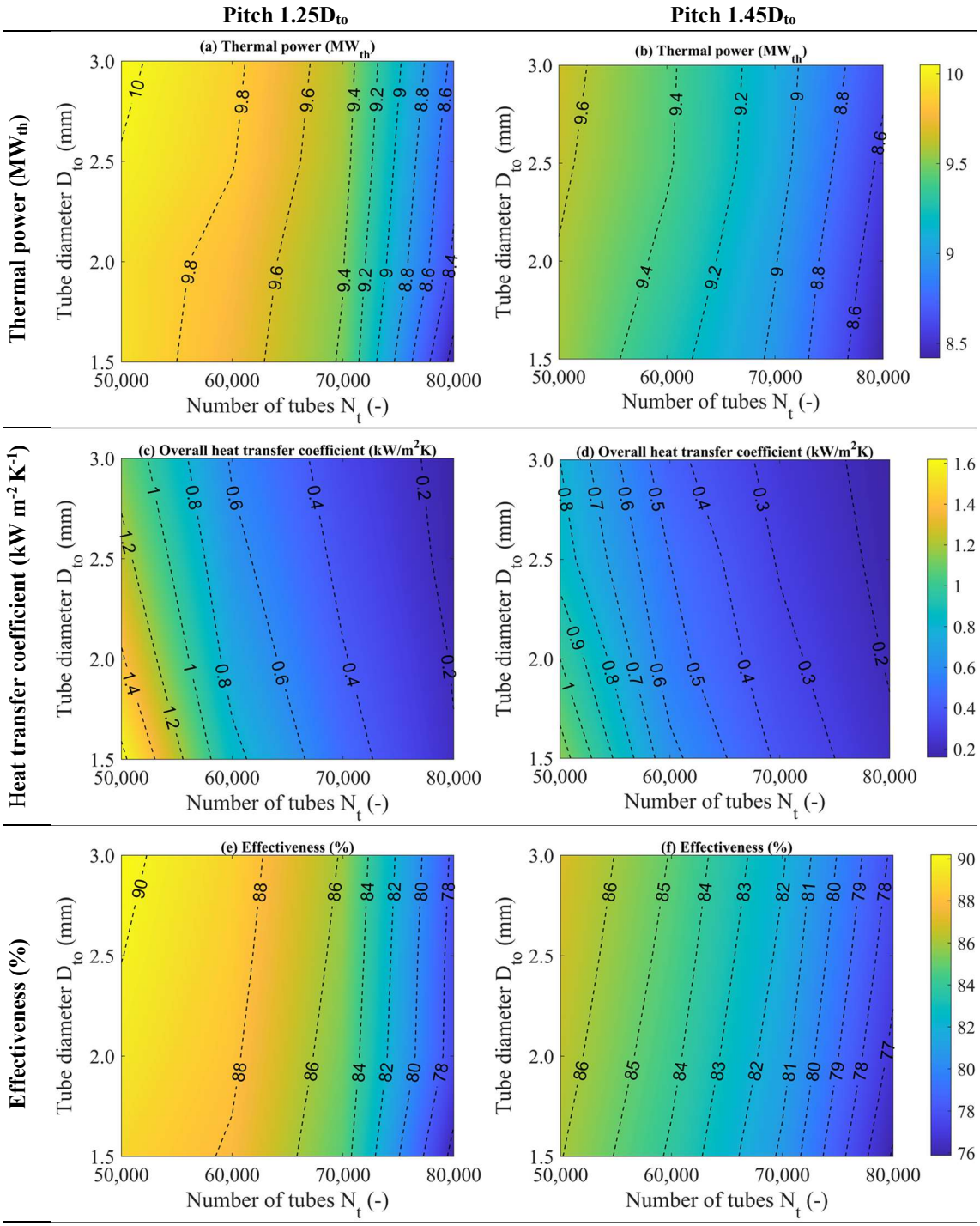

Fig. 6.25. Performance maps of the MSTHE as a function of the number of tubes N_t and tube diameter D_{to}, for two pitch values: $P_t = 1.25D_{to}$ and $P_t = 1.45D_{to}$.

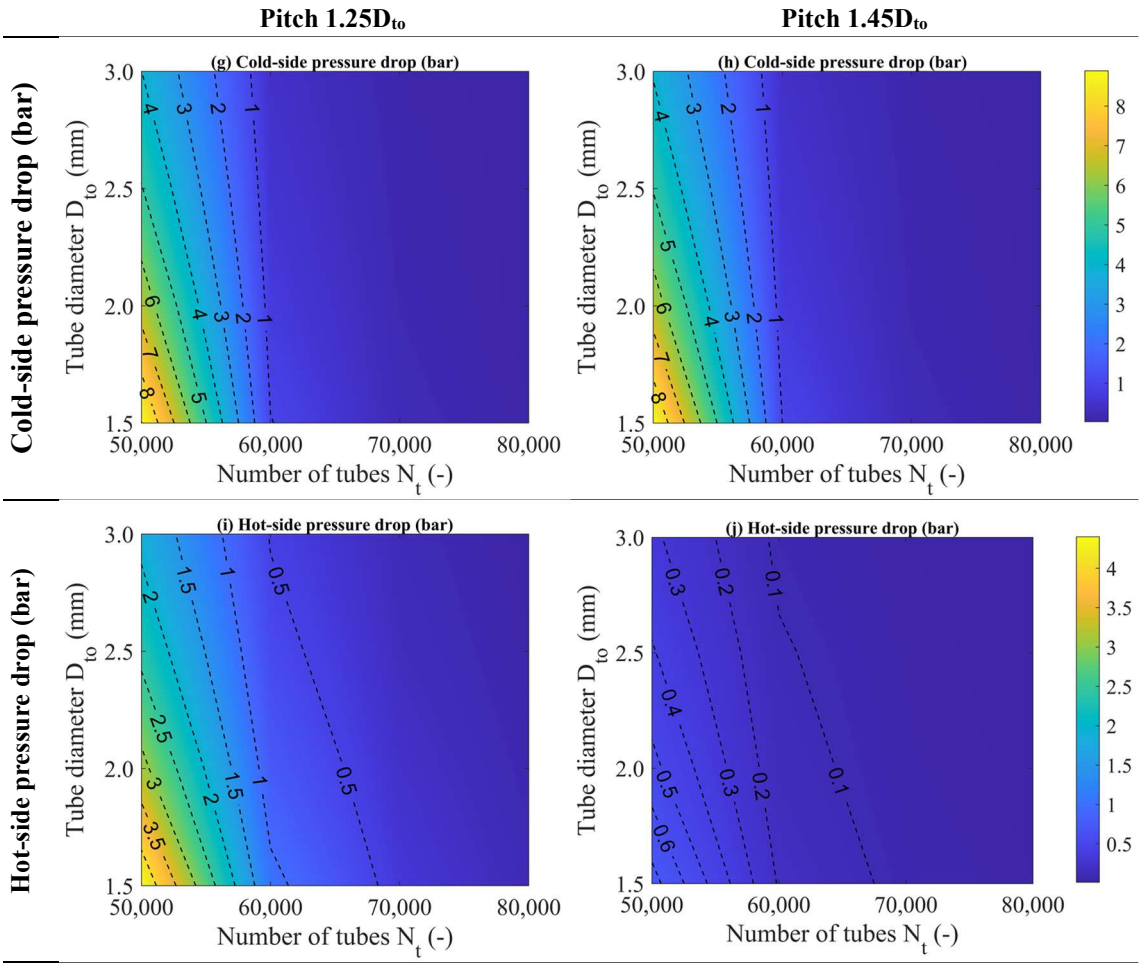

Fig. 6.25 (continued). Performance maps of the MSTHE as a function of the number of tubes N_t and tube diameter D_{to}, for two pitch values: $P_t = 1.25D_{to}$ and $P_t = 1.45D_{to}$.

Fig. 6.25(a) shows that increasing the number of tubes causes a reduction of the thermal power exchanged in the MSTHE, for a constant pitch and tube diameter. For a pitch value of $1.25D_{to}$, the thermal power drops from 10 MW_{th} for 50,000 tubes to about 8.3 MW_{th} for 80,000 tubes. This thermal power drop is caused by the reduction of the flow velocities on both the shell and tube sides, which diminish the heat transfer rates and the operating effectiveness, as illustrated in Figs. 6.25(c) and 6.25(e). The reduction in the tube-side velocity is directly related to the increase of the cross-sectional flow area, while it was found that the shell-side flow passage area scales proportionally with the number of tubes. This conclusion is further detailed in Section 10.3 of Appendix C. Lower flow velocities throughout the exchanger also lead to a decrease in pressure drops, as shown in Figs. 6.25(g) and 6.25(i). When the pitch is fixed at $1.25D_{to}$, the tube-side pressure drop ranges from 4 bar to 8 bar for 50,000 tubes depending on tube diameter, but falls below 1 bar when the number of tubes exceeds 60,000, regardless of the pitch value. This finding suggests that, under the studied boundary conditions, a single MSTHE

bundle should contain more than 60,000 tubes to maintain the tube-side pressure drop under 1 bar, which is favorable for an efficient operation of the NET Power cycle.

For a fixed pitch and number of tubes, increasing the tube diameter results in a slight increase in both the thermal power and effectiveness, as shown in Figs. 6.25(a) and 6.25(e). This increase is due to a larger heat exchange area, which exceeds the decrease of the heat transfer coefficient. Consequently, the thermal power and effectiveness reach maximum values of 10 MW_{th} and 90%, respectively, for 50,000 microtubes with a diameter of 3 mm. However, the resulting MSTHE configuration would lack compactness and require a substantial amount of material, leading to higher costs and a slower dynamic response to operational changes. The heat transfer coefficient reaches a maximum value of about 1.6 $kW \cdot m^{-2} \cdot K^{-1}$ for 50,000 tubes with a 1.5 mm diameter, as a consequence of the high Reynolds numbers. Nevertheless, as plotted in Figs. 6.25(g) and 6.25(i), the corresponding pressure drops are excessively high, and would compromise the efficient operation of the NET Power cycle.

Increasing the pitch, while keeping the number of tubes and tube diameter constant, leads to an increase of the shell diameter and shell flow passage area. This diminishes the shell flow velocity and, consequently, reduces the thermal power, heat transfer coefficient, effectiveness, and pressure drop on the shell-side, as depicted in Figs. 6.25(b), 6.25(d), 6.24(f) and 6.24(j), respectively. In particular, increasing the pitch from $1.25D_{to}$ to $1.45D_{to}$ causes the maximum thermal power to drop from 10.04 MW_{th} to 9.70 MW_{th}, the heat transfer coefficient to decrease from 1.64 $kW \cdot m^{-2} \cdot K^{-1}$ to 1.15 $kW \cdot m^{-2} \cdot K^{-1}$, the effectiveness to fall from 90.35% to 87.00%, and the shell-side pressure drop to reduce from 4.38 bar to 0.74 bar. Since the tube-side flow velocity remains constant regardless of the pitch, the pressure drop on the tube-side is unaffected by changes in the pitch value.

To further investigate the effect of each particular geometric variable on MSTHE performance, sensitivity analyses for each variable; D_{to}, P_t and N_t, are conducted in the Appendix C.

6.4.2 Part-load behavior of the micro shell-and-tube heat exchanger

To assess the performance of the MSTHE under partial cycle load conditions, the heat exchanger model was evaluated using the off-design boundary conditions obtained in Section 4.3.2, and presented again in Table 6.8. All variables, except the shell fluid pressure, decrease as the cycle load is reduced. Fig. 6.26 illustrates the variation of (a) the thermal power and effectiveness of the MSTHE, and (b) the overall heat transfer coefficient and pressure drops, as a function of the cycle load degree (based on the fuel input).

Table 6.8. Boundary conditions (BCs) for part load degrees from 100% to 20% (fuel-based).

		NET Power cycle part load degree (fuel-based)								
BC	Unit	100%	90%	80%	70%	60%	50%	40%	30%	20%
$\dot{m}_c$	kg s^{-1}	57.71	56.21	54.31	51.94	49.01	45.39	40.92	35.31	28.10
$\dot{m}_h$	kg s^{-1}	71.44	69.58	67.23	64.29	60.66	56.19	50.65	43.72	34.78
T_c^{in}	ºC	44.40	42.64	40.74	38.66	36.36	33.81	30.94	27.72	23.89
T_h^{in}	ºC	138.00	136.66	135.16	133.47	131.52	129.22	126.43	122.86	117.92
p_c^{in}	bar	278.99	261.95	243.79	224.34	203.39	180.60	155.54	127.56	95.53
p_h^{in}	bar	44.80	44.80	44.80	44.80	44.80	44.80	44.80	44.80	44.80
$\hat{y}_{H_2O,h}^{in}$	%	4.85	4.67	4.48	4.28	4.05	3.81	3.54	3.23	2.86

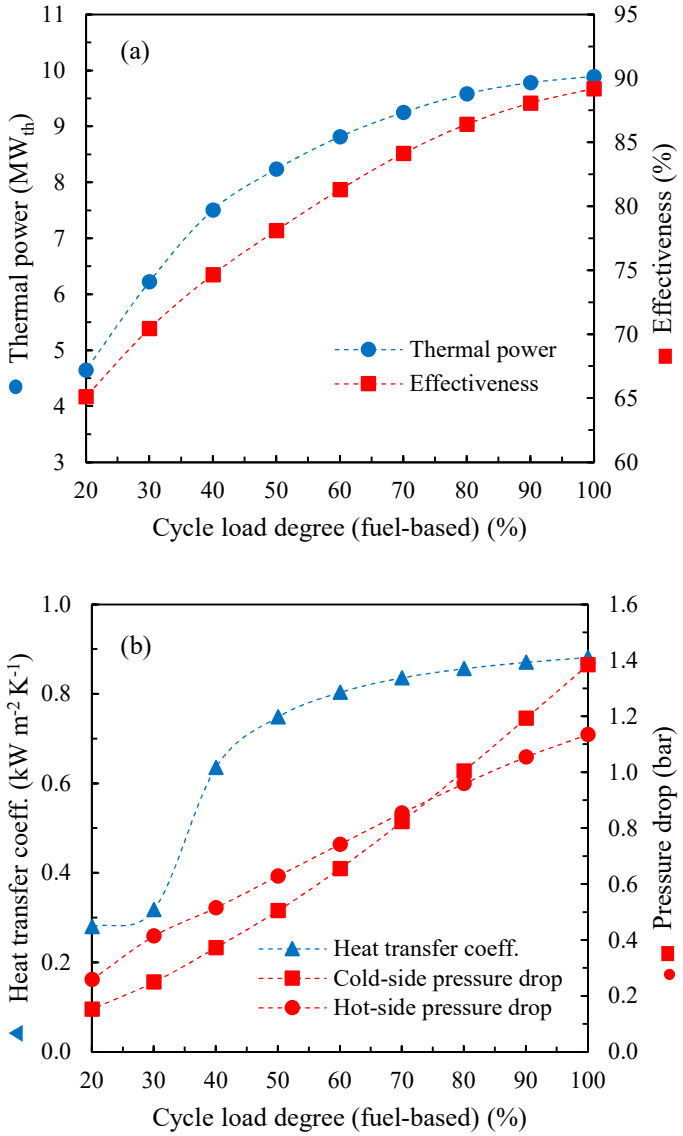

Fig. 6.26. Performance indexes of the MSTHE as a function of the fuel-based load degree. (a) Thermal power and effectiveness, and (b) overall heat transfer coefficient and pressure drops. These thermodynamic indexes decrease as the cycle load decreases.

As shown in Fig. 6.26(a), the thermal power transferred in the heat exchanger decreases with the reduction of the cycle load degree. This is due to the decrease in the mass flow rates on both the shell and tube sides. The effectiveness of the heat exchanger follows a parabolic decline from 89.22%, under design conditions, to 65.13% at 20% of cycle load. Despite the decrease of the inlet temperatures of both the hot and cold fluids with decreasing the load (as listed in Table 6.7), the maximum temperature difference in the exchanger, $T_{h,in}$ - $T_{c,in}$, remains approximately constant. Consequently, according to the definition of the effectiveness in Eq. (6.28), the combination of this effect with the lower thermal power results in the observed drop of the effectiveness.

A lower thermal power also leads to a reduction in the flow velocities on both sides of the exchanger, weakening the heat transfer by turbulent action. As a result, both the heat transfer coefficient and the pressure drops diminish, as can be seen in Fig. 6.26(b). The pressure drop on the tube-side drops more steeply than on the shell-side as the cycle load decreases. Furthermore, the heat transfer coefficient shows a moderate decline from nominal conditions down to a 50% of cycle load. Below 50%, it drops rapidly to 30%, and then remains nearly constant between 30% and 20% of cycle load. This behavior can be attributed to the evolution of the hot- and cold- side heat transfer coefficients, α_h and α_c , respectively, as a function of the cycle load, shown in Figs. 6.27(a) and 6.27(b).

α_h and α_c decrease smoothly as the cycle load decreases from 100% to approximately 50%. This trend is attributed to the moderate reduction in the mass flow rates with the cycle load through the MSTHE, as indicated in Table 6.8. Below a cycle load of 40%, the pressure reduction in the tube-side fluid leads to a significant reduction in α_c, due to the presence of a low-density, gas-like supercritical phase. As the cycle load degree is further reduced to 20%, and the tube-side $scCO_2$ approaches its critical pressure, the change in the Prandtl number becomes steep, and its peak value increases significantly. This results in a substantial local increase of α_c at a distance between 2500 mm and 3500 mm along the tube length, corresponding to the region where the supercritical phase transition from gas-like to liquid-like properties occurs, as shown in Fig. 6.27(b).

In addition, the reduction of the thermal power and inlet temperature at low cycle loads amplifies the peak values of α_c, as previously concluded in Section 6.1.2 based on the experimental observations. Consequently, the sudden rise in α_c at a 20% of cycle load causes the overall heat transfer coefficient to remain nearly constant between 20% and 30% of cycle load. This finding suggests that operating conditions near the critical pressure of the tube-side $scCO_2$ enhance the heat transfer effectiveness of the MSTHE at minimum NET Power cycle load degrees.

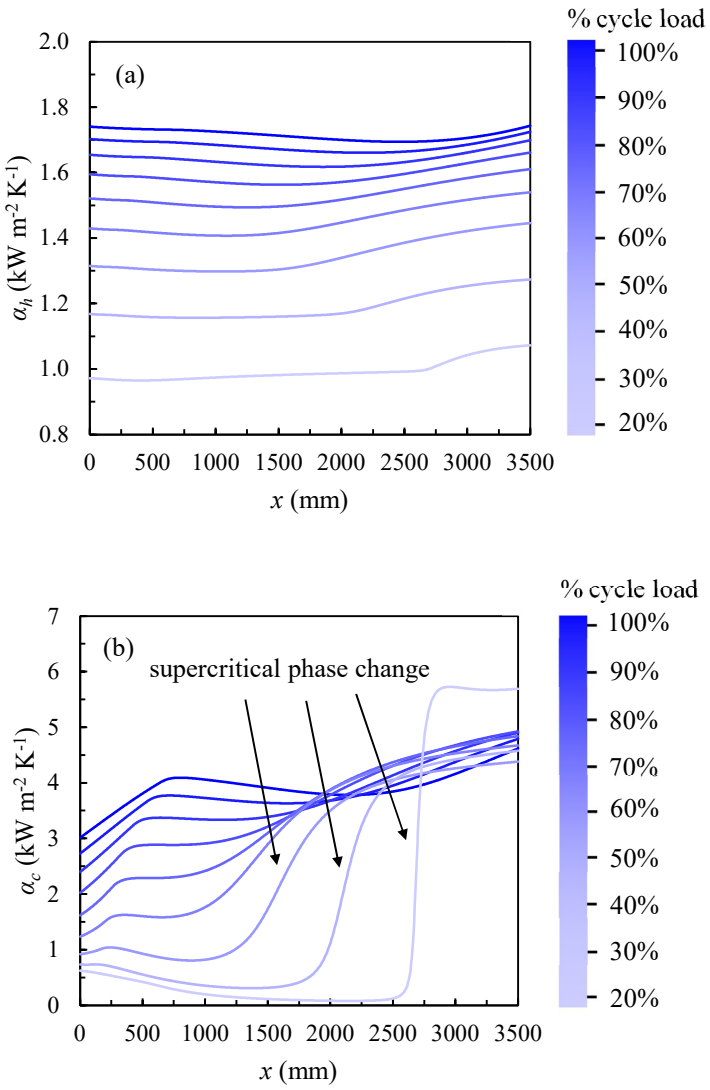

Fig. 6.27. Evolution of (a) α_h and (b) α_c along the heat exchanger x-direction, as a function of the cycle load degree (fuel-based). In the supercritical phase change, α_c changes rapidly due to the variation in the Prandtl number of the fluid near the pseudo-critical temperature.

However, the sharp variation of α_c near the pseudo-critical temperature of the scCO$_2$ at low cycle loads, leads to a decrease in the condensate film temperature. This, in turn, results in: (i) an increase in the sensible heat transferred from the shell-side hot gas to the condensate phase, and (ii) a higher condensate formation rate. These effects cause a localized surge in the heat flux from the shell-side to the tube-side in the region of the MSTHE where the tube-side scCO$_2$ approaches its pseudo-critical temperature. Consequently, the axial temperature gradients of both the hot and cold fluids become markedly steep at this location. This behavior can be seen in Fig. 6.28, which shows the

evolution of (a) dT_h/dx and (b) dT_c/dx along the MSTHE, as a function of the cycle load degree.

Such abrupt temperature gradients can compromise the structural integrity of the microtubes, potentially inducing thermal chock, which leads to material cracking and differential thermal expansion, which contributes to thermal fatigue issues. Moreover, these conditions may accelerate corrosion processes on the heat exchanger surfaces. This finding reveals an additional advantage of MSTHEs over PCHEs. The floating microtube bundle can accommodate the thermal stresses induced by the sudden differential expansion of the microtubes, whereas in the rigid compact block of PCHE, such stresses may result in structural damage.

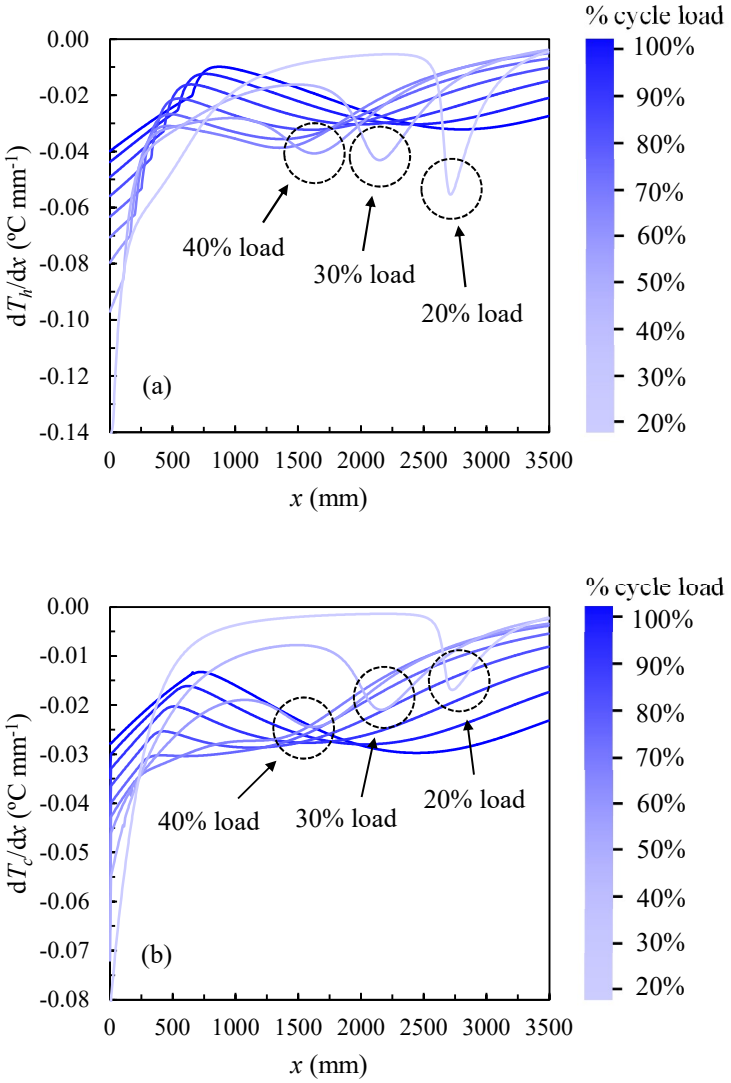

Fig. 6.28. Evolution of (a) dT_h/dx and (b) dT_c/dx along the heat exchanger x-direction, as a function of the cycle part load degree (fuel-based). The strong axial temperature gradients, caused by the supercritical phase-change, may compromise the mechanical integrity of the MSTHE.

The proximity of the $scCO_2$-side to its critical point at low cycle loads has significant implications for the filmwise condensation process occurring on the microtube walls. Fig. 6.29 depicts the evolution of (a) $\dot{n}$, (b) $\hat{y}_{H_2O,h} - \hat{y}_{H_2O,f}$, and (c) δ along the MSTHE, as a function of the cycle load degree.

It can be found in Fig. 6.29(a) that the shell-side wet gases reach the saturation point progressively closer to the hot-side inlet of the MSTHE as the cycle load degree decreases. The overall trend of $\dot{n}$ along the MSTHE results similar for all cycle load degrees; $\dot{n}$ initially increases, reaches a peak value, and then gradually declines due to the reduction in the vapor partial pressure in the shell-side fluid flow. However, for cycle load degrees of 40%, 30% and 20%, $\dot{n}$ exhibits a second peak at axial positions of about 1500 mm, 2000 mm and 2750 mm, respectively. This second peak of $\dot{n}$ increases the amount of released heat in those regions of the MSTHE.

When observing Figs. 6.29(a) and 6.27(b), it can be seen that the peaks of $\dot{n}$ occur when the tube-side $scCO_2$ reaches the pseudo-critical temperature. The sudden increase of α_c within the pseudo-critical region causes a sharp reduction of the condensate film temperature, as previously stated. This drop leads to a higher difference of the H_2O mole fraction between the hot gas bulk and the film interface, $\hat{y}_{H_2O,h} - \hat{y}_{H_2O,f}$, as illustrated in Fig. 6.29(b). Consequently, the vapor transport rate from the gas bulk to the vapor-liquid interface is locally intensified, with a consequent improvement of the heat transfer performance. Conversely, the second peak of $\dot{n}$ leads to a rapid increase in the condensate molar flow rate $\dot{N}_f$, resulting in a sudden thickening of the condensate film, as shown in Fig. 6.29(c). Consequently, the thermal resistance of the film slightly increases in the region near the pseudo-critical temperature of the tube-side $scCO_2$ at low cycle load conditions.

In general, as can be found in Fig. 6.29(c), the condensate film thickens as the cycle load decreases. This behavior is attributed to the reduction in mass flow rates through the heat exchanger, which leads to a lower shell-side flow velocity. As a result, the velocity gradient near the vapor-liquid interface diminishes, thereby reducing the interfacial shear stress τ_{hf}. The reduction of the shear stress at the interface, under partial loads, also causes a mitigation of turbulent fluctuations within the condensate film. As a result, both heat and mass transfer rates within the condensate are reduced. This reduced transport promotes the accumulation of CO_2 molecules at the film interface, further increasing the resistance to vapor transfer in the wet gas phase.

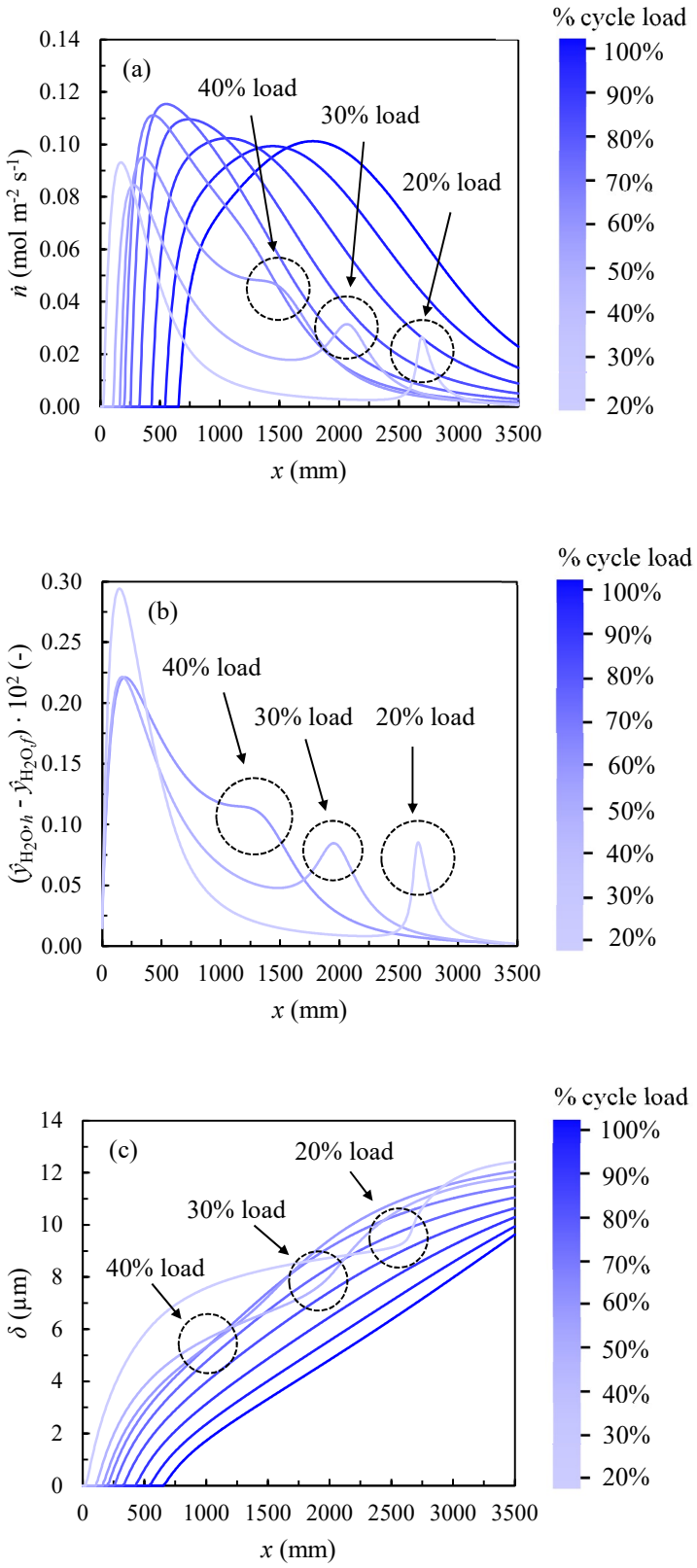

Fig. 6.29. Evolution of (a) $\dot{n}$, (b) $\hat{y}_{H_2O,h} - \hat{y}_{H_2O,f}$ and (c) δ along the heat exchanger x-direction, as a function of the cycle load degree (fuel-based). The rapid increase in α_c during the supercritical phase change instantaneously lowers the condensate temperature, leading to secondary peaks in $\dot{n}$ and $\hat{y}_{H_2O,h} - \hat{y}_{H_2O,f}$. The condensate film thickens as the cycle load decreases.

Fig. 6.30 represents the evolution of the pinch-point as a function of the cycle load degree. At nominal conditions, the pinch-point presents a value of 4.7 ºC and is located 700 mm from the hot-end of the heat exchanger, which coincides with the saturation temperature of the shell-side hot gases. As the cycle load is reduced from 100% to 90%, the pinch-point shifts towards the cold-end of the exchanger, and rises slightly to 5.6 ºC. Thereafter, as the cycle load degree decreases further from 90% to 20%, the pinch-point gradually declines while remaining at the cold-end of the MSTHE.

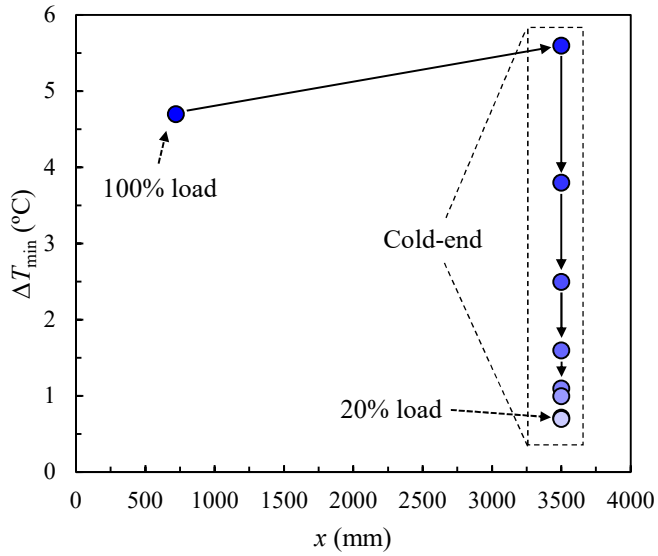

Fig. 6.30. Evolution of the pinch-point as a function of the cycle load degree (fuel-based). Under nominal conditions, the pinch point is 4.7 ºC and is located at the saturation point of the shell-side gases. As the cycle load decreases, the pinch point lowers and shifts toward the cold-end of the MSTHE.

Chapter 7
Conclusions and main contributions

7 Conclusions and main contributions

This PhD Thesis focuses on contributing to the technological development and performance improvement of the innovative oxy-combustion-based NET Power thermodynamic cycle. To this end, a detailed thermodynamic modeling of the cycle and its supercritical CO_2 ($scCO_2$)-rich working fluid was carried out, along with a thorough investigation on heat transfer in $scCO_2$ microflows, under the particular operating conditions of the NET Power cycle.

This study represents a first step towards the potential technological migration from the currently used printed circuit heat exchangers (PCHE) to micro shell-and-tube heat exchangers (MSTHE) in the cycle thermal recuperator, which is the key component for achieving high efficiency zero-emission power generation. Given the extremely high heat flux and the demanding operating conditions, highly compact heat exchange technologies are required. In this context, the proposed high-performance MSTHE solution shows significant potential to reduce the recuperator material mass and manufacturing cost, while also improving the dynamic response of the NET Power cycle.

7.1 General conclusions and key findings

The research work began with a thorough literature survey of the state of art in Section 2, which placed the NET Power cycle within the current environmental context. This review identified the NET Power cycle as the most efficient oxy-combustion power cycle, including almost full emissions capture, with the lowest specific plant cost. The main advances and contributions to the development and understanding of the cycle since its patent in 2011 were analyzed, establishing the current most advanced power cycle embodiment.

The state of the art review revealed three critical areas requiring specific investigation: (i) the thermodynamic characterization of the supercritical working fluid, (ii) the modeling of the most up-to-date power cycle embodiment, and (iii) an in-depth study on heat transfer in $scCO_2$ through microtubes, under the operation conditions of the NET Power cycle. The reliable NET Power cycle model allowed finding the operating ranges for the heat transfer study. These three research challenges constitute the basis for designing high-performance, compact MSTHE heat exchangers for the thermal recuperator. These three research challenges have been further developed in the present work.

Section 3 presented the methodology used for modeling the thermophysical properties of the working fluid, composed of $scCO_2$-rich mixtures (Section 3.1), as well as the power cycle (Section 3.2). The binary interaction parameters of the six EoSs: PR, SRK, LKP, BWRS, PC-SAFT, and CPA were optimized using experimental density and vapor-liquid equilibrium (VLE) data collected from the literature. As a novelty, the optimization was

conducted over a pressure, temperature, and composition (p, T, $\bar{x}$) ranges representative of the NET Power cycle conditions: 1 – 49 MPa, 293.18 – 423.15 K, and 72.6 – 99.8% mol CO_2. Subsequently, the thermodynamic modeling approach of the NET Power cycle, under off-design conditions, was developed, resulting in the most advanced cycle model reported to date in the literature. In addition, a novel global optimization algorithm was presented, which enabled the finding of the optimal NET Power cycle configuration for maximum efficiency more efficiently than conventional optimization methods.

The resulting calibrated binary interaction parameters, used to evaluate the performance of the EoSs, including the GERG-2008 EoS, were presented in Section 4. It was found that the combination of GERG-2008 + LKP EoSs is the most accurate for modeling both the VLE of CO_2 – H_2O mixtures and volumetric data of scCO_2-rich mixtures (with deviations of 1.34% and 2.03%). These findings were published in Velázquez et al. [286]. The thermodynamic performance of the NET Power cycle is analyzed under nominal and off-design conditions, showing that the choice of EoS significantly affects key metrics: the thermal efficiency can be underestimated by 2.11%, while pump sizing and recuperator surface may be overestimated by 7.49% and 6.46%, respectively. Optimal turbine pressures (27.4 MPa inlet and 4.5 MPa outlet) differ from base values, with implications for efficiency and design stress. These findings were published in Velázquez et al. [234]. Under part-load operations, cycle efficiency drops from 55.94% up to 14.26% (at 20% cycle load), with the scCO_2 pressure ranging between 9.5 – 27.9 MPa, and the mass flow accordingly, while exhaust gas conditions remain constant. These outcomes defined the operating conditions for the subsequent heat transfer investigation.

The methodology for investigating heat transfer in scCO_2 microflows, aimed at implementing a MSTHE in the condensative low-temperature section of the NET Power cycle recuperator, was presented in Section 5. The research was divided into: (i) an experimental study, (ii) a computational investigation of buoyancy and flow acceleration effects, and (iii) an off-design thermal-hydraulic evaluation of the MSTHE. The experimental system, built to measure local convective heat transfer coefficients for scCO_2 flowing through a uniformly heated horizontal microtube of 1700 mm length and 0.88 mm inner diameter, was exposed in Section 5.1. As a main novelty of this work versus previous studies, which focused on near critical pressures and larger tube diameters, this work significantly expanded the investigated pressure range (10 – 30 MPa) and employed a microtube, exploring operating conditions that had not been previously researched. Operating conditions (pressure, temperature, mass flux, and heat flux) were defined from the partial-load analysis of Section 4.2. Section 5.2 introduced a CFD model, whose turbulent models (SST k-ω, RNG k-ε, LS, YS, and AKN) were validated against experimental data, enabling analysis of the heat transfer mechanisms via a detailed flow field study. The MSTHE thermal-hydraulic model was presented in Section

5.3. The heat transfer model for the tube-side $scCO_2$ was based on experimental data, while a filmwise partial condensation model, to capture both heat and mass transfer, was developed for the shell-side hot CO_2 – H_2O mixture.

Findings of the heat transfer investigation in $scCO_2$ for application in MSTHEs were discussed in Section 6, where experimental results showed that the heat transfer coefficient increases with mass flow. At 10 MPa, an enhancement of the heat transfer coefficient was observed near the pseudo-critical point, followed by a deterioration attributed to buoyancy effects (which induce thermal stratification and potential fatigue issues), and a subsequent recovery driven by flow acceleration. Except at 10 MPa, heat transfer rates improve with increasing heat flux and inlet temperature.

As a novel contribution, two empirical models were proposed to predict heat transfer coefficients, within previously unforeseen application ranges: a correlation and an artificial deep neural network, with deviations of 18.73% and 6.74%, respectively. Then, turbulence models were validated through CFD simulations, with the YS model showing the best agreement with experimental data, reporting an error of 3.07%. Numerical analysis revealed that buoyancy induces asymmetry in the radial velocity profile, enhancing turbulent kinetic energy production at the bottom of the tube and attenuating it at the top. Axial flow acceleration increases the near-wall velocity gradient, which enhances thermal diffusion by turbulent action.

Finally, the thermal-hydraulic performance of the MSTHE was evaluated under partial load conditions of the cycle. High effectiveness was found under nominal conditions (89.2%), decreasing to 65.1% at 20% cycle load. However, strong axial thermal gradients were identified, which could compromise the structural integrity of the microtubes.

7.2 Summary of the main contributions

The main contributions to the research field of the oxy-combustion NET Power cycle, which aim to address the objectives stated in Section 1 and the scientific question in Section 2, are summarized as follows:

- Calibration of binary interaction parameters for the PR, SRK, LKP, BWRS, PC-SAFT and CPA EoSs over the particular p, T, $\bar{x}$ ranges relevant to the NET Power cycle working fluid. This led to the development of a reliable thermodynamic property model personalized for NET Power cycle applications.
- Development of a novel hybrid optimization algorithm (PSO + Complex), particularly efficient for computationally expensive objective functions, such as the NET Power cycle thermodynamic model developed in this work.
- Useful thermodynamic model of the most advanced NET Power cycle embodiment under nominal and off-design cycle conditions.

- Proposal of the optimal parametric configuration that maximizes thermal efficiency at full load for the most up-to-date NET Power cycle embodiment.
- In-depth analysis of the part-load thermodynamic performance of the NET Power cycle.
- Experimental investigation on heat transfer in $scCO_2$ microflows, under previously unexplored conditions, i.e., using a 0.88 mm inner diameter microtube and a wide pressure range from 10 MPa to 30 MPa.
- Development of an empirical artificial deep neural network-based heat transfer model for $scCO_2$, applicable up to 30 MPa, enabling the prediction of local convective heat transfer coefficients for design purposes of high-performance MSTHEs for the low-temperature section of the NET Power cycle recuperator.
- Off-design thermal-hydraulic modeling and performance assessment of a MSTHE, specifically intended for the condensative low-temperature section of the NET Power cycle recuperator.

7.3 Future work

Future research could focus on:

- Precise measurement of thermodynamic properties and transport coefficients of $scCO_2$-rich mixtures specific to the NET Power cycle, aimed at improving the predictive accuracy of the thermodynamic property methods.
- Experimental validation of turbomachinery performance maps at the NET Power pilot plant to enable more accurate calibration of the thermodynamic cycle model.
- Introduction of impurities into the $scCO_2$ flow to assess their effect on heat transfer performance. Additionally, experimental ranges of pressure, temperature, and mass flow rates could be further extended.
- Investigation of heat transfer in in vertically oriented microtubes to mitigate the temperature stratification observed in horizontal configurations. Furthermore, the effect of tube wall corrugation on heat transfer efficiency and pressure drop could be explored.

Appendices

8 Appendix A. Pure components parameters, and expressions and constants of the LKP, BWRS, and PC-SAFT equations of state

Pure component parameters of CO_2, H_2O, CO, H_2, O_2, N_2, Ar and CH_4 are presented in Table A.1.

Table A.1. Critical parameters ($p_{c,i}, T_{c,i}, \rho_{c,i}$), acentric factors ($\omega_i$), number of spherical segments in a chain (m_i), segment diameters (σ_i), dispersion energies (ε_i/k), number of sites (N_i), and association volume parameters (β_i) of the components CO_2, H_2O, CO, H_2, O_2, N_2, Ar and CH_4.

Molecule i	$p_{c,i}$ (MPa)	$T_{c,i}$ (K)	$\rho_{c,i}$ (kg m^{-3})	ω_i	m_i	σ_i (Å)	ε_i/k (K)	N_i	β_i
CO_2	7.377	304.13	467.6	0.224	2.073	2.785	169.2	0	-
H_2O	22.064	647.10	322.0	0.344	1.066	3.001	366.5	4	0.0692
CO	3.494	132.86	303.9	0.050	1.310	3.251	92.2	0	-
H_2	1.296	33.15	31.3	-0.219	1.000	2.829	33.3	0	-
O_2	5.043	154.58	436.1	0.022	1.1217	3.2098	114.9	0	-
N_2	3.396	126.19	313.3	0.037	1.205	3.313	91.0	0	-
Ar	4.863	150.69	535.6	-0.002	0.929	3.478	122.2	0	-
CH_4	4.599	190.56	162.7	0.011	1.000	3.704	1.0	0	-

Expressions and constants of the Lee-Kesler-Plöcker (LKP) EoS are given in Table A.2.

Table A.2. Parameters of the Lee-Kesler-Plöcker (LKP) equation of state

Parameter	Simple fluid	Reference fluid
b_1	0.1181193	0.2026579
b_2	0.265728	0.331511
b_3	0.154790	0.027655
b_4	0.030323	0.203488
c_1	0.0236744	0.0313385
c_2	0.0186984	0.0503618
c_3	0.0	0.016901
c_4	0.042724	0.041577
$d_1 \cdot 10^4$	0.155488	0.48736
$d_2 \cdot 10^4$	0.623689	0.0740336
β	0.65392	1.226
γ	0.060167	0.03754

Expressions and constants of the Benedict-Webb-Rubin-Starling (BWRS) EoS are provided in Eqs. (A.1) – (A.11), and in Table A.3, respectively.

$$\rho_{c,i} \cdot B_{0,i} = A_1 + B_1 \omega_i \tag{A.1}$$

$$\frac{\rho_{c,i}A_{0,i}}{RT_{c,i}} = A_2 + B_2\omega_i \tag{A.2}$$

$$\frac{\rho_{c,i}C_{0,i}}{RT_{c,i}^3} = A_3 + B_3\omega_i \tag{A.3}$$

$$\rho_{c,i}^2\gamma_i = A_4 + B_4\omega_i \tag{A.4}$$

$$\rho_{c,i}^2 b_i = A_5 + B_5\omega_i \tag{A.5}$$

$$\frac{\rho_{c,i}^2 a_i}{RT_{c,i}} = A_6 + B_6\omega_i \tag{A.6}$$

$$\rho_{c,i}^3\alpha_i = A_7 + B_7\omega_i \tag{A.7}$$

$$\frac{\rho_{c,i}^2 c_i}{RT_{c,i}^3} = A_8 + B_8\omega_i \tag{A.8}$$

$$\frac{\rho_{c,i}D_{0,i}}{RT_{c,i}^4} = A_9 + B_9\omega_i \tag{A.9}$$

$$\frac{\rho_{c,i}^2 d_i}{RT_{c,i}^2} = A_{10} + B_{10}\omega_i \tag{A.10}$$

$$\frac{\rho_{c,i}E_{0,i}}{RT_{c,i}^5} = A_{11} + B_{11}\omega_i \exp(-3.8\omega_i) \tag{A.11}$$

Table A.3. Parameters A_j and B_j for Eqs. (A.1) - (A.11).

Subscript j	A_j	B_j
1	0.4436900	0.115449
2	1.2843800	-0.920731
3	0.3563060	1.708710
4	0.5449790	-0.270896
5	0.5286290	0.349621
6	0.4840110	0.754130
7	0.0705233	-0.044448
8	0.5040870	1.322450
9	0.0307452	0.179433
10	0.0732828	0.463492
11	0.0064500	-0.022143

The hard-chain, dispersion, association and polar contribution terms of the Perturbed Chain – Statistical Associating Fluid Theory (PC-SAFT) EoS are provided in the following.

Hard-chain term contribution: $\frac{\hat{a}^{\mathrm{hc}}}{RT} = \bar{m}\frac{\hat{a}^{\mathrm{hs}}}{RT} - \sum_i x_i(m_i - 1)\ln g_{ij}^{\mathrm{hs}}$.

$\bar{m}$ denotes the mean segment number in the mixture, and is calculated as follows:

$$\bar{m} = \sum_i x_i m_i, \tag{A.12}$$

where x_i represents the molar fraction of component i in the mixture, and m_i is the segment number of the component i. The term $\hat{a}^{\mathrm{hs}}/(RT)$ represents the contribution from hard-sphere mixtures on a per-segment basis, which is given by the following equation:

$$\frac{a^{\mathrm{hs}}}{RT} = \frac{1}{\xi_0}\left[\frac{3\xi_1\xi_2}{(1-\xi_3)} + \frac{\xi_2^3}{\xi_3(1-\xi_3)^2} + \left(\frac{\xi_2^3}{\xi_3^2} - \xi_0\right)\ln(1-\xi_3)\right]. \tag{A.13}$$

The radial distribution function of hard-sphere mixtures in contact, g_{ij}^{hs}, is expressed by Eq. (A.14),

$$g_{ij}^{\mathrm{hs}} = \frac{1}{(1-\xi_3)} + \left(\frac{d_{\mathrm{i}}d_{\mathrm{j}}}{d_{\mathrm{i}}+d_{\mathrm{j}}}\right)\frac{3\xi_2}{(1-\xi_3)^2} + \left(\frac{d_{\mathrm{i}}d_{\mathrm{j}}}{d_{\mathrm{i}}+d_{\mathrm{j}}}\right)^2\frac{2\xi_2^2}{(1-\xi_3)^3}, \tag{A.14}$$

with ξ_n defined as follows:

$$\xi_n = \frac{\pi}{6}\hat{\rho}\sum_i x_i m_i d_i^n, \quad n = 0, 1, 2, 3. \tag{A.15}$$

The temperature-dependent segment diameter d_i of component i is calculated as:

$$d_i = \sigma_i\left[1 - 0.12\exp\left(-3\frac{\varepsilon_i}{kT}\right)\right], \tag{A.16}$$

where σ_i is the segment diameter of component i and ε_i is the dispersion energy. The parameters m_i, σ_i and ε_i/k (k is the Boltzmann constant) are provided in Table A.1 for each component considered in this study.

Dispersion term contribution: $\frac{\hat{a}^{\mathrm{disp}}}{RT} = -2\pi\hat{\rho}I_1X - \pi\hat{\rho}\bar{m}C_1I_2Y$.

The compressibility parameter, C_1, is expressed as follows

$$C_1 = \left\{1 + \bar{m}\frac{2\eta(4-\eta)}{(1-\eta)^4} + (1-\bar{m})\frac{\eta(20-27\eta+12\eta^2-2\eta^3)}{[(1-\eta)(2-\eta)]^2}\right\}^{-1}. \tag{A.17}$$

The abbreviated parameters X and Y are defined in Eqs. (A.18) and (A.19) as:

$$X = \sum_i \sum_j x_i x_j m_i m_j \left(\frac{\varepsilon_{ij}}{kT}\right) \sigma_{ij}^3, \tag{A.18}$$

$$Y = \sum_i \sum_j x_i x_j m_i m_j \left(\frac{\varepsilon_{ij}}{kT}\right)^2 \sigma_{ij}^3, \tag{A.19}$$

where σ_{ij} and ε_{ij} are the cross segment diameter and energy parameters, respectively, which are calculated based on conventional combining rules as follows:

$$\sigma_{ij} = \frac{1}{2}(\sigma_i + \sigma_j), \tag{A.20}$$

$$\varepsilon_{ij} = (1 - k_{ij})\sqrt{\varepsilon_i \varepsilon_j}. \tag{A.21}$$

In Eq. (A.21), k_{ij} denotes the binary interaction parameters, which are temperature-dependent as follows:

$$k_{ij} = \boldsymbol{k}_{\boldsymbol{ij}}^{(\mathbf{1})} + \boldsymbol{k}_{\boldsymbol{ij}}^{(\mathbf{2})}/T_r + \boldsymbol{k}_{\boldsymbol{ij}}^{(\mathbf{3})} \ln T_r + \boldsymbol{k}_{\boldsymbol{ij}}^{(\mathbf{4})} T_r + \boldsymbol{k}_{\boldsymbol{ij}}^{(\mathbf{5})} T_r^2, \tag{A.22}$$

with $T_r = T/T_{\mathrm{ref}}$. T_{ref} is a reference temperature, and the default value is 298.15 K. The terms I_1 and I_2 are expressed as follows:

$$I_1 = \sum_{l=1}^{7} a_l \eta^{l-1}, \tag{A.23}$$

$$I_2 = \sum_{l=1}^{7} b_l \eta^{l-1}, \tag{A.24}$$

where the coefficients a_l and b_l depend on the chain length according to

$$a_l = a_{1,l} + \frac{\bar{m} - 1}{\bar{m}} a_{2,l} + \left(\frac{\bar{m} - 1}{\bar{m}}\right)\left(\frac{\bar{m} - 2}{\bar{m}}\right) a_{3,l}, \tag{A.25}$$

$$b_l = b_{1,l} + \frac{\bar{m} - 1}{\bar{m}} b_{2,l} + \left(\frac{\bar{m} - 1}{\bar{m}}\right)\left(\frac{\bar{m} - 2}{\bar{m}}\right) b_{3,l}. \tag{A.26}$$

$\eta = \xi_3$, and the model constants $a_{1,i}$, $a_{2,i}$, $a_{3,i}$, $b_{1,i}$, $b_{2,i}$, and $b_{3,i}$ are given in Table A.4.

Table A.4. Constants for Eqs. (A.25) and (A.26).

i	$a_{1,i}$	$a_{2,i}$	$a_{3,i}$	$b_{1,i}$	$b_{2,i}$	$b_{3,i}$
1	0.9105631445	-0.3084016918	-0.0906148351	0.7240946941	-0.5755498075	0.0976883116
2	0.6361281449	0.1860531159	0.4527842806	2.2382791861	0.6995095521	-0.2557574982
3	2.6861347891	-2.5030047259	0.5962700728	-4.0025849485	3.8925673390	-9.1558561530
4	-26.547362491	21.419793629	-1.7241829131	-21.003576815	-17.215471648	20.642075974
5	97.759208784	-65.255885330	-4.1302112531	26.855641363	192.67226447	-38.804430052
6	-159.59154087	83.318680481	13.776631870	206.55133841	-161.82646165	93.626774077
7	91.297774084	-33.746922930	-8.6728470368	-355.60235612	-165.20769346	-29.666905585

Association term contribution: $\frac{\hat{a}^{\text{assoc}}}{RT} = \sum_i x_i \sum_A N_i \left(\ln X^{A_i} - \frac{X^{A_i}}{2} + \frac{1}{2}\right)$.

In the expression of the contribution of the association term, N_i is the number of sites of type a in component i, that are listed in Table A.1 for the molecules considered in this study. The term X^{A_i}, which is defined in Eq. (A.27), denotes the fraction of molecules of species i not bonded at site a.

$$X^{A_i} = \left(1 + \hat{\rho} \sum_j x_j \sum_B X^{B_j} \Delta^{A_i B_j}\right)^{-1} \tag{A.27}$$

$\Delta^{A_i B_j}$ is the association strength between position A of a molecule i and position B of a molecule j, and is expressed as follows:

$$\Delta^{A_i B_j} = g_{ij}^{\text{hs}} \kappa^{A_i B_j} \sigma_{ij}^3 \left[\exp\left(\frac{\varepsilon^{A_i B_j}}{kT}\right) - 1\right], \tag{A.28}$$

where $\kappa^{A_i B_j}$ is the effective cross-association and solvation volume, given in Eq. (A.29), and $\varepsilon^{A_i B_j}$ is the cross-association and solvation energy, given in Eq. (A.30).

$$\kappa^{A_i B_j} = \sqrt{\kappa^{A_i B_i} \kappa^{A_j B_j}} \left(\frac{\sqrt{\sigma_{ii}\sigma_{jj}}}{0.5(\sigma_{ii} + \sigma_{jj})}\right)^3 \tag{A.29}$$

$$\varepsilon^{A_i B_j} = \frac{1}{2}(\varepsilon^{A_i B_i} + \varepsilon^{A_i B_i}) \tag{A.30}$$

Polar term contribution: $\frac{\hat{a}^{\text{polar}}}{RT} = \frac{[\hat{a}_2/(RT)]}{1 - [\hat{a}_3/(RT)]/[\hat{a}_2/(RT)]}$.

The terms $\frac{\hat{a}_2}{RT}$ and $\frac{\hat{a}_3}{RT}$ are defined as follows:

$$\frac{\hat{a}_2}{RT} = -\frac{2\pi}{9}\frac{\hat{\rho} I_2}{(kT)^2}\sum_i\sum_j x_i x_j m_i m_j \frac{\mu_i^2 \mu_j^2}{d_{ij}^3}, \tag{A.31}$$

$$\frac{\hat{a}_3}{RT} = \frac{5\pi^2}{162}\frac{\hat{\rho}^2 I_3}{(kT)^3}\sum_i\sum_j\sum_k x_i x_j x_k m_i m_j m_k \left(x_p\right)_i \left(x_p\right)_j \left(x_p\right)_k \frac{\mu_i^2 \mu_j^2 \mu_k^2}{d_{ij} d_{jk} d_{ik}}, \tag{A.32}$$

where μ_i and $\left(x_p\right)_i$ are the dipole moment and dipolar function of the segment type a within the component i, respectively, and the term d_{ij} can be computed as follows:

$$d_{ij} = \frac{1}{2}\left(d_i + d_j\right). \tag{A.33}$$

The parameters I_2 and I_3 of Eqs. (A.31) and (A.32) are provided in Eqs. (A.34) and (A.35), respectively.

$$I_2 = \frac{1 - 0.69099\eta - 1.16904\eta^2 + 0.75097\eta^3}{(1-\eta)^2} \tag{A.34}$$

$$I_3 = \frac{1 + 1.19133\eta - 0.42523\eta^2}{1 - 1.12789\eta + 0.73166\eta^2} \tag{A.35}$$

9 Appendix B. Calculation of the coefficients K_τ, $K_{f,lam}$ and $K_{f,tur}$

In the following analysis, a relationship between the Nusselt number with (Nu^o) and without the consideration of interfacial shear stress is derived using a model of a laminar condensate film flowing over a vertical flat plate. The results obtained from this configuration are directly transferable to the case of a horizontal tube, as encountered in the MSTHE. Fig B.1 illustrates the condensate film over a vertical plate, both in the absence and presence of gas flow-induced shear, along with a differential control volume encompassing body and viscous forces. The following assumption were made: the plate has a unit width; the condensate flow is laminar and two-dimensional; condensate properties are constant; the liquid density is significantly greater than that of the gas ($\rho_l \gg \rho_h$), such that buoyancy effects are negligible; the transverse velocity $u_{f,y}$ is much smaller than the axial velocity $u_{f,x}$, so $u_{f,x}$ is referred to as u_f in the following; and axial acceleration of the condensate is negligible.

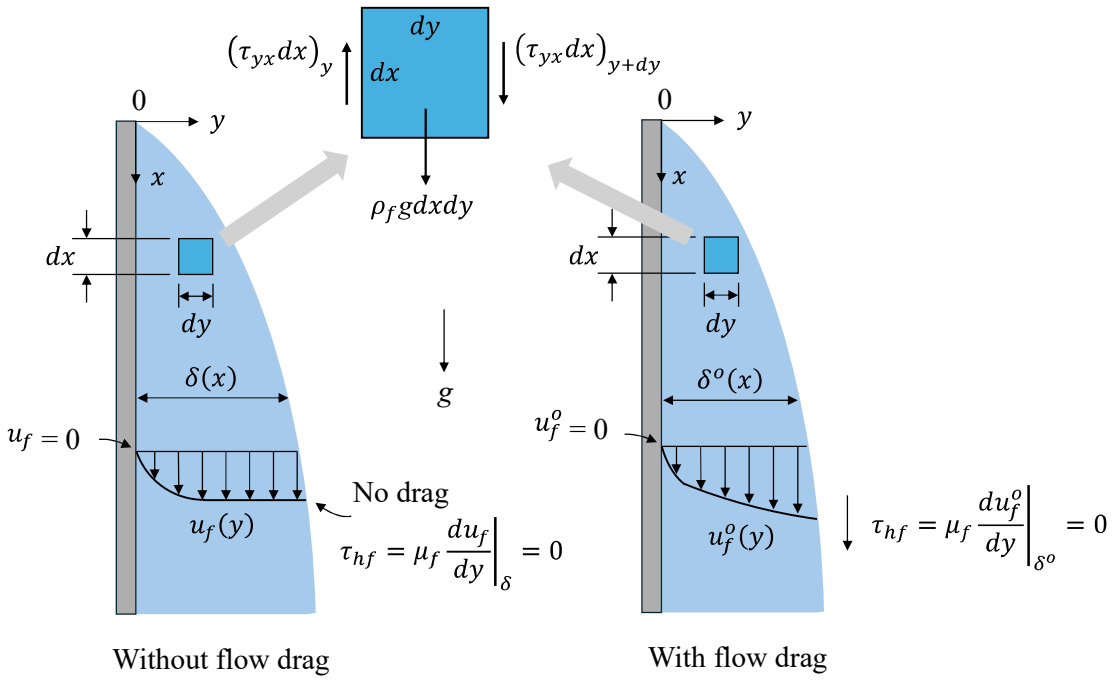

Fig. B.1. Laminar condensate film over a vertical flat plate without (left) and with considering (right) the effect of the gas flow drag upon the film and the forces acting on a differential control volume.

Thus, the momentum conservation equation in the vertical x-direction, applied to the control volume of Fig B.1, can be written as $\sum F_x = 0$, since film acceleration is zero. From the equilibrium of forces, and defining the viscous shear stress as $\tau_{yx} = \rho_f \nu_f (du_f/dy)$, the following equation of motion is obtained:

$$\frac{d^2u_f}{dy^2} = -\frac{g}{v_f} \tag{B.1}$$

Integrating Eq. (B.1) twice, the axial velocity of the condensate is expressed as follows:

$$u_f(y) = -\frac{g}{2v_f}y^2 + C_1 y + C_2. \tag{B.2}$$

To obtain the integration constants C_1 and C_2, the velocity boundary conditions, which depend on whether the gas flow drag is considered or not, have to be applied. If drag is not considered, boundary conditions are found from the no-slip condition at $y = 0$ and zero viscous shear stress at $y = \delta$:

$$u_f(y = 0) = 0, \tag{B.3}$$

$$\left.\frac{du_f(y)}{dy}\right|_{y=\delta} = 0, \tag{B.4}$$

Solving the velocity profile $u_f(y)$ without drag results:

$$u_f(y) = \frac{g}{v_f}\left(\delta y - \frac{y^2}{2}\right). \tag{B.5}$$

When considering the drag effect, the no-slip condition at the plate wall still applies, but the viscous shear stress at $y = \delta^o$ now is τ_{hf}, which is induced by the velocity gradient between the condensate and gas flow. Then, the boundary conditions would result:

$$u_f^o(y = 0) = 0, \tag{B.6}$$

$$\left.\frac{du_f^o(y)}{dy}\right|_{y=\delta^o} = \frac{\tau_{hf}}{\rho_f v_f}, \tag{B.7}$$

where the exponent "o" was introduced to note that gas drag is taken into account. Solving the constants of Eq. (B.2), the velocity profile affected by the shear stress at the interface is:

$$u_f^o(y) = -\frac{g}{2v_f}y^2 + \frac{1}{v_f}\left(\frac{\tau_{hf}}{\rho_f} + g\delta^o\right)y. \tag{B.8}$$

τ_{hf} increases the average condensate velocity. As a result, the liquid film becomes thinner while the film Reynolds number, Re_f, remains constant locally because it is independent of the gas flow. Accordingly, the condensate mass fluxes at a location "x"; without and with considering drag $\dot{m}_f(x)$ and $\dot{m}_f^o(x)$, must be equal. The mass flow rates are determined from:

$$\dot{m}_f(x) = \int_0^{\delta} \rho_l u_f(y) dy. \tag{B.9}$$

Substituting the velocity profiles of Eqs. (B.5) and (B.8) into Eq. (B.9), the local mass flow rates result:

$$\dot{m}_f(x) = \frac{\rho_f g \delta^3}{3\nu_f}, \tag{B.10}$$

and

$$\dot{m}_f^o(x) = \frac{\rho_f g {\delta^o}^3}{3\nu_f}\left(1 + \frac{3}{2}\tau_{hf}^+\right), \tag{B.11}$$

where the dimensional shear stress, $\tau_{hf}^+ = \tau_{hf}/\left(\rho_f g \delta^o\right)$, was substituted in Eq. (B.11). Equating Eqs. (B.10) and (B.11), the relationship between the film thickness with and without application of interface shear stress results:

$$\frac{\delta^o}{\delta} = \left(1 + \frac{3}{2}\tau_{hf}^+\right)^{-1/3}. \tag{B.12}$$

By assuming that, in laminar regime, the heat transfer coefficient $\alpha_f \propto \lambda_f/\delta$, the ratio of Nusselt numbers, and hence of heat transfer coefficients, with and without influence of gas flow, can be represented by the shear stress coefficient K_τ as follows:

$$\frac{Nu_f^o}{Nu_f} = \frac{\alpha_f^o}{\alpha_f} = \frac{\delta}{\delta^o} = K_\tau = \left(1 + \frac{3}{2}\tau_{hf}^+\right)^{1/3}. \tag{B.13}$$

The relationship of Eq. (B.13), which was derived for laminar flow regime, shows good agreement at high liquid Reynolds numbers, and hence for turbulent flow conditions [254].

The coefficients $K_{f,lam}$ and $K_{f,tur}$ are calculated using Eqs. (B.14) and (B.15).

$$K_{f,lam} = 1 + \left({Pr_f}^{0.56} - 1\right)\tanh \tau_{hf}^+ \tag{B.14}$$

$$K_{f,tur} = 1 + \left(Pr_f{}^{0.08} - 1\right) \tanh \tau_{hf}^{+}. \tag{B.15}$$

The calculation procedures for K_τ, $K_{f,lam}$ and $K_{f,tur}$ in Eqs. (B.13), (B.14) and (B.15) require the dimensionless shear stress, τ_{hf}^{+}, which is expressed as follows:

$$\tau_{hf}^{+} = \frac{\tau_{hf}}{\rho_f g \delta}. \tag{B.16}$$

In order to calculate τ_{hf}, the definition of drag force per unit of interfacial area, which is expressed as a function of the friction factor of the condensate film and the dynamic pressure, is used as follows:

$$\tau_{hf} = \frac{f_{hf}}{8} \rho_h \bar{u}_{hf}^2. \tag{B.17}$$

$\bar{u}_{hf}$ denotes the relative mean velocity between the shell gas flow and the film flow. f_{hf} is calculated as [287]

$$f_{hf} = 0.184 Re_{hf}^{-0.2} (1 + 850F), \tag{B.18}$$

with $Re_{hf} = \left(\bar{u}_{hf} D_{to}\right)/v_h$. In Eq. (B.18), F is the flow parameter, defined in Eq. (B.19).

$$F = \frac{\max\left\{\left(2Re_f\right)^{0.5}; 0.132 Re_f{}^{0.9}\right\}}{Re_{hf}{}^{0.9}} \frac{\mu_f}{\mu_h} \sqrt{\frac{\rho_h}{\rho_f}}. \tag{B.19}$$

The volumetric vapor content, ϑ, used to calculate the film thickness, δ, in Eq. (5.86), is also a function of F as follows [288]:

$$\vartheta = 1 - \frac{1}{1 + \frac{1}{8.48F}}. \tag{B.20}$$

10 Appendix C. Thermal-hydraulic performance of the micro shell-and-tube heat exchanger as a function of D_{to}, P_t and N_t

10.1 Tube diameter, D_{to}

To evaluate the influence of D_{to} on the thermal-hydraulic performance of the MSTHE, D_{to} was varied between 1.5 – 3 mm. The remaining geometric variables were kept constant and equal to those specified in Table 6.7.

Fig. C.1 represents the evolution of α_c, α_h, $\dot{n}$ and ΔT along the MSTHE length as a function of D_{to}. For a constant number of tubes per shell and fixed mass flow rates, increasing D_{to} leads to a larger heat transfer area. However, it also result in a lower flow velocity on the tube side. According to the empirical heat transfer correlation in Eq. (5.80), this velocity reduction significantly decreases α_c, as shown in Fig. C.1(a). The approach of the tube-side $scCO_2$ flow to the pseudo-critical temperature explains the α_c peak at a distance of about 700 mm from the hot-side of the MSTHE that can be seen in Fig. C.1(a).

Similarly, α_h decreases markedly from values of 2.14 $kW{\cdot}m^{-2}{\cdot}K^{-1}$ for D_{to} = 1.5 mm to 0.44 $kW{\cdot}m^{-2}{\cdot}K^{-1}$ for D_{to} = 3 mm. This decline is attributed to a reduction in the MSTHE compactness with increasing D_{to}, which enlarges the shell diameter and flow cross-sectional area, thereby reducing the shell-side flow velocity. The lower α_h also diminishes the mass transfer coefficient θ_h according to the Chilton-Colburn analogy (Eq. (5.87)), which leads to a drop of $\dot{n}$ due to the attenuation of turbulent mixing in the shell flow, as depicted in Fig. C.1(c). Consequently, less latent heat is released, resulting in a lower condensate molar flow rate.

Furthermore, the reduced shell-side velocity affects the dynamics of the condensate film by decreasing the shear stress at the vapor-liquid interface. This promotes a thicker condensate layer and reduces turbulent fluctuations, further impairing overall shell-side heat transfer. These combined effects lead to an overall decline in heat transfer performance and, as seen in Fig. C.1(d), to an increase in the temperature difference between the fluid within the MSTHE. For instance, on the hot side, ΔT increases from 10 ºC for D_{to} = 1.5 mm, to approximately 23 ºC for D_{to} = 3 mm. Additionally, the pinch-point, located at the dew point temperature of the hot gases (~ 118 ºC), rises from 3.9 ºC to 17.5 ºC. Fig. C.1(d) also shows that the outlet temperature of the shell-side gas increases significantly with D_{to}: from 48.5 ºC for D_{to} = 1.5 mm to 75 ºC for D_{to} = 3 mm.

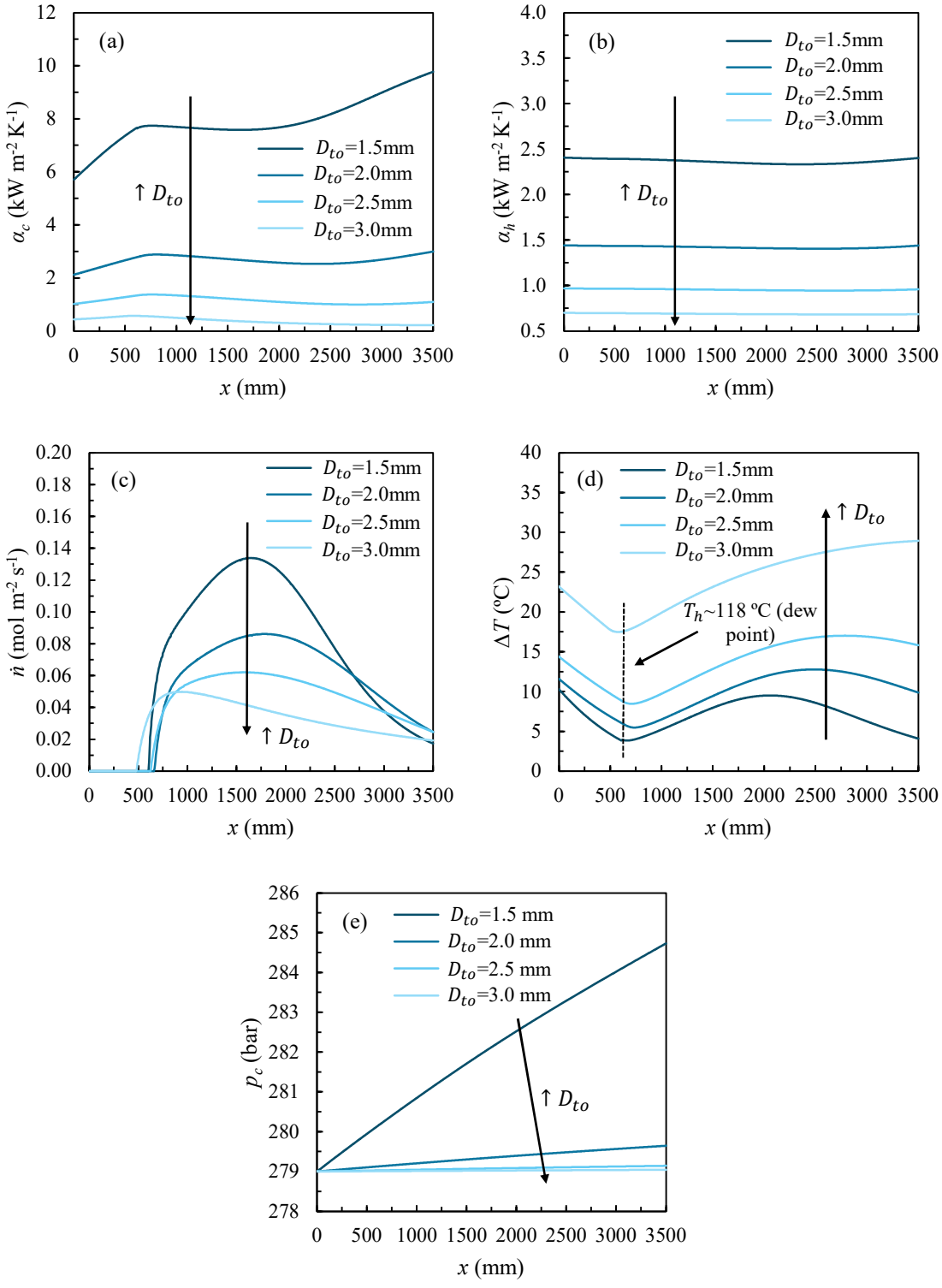

Fig. C.1. Evolution of (a) α_c, (b) α_h, (c) $\dot{n}$, (d) ΔT and (e) p_c along the MSTHE length as a function of D_{to}.

Although a lower D_{to} improves the thermal performance of the MSTHE, it also causes a significant increase in the tube-side pressure drop, as presented in Fig. C.1(e). For D_{to} values of 1.5 mm, 2.0 mm, 2.5 mm and 3.0 mm, the pressure drops result 5.75 bar, 0.65 bar, 0.14 bar and 0.05 bar, respectively. Therefore, the maximum allowable pressure drop is the limiting parameter for the minimum achievable D_{to} and compactness of the MSTHE.

10.2 Distance between tubes (pitch, P_t)

The distance between the tubes in the bundle, P_t, varied between $1.25D_{to}$ and $1.55D_{to}$ to analyze the effect on the thermal-hydraulic performance of the MSTHE. The remaining geometrical input parameters were maintained constant and equal to those specified for the baseline MSTHE configuration of Table 6.7.

Fig. C.2 illustrates the evolution of α_h, p_h, $\dot{n}$, $\dot{N}_f$ and ΔT along the MSTHE length as a function of P_t. Since the tube-side flow velocity is unaffected by P_t, α_c remains approximately constant. However, increasing P_t reduces the compactness of the tube bundle, leading to a larger shell inner diameter from 624.6 mm for $P_t = 1.25D_{to}$ to 774.5 mm for $P_t = 1.55D_{to}$. Consequently, the shell-side flow velocity decreases, resulting in a significant drop of α_h as shown in Fig. C.2(a), and a corresponding degradation of the overall heat transfer performance.

As depicted in Fig. C.2(b), the reduced shell-side velocity also leads to a marked decrease in pressure drop, from 1.13 bar for $P_t = 1.25D_{to}$ to 0.1 bar for $P_t = 1.55D_{to}$. The decline in α_h, while α_c remains constant, causes a reduction in the outer-wall temperature of the tube, T_{wo}, with increasing P_t, thereby increasing the thermal driving force on the gas side. As a result, the near-wall gas region reaches its saturation temperature sooner, initiating condensation closer to the hot-side inlet of the MSTHE. This behavior is evidenced by the leftward shift of the $\dot{n}$ curves in Fig. C.2(c). Despite this shift, the similarity in the qualitative shape, and magnitude, of the $\dot{n}$ curves indicates that the total amount of condensed vapor remains nearly unchanged, as the overall heat transfer surface is constant with varying P_t. Consequently, $\dot{N}_f$ increases along the MSTHE with increasing P_t, but results in a similar output value of about 74 mol·s^{-1}, as depicted in Fig. C.2(d). As the condensate film thickens, the available flow are for the gas phase in the stratified region narrows. This leads to a slight increase in shell-side gas velocity, which in turn enhances gas-phase heat transfer and intensifies turbulent fluctuations within the film by increasing interfacial shear stress.

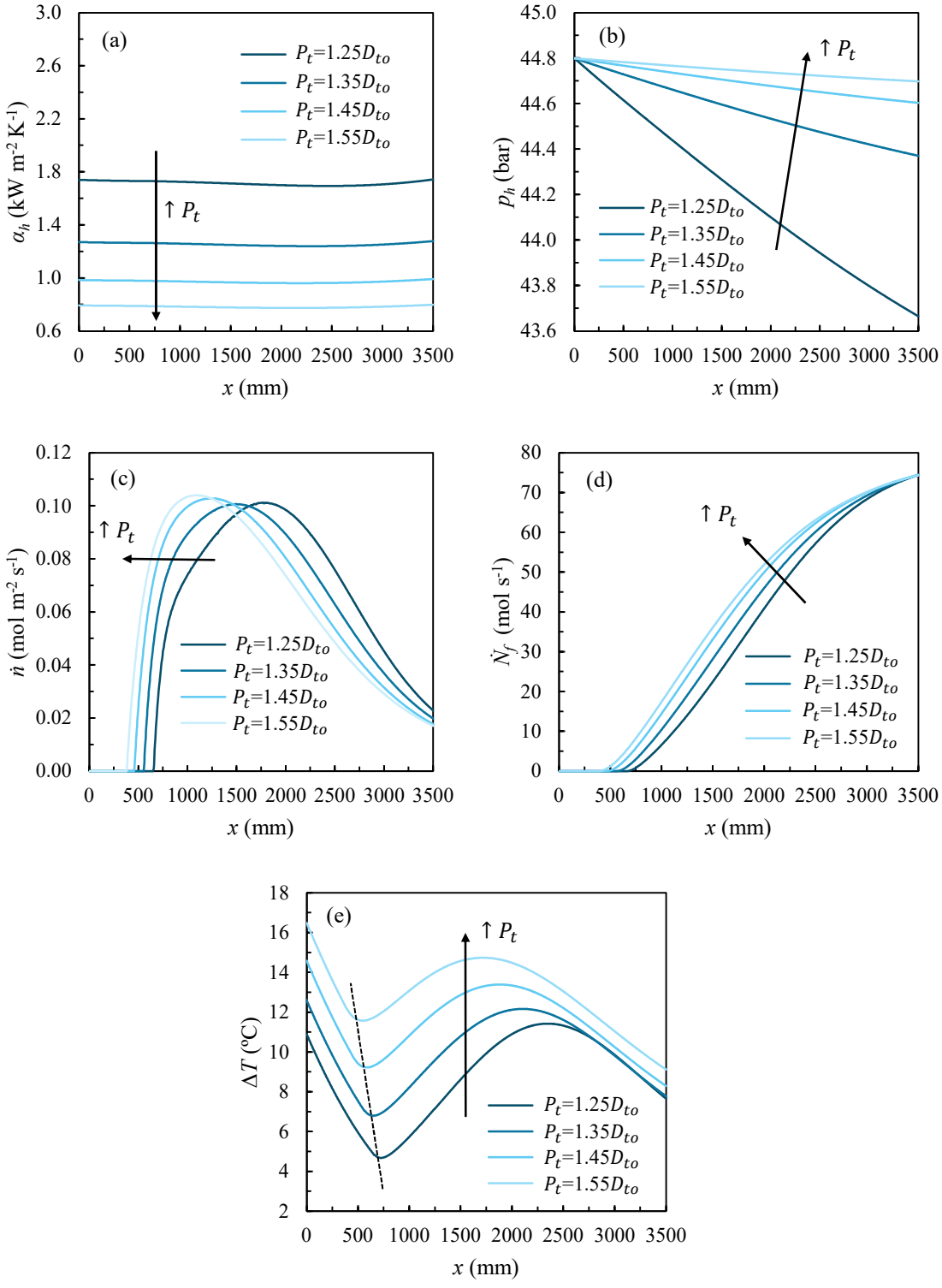

Fig. C.2. Evolution of (a) α_h, (b) p_h, (c) $\dot{n}$, (d) $\dot{N}_f$ and (e) ΔT along the MSTHE length as a function of the tube pitch P_t.

The reduction of α_h with P_t decreases the overall heat transfer performance in the MSTHE, resulting in the augment of ΔT, as shown in Fig. C.2(e). The temperature approach on the hot-side increases from 10.9 ºC for P_t = 1.25D_{to} to 16.5 ºC for P_t = 1.55D_{to}, which implies that the scCO$_2$ flow leaves the MSTHE at a lower temperature. The pinch-point also rises with P_t. Moreover, the pinch-point shifts to the hot-side of the MSTHE due to the frontward onset of condensation, as previously explained.

10.3 Number of tubes in the bundle, N_t

To clarify the influence of the number of tubes per shell, N_t, on the thermal-hydraulic performance of the MSTHE, the model was evaluated for N_t values between 50,000 and 80,000. The rest of the design parameters were maintained constant and equal to those indicated in the baseline design in Table 6.7.

Fig. C.3 presents the trends of α_c, α_h, P_c, P_h, $\dot{n}$, and T_h and T_c along the MSTHE as a function of N_t. Increasing N_t leads to a reduction of the tube-side flow velocity, which lowers the Reynolds number and weakens turbulent heat transfer on the tube side. This results in a decline in α_c, shown in Fig. C.3(a). The shell-side flow passage area A_{ph}, is calculated according to the following expression:

$$A_{ph} = \frac{\pi N_t}{4}\left[\frac{4P_t^2(CL)}{\pi(CTP)} - D_{to}^2\right]. \tag{C.1}$$

Eq. (C.1) was derived by substituting Eq. (5.48) into the expression for the calculation of the inner diameter of the shell. As can be seen in Eq. (C.1), when P_t and D_{to} are held constant, A_{ph} results proportional to N_t. Thus, increasing N_t at a fixed shell-side mass flow reduces the shell-side velocity and consequently α_h, as previously discussed in Section 6.4.1.

The reduction in both tube- and shell-side flow velocities leads to significantly lower pressure drops, as illustrated in Figs. C.3(c) and C.3(d). Furthermore, as depicted in Fig. C.3(e), $\dot{n}$ decreases with increasing N_t, due to the decline in the shell-side mass transfer coefficient caused by the lower α_h. The simultaneous reductions in α_c, α_h and $\dot{n}$ impair the heat transfer performance of the MSTHE. However, it is important to note that the total heat exchange area increases significantly with higher N_t, partially compensating for the deteriorated convective performance. As a result, under the specific conditions of this parametric study, the outlet temperatures of the fluids remain nearly unaffected by changes in N_t. This is clearly shown in Fig. C.3(f), where the evolution of T_h and T_c is plotted along the MSTHE length as a function of N_t.

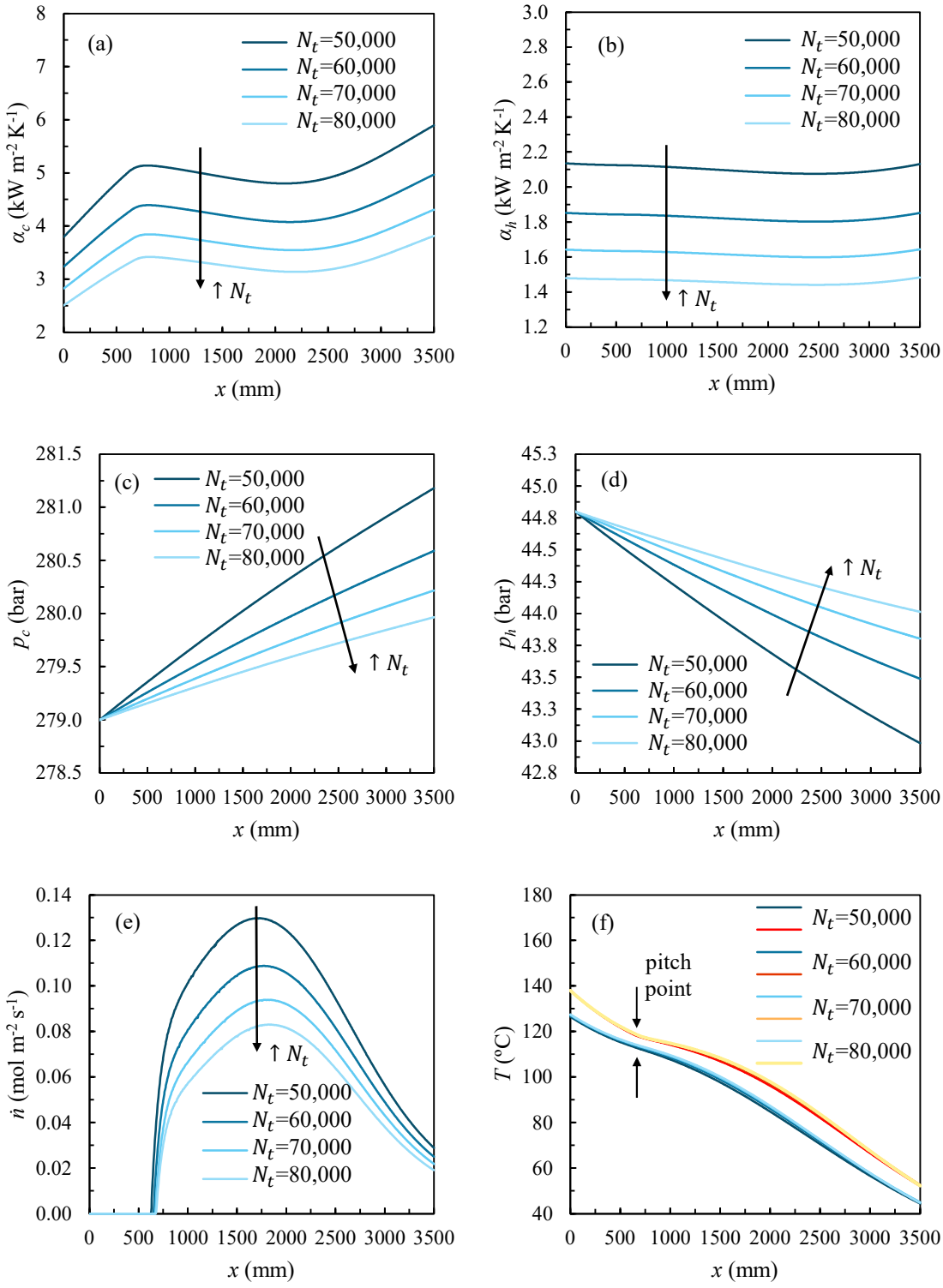

Fig. C.3. Evolution of (a) α_c, (b) α_h, (c) p_c, (d) p_h, (e) $\dot{n}$, and (f) T_h and T_c along the MSTHE length as a function of the number of tubes N_t.

11 Appendix D. Publications and contributions

11.1 Publications

Paper 1: Thesis chapters 3.1 & 4.1

Title	Optimization and performance evaluation of equations of state for supercritical CO_2-rich mixtures for application in the NET Power cycle.
Journal	The Journal of Supercritical Fluids.
Authors	Iván Velázquez*, Frederiek Demeyer, Miriam Reyes.
DOI	https://doi.org/10.1016/j.supflu.2025.106693.
Status	Published. (Received 30 April 2025; Received in Revised form 28 May; Accepted 9 June 2025; Available online 11 June 2025).
Abstract	In this paper the interaction parameters of six equations of state (EoS) were calibrated from density and phase equilibrium experimental data of supercritical CO_2-rich mixtures. The Peng-Robinson (PR), Soave-Redlich- Kwong (SRK), Lee-Kesler-Plöcker (LKP), Benedict-Webb-Rubin-Starling (BWRS), perturbed chain SAFT (PC-SAFT) and Cubic-Plus-Association (CPA) EoSs were considered. As a novelty, the pressure, temperature and composition ranges for calibration were (1 – 49) MPa, (293.18 – 423.15) K, and (72.6 – 99.8)% mol CO_2, which are close to those found in the innovative oxy-combustion NET Power cycle, particularizing the optimization of the EoSs for application in this power cycle. The performance of the EoSs, including the GERG-2008 EoS, was assessed in an isentropic compression process from 7.4 MPa to 30 MPa. The LKP EoS reported the lowest average deviation, 2.03%, in modeling the bubble and dew lines of the supercritical CO_2 – H_2O mixture. The GERG-2008 EoS was the most reliable model capturing the density of the supercritical CO_2-rich mixtures, reporting an average deviation of 1.34%. Therefore, the combination GERG-2008 + LKP is recommended for NET Power cycle modeling purposes. Only the CPA and GERG-2008 models captured the liquid-like properties of the CO_2-rich mixture during the compression. This resulted in a specific compression work of 33.02 kJ kg^{-1} for GERG-2008, while the PR, SRK, LKP, and PC-SAFT EoSs reported a value up to 1.54, 1.65, 1.53, and 1.70 times higher.
Keywords	NET Power cycle; Supercritical carbon dioxide; Equations of state; Interaction parameters.
Highlights	Equations of state were optimized for application in the novel NET Power cycle. LKP EoS captured the CO_2 – H_2O bubble and dew lines with the lowest error, 2.03%. GERG-2008 captured the density of the $scCO_2$ mixtures with the lowest error, 1.34%. The GERG-2008 specific work was 32.91 kJ kg^{-1}, up to 1.71 lower than other EoSs.
Thesis chapters	3.1 & 4.1.

Paper 2: Thesis chapters 3.2 & 4.2

Title	Investigation of the impact of the thermodynamic property method on the performance, preliminary component sizing and maximum efficiency configuration of the NET Power cycle.
Journal	Applied Thermal Engineering.
Authors	Iván Velázquez*, Frederiek Demeyer, Miriam Reyes.
DOI	https://doi.org/10.1016/j.applthermaleng.2025.126491.
Status	Published. (Received 11 February 2025; Received in Revised form 25 March; Accepted 13 April 2025; Available online 15 April 2025).
Abstract	This paper investigates the effect of thermodynamic property methods on the NET Power cycle, which is a novel supercritical CO_2 cycle power cycle based on the oxy-combustion technology. A numerical model of the most advanced configuration of NET Power cycle and air separation unit was developed in Aspen Plus to characterize the thermodynamic performance, key components presizing, and maximum efficiency operating configuration. The Peng-Robinson cubic Equation of State (EoS) has traditionally been adopted as the reference EoS (REF EoS) in previous thermodynamic studies on the NET Power cycle. However, its elevated predictive uncertainty, especially in phase modeling, may have led to inconsistent results. For that reason, and as a novelty, in present work, different EoS such as cubic, viral, SAFT and multiparametric Helmholtz free energy-based methods were considered, to evaluate the effect of the EoS on the cycle components and to optimize the operating conditions of the cycle. GERG-2008 + LKP was also included as the most reliable method. The results reveal that GERG-2008 + LKP estimates a fluid density in the liquid-like phase pumping stages 25% higher than the cubic EoSs at nominal conditions. Thus, the compression work is 11.57% lower and the net cycle efficiency 1.48% higher. The higher relative deviations in cycle efficiency were obtained with PC-SAFT and GERG-2008 models. REF EoS estimates a recirculation pump impeller diameter 7.49% larger than GERG-2008 + LKP. An oversized pump would operate outside the design point with low efficiency, flow control difficulties, and potential vibration and overpressure issues. For GERG-2008 + LKP, the heat exchange area required by the recuperator is 6.46% lower than that estimated by REF EoS. This suggests that the manufacturing costs are significantly lower and transient response faster than expected. The maximum cycle efficiency resulted in 55.94%, for a combustor outlet temperature of 1103.93 ºC, turbine inlet and outlet pressures of 273.99 bar and 44.83 bar, and bypass split fraction of 11.37%.
Keywords	Oxy-combustion; NET Power cycle; Supercritical CO_2 cycle; Equations of state; CO_2-capture.
Highlights	The TPM influence on the NET Power cycle thermal performance was studied. REFPROP + LKP predict a net cycle efficiency of 0.5 – 2.5% higher than cubic EoSs. The impeller diameter of the recirculation pump is 7.49% smaller for GERG-2008 + LKP. The recuperator's heat exchanger area is 6.46% lower for GERG-2008 + LKP. The maximum cycle efficiency for GERG-2008 + LKP is 55.94%.
Thesis chapters	3.2 & 4.2

Paper 3: Thesis chapters 5.1; 6.1 & 6.2

Title	Experimental investigation and modeling of heat transfer to supercritical CO_2 in a microtube up to 30 MPa: towards high-performance compact heat exchangers for the NET Power cycle
Journal	Energy
Authors	Iván Velázquez*, Danilo A. Cantero, Frederiek Demeyer, Miriam Reyes.
DOI	-
Status	Under review. (Date of submission: 27 May 2025).
Abstract	Microtube heat exchangers offer a high-performance alternative to conventional printed circuit designs in the thermal recuperator of the innovative oxy-combustion NET Power cycle, with the potential to enhance system efficiency and compactness. To initiate this heat exchange technology migration, this paper presents as a novelty an experimental investigation on heat transfer to CO_2 at supercritical pressures up to 30 MPa. The data was generated in a 1700 mm length, 0.88 mm inner diameter, uniformly heated horizontal microtube, which mimics the operative conditions of the microtube heat exchanger. To this end, an experimental system was built to measure local convective heat transfer coefficients of CO_2. The effects of mass flux (447.4 – 1044.5 kg/m^2 s), heat flux (8.3 – 21.3 kW/m^2), inlet temperature (19.8 – 30.1 ºC), buoyancy and flow acceleration on heat transfer were investigated for pressures of 10, 15, 20, 25 and 30 MPa. The heat transfer rates improved with increasing the mass flux. For 10 MPa, the heat transfer coefficient enhances near the pseudo-critical point, followed by a deteriorative region and a subsequent recovery. By increasing the thermal input, the heat transfer peak value at 10 MPa is attenuated, and the heat transfer coefficients are improved at higher pressures. By rising the inlet temperature, the heat transfer improves in the thermal inflow length, the heat transfer peaks at a lower value for 10 MPa, and the heat transfer coefficients converge to similar values at higher pressures. The higher the pressure, the lower the strength of the buoyancy effects, being significant at 10 MPa. A new artificial deep neural network based heat transfer model was developed, which captures the data points with a deviation of 6.74%.
Keywords	NET Power cycle; Oxy-combustion; Compact heat exchangers; Neural network; Heat transfer: Supercritical carbon dioxide; Microtube heat exchanger.
Highlights	Heat transfer to scCO_2, up to 30 MPa, in a microtube was experimentally studied. An increase in mass flux enhances heat transfer rates at all pressures tested. Higher heat flux and inlet temperature improve heat transfer at high pressures. Buoyancy effects diminish with increasing pressure and are more marked at 10 MPa. The new heat transfer model captures the data points with a 6.74% of error.
Thesis chapters	5.1; 6.1 & 6.2.

Paper 4: Thesis chapters 5.3 & 6.4

Title	Assessment of the thermal-hydraulic behavior of a micro shell-and-tube heat exchanger operating under part-load conditions in the condensative low-temperature section of the NET Power cycle recuperator
Journal	-
Authors	Iván Velázquez*, Frederiek Demeyer, Miriam Reyes.
DOI	-
Status	Waiting for acceptance of Paper 3.
Abstract	This paper presents a novel investigation of the thermal-hydraulic performance of a micro shell-and-tube heat exchanger (MSTHE) for application in the thermal recuperator of the innovative oxy-combustion-based NET Power cycle, operating under cycle partial load conditions. The aim is to support the technological transition from the established printed circuit heat exchangers (PCHE) to MSTHE, which offer a more compact, cost-effective, and maintenance-friendly high-performance alternative. To this end, a thermal-hydraulic model of the MSTHE was developed, capable of capturing the rapid variation of the supercritical CO_2 ($scCO_2$) properties and the partial filmwise condensation of the turbine exhaust gases. Results show that the MSTHE effectiveness decreases from 89.2% to 65.1% as the cycle load is reduced from 100% to 20%. The overall heat transfer coefficient gradually decreases between 100% and 40% cycle load, drops sharply between 40% and 30%, and then stabilizes between 30% and 20%. This stabilization is attributed to the abrupt local increase of the heat capacity on the $scCO_2$-side during the pseudo-critical phase transition, which also enhances local condensation heat release and thickens the condensate film on the shell side. However, this phenomenon induces strong axial temperature gradients that may induce thermal stresses compromising the structural integrity of the microtubes. While the floating microtube bundle of MSTHEs can accommodate these thermal stresses, the rigid, compact block of PCHEs is more prone to damage, revealing an additional key advantage of MSTHEs.
Keywords	NET Power cycle; Oxy-combustion; Microtube heat exchanger; Supercritical carbon dioxide; Heat transfer.
Highlights	The thermal behavior of a microtube exchanger for the NET Power cycle was assessed. The effectiveness falls from 89 to 65% as the cycle load drops from 100 to 20%. The pseudo-critical phase change of $scCO_2$ enhances heat transfer at minimum load. Steep axial temperature gradients appear that may affect the structural integrity.
Thesis chapters	5.3 & 6.4.

11.2 Contributions to congresses

Description	Meeting of the Spanish Section of the Combustion Institute
Start date	07/11/2023
End date	08/11/2023
Location	University of Zaragoza, Spain

Description	The 8th International Supercritical CO_2 Power Cycles Symposium
Start date	26/2/2024
End date	29/02/2024
Location	San Antonio, Texas, United States.

Description	Hydrogen conference
Start date	08/07/2024
End date	08/07/2024
Location	University of Leon, Spain

References

References

[1] Energy institute, Statistical Review of World Energy. 73rd edition, 2024.

[2] IPCC, 2023: Climate Change 2023: Synthesis Report. Contribution of Working Groups I, II and III to the Sixth Assessment Report of the Intergovernmental Panel on Climate Change [Core Writing Team, H. Lee and J. Romero (eds.)]. IPCC, Geneva, Switzerland., 2023. https://doi.org/10.59327/IPCC/AR6-9789291691647.

[3] D.Y.C. Leung, G. Caramanna, M.M. Maroto-Valer, An overview of current status of carbon dioxide capture and storage technologies, Renew. Sustain. Energy Rev. 39 (2014) 426–443. https://doi.org/10.1016/j.rser.2014.07.093.

[4] T. Kuramochi, A. Ramírez, W. Turkenburg, A. Faaij, Comparative assessment of CO_2 capture technologies for carbon-intensive industrial processes, Prog. Energy Combust. Sci. 38 (2012) 87–112. https://doi.org/10.1016/j.pecs.2011.05.001.

[5] M.A. Nemitallah, M.A. Habib, H.M. Badr, S.A. Said, A. Jamal, R. Ben-Mansour, E.M.A. Mokheimer, K. Mezghani, Oxy-fuel combustion technology: current status, applications, and trends, Int. J. Energy Res. 41 (2017) 1670–1708. https://doi.org/10.1002/er.3722.

[6] F. Climent Barba, G. Martínez-Denegri Sánchez, B. Soler Seguí, H. Gohari Darabkhani, E.J. Anthony, A technical evaluation, performance analysis and risk assessment of multiple novel oxy-turbine power cycles with complete CO_2 capture, J. Clean Prod. 133 (2016) 971–985. https://doi.org/10.1016/j.jclepro.2016.05.189.

[7] R. Allam, S. Martin, B. Forrest, J. Fetvedt, X. Lu, D. Freed, G.W. Brown, T. Sasaki, M. Itoh, J. Manning, Demonstration of the Allam Cycle: An Update on the Development Status of a High Efficiency Supercritical Carbon Dioxide Power Process Employing Full Carbon Capture, Energy Procedia, Elsevier Ltd, 2017: pp. 5948–5966. https://doi.org/10.1016/j.egypro.2017.03.1731.

[8] J.S. Kwon, S. Son, J.Y. Heo, J.I. Lee, Compact heat exchangers for supercritical CO_2 power cycle application, Energy Convers. Manag. 209 (2020) 112666. https://doi.org/10.1016/j.enconman.2020.112666.

[9] Y. Jiang, E.A. Liese, S.E. Zitney, D. Bhattacharyya, Dynamic modeling of microtube recuperators in an indirect supercritical carbon dioxide recompression closed Brayton power cycle, The 6th International Supercritical CO_2 Power Cycles Symposium (2018).

[10] W. Chan, T. Morosuk, X. Li, H. Li, Allam cycle: Review of research and development, Energy Convers. Manag. 294 (2023) 117607. https://doi.org/10.1016/j.enconman.2023.117607.

[11] S. Jenkins, E. Mitchell-Larson, M.C. Ives, S. Haszeldine, M. Allen, Upstream decarbonization through a carbon takeback obligation: An affordable backstop climate policy, Joule. 5 (2021) 2777–2796. https://doi.org/10.1016/j.joule.2021.10.012.

[12] V. Masson-Delmotte, A. P. Zhai, S.L. Pirani, C. Connors, S. Péan, N. Berger, Y. Caud, L. Chen, M.I. Goldfarb, M. Gomis, K. Huang, E. Leitzell, J.B.R. Lonnoy, T.K. Matthews, T. Maycock, O. Waterfield, R. Yelekçi, IPCC 2021: Climate Change 2021: The Physical Science Basis. Contribution of Working Group I to the Sixth Assessment Report of the Intergovernmental Panel on Climate Change, United Kingdom and New York, 2021.

[13] Global CO_2 Storage Resource Database a critical step forward for the deployment of CCS - Global CCS Institute, (n.d.). https://www.globalccsinstitute.com/news-media/insights/global-co2-storage-resource-database-a-critical-step-forward-for-the-deployment-of-ccs/ (accessed April 6, 2022).

[14] J. Liu, C.-Y. Hsu, S.F. Ahmad, M.A. Alotaibi, M.I. Allahham, M. Qin, Design and energy, exergy, thermoeconomic, and exergo-environmental (4E) analyses of a novel hybrid geothermal/biogas-powered green multi-generation system using a post-combustion CO_2 capture unit, Appl. Energy. 377 (2025) 124662. https://doi.org/10.1016/j.apenergy.2024.124662.

[15] D. Jansen, M. Gazzani, G. Manzolini, E. Van Dijk, M. Carbo, Pre-combustion CO_2 capture, Int. J. Greenh. Gas Control. 40 (2015) 167–187. https://doi.org/10.1016/J.IJGGC.2015.05.028.

[16] I. Pfaff, A. Kather, Comparative thermodynamic analysis and integration issues of CCS steam power plants based on oxy-combustion with cryogenic or membrane based air separation, Energy Procedia. 1 (2009) 495–502. https://doi.org/10.1016/J.EGYPRO.2009.01.066.

[17] M. Saedi, M. Mehrpooya, A. Shabani, A. Zaitsev, A. Nikitin, Proposal and investigation of a novel process configuration for production of neon from cryogenic air separation unit, Sustain. Energy Technol. Assess. 50 (2022). https://doi.org/10.1016/j.seta.2021.101875.

[18] F. Bisotti, A. Galeazzi, L. Galatioto, F. Masserdotti, A. Bigi, P. Gritti, F. Manenti, Implementing robust thermodynamic model for reliable bubble/dew problem

solution in cryogenic distillation of air separation units, Int, J. Thermofluids. 10 (2021). https://doi.org/10.1016/j.ijft.2021.100083.

[19] E. de Visser, C. Hendriks, M. Barrio, M.J. Mølnvik, G. de Koeijer, S. Liljemark, Y. Le Gallo, Dynamis CO_2 quality recommendations, Int. J. Greenh. Gas Control. 2 (2008) 478–484. https://doi.org/10.1016/j.ijggc.2008.04.006.

[20] Y.H. Fan, G.H. Tang, X.L. Li, D.L. Yang, General and unique issues at multiple scales for supercritical carbon dioxide power system: A review on recent advances, Energy Convers. Manag. 268 (2022) 115993. https://doi.org/10.1016/j.enconman.2022.115993.

[21] Z.X. Zhang, G.X. Wang, P. Massarotto, V. Rudolph, Optimization of pipeline transport for CO2 sequestration, Energy Convers. Manag. 47 (2006) 702–715. https://doi.org/10.1016/j.enconman.2005.06.001.

[22] J. Koornneef, M. Spruijt, M. Molag, A. Ramirez, A. Faaij, W. Turkenburg, Uncertainties in risk assessment of CO_2 pipelines, Energy Procedia. 1 (2009) 1587–1594. https://doi.org/10.1016/j.egypro.2009.01.208.

[23] R.M. Cuéllar-Franca, A. Azapagic, Carbon capture, storage and utilisation technologies: A critical analysis and comparison of their life cycle environmental impacts, J. CO_2 Util. 9 (2015) 82–102. https://doi.org/10.1016/j.jcou.2014.12.001.

[24] X. Song, Y. Guo, J. Zhang, N. Sun, G. Shen, X. Chang, W. Yu, Z. Tang, W. Chen, W. Wei, L. Wang, J. Zhou, X. Li, X. Li, J. Zhou, Z. Xue, Fracturing with Carbon Dioxide: From Microscopic Mechanism to Reservoir Application, Joule. 3 (2019) 1913–1926. https://doi.org/10.1016/j.joule.2019.05.004.

[25] D. Hidalgo, J.M. Martín-Marroquín, Power-to-methane, coupling CO_2 capture with fuel production: An overview, Renewable and Sustainable Energy Reviews 132 (2020). https://doi.org/10.1016/j.rser.2020.110057.

[26] R.M. Cuéllar, Oxy-Fuel Combustion Capture Sustainable Energy Technologies & Sus-tainable Chemical Processes Oxy-fuel combustion capture, 2017.

[27] B.S. Choi, M.J. Kim, J.H. Ahn, T.S. Kim, Influence of a recuperator on the performance of the semi-closed oxy-fuel combustion combined cycle, Appl. Therm. Eng. 124 (2017) 1301–1311. https://doi.org/10.1016/j.applthermaleng.2017.06.055.

[28] P. Mathieu, R. Nihart, Sensitivity analysis of the MATIANT cycle, Energy Convers. Manag. 40 (1999) 1687–1700. https://doi.org/10.1016/S0196-8904(99)00062-X.

[29] R.J. Allam, B.A. Forrest, J.E. Fetvedt, Method and System for Power Production With Improved Efficiency. U.S. Pat. Appl. No. 2018/0073434 A1, 15 March 2018.

[30] B. Mitterrutzner, W. Sanz, L.O. Nord, A part-load analysis and control strategies for the Graz Cycle, Int. J. Greenh. Gas Control. 113 (2022). https://doi.org/10.1016/j.ijggc.2021.103521.

[31] R.L. Bannister, R.A. Newby, W.C. Yang, Final Report on the Development of a Hydrogen-Fueled Combustion Turbine Cycle for Power Generation, J. Eng. Gas Turbine Power. 121 (1999) 38–45. https://doi.org/10.1115/1.2816310.

[32] S.G. Sundkvist, S. Julsrud, B. Vigeland, T. Naas, M. Budd, H. Leistner, D. Winkler, Development and testing of AZEP reactor components, Int. J. Greenh. Gas Control. 1 (2007) 180–187. https://doi.org/10.1016/S1750-5836(07)00025-4.

[33] L. Mancuso, N. Ferrar, P. Chiesa, E. Martelli, M. Romano, oxy-combustion turbine power plants, 2015. www.ieaghg.org. (accessed March 9, 2023).

[34] R.E. Anderson, S. MacAdam, F. Viteri, D.O. Davies, J.P. Downs, A. Paliszewski, Adapting Gas Turbines to Zero Emission Oxy-Fuel Power Plants, in: Volume 2: Controls, Diagnostics and Instrumentation; Cycle Innovations; Electric Power, ASMEDC, 2008: pp. 781–791. https://doi.org/10.1115/GT2008-51377.

[35] A. Rogalev, N. Rogalev, V. Kindra, I. Komarov, O. Zlyvko, Research and Development of the Oxy-Fuel Combustion Power Cycles with CO_2 Recirculation, Energies. 14 (2021) 2927. https://doi.org/10.3390/en14102927.

[36] R. Allam, M. Palmer, G. Brown, System and method for high efficiency power generation using carbon dioxide circulating working fluid. U.S. Pat. Appl. No. 12/872,777, 2011.

[37] J. Luo, O. Emelogu, T. Morosuk, G. Tsatsaronis, Exergy-based investigation of a coal-fired Allam cycle, Energy. 218 (2021) 119471. https://doi.org/10.1016/j.energy.2020.119471.

[38] R. Scaccabarozzi, M. Gatti, E. Martelli, Thermodynamic analysis and numerical optimization of the NET Power oxy-combustion cycle, Appl. Energy. 178 (2016) 505–526. https://doi.org/10.1016/j.apenergy.2016.06.060.

[39] A. Rogalev, E. Grigoriev, V. Kindra, N. Rogalev, Thermodynamic optimization and equipment development for a high efficient fossil fuel power plant with zero emissions, J. Clean Prod. 236 (2019). https://doi.org/10.1016/j.jclepro.2019.07.067.

[40] R.J. Allam, Cryogenic Air Separation Method for Producing Oxygen at High Pressures. U.S. Pat. Appl. No. 2018/0073804 A1, 15 March 2018.

[41] C. Mitchell, V. Avagyan, H. Chalmers, M. Lucquiaud, An initial assessment of the value of Allam Cycle power plants with liquid oxygen storage in future GB electricity system, Int. J. Greenh. Gas Control. 87 (2019) 1–18. https://doi.org/10.1016/j.ijggc.2019.04.020.

[42] Y. Haseli, N.S. Sifat, Performance modeling of Allam cycle integrated with a cryogenic air separation process, Comput. Chem. Eng. 148 (2021) 107263. https://doi.org/10.1016/j.compchemeng.2021.107263.

[43] L. Colleoni, A. Sindoni, S. Ravelli, Comprehensive Thermodynamic Evaluation of the Natural Gas-Fired Allam Cycle at Full Load, Energies. 16 (2023) 2597. https://doi.org/10.3390/en16062597.

[44] S.A. Zaryab, R. Scaccabarozzi, E. Martelli, Advanced part-load control strategies for the Allam cycle, Appl. Therm. Eng 168 (2020). https://doi.org/10.1016/j.applthermaleng.2019.114822.

[45] Y. Haseli, G.F. Naterer, Optimization of turbine pressures in a net-zero supercritical Allam cycle, J. Clean Prod. 400 (2023) 136639. https://doi.org/10.1016/j.jclepro.2023.136639.

[46] J.J. Moore, O. Pryor, I. Cormier, J. Fetvedt, Oxygen Storage Incorporated Into Net Power and the Allam-Fetvedt Oxy-Fuel sCO$_2$ Power Cycle – Technoeconomic Analysis, in: Volume 9: Supercritical CO$_2$, ASME, 2022. https://doi.org/10.1115/GT2022-82060.

[47] W. Chan, X. Lei, F. Chang, H. Li, Thermodynamic analysis and optimization of Allam cycle with a reheating configuration, Energy Convers. Manag. 224 (2020) 113382. https://doi.org/10.1016/j.enconman.2020.113382.

[48] M. Xie, S. Liu, L. Chen, Y. Zhang, Y. Wang, S. Xie, Y. Zhao, Techno-economic and environmental assessment of a novel co-generation system integrating heat pump with Allam cycle, Energy Convers. Manag. 277 (2023) 116606. https://doi.org/10.1016/j.enconman.2022.116606.

[49] H. Yu, T. Gundersen, E. Gençer, Optimal liquified natural gas (LNG) cold energy utilization in an Allam cycle power plant with carbon capture and storage, Energy Convers. Manag. 228 (2021) 113725. https://doi.org/10.1016/j.enconman.2020.113725.

[50] L. Wang, S.M. Alirahmi, H. Yu, Development and analysis of a novel power-to-gas-to-power system driven by the Allam cycle for simultaneous electricity and water production, Energy Convers. Manag. 319 (2024) 118934. https://doi.org/10.1016/j.enconman.2024.118934.

[51] M. Xie, X. Chen, L. Chen, M. Zhou, Y. Liu, L. Zeng, H. Shi, F. Zhang, S. Xie, Y. Zhao, Evaluating the feasibility of a novel Allam cycle for co-generating power and water in hot regions, Energy Convers. Manag. 309 (2024) 118447. https://doi.org/10.1016/j.enconman.2024.118447.

[52] Y. Zhao, B. Wang, J. Chi, Y. Xiao, Parametric study of a direct-fired supercritical carbon dioxide power cycle coupled to coal gasification process, Energy Convers. Manag. 156 (2018) 733–745. https://doi.org/10.1016/j.enconman.2017.11.044.

[53] Cengel Yunus A., Boles Michael A., Thermodynamics. An Engineering Approach., 7th ed., Nevada, 2011.

[54] L.F. González-Portillo, J. Muñoz-Antón, J.M. Martínez-Val, Thermodynamic analysis of multi-heating cycles working around the critical point, Appl. Therm. Eng. 174 (2020). https://doi.org/10.1016/j.applthermaleng.2020.115292.

[55] R. Span, W. Wagner, A new equation of state for carbon dioxide covering the fluid region from the triple-point temperature to 1100 K at pressures up to 800 MPa, J. Phys. Chem. Ref. Data. 25 (1996) 1509–1596. https://doi.org/10.1063/1.555991.

[56] I. Al-Siyabi, Effect of impurities on CO_2 stream properties, Institute of Petroleum Engineering, 2013.

[57] I. Tsivintzelis, G.M. Kontogeorgis, M.L. Michelsen, E.H. Stenby, Modeling phase equilibria for acid gas mixtures using the CPA equation of state. Part II: Binary mixtures with CO_2, Fluid Phase Equilib. 306 (2011) 38–56. https://doi.org/10.1016/j.fluid.2011.02.006.

[58] M. Carolina, D. Ramos, F.J. Blas, A. Galindo, Modelling the phase equilibria and excess properties of the water + carbon dioxide binary mixture, Fluid Phase Equilib. 261 (2007) 359–365. https://doi.org/https://doi.org/10.1016/j.fluid.2007.07.012.

[59] D. Lozano-Martín, G.U. Akubue, A. Moreau, D. Tuma, C.R. Chamorro, Accurate experimental (p, ρ, T) data of the (CO_2 + O_2) binary system for the development of models for CCS processes, J. Chem. Thermodyn. 150 (2020). https://doi.org/10.1016/j.jct.2020.106210.

[60] H. Li, J.P. Jakobsen, Ø. Wilhelmsen, J. Yan, PVTxy properties of CO_2 mixtures relevant for CO_2 capture, transport and storage: Review of available experimental data and theoretical models, Appl. Energy. 88 (2011) 3567–3579. https://doi.org/10.1016/j.apenergy.2011.03.052.

[61] G.M. Kontogeorgis, M.L. Michelsen, G.K. Folas, S. Derawi, N. Von Solms, E.H. Stenby, Ten Years with the CPA (Cubic-Plus-Association) equation of state. Part

1. Pure compounds and self-associating systems, Ind. Eng. Chem. Res. 45 (2006) 4855–4868. https://doi.org/10.1021/ie051305v.

[62] O. Kunz, W. Wagner, The GERG-2008 wide-range equation of state for natural gases and other mixtures: An expansion of GERG-2004, J. Chem. Eng. Data. 57 (2012) 3032–3091. https://doi.org/10.1021/je300655b.

[63] J. Gernert, R. Span, EOS-CG: A Helmholtz energy mixture model for humid gases and CCS mixtures, J. Chem. Thermodyn. 93 (2016) 274–293. https://doi.org/10.1016/j.jct.2015.05.015.

[64] H. Li, J. Yan, Impacts of equations of state (EOS) and impurities on the volume calculation of CO_2 mixtures in the applications of CO_2 capture and storage (CCS) processes, Appl. Energy. 86 (2009) 2760–2770. https://doi.org/10.1016/j.apenergy.2009.04.013.

[65] F. Okoro, A. Chapoy, P. Ahmadi, R. Burgass, Validation of cubic EoS mixing rules and multi-fluid Helmholtz energy approximation EoS for the phase behaviour modelling of CO_2-rich binary mixtures at low temperatures, Greenh. Gases Sci. Technol. 14 (2024) 829–858. https://doi.org/10.1002/ghg.2300.

[66] W. Xiong, L.-H. Zhang, Y.-L. Zhao, S.-M. Wen, L.-L. Liu, Z.-L. Cao, Y.-C. Wang, S.-G. Luo, X.-Y. Jiang, Phase equilibrium modeling for CCUS fluids using a modified association equation of state, J. Supercrit. Fluids. 219 (2025) 106543. https://doi.org/10.1016/j.supflu.2025.106543.

[67] M. Mazzoccoli, B. Bosio, E. Arato, Analysis and comparison of equations-of-state with p-ρ-T experimental data for CO_2 and CO_2-mixture pipeline transport, Energy Procedia. 23 (2012) 274–283. https://doi.org/10.1016/j.egypro.2012.06.052.

[68] T. Neumann, S. Herrig, I.H. Bell, R. Beckmüller, E.W. Lemmon, M. Thol, R. Span, EOS-CG-2021: A Mixture Model for the Calculation of Thermodynamic Properties of CCS Mixtures, Int. J. Thermophys. 44 (2023) 178. https://doi.org/10.1007/s10765-023-03263-6.

[69] C. Rivas, S.T. Blanco, J. Fernández, M. Artal, I. Velasco, Influence of methane and carbon monoxide in the volumetric behaviour of the anthropogenic CO_2: Experimental data and modelling in the critical region, Int. J. Greenh. Gas Control. 18 (2013) 264–276. https://doi.org/10.1016/j.ijggc.2013.07.019.

[70] A.G. Perez, C. Coquelet, P. Paricaud, A. Chapoy, Comparative study of vapour-liquid equilibrium and density modelling of mixtures related to carbon capture and storage with the SRK, PR, PC-SAFT and SAFT-VR Mie equations of state for industrial uses, Fluid Phase Equilib. 440 (2017) 19–35. https://doi.org/10.1016/j.fluid.2017.02.018.

[71] X. Yang, M. Richter, Z. Wang, Z. Li, Density measurements on binary mixtures (nitrogen + carbon dioxide and argon + carbon dioxide) at temperatures from (298.15 to 423.15) K with pressures from (11 to 31) MPa using a single-sinker densimeter, J. Chem. Thermodyn. 91 (2015) 17–29. https://doi.org/10.1016/j.jct.2015.07.014.

[72] J. Ke, N. Suleiman, Y. Sanchez-Vicente, T.S. Murphy, J. Rodriguez, A. Ramos, M. Poliakoff, M.W. George, The phase equilibrium and density studies of the ternary mixtures of CO_2 + Ar + N_2 and CO_2 + Ar + H_2, systems relevance to CCS technology, Int. J. Greenh. Gas Control. 56 (2017) 55–66. https://doi.org/10.1016/j.ijggc.2016.11.003.

[73] C. McKay, M. Nazeri, H. Haghighi, D. Erickson, Recommendations for the selection of equation of state during design and operation of impure CO_2 transport and storage, 16th International Conference on Greenhouse Gas Control Technologies, GHGT-16 (2022).

[74] L.F. González-Portillo, J. Muñoz-Antón, J.M. Martínez-Val, Thermodynamic mapping of power cycles working around the critical point, Energy Convers. Manag. 192 (2019) 359–373. https://doi.org/10.1016/j.enconman.2019.04.022.

[75] Y. Demirel, V. Gerbaud, Fundamentals of Nonequilibrium Thermodynamics, in: Nonequilibrium Thermodynamics, Elsevier, 2019: pp. 135–186. https://doi.org/10.1016/B978-0-444-64112-0.00003-4.

[76] K. Brun, P. Friedman, R. Dennis, Fundamentals and Applications of Supercritical Carbon Dioxide (sCO_2) Based Power Cycles, Woodhead Publishing Series in Energy, 2017.

[77] M. Bernades, F. Capuano, L. Jofre, Microconfined high-pressure transcritical fluid turbulence, Phys. Fluids. 35 (2023). https://doi.org/10.1063/5.0135388.

[78] R. Le Pierres, Primary Heat Exchangers “a la Heatric,” 2024 Supercritical CO_2 Power Cycles Symposium (2024).

[79] A.M. Johnston, W. Levy, S.O. Rumbold, Application of Printed Circuit Heat Exchanger Technology within Heterogeneous Catalytic Reactors, AIChE Annual Meeting 2001 (2001).

[80] N. Kazakov, Diffusion bonding of materials, Elsevier, 2013.

[81] A. Meshram, A.K. Jaiswal, S.D. Khivsara, J.D. Ortega, C. Ho, R. Bapat, P. Dutta, Modeling and analysis of a printed circuit heat exchanger for supercritical CO_2 power cycle applications, Appl. Therm. Eng. 109 (2016) 861–870. https://doi.org/10.1016/j.applthermaleng.2016.05.033.

[82] M. Marchionni, L. Chai, G. Bianchi, S.A. Tassou, Numerical modelling and transient analysis of a printed circuit heat exchanger used as recuperator for supercritical CO_2 heat to power conversion systems, Appl. Therm. Eng. 161 (2019) 114190. https://doi.org/10.1016/j.applthermaleng.2019.114190.

[83] X.R. Zhang, H. Yamaguchi, Forced convection heat transfer of supercritical CO_2 in a horizontal circular tube, J. Supercrit. Fluids. 41 (2007) 412–420. https://doi.org/10.1016/j.supflu.2006.11.003.

[84] D. Wu, M. Wei, R. Tian, S. Zheng, J. He, A Review of Flow and Heat Transfer Characteristics of Supercritical Carbon Dioxide under Cooling Conditions in Energy and Power Systems, Energies. 15 (2022) 8785. https://doi.org/10.3390/en15238785.

[85] J.H. Song, H.Y. Kim, H. Kim, Y.Y. Bae, Heat transfer characteristics of a supercritical fluid flow in a vertical pipe, J. Supercrit. Fluids. 44 (2008) 164–171. https://doi.org/10.1016/j.supflu.2007.11.013.

[86] X. Lei, J. Zhang, L. Gou, Q. Zhang, H. Li, Experimental study on convection heat transfer of supercritical CO_2 in small upward channels, Energy. 176 (2019) 119–130. https://doi.org/10.1016/j.energy.2019.03.109.

[87] Y.-Y. Bae, H.-Y. Kim, Convective heat transfer to CO_2 at a supercritical pressure flowing vertically upward in tubes and an annular channel, Exp. Therm. Fluid Sci. 33 (2009) 329–339. https://doi.org/10.1016/j.expthermflusci.2008.10.002.

[88] S. He, W.S. Kim, J.H. Bae, Assessment of performance of turbulence models in predicting supercritical pressure heat transfer in a vertical tube, Int. J. Heat Mass Transf. 51 (2008) 4659–4675. https://doi.org/10.1016/j.ijheatmasstransfer.2007.12.028.

[89] K.T. Lau, S.A. Khan, C. Eze, B. Tan, J. Zhao, Numerical investigation on deteriorated heat transfer of supercritical water flowing upward in tubes with variable cross-sectional geometries, Int. Commun. Heat and Mass Transfer. 136 (2022) 106203. https://doi.org/10.1016/j.icheatmasstransfer.2022.106203.

[90] Y.H. Fan, G.H. Tang, Numerical investigation on heat transfer of supercritical carbon dioxide in a vertical tube under circumferentially non-uniform heating, Appl. Therm. Eng. 138 (2018) 354–364. https://doi.org/10.1016/j.applthermaleng.2018.04.060.

[91] H. Cheng, J. Zhao, M.K. Rowinski, Study on two wall temperature peaks of supercritical fluid mixed convective heat transfer in circular tubes, Int. J. Heat Mass Transf. 113 (2017) 257–267. https://doi.org/10.1016/j.ijheatmasstransfer.2017.05.078.

[92] O. Gökkaya, E. Öztabak, H. Ahn, Experimental investigation on heat transfer characteristics of supercritical CO_2 flowing upward and downward through a microtube at low Reynolds numbers, Exp. Therm. Fluid Sci. 139 (2022) 110717. https://doi.org/10.1016/j.expthermflusci.2022.110717.

[93] D.E. Kim, M.-H. Kim, Experimental investigation of heat transfer in vertical upward and downward supercritical CO_2 flow in a circular tube, Int. J. Heat Fluid Flow. 32 (2011) 176–191. https://doi.org/10.1016/j.ijheatfluidflow.2010.09.001.

[94] J.D. Jackson, Models of heat transfer to fluids at supercritical pressure with influences of buoyancy and acceleration, Appl. Therm. Eng. 124 (2017) 1481–1491. https://doi.org/10.1016/j.applthermaleng.2017.03.146.

[95] M. Xiang, J. Guo, X. Huai, X. Cui, Thermal analysis of supercritical pressure CO_2 in horizontal tubes under cooling condition, J. Supercrit. Fluids. 130 (2017) 389–398. https://doi.org/10.1016/j.supflu.2017.04.009.

[96] H. Zhang, J. Guo, X. Cui, X. Huai, Heat transfer performance of supercritical pressure CO_2 in a non-uniformly heated horizontal tube, Int. J. Heat Mass Transf. 155 (2020) 119748. https://doi.org/10.1016/j.ijheatmasstransfer.2020.119748.

[97] G.A. Adebiyi, W.B. Hall, Experimental Investigation of heat transfer to supercritical pressure carbon dioxide in a horizontal pipe, Int. J. Heat Mass Transf. 19 (1975). https://doi.org/10.1016/0017-9310(76)90123-X-.

[98] T.H. Kim, J.G. Kwon, J.H. Park, H.S. Park, M.H. Kim, Heat transfer model for horizontal flows of CO_2 at supercritical pressures in terms of mixed convection, Int. J. Heat Mass Transf. 131 (2019) 1117–1128. https://doi.org/10.1016/j.ijheatmasstransfer.2018.11.075.

[99] X. Chu, E. Laurien, Flow stratification of supercritical CO_2 in a heated horizontal pipe, J. Supercrit. Fluids 116 (2016) 172–189. https://doi.org/10.1016/j.supflu.2016.05.003.

[100] S.M. Liao, T.S. Zhao, An experimental investigation of convection heat transfer to supercritical carbon dioxide in miniature tubes, Int. J. Heat Mass Transf. (2002) 5025–5034. https://doi.org/10.1016/S0017-9310(02)00206-5.

[101] S.H. Yoon, J.H. Kim, Y.W. Hwang, M.S. Kim, K. Min, Y. Kim, Heat transfer and pressure drop characteristics during the in-tube cooling process of carbon dioxide in the supercritical region, Int. J. Refrig. 26 (2003) 857–864. https://doi.org/10.1016/S0140-7007(03)00096-3.

[102] C. Dang, E. Hihara, In-tube cooling heat transfer of supercritical carbon dioxide. Part 1. Experimental measurement, Int. J. Refrig. 27 (2004) 736–747. https://doi.org/10.1016/j.ijrefrig.2004.04.018.

[103] X.L. Huai, S. Koyama, T.S. Zhao, An experimental study of flow and heat transfer of supercritical carbon dioxide in multi-port mini channels under cooling conditions, Chem. Eng. Sci. 60 (2005) 3337–3345. https://doi.org/10.1016/j.ces.2005.02.039.

[104] C.-H. Son, S.-J. Park, An experimental study on heat transfer and pressure drop characteristics of carbon dioxide during gas cooling process in a horizontal tube, Int. J. Refrig. 29 (2006) 539–546. https://doi.org/10.1016/j.ijrefrig.2005.10.010.

[105] H.-K. Oh, C.-H. Son, New correlation to predict the heat transfer coefficient in-tube cooling of supercritical CO_2 in horizontal macro-tubes, Exp. Therm. Fluid Sci. 34 (2010) 1230–1241. https://doi.org/10.1016/j.expthermflusci.2010.05.002.

[106] S.S. Pitla, E.A. Groll, S. Ramadhyani, Convective Heat Transfer from In-Tube Cooling of Turbulent Supercritical Carbon Dioxide: Part 2—Experimental Data and Numerical Predictions, HVAC&R Res. 7 (2001) 367–382. https://doi.org/10.1080/10789669.2001.10391281.

[107] Z.-B. Liu, Y.-L. He, Y.-F. Yang, J.-Y. Fei, Experimental study on heat transfer and pressure drop of supercritical CO_2 cooled in a large tube, Appl. Therm. Eng. 70 (2014) 307–315. https://doi.org/10.1016/j.applthermaleng.2014.05.024.

[108] S.A. Jajja, K.R. Zada, B.M. Fronk, Experimental investigation of supercritical carbon dioxide in horizontal microchannels with non-uniform heat flux boundary conditions, Int. J. Heat Mass Transf. 130 (2019) 304–319. https://doi.org/10.1016/j.ijheatmasstransfer.2018.10.027.

[109] L. Wang, Y.C. Pan, J. Der Lee, Y. Wang, B.-R. Fu, C. Pan, Experimental investigation in the local heat transfer of supercritical carbon dioxide in the uniformly heated horizontal miniature tubes, Int. J. Heat Mass Transf. 159 (2020) 120136. https://doi.org/10.1016/j.ijheatmasstransfer.2020.120136.

[110] K. Theologou, R. Mertz, E. Laurien, J. Starflinger, Experimental investigations on heat transfer of CO_2 under supercritical pressure in heated horizontal pipes, Energy. 254 (2022) 124171. https://doi.org/10.1016/j.energy.2022.124171.

[111] E. Öztabak, O. Gökkaya, H. Ahn, Heat transfer characteristics of horizontal supercritical CO_2 flow through a microtube at low Reynolds numbers and its comparison with vertical flows, Exp. Therm. Fluid Sci. 147 (2023) 110957. https://doi.org/10.1016/j.expthermflusci.2023.110957.

[112] M. Xiang, J. Guo, X. Huai, X. Cui, Thermal analysis of supercritical pressure CO_2 in horizontal tubes under cooling condition, J. Supercrit. Fluids. 130 (2017) 389–398. https://doi.org/10.1016/j.supflu.2017.04.009.

[113] Y. Zhang, M. Peng, G. Xia, T. Cong, Numerical investigation on local heat transfer characteristics of S-CO_2 in horizontal semicircular microtube, Appl. Therm. Eng. 154 (2019) 380–392. https://doi.org/10.1016/j.applthermaleng.2019.03.082.

[114] J. Wang, Z. Guan, H. Gurgenci, K. Hooman, A. Veeraragavan, X. Kang, Computational investigations of heat transfer to supercritical CO_2 in a large horizontal tube, Energy Convers. Manag. 157 (2018) 536–548. https://doi.org/10.1016/j.enconman.2017.12.046.

[115] H. Cai, S. Liang, C. Guo, T. Wang, Y. Zhu, Y. Jiang, Numerical investigation on heat transfer of supercritical carbon dioxide in the microtube heat exchanger at low Reynolds numbers, Int. J. Heat Mass Transf. 151 (2020) 119448. https://doi.org/10.1016/j.ijheatmasstransfer.2020.119448.

[116] H. Cai, Y. Jiang, T. Wang, S. Liang, Y. Zhu, Experimental investigation on convective heat transfer and pressure drop of supercritical CO_2 and water in microtube heat exchangers, Int. J. Heat Mass Transf. 163 (2020) 120443. https://doi.org/10.1016/j.ijheatmasstransfer.2020.120443.

[117] H. Cai, Y. Jiang, T. Wang, S. Liang, C. Guo, Y. Zhu, An optimization of microtube heat exchangers for supercritical CO_2 cooling based on numerical and theoretical analysis, Int. Commun. Heat Mass Transf. 127 (2021) 105532. https://doi.org/10.1016/j.icheatmasstransfer.2021.105532.

[118] K. Jin, A.B. Krishna, Z. Wong, P.S. Ayyaswamy, I. Catton, T.S. Fisher, Thermohydraulic experiments on a supercritical carbon dioxide–air microtube heat exchanger, Int. J. Heat Mass Transf. 203 (2023) 123840. https://doi.org/10.1016/j.ijheatmasstransfer.2022.123840.

[119] A.B. Krishna, K. Jin, P.S. Ayyaswamy, I. Catton, T.S. Fisher, Technoeconomic optimization of superalloy supercritical CO_2 microtube shell-and-tube-heat exchangers, Appl. Therm. Eng. 220 (2023) 119578. https://doi.org/10.1016/j.applthermaleng.2022.119578.

[120] A.B. Krishna, K. Jin, P.S. Ayyaswamy, I. Catton, T.S. Fisher, Modeling of Supercritical CO_2 Shell-and-Tube Heat Exchangers Under Extreme Conditions: Part II: Heat Exchanger Model, J. Heat Transf. 144 (2022). https://doi.org/10.1115/1.4053511.

[121] L. Chordia, M.A. Portnoff, E. Green, High Temperature Heat Exchanger Design and Fabrication for Systems with Large Pressure Differentials, Pittsburgh, PA, and Morgantown, WV (United States), 2017. https://doi.org/10.2172/1349235.

[122] S.A. Cetegen, T. Gundersen, P.I. Barton, Evaluating economic feasibility of liquid air energy storage systems in US and European markets, Energy. 300 (2024) 131524. https://doi.org/10.1016/j.energy.2024.131524.

[123] A. Castillo, D.F. Gayme, Grid-scale energy storage applications in renewable energy integration: A survey, Energy Convers. Manag. 87 (2014) 885–894. https://doi.org/10.1016/j.enconman.2014.07.063.

[124] S. Ould Amrouche, D. Rekioua, T. Rekioua, S. Bacha, Overview of energy storage in renewable energy systems, Int. J. Hydrogen Energy. 41 (2016) 20914–20927. https://doi.org/10.1016/j.ijhydene.2016.06.243.

[125] J. Xu, J. Zeng, J. Huang, A management system for energy storage, Appl. Energy. 368 (2024) 123434. https://doi.org/10.1016/j.apenergy.2024.123434.

[126] Z. Zhu, Y. Cheng, B. Xiao, H.I. Khan, H. Xu, N. Zhang, Corrosion behavior of ferritic and ferritic-martensitic steels in supercritical carbon dioxide, Energy. 175 (2019) 1075–1084. https://doi.org/10.1016/j.energy.2019.03.146.

[127] L. Teeter, B. Adam, T. Wood, J.D. Tucker, Comparison of the corrosion of materials in supercritical carbon dioxide, air, and argon environments, Corros. Sci. 192 (2021) 109752. https://doi.org/10.1016/j.corsci.2021.109752.

[128] S.H. Kim, J.-H. Cha, C. Jang, Corrosion and creep behavior of a Ni-base alloy in supercritical-carbon dioxide environment at 650 °C, Corros. Sci. 174 (2020) 108843. https://doi.org/10.1016/j.corsci.2020.108843.

[129] H. Yang, W. Liu, B. Gong, E. Jiang, Y. Huang, G. Zhang, Y. Zhao, Corrosion behavior of typical structural steels in 500 ℃, 600 ℃ and high pressure supercritical carbon dioxide conditions, Corros. Sci. 192 (2021) 109801. https://doi.org/10.1016/j.corsci.2021.109801.

[130] V. Firouzdor, K. Sridharan, G. Cao, M. Anderson, T.R. Allen, Corrosion of a stainless steel and nickel-based alloys in high temperature supercritical carbon dioxide environment, Corros. Sci. 69 (2013) 281–291. https://doi.org/10.1016/j.corsci.2012.11.041.

[131] G. Cao, V. Firouzdor, K. Sridharan, M. Anderson, T.R. Allen, Corrosion of austenitic alloys in high temperature supercritical carbon dioxide, Corros. Sci. 60 (2012) 246–255. https://doi.org/10.1016/j.corsci.2012.03.029.

[132] J. Lehmusto, J.M. Kurley, M.J. Lance, J.R. Keiser, B.A. Pint, The Impact of Impurities on Alloy Behavior in Supercritical CO_2 at 700 °C, Oxid. Met. 94 (2020) 95–111. https://doi.org/10.1007/s11085-020-09980-9.

[133] M. Mazzoccoli, B. Bosio, E. Arato, Pressure-density-temperature measurements of binary mixtures rich in CO_2 for pipeline transportation in the CCS process, J. Chem. Eng. Data. 57 (2012) 2774–2783. https://doi.org/10.1021/je300590v.

[134] M. Vitali, M. Leporini, O. Masi, A. Speranza, F. Corvaro, B. Marchetti, Net zero Flow Assurance - Validation of various equations of state for the prediction of VLE and density of CO_2-rich mixtures for CCUS applications, Int. J. Greenh. Gas Control. 125 (2023) 103877. https://doi.org/10.1016/j.ijggc.2023.103877.

[135] I.E.J. Ch, R.E. Plevan, J.A. Quinn, A.I.E.J. Ch, F.H. Rhodes, C. Bridges, I.D. Robb, A.E. Alexander, H. Rosano, V.K. Lamer, T.G. Springer, R.L. Plgford, S.J.D. Van Stralen, Nether, A New Two-Constant Equation of State, Int. J. Heat Mass Transf. 19 (1973) 1469. https://doi.org/https://doi.org/10.1021/i160057a011.

[136] G. Soave, Equilibrium constants from a modified Redlich-Kwong equation of state, Chem. Eng. Sci. 27 (1972) 1197–1203. https://doi.org/https://doi.org/10.1016/0009-2509(72)80096-4.

[137] B.I. Lee, M.G. Kesler, A generalized thermodynamic correlation based on three-parameter corresponding states, AIChE J. 21 (1975) 510–527. https://doi.org/10.1002/aic.690210313.

[138] F. Sabozin, A. Jäger, M. Thol, Enhancement of the Lee–Kesler–Plöcker Equation of State for Calculating Thermodynamic Properties of Long-Chain Alkanes, Int. J. Thermophys. 45 (2024) 69. https://doi.org/10.1007/s10765-024-03360-0.

[139] F.J. Ackerman, O. Redlich, On the Thermodynamics of Solutions. IX. Critical Properties of Mixtures and the Equation of Benedict, Webb, and Rubin, J. Chem. Phys. 38 (1963) 2740–2742. https://doi.org/10.1063/1.1733582.

[140] C. You, Z. Chen, X. Li, Q. Zhao, Y. Feng, C. Wang, Benedict–Webb–Rubin–Starling Equation of State + Hydrate Thermodynamic Theories: An Enhanced Prediction Method for CO_2 Solubility and CO_2 Hydrate Phase Equilibrium in Pure Water/NaCl Aqueous Solution System, Energies. 17 (2024) 2356. https://doi.org/10.3390/en17102356.

[141] J. Gross, G. Sadowski, Perturbed-chain SAFT: An equation of state based on a perturbation theory for chain molecules, Ind. Eng. Chem. Res. 40 (2001) 1244–1260. https://doi.org/10.1021/ie0003887.

[142] J. Gross, G. Sadowski, Application of the Perturbed-Chain SAFT Equation of State to Associating Systems, Ind. Eng. Chem. Res. 41 (2002) 5510–5515. https://doi.org/10.1021/ie010954d.

[143] I.K. Nikolaidis, R. Privat, J.-N. Jaubert, I.G. Economou, Assessment of the Perturbed Chain-Statistical Associating Fluid Theory Equation of State against a Benchmark Database of High-Quality Binary-System Data, Ind. Eng. Chem. Res. 60 (2021) 8935–8946. https://doi.org/10.1021/acs.iecr.1c01234.

[144] S. Arvelos, L.L. Rade, E.O. Watanabe, C.E. Hori, L.L. Romanielo, Evaluation of different contribution methods over the performance of Peng-Robinson and CPA equation of state in the correlation of VLE of triglycerides, fatty esters and glycerol + CO_2 and alcohol, Fluid Phase Equilib. 362 (2014) 136–146. https://doi.org/10.1016/j.fluid.2013.09.040.

[145] G.M. Kontogeorgis, E.C. Voutsas, I. V. Yakoumis, D.P. Tassios, An Equation of State for Associating Fluids, Ind Eng Chem Res 35 (1996) 4310–4318. https://doi.org/10.1021/ie9600203.

[146] S.X. Hou, G.C. Maitland, J.P.M. Trusler, Measurement and modeling of the phase behavior of the (carbon dioxide + water) mixture at temperatures from 298.15 K to 448.15 K, Journal of Supercritical Fluids 73 (2013) 87–96. https://doi.org/10.1016/j.supflu.2012.11.011.

[147] A. Valtz, A. Chapoy, C. Coquelet, P. Paricaud, D. Richon, Vapour-liquid equilibria in the carbon dioxide-water system, measurement and modelling from 278.2 to 318.2 K, Fluid Phase Equilib. 226 (2004) 333–344. https://doi.org/10.1016/j.fluid.2004.10.013.

[148] M.B. King, A. Mubarak, J.D. Kim, T.R. Bott, The Mutual Solubilities of Water with Supercritical and Liquid Carbon Dioxide, J. Supercrit. Fluids. 5 (1992) 296–302. https://doi.org/https://doi.org/10.1016/0896-8446(92)90021-B.

[149] A. Bamberger, G. Sieder, G. Maurer, High-pressure (vapor + liquid) equilibrium in binary mixtures of (carbon dioxide + water or acetic acid) at temperatures from 313 to 353 K, J. Supercrit. Fluids. 17 (2000). https://doi.org/https://doi.org/10.1016/S0896-8446(99)00054-6.

[150] I. Dalmolin, E. Skovroinski, A. Biasi, M.L. Corazza, C. Dariva, J.V. Oliveira, Solubility of carbon dioxide in binary and ternary mixtures with ethanol and water, Fluid Phase Equilib. 245 (2006) 193–200. https://doi.org/10.1016/j.fluid.2006.04.017.

[151] L.L. Hnedkovsky, H. Hnedkovsky, R.H. Wood, V. Majer, Volumes of aqueous solutions of CH_4, CO_2, H_2S, and NH_3 at temperatures from 298.15 K to 705 K

and pressures to 35 MPa, J. Chem. Thermodyn. 28 (1996) 125–142. https://doi.org/https://doi.org/10.1006/jcht.1996.0011.

[152] H.J. Greenwood, The compressibility of gaseous mixtures of carbon dioxide and water between 0 and 500 bars pressure and 450° and 800° centigrade, Am J Sci 267.A (1969) 191–208. https://doi.org/10.2475/001c.125218.

[153] A. Fenghour, W.A. Wakeham, J.T.R. Watson, Densities of (water + carbon dioxide) in the temperature range 415 K to 700 K and pressures up to 35 MPa, J. Chem. Thermodyn. 28 (1996) 433–446. https://doi.org/https://doi.org/10.1006/jcht.1996.0043.

[154] P. Chiquet, J.L. Daridon, D. Broseta, S. Thibeau, CO_2/water interfacial tensions under pressure and temperature conditions of CO_2 geological storage, Energy Convers. Manag. 48 (2007) 736–744. https://doi.org/10.1016/j.enconman.2006.09.011.

[155] M.R. Patel, P.T. Eubank, Experimental Densities and Derived Thermodynamic Properties for Carbon Dioxide - Water Mixtures, J. Chem. Eng. Data. 33 (1988) 185–193. https://doi.org/https://doi.org/10.1021/je00052a037.

[156] M.R. Patel, J.C. Holste, K.R. Hall, P.T. Eubank, Thermophysical properties of gaseous carbon dioxide-water mixtures, Fluid Phase Equilib. 36 (1987) 279–299. https://doi.org/10.1016/0378-3812(87)85029-X.

[157] L.F.S. Souza, S. Herrig, R. Span, J.P.M. Trusler, Experimental density and an improved Helmholtz-energy-explicit mixture model for (CO_2 + CO), Appl. Energy. 251 (2019). https://doi.org/10.1016/j.apenergy.2019.113398.

[158] A. Cipollina, R. Anselmo, O. Scialdone, G. Filardo, A. Galia, Experimental P-T-ρ measurements of supercritical mixtures of carbon dioxide, carbon monoxide, and hydrogen and semiquantitative estimation of their solvent power using the solubility parameter concept, J. Chem. Eng. Data. 52 (2007) 2291–2297. https://doi.org/10.1021/je700307r.

[159] Y. Sanchez-Vicente, T.C. Drage, M. Poliakoff, J. Ke, M.W. George, Densities of the carbon dioxide + hydrogen, a system of relevance to carbon capture and storage, Int. J. Greenh. Gas Control 13 (2013) 78–86. https://doi.org/10.1016/j.ijggc.2012.12.002.

[160] S. Ahamada, A. Valtz, S. Chabab, L. Blanco-Martín, C. Coquelet, Experimental Density Data of Three Carbon Dioxide and Oxygen Binary Mixtures at Temperatures from 276 to 416 K and at Pressures up to 20 MPa, J. Chem. Eng. Data. 65 (2020) 5313–5327. https://doi.org/10.1021/acs.jced.0c00484.

[161] H.B. Brugge, J.C. Holste, K.R. Hall, B.E. Gammon, K.N. Marsh, Densities of Carbon Dioxide + Nitrogen from 225 K to 450 K at Pressures up to 70 MPa, J. Chem. Eng. Data. 42 (1997). https://doi.org/https://doi.org/10.1021/je970044w.

[162] H.A. Duarte-Garza, J.C. Holste, K.R. Hall, K.N. Marsh, B.E. Gammon, Isochoric pVT and Phase Equilibrium Measurements for Carbon Dioxide + Nitrogen, J. Chem. Eng. Data. 40 (1995) 704–711. https://doi.org/https://doi.org/10.1021/je00019a038.

[163] M.E. Mondéjar, M.C. Martín, R. Span, C.R. Chamorro, New (p, ρ, T) data for carbon dioxide - Nitrogen mixtures from (250 to 400) K at pressures up to 20 MPa, J. Chem. Thermodyn. 43 (2011) 1950–1953. https://doi.org/10.1016/j.jct.2011.07.006.

[164] J.C. Seitz, J.G. Blencoe, Volumetric properties for {(1-x)CO_2 + xCH_4}, {(1-x)CO_2 + xN_2}, and {(1-x)CH_4 + xN_2} at the pressures (19.94, 29.94, 39.94, 59.93, 79.93, and 99.93) MPa and the temperature 673.15 K, J. Chem. Thermodyn. (1996) 1207–1213. https://doi.org/https://doi.org/10.1006/jcht.1996.0107.

[165] J.F. Ely, W.M. Haynes, B.C. Bain, Isochoric (p, V_m, T) measurements on CO_2 and on (0.982CO_2 + 0.018N_2) from 250 to 330 K at pressures to 35 MPa, J. Chem. Thermodyn. (1989) 879–894. https://doi.org/https://doi.org/10.1016/0021-9614(89)90036-0.

[166] C. Zhao, J. Lv, G. Li, Q. Zhang, Y. Zhang, S. Liu, Y. Chi, Densities of CO_2/N_2/O_2 ternary mixtures at temperatures from (300.15 to 353.15) K and pressures from (5 to 18) MPa, Thermochim. Acta. 676 (2019) 20–26. https://doi.org/10.1016/j.tca.2019.03.032.

[167] M. Mantovani, P. Chiesa, G. Valenti, M. Gatti, S. Consonni, Supercritical pressure-density-temperature measurements on CO_2-N_2, CO_2-O_2 and CO_2-Ar binary mixtures, J. Supercrit. Fluids. 61 (2012) 34–43. https://doi.org/10.1016/j.supflu.2011.09.001.

[168] C. Rivas, S.T. Blanco, J. Fernández, M. Artal, I. Velasco, Influence of methane and carbon monoxide in the volumetric behaviour of the anthropogenic CO_2. Experimental data and modelling in the critical region, Int. J. Greenh. Gas Control. 18 (2013) 264–276. https://doi.org/https://doi.org/10.1016/j.ijggc.2013.07.019.

[169] S. Liu, C. Zhao, J. Lv, P. Lv, Y. Zhang, Density Characteristics of the CO_2-CH_4 Binary System: Experimental Data at 313-353 K and 3-18 MPa and Modeling from the PC-SAFT EoS, J. Chem. Eng. Data. 63 (2018) 4368–4380. https://doi.org/10.1021/acs.jced.8b00433.

[170] Aspen Plus | Leading Process Simulation Software | AspenTech, (n.d.). https://www.aspentech.com/en/products/engineering/aspen-plus (accessed June 12, 2023).

[171] The MathWorks Inc, MATLAB version: 9.13.0 (R2022b), (2022). https://www.mathworks.com (accessed June 12, 2023).

[172] H. Wu, B. Zhang, W. Wang, H. Jin, Optimizing phase equilibrium predictions for the liquefaction of supercritical water gasification products: Enhancing energy storage solutions through advanced thermodynamic modeling, Energy. 308 (2024) 132845. https://doi.org/10.1016/j.energy.2024.132845.

[173] E. Cruz Sánchez-Alarcos, M.T. Garcia, I. Gracia, J.F. Rodriguez, J.M. Garcia-Vargas, Modelling of the equilibrium of supercritical CO_2 + lavender essential oil with Aspen Plus®, J. Supercrit. Fluids. 209 (2024) 106239. https://doi.org/10.1016/j.supflu.2024.106239.

[174] H.I. Britt, R.H. Luecke, The Estimation of Parameters in Nonlinear, Implicit Models, Technometrics. 15 (1973) 233. https://doi.org/10.2307/1266984.

[175] J.H. Horlock, D.T. Watson, T. V. Jones, Limitations on Gas Turbine Performance Imposed by Large Turbine Cooling Flows, J. Eng. Gas Turbine Power. 123 (2001) 487–494. https://doi.org/10.1115/1.1373398.

[176] M.A. El-Masri, On Thermodynamics of Gas-Turbine Cycles: Part 2—A Model for Expansion in Cooled Turbines, J. Eng. Gas Turbine Power. 108 (1986) 151–159. https://doi.org/10.1115/1.3239862.

[177] T.S. Kim, Comparative analysis on the part load performance of combined cycle plants considering design performance and power control strategy, Energy. 29 (2004) 71–85. https://doi.org/10.1016/S0360-5442(03)00157-9.

[178] F. Capra, E. Martelli, Numerical optimization of combined heat and power Organic Rankine Cycles – Part B: Simultaneous design & part-load optimization, Energy. 90 (2015) 329–343. https://doi.org/10.1016/j.energy.2015.06.113.

[179] K. Wimmer, W. Sanz, Optimization and comparison of the two promising oxy-combustion cycles NET Power cycle and Graz Cycle, Int. J. Greenh. Gas Control 99 (2020). https://doi.org/10.1016/j.ijggc.2020.103055.

[180] T. Xin, C. Xu, Y. Yang, V. Kindra, A. Rogalev, A new process splitting analytical method for the coal-based Allam cycle: Thermodynamic assessment and process integration, Energy. 267 (2023) 126634. https://doi.org/10.1016/j.energy.2023.126634.

[181] Verein Deutscher Ingenieure, VDI Heat Atlas, Springer Berlin Heidelberg, 2010. https://doi.org/10.1007/978-3-540-77877-6.

[182] K. Hoopes, D. Sánchez, F. Crespi, A new method for modelling off-design performance of sCO_2 heat exchangers without specifying detailed geometry, International sCO_2 power cycles symposium, San Antonio, Texas, 2016.

[183] Ramesh K. Shah, Dusan P. Srkulic, Fundamentals of heat exchanger design, John Wiley & Sons, Inc., 2003.

[184] C.G. Broyden, A class of methods for solving nonlinear simultaneous equations, Math Comput. 19 (1965) 577–593. https://doi.org/10.1090/S0025-5718-1965-0198670-6.

[185] D.M. Gay, Some Convergence Properties of Broyden's Method, SIAM J. Numer. Anal. 16 (1979) 623–630. https://doi.org/10.1137/0716047.

[186] D. Alfani, M. Astolfi, M. Binotti, P. Silva, G. Persico, Part-load analysis and preliminary annual simulation of a constant inventory supercritical CO_2 power plant for waste heat recovery in cement industry, Energy. 308 (2024) 132844. https://doi.org/10.1016/j.energy.2024.132844.

[187] Seppo A. Korpela, Principles of Turbomachinery, Second, John Wiley & Sons., Inc, The Ohio Sate, 2020.

[188] J. Andersson, Multiobjective optimization in engineering design : applications to fluid power systems, PhD dissertation, Linköpings universitet, Linköping, 2001., n.d.

[189] R. Eberhart, J. Kennedy, A new optimizer using particle swarm theory, in: MHS'95. Proceedings of the Sixth International Symposium on Micro Machine and Human Science, IEEE, n.d.: pp. 39–43. https://doi.org/10.1109/MHS.1995.494215.

[190] Joaquin R.R.A, Martins and Andrew Ning, Engineering Design Optimization., Cambridge University Press, 2021. ISBN: 9781108833417, n.d.

[191] M.J. Box, A New Method of Constrained Optimization and a Comparison With Other Methods, Comput. J. 8 (1965) 42–52. https://doi.org/10.1093/comjnl/8.1.42.

[192] J.A. Nelder, R. Mead, A Simplex Method for Function Minimization, Comput. J. 7 (1965) 308–313. https://doi.org/10.1093/comjnl/7.4.308.

[193] W. Spendley, G.R. Hext, F.R. Himsworth, Sequential Application of Simplex Designs in Optimisation and Evolutionary Operation, Technometrics. 4 (1962) 441–461. https://doi.org/10.1080/00401706.1962.10490033.

[194] E. Martelli, E. Amaldi, PGS-COM: A hybrid method for constrained non-smooth black-box optimization problems, Comput. Chem. Eng. 63 (2014) 108–139. https://doi.org/10.1016/j.compchemeng.2013.12.014.

[195] Q. Zhao, M. Mecheri, T. Neveux, R. Privat, J.N. Jaubert, Selection of a Proper Equation of State for the Modeling of a Supercritical CO_2 Brayton Cycle: Consequences on the Process Design, Ind. Eng. Chem. Res. 56 (2017) 6841–6853. https://doi.org/10.1021/acs.iecr.7b00917.

[196] O.E. Balje´, A Study on Design Criteria and Matching of Turbomachines: Part A—Similarity Relations and Design Criteria of Turbines, J. Eng. Power. 84 (1962) 83–102. https://doi.org/10.1115/1.3673386.

[197] D. Fleming, T. Holschuh, T. Conboy, G. Rochau, R. Fuller, Scaling Considerations for a Multi-Megawatt Class Supercritical CO_2 Brayton Cycle and Path Forward for Commercialization, in: Volume 5: Manufacturing Materials and Metallurgy; Marine; Microturbines and Small Turbomachinery; Supercritical CO_2 Power Cycles, ASME. 2012: pp. 953–960. https://doi.org/10.1115/GT2012-68484.

[198] Y. Du, C. Yang, H. Wang, C. Hu, One-dimensional optimisation design and off-design operation strategy of centrifugal compressor for supercritical carbon dioxide Brayton cycle, Appl. Therm. Eng. 196 (2021) 117318. https://doi.org/10.1016/j.applthermaleng.2021.117318.

[199] E.E. Didier, G.A. Perez, Short cut method for cost estimation in distillation columns, Cost Engineering (2003).

[200] H. Li, B. Dong, Z. Yu, J. Yan, K. Zhu, Thermo-physical properties of CO_2 mixtures and their impacts on CO_2 capture, transport and storage: Progress since 2011, Appl. Energy. 255 (2019). https://doi.org/10.1016/j.apenergy.2019.113789.

[201] M. Ibrahim, G. Skaugen, I.S. Ertesvåg, T. Haug-Warberg, Modelling CO_2 - water mixture thermodynamics using various equations of state (EoSs) with emphasis on the potential of the SPUNG EoS, Chem. Eng. Sci. 113 (2014) 22–34. https://doi.org/https://doi.org/10.1016/j.ces.2014.03.025.

[202] F. Wu, M.D. Argyle, P.A. Dellenback, M. Fan, Progress in O_2 separation for oxy-fuel combustion–A promising way for cost-effective CO_2 capture: A review, Prog. Energy Combust. Sci. 67 (2018) 188–205. https://doi.org/10.1016/j.pecs.2018.01.004.

[203] F. Okoro, A. Chapoy, P. Ahmadi, R. Burgass, Effects of non-condensable CCUS impurities (CH_4, O_2, Ar and N_2) on the saturation properties (bubble points) of CO_2-rich binary systems at low temperatures (228.15 – 273.15 K), Greenh. Gases Sci. Technol. 14 (2024) 62–94. https://doi.org/10.1002/ghg.2252.

[204] National Instruments Corp., LabVIEW 2024 Q1, (2024).

[205] Y. Jiang, E. Liese, S.E. Zitney, D. Bhattacharyya, Optimal design of microtube recuperators for an indirect supercritical carbon dioxide recompression closed Brayton cycle, Appl. Energy. 216 (2018) 634–648. https://doi.org/10.1016/j.apenergy.2018.02.082.

[206] T.K. Chu, C.Y. Ho, Thermal Conductivity and Electrical Resistivity of Eight Selected AISI Stainless Steels, in: Thermal Conductivity 15, Springer US, Boston, MA, 1978: pp. 79–104. https://doi.org/10.1007/978-1-4615-9083-5_12.

[207] E. W. Lemmon and I. H. Bell and M. L. Huber and M. O. McLinden, NIST Standard Reference Database 23: Reference Fluid Thermodynamic and Transport Properties-REFPROP, Version 10.0, National Institute of Standards and Technology, (2018).

[208] S.J. Kline, F.A. McClintock, Describing uncertainties in single-sample experiments, Mechanical Engineering (1953).

[209] Inc. Statgraphics Technologies, Statgraphics Centurion 19, (2024).

[210] INC. ANSYS, ANSYS Fluent 12.0 Theory Guide, 2024.

[211] V. Michalcová, K. Kotrasová, The Numerical Diffusion Effect on the CFD Simulation Accuracy of Velocity and Temperature Field for the Application of Sustainable Architecture Methodology, Sustainability. 12 (2020) 10173. https://doi.org/10.3390/su122310173.

[212] H. Schlichting, K. Gersten, Boundary-Layer Theory, 9th ed., Springer Berlin Heidelberg, Berlin, Heidelberg, 2017. https://doi.org/10.1007/978-3-662-52919-5.

[213] O. Reynolds, IV. On the dynamical theory of incompressible viscous fluids and the determination of the criterion, Philos. Trans. R. Soc. Lond. A. 186 (1895) 123–164. https://doi.org/10.1098/rsta.1895.0004.

[214] C. Chen, J.J. Riley, P.A. McMurtry, A study of Favre averaging in turbulent flows with chemical reaction, Combust. Flame. 87 (1991) 257–277. https://doi.org/10.1016/0010-2180(91)90112-O.

[215] J. Tu, C. Liu, G.-H. Yeoh, Computational Fluid Dynamics, 3rd ed., Elsevier, 2018. https://doi.org/10.1016/C2015-0-06135-4.

[216] F.G. Schmitt, About Boussinesq's turbulent viscosity hypothesis: historical remarks and a direct evaluation of its validity, Comptes. Rendus. Mécanique. 335 (2007) 617–627. https://doi.org/10.1016/j.crme.2007.08.004.

[217] O. Reynolds, On the extent and action of the heating surface of steam boilers, Int J. Heat Mass Transf. 3 (1961) 163–166. https://doi.org/10.1016/0017-9310(61)90087-4.

[218] J. Smagorinsky, General circulation experiments with the primitive equations, Mon Weather Rev 91 (1963) 99–164. https://doi.org/10.1175/1520-0493(1963)091<0099:GCEWTP>2.3.CO;2.

[219] Q. Li, P. Schlatter, L. Brandt, D.S. Henningson, DNS of a spatially developing turbulent boundary layer with passive scalar transport, Int. J. Heat Fluid Flow. 30 (2009) 916–929. https://doi.org/10.1016/j.ijheatfluidflow.2009.06.007.

[220] D. Elkaim, M. Reggio, R. Camarero, Simulating two-dimensional turbulent flow by using the k-ε model and the vorticity-streamfunction formulation, Int. J. Numer. Methods Fluids. (1992) 961–980. https://doi.org/10.1002/fld.1650140806.

[221] S.H. Kim, Y.I. Kim, B.H. Joe, Y.Y. Bae, Numerical simulation of the vertical upward flow of water in a heated tube at the supercritical pressure, 2003 Autumn Meeting of the KNS (2003).

[222] B.E. Launder, B.I. Sharma, Application of the energy-dissipation model of turbulence to the calculation of flow near a spinning disc, Lett. Heat Mass Transf. 1 (1974) 131–137. https://doi.org/10.1016/0094-4548(74)90150-7.

[223] Z. Yang, T.H. Shih, New time scale based k-epsilon model for near-wall turbulence, AIAA J. 31 (1993) 1191–1198. https://doi.org/10.2514/3.11752.

[224] K. Abe, T. Kondoh, Y. Nagano, A new turbulence model for predicting fluid flow and heat transfer in separating and reattaching flows—I. Flow field calculations, Int. J. Heat Mass Transf. 37 (1994) 139–151. https://doi.org/10.1016/0017-9310(94)90168-6.

[225] F.R. Menter, Two-equation eddy-viscosity turbulence models for engineering applications, AIAA J. 32 (1994) 1598–1605. https://doi.org/10.2514/3.12149.

[226] C.J. Chen, Fundamentals of Turbulence Modelling, CRC Press, 1997.

[227] H.K. Versteeg, W. Malalasekera, An Introduction to Computational Fluid Dynamics. The Finite Volume Method., 2nd ed., Prentice Hall, 2007.

[228] B.P. Leonard, A stable and accurate convective modelling procedure based on quadratic upstream interpolation, Comput. Methods Appl. Mech. Eng. 19 (1979) 59–98. https://doi.org/10.1016/0045-7825(79)90034-3.

[229] M. Sharabi, W. Ambrosini, S. He, J.D. Jackson, Prediction of turbulent convective heat transfer to a fluid at supercritical pressure in square and

triangular channels, Ann. Nucl. Energy. 35 (2008) 993–1005. https://doi.org/10.1016/j.anucene.2007.11.006.

[230] D.K. Kolmogorov, W.Z. Shen, N.N. Sørensen, J.N. Sørensen, Fully Consistent SIMPLE-Like Algorithms on Collocated Grids, Num. Heat Transf., Part B: Fundamentals 67 (2015) 101–123. https://doi.org/10.1080/10407790.2014.949583.

[231] A. Brandt, Algebraic multigrid theory: The symmetric case, Appl. Math Comput. 19 (1986) 23–56. https://doi.org/10.1016/0096-3003(86)90095-0.

[232] J. Blazek, Computational Fluid Dynamics: Principles and Applications, 3rd ed., Elsevier, 2015. https://doi.org/10.1016/C2013-0-19038-1.

[233] G. Kalitzin, G. Medic, G. Iaccarino, P. Durbin, Near-wall behavior of RANS turbulence models and implications for wall functions, J. Comput. Phys. 204 (2005) 265–291. https://doi.org/10.1016/j.jcp.2004.10.018.

[234] I. Velázquez, F. Demeyer, M. Reyes, Investigation of the impact of the thermodynamic property method on the performance, preliminary component sizing and maximum efficiency configuration of the NET power cycle, Appl. Therm. Eng. (2025) 126491. https://doi.org/10.1016/j.applthermaleng.2025.126491.

[235] J.M. Coulson, J.F. Richardson, Chemical Engineering, 6th ed., Elsevier, 1993. https://doi.org/10.1016/C2009-0-11215-1.

[236] Tubular Exchanger Manufacturers Association (TEMA), Standards of the tubular exchanger manufacturers association, 11th ed., 2023.

[237] M. Carlson, T. Conboy, D. Fleming, J. Pasch, Scaling Considerations for SCO_2 Cycle Heat Exchangers, in: Volume 3B: Oil and Gas Applications; Organic Rankine Cycle Power Systems; Supercritical CO_2 Power Cycles; Wind Energy, ASME, 2014. https://doi.org/10.1115/GT2014-27233.

[238] ASME International, ASME Boiler and Pressure Vessel, An International Code: Section 2 Materials, Part D: Properties., 2019.

[239] P. Rączka, K. Wójs, Methods of Thermal Calculations for a Condensing Waste-Heat Exchanger, Chem. Process Eng. 35 (2014) 447–461. https://doi.org/10.2478/cpe-2014-0034.

[240] K. Jeong, M.J. Kessen, H. Bilirgen, E.K. Levy, Analytical modeling of water condensation in condensing heat exchanger, Int. J. Heat Mass Transf. 53 (2010) 2361–2368. https://doi.org/10.1016/j.ijheatmasstransfer.2010.02.004.

[241] Y.A. Cengel, A.J. Ghajar, Heat and Mass Transfer: Fundamentals and Applications, 4th ed., McGraw-Hill Education, 2011.

[242] M.F. Monteiro, M.H. Moura-Neto, C.G. Pereira, O. Chiavone-Filho, Description of phase equilibrium and volumetric properties for CO_2 + water and CO_2 + ethanol using the CPA equation of state, J. Supercrit. Fluids. 161 (2020). https://doi.org/10.1016/j.supflu.2020.104841.

[243] J.S. Gallagher, R. Crovetto, J.M.H.L. Sengers, The Thermodynamic Behavior of the CO_2-H_2O System from 400 to 1000 K, up to 100 MPa and 30% Mole Fraction of CO_2, J. Phys. Chem. Ref. Data. 22 (1993) 431–513. https://doi.org/10.1063/1.555938.

[244] T.H. Chilton, A.P. Colburn, Mass Transfer Coefficients: Prediction from Data on Heat Transfer and Fluid Friction, Ind. Eng. Chem. (1934). https://doi.org/10.1021/ie50299a012.

[245] A.P. Colburn, T.N. Drew, The condensation of mixed vapors, American Institute of Chemical Engineers New York (1937).

[246] G. Ackermann, Combined Heat and Mass Transfer at High Temperature and Partial Pressure Differences, Porsch. Ing. Wes. (1937).

[247] L. Cheng, G. Ribatski, J.R. Thome, Analysis of supercritical CO_2 cooling in macro- and micro-channels, Int. J. Refrig. 31 (2008) 1301–1316. https://doi.org/10.1016/j.ijrefrig.2008.01.010.

[248] H. Martin, Lecture on heat transfer II, Universitaet Karlsruhe (TH) (1990).

[249] V. Gnielinski, New equations for heat and mass transfer in the turbulent flow in pipes and channels, NASA STI/Recon Technical Report A. 41 (1975) 8–16.

[250] X. Huai, S. Koyama, Heat Transfer Characteristics of Supercritical CO_2 Flow in Small-Channeled Structures, Exp. Heat Transf. 20 (2007) 19–33. https://doi.org/10.1080/08916150600977424.

[251] W. Nusslet, Die Oberflächenkondensation des Wasserdampfes, Z VDI 60 (1916) 541–546.

[252] J. Müller, Wärmeübergang bei der Filmkondensation und seine Einordnung in Wärme- und Stoffübertragungsvorgänge bei Filmströmungen, Fortsch Ber VDI 3 (1992).

[253] Y.A. Cengel, J.M. Cimbala, Fluid mechanics: Fundamentals and applications, 4th ed., McGraw-Hill Education, Columbus, OH, 2024.

[254] R. Numrich, Influence of Gas Flow on Heat Transfer in Film Condensation, Chem. Eng. Technol. 13 (1990) 136–143. https://doi.org/10.1002/ceat.270130119.

[255] R. Numrich, N. Claus, M. Hadley, Influence of gas flow on condensation process, Eurotherm Seminar, Paris (1995). https://doi.org/10.1002/ceat.270130119.

[256] E.N. Fuller, K. Ensley, J.C. Giddings, Diffusion of halogenated hydrocarbons in helium. The effect of structure on collision cross sections, J. Phys. Chem. 73 (1969) 3679–3685. https://doi.org/10.1021/j100845a020.

[257] B.E. Poling, J.M. Prausnitz, J.P. O'Connell, Properties of Gases and Liquids, 5th edition, McGraw-Hill Education, New York, 2001.

[258] I.E. Idelchik, Handbook of Hydraulic Resistance, Begell House, New York, 2007.

[259] E. Romeo, C. Royo, A. Monzón, Improved explicit equations for estimation of the friction factor in rough and smooth pipes, Chem. Eng. J. 86 (2002) 369–374. https://doi.org/10.1016/S1385-8947(01)00254-6.

[260] G. Musgrove, S. Sullivan, D. Shiferaw, P. Fourspring, L. Chordia, Heat exchangers, in: Fundamentals and Applications of Supercritical Carbon Dioxide (SCO_2) Based Power Cycles, Elsevier, 2017: pp. 217–244. https://doi.org/10.1016/B978-0-08-100804-1.00008-6.

[261] J. Arrieta, R. Ferreira, Pardo, A. Rodríguez-Bernal, Análisis Numérico de Ecuaciones Diferenciales Ordinarias, Paraninfo, Madrid, 2020.

[262] J. Xie, D. Liu, H. Yan, G. Xie, S.K.S. Boetcher, A review of heat transfer deterioration of supercritical carbon dioxide flowing in vertical tubes: Heat transfer behaviors, identification methods, critical heat fluxes, and heat transfer correlations, Int. J. Heat Mass Transf. 149 (2020) 119233. https://doi.org/10.1016/j.ijheatmasstransfer.2019.119233.

[263] B. Zhu, J. Xu, X. Wu, J. Xie, M. Li, Supercritical "boiling" number, a new parameter to distinguish two regimes of carbon dioxide heat transfer in tubes, Int. J. Therm. Sci. 136 (2019) 254–266. https://doi.org/10.1016/j.ijthermalsci.2018.10.032.

[264] B.S. Petukhov, A.F. Poliakov, B.E. Launder, A.F. Polëiakov, Heat transfer in turbulent mixed convection, Hemisphere Pub. Corp., 1988. https://inis.iaea.org/search/search.aspx?orig_q=RN:19092970 (accessed December 13, 2024).

[265] K. Tanimizu, R. Sadr, Experimental investigation of buoyancy effects on convection heat transfer of supercritical CO_2 flow in a horizontal tube, Heat Mass Transf. 52 (2016) 713–726. https://doi.org/10.1007/s00231-015-1580-9.

[266] P.-X. Jiang, B. Liu, C.-R. Zhao, F. Luo, Convection heat transfer of supercritical pressure carbon dioxide in a vertical micro tube from transition to turbulent flow regime, Int. J. Heat Mass Transf. 56 (2013) 741–749. https://doi.org/10.1016/j.ijheatmasstransfer.2012.08.038.

[267] D.M. McEligot, C.W. Coon, H.C. Perkins, Relaminarization in tubes, Int. J. Heat Mass Transf. 13 (1970) 431–433. https://doi.org/10.1016/0017-9310(70)90118-3.

[268] B. Petukhov, B. Kurganov, B. Ankudinov, Heat transfer and flow resistance in the turbulent pipe flow of a fluid with near-critical state parameters, Inst. High Temps. 21 (1983) 92–100.

[269] J.D. Jackson, Fluid flow and convective heat transfer to fluids at supercritical pressure, Nucl. Eng. Des. 264 (2013) 24–40. https://doi.org/10.1016/j.nucengdes.2012.09.040.

[270] L.F. Cabeza, A. de Gracia, A.I. Fernández, M.M. Farid, Supercritical CO_2 as heat transfer fluid: A review, Appl. Therm. Eng. 125 (2017) 799–810. https://doi.org/10.1016/j.applthermaleng.2017.07.049.

[271] I.L. Pioro, H.F. Khartabil, R.B. Duffey, Heat transfer to supercritical fluids flowing in channels - empirical correlations (survey), Nucl. Eng. Des. 230 (2004) 69–91. https://doi.org/10.1016/j.nucengdes.2003.10.010.

[272] H.S. Swenson, J.R. Carver, C.R. Kakarala, Heat Transfer to Supercritical Water in Smooth-Bore Tubes, J. Heat Transf. 87 (1965) 477–483. https://doi.org/10.1115/1.3689139.

[273] T. Preda, E. Saltanov, I. Pioro, K.S. Gabriel, Development of a Heat Transfer Correlation for Supercritical CO_2 Based on Multiple Data Sets, in: Volume 5: Fusion Engineering; Student Paper Competition; Design Basis and Beyond Design Basis Events; Simple and Combined Cycles, ASME. 2012: pp. 211–217. https://doi.org/10.1115/ICONE20-POWER2012-54516.

[274] F. Dittus, L. Boelter, Heat transfer in automobile radiators of the tubular type, Int. Commun. Heat Mass Transf. 12 (1985) 3–22. https://doi.org/10.1016/0735-1933(85)90003-X.

[275] J.H. Park, M.H. Kim, Modeling of local heat transfer on supercritical pressure CO_2 in horizontal semicircular tube, Int. J. Heat Mass Transf. 184 (2022) 122197. https://doi.org/10.1016/j.ijheatmasstransfer.2021.122197.

[276] T.H. Kim, J.G. Kwon, J.H. Park, H.S. Park, M.H. Kim, Heat transfer model for horizontal flows of CO_2 at supercritical pressures in terms of mixed convection, Int. J. Heat Mass Transf. 131 (2019) 1117–1128. https://doi.org/10.1016/j.ijheatmasstransfer.2018.11.075.

[277] D.E. Kim, M.H. Kim, Two layer heat transfer model for supercritical fluid flow in a vertical tube, J. Supercrit. Fluids. 58 (2011) 15–25. https://doi.org/10.1016/j.supflu.2011.04.014.

[278] X. Lei, H. Li, N. Dinh, W. Zhang, A study of heat transfer scaling of supercritical pressure water in horizontal tubes, Int. J. Heat Mass Transf. 114 (2017) 923–933. https://doi.org/10.1016/j.ijheatmasstransfer.2017.06.052.

[279] S. Mokry, I. Pioro, A. Farah, K. King, S. Gupta, W. Peiman, P. Kirillov, Development of supercritical water heat-transfer correlation for vertical bare tubes, Nucl. Eng. Des. 241 (2011) 1126–1136. https://doi.org/10.1016/j.nucengdes.2010.06.012.

[280] J. Wang, Z. Guan, H. Gurgenci, A. Veeraragavan, X. Kang, K. Hooman, A computationally derived heat transfer correlation for in-tube cooling turbulent supercritical CO_2, Int. J. Therm. Sci. 138 (2019) 190–205. https://doi.org/10.1016/j.ijthermalsci.2018.12.045.

[281] A. Menon, K. Mehrotra, C.K. Mohan, S. Ranka, Characterization of a Class of Sigmoid Functions with Applications to Neural Networks, Neural Networks 9 (1996) 819–835. https://doi.org/10.1016/0893-6080(95)00107-7.

[282] K. Xu, B. Ruan, H. Meng, Validation and analyses of RANS CFD models for turbulent heat transfer of hydrocarbon fuels at supercritical pressures, Int. J. Therm. Sci. 124 (2018) 212–226. https://doi.org/10.1016/j.ijthermalsci.2017.10.019.

[283] Z. Du, W. Lin, A. Gu, Numerical investigation of cooling heat transfer to supercritical CO_2 in a horizontal circular tube, J. Supercrit. Fluids. 55 (2010) 116–121. https://doi.org/10.1016/j.supflu.2010.05.023.

[284] U. Manda, A. Parahovnik, S. Mazumdar, Y. Peles, Heat transfer characteristics of turbulent flow of supercritical carbon dioxide (sCO_2) in a short-heated microchannel, Int. J. Therm. Sci. 192 (2023) 108389. https://doi.org/10.1016/j.ijthermalsci.2023.108389.

[285] P. Bergé, M. Dubois, Rayleigh-bénard convection, Contemp. Phys. 25 (1984) 535–582. https://doi.org/10.1080/00107518408210730.

[286] I. Velázquez, F. Demeyer, M. Reyes, Optimization and performance evaluation of equations of state for supercritical CO_2-rich mixtures for application in the NET Power cycle, J. Supercrit. Fluids. (2025) 106693. https://doi.org/10.1016/j.supflu.2025.106693.

[287] P. Andreussi, The onset of droplet entrainment in annular downward flows, Can J. Chem. Eng. 58 (1980) 267–270. https://doi.org/10.1002/cjce.5450580220.

[288] RG. Owen, WC. Lee, A review of Some Recent Developments in Condensation Theory, Inst. Chem. Eng. Symp. 74 (1983) 261–293. https://doi.org/10.31026/j.eng.2010.01.25.